Stress and creep damage evolution in materials for ultra-supercritical power plants

Thesis

The Open University

Faculty of Mathematics, Computing & Technology

Department of Design, Development, Environment and Materials

Materials Engineering Group

STRESS AND CREEP DAMAGE EVOLUTION IN MATERIALS FOR ULTRA-SUPERCRITICAL POWER PLANTS

by

Sanjooram Paddea

August 2013

A THESIS SUMMITTED TO THE DEPARTMENT OF DESIGN, DEVELOPMENT, ENVIRONMENT AND MATERIALS OF THE OPEN UNIVERSITY FOR THE DEGREE OF DOCTOR OF PHILOSOPHY

DATE OF SUBMISSION : 21 AUGUST 2013

DATE OF AWARD : 23 OCTOBER 2013

Abstract

The so-called creep strength enhanced ferritic (CSEF) 9-12% Cr steels have been identified as the most promising class of materials for some of the key components in ultra-supercritical fossil-fired power plants, including the main steam pipes, headers and superheater tubings. These steels are less costly, and they have a lower coefficient of thermal expansion and a higher thermal conductivity when compared with austenitic stainless steels, making them less susceptible to degradation through thermal fatigue. However, experience has shown that the weldments in these steels are particularly prone to premature creep failure, due to a localised form of cracking in the heat-affected zone (HAZ), which is referred to as Type IV cracking.

The work presented in this thesis is concerned with the effects of residual stresses and constraint on Type IV cracking. In the first part of this work, the residual stresses in a 25.4 mm thick, 324 mm diameter pipe girth weld, made in a P91 steel pipe, have been measured in both the as-welded and post weld heat treated (PWHT) conditions using neutron diffraction, and compared with the corresponding metallurgical zones across each weld. It was found that the highest as-welded tensile stresses resided near the outer boundary of the HAZ, and towards the weld root region and these were not fully relieved by the applied PWHT. In both conditions substantial tensile direct and hydrostatic stresses existed across the HAZ, including the fine-grained and intercritically-annealed regions, where premature Type IV creep failures manifest in 9-12% Cr steel welds.

Compressive stresses were found in the weld metal coinciding with the last weld bead to be deposited.

In the second part of the work, creep tests were conducted at 625°C on cross-weld and simulated fine-grained HAZ specimens. The contributions of specific influences on creep performance (such as residual stress, constraint and creep damage associated with relaxation of residual stresses during PWHT) were then systematically examined. It was found that the geometric constraint (introducing a triaxial stress state) was beneficial in improving creep rupture life and that residual stresses (of the order of 50 MPa) showed a clear reduction in life. Moreover there was some evidence that residual stress relaxation associated with PWHT may introduce some creep damage.

The digital image correlation (DIC) technique was applied to resolve tensile and time-dependent creep deformation properties along the length of P91 cross-weld samples. The results demonstrated the capability of the DIC technique for full field measurement of strain during both room-temperature-tensile and high temperature creep tests in the vicinity of welded joints, where the gradients in microstructure and mechanical properties can be steep.

Acknowledgements

I would like to acknowledge the Engineering & Physical Sciences Research Council (U.K.) for the provision of financial support under Grant Number EP/G068305/1, which made this work possible.

My deepest gratitude to Dr. John Francis (University of Manchester), Professor John Bouchard, Dr. Anna Paradowska (ANSTO, formerly with ISIS), Dr. Ahmed Shibli (European Technology Development) and Professor Michael Fitzpatrick for their supervision, advice, support and crucial contribution throughout this project.

Neutron beamtime allocation at the ISIS Pulsed Neutron and Muon Source and ANSTO OPAL research reactor are gratefully acknowledged.

I am grateful to the following people for their assistance with my work:

- Professor Sayee Raghunathan, Mr. Marcello Consonni and Dr. John Rothwell at TWI for carrying out the welding experiments.
- Mr. Pete Ledgard, Mr. Damian Flack, Mr. Stan Hiller, Dr. Colin Gagg (formerly at The Open University) and Mr. Gordon Imlach for their workshop support and assistance with many of the experiments.
- Mr. Stuart Morse at The University of Manchester for assistance with the Gleeble 3500 thermo-mechanical simulator.

- Dr. Andreas Klenk and Mr. Theofel Henrich at MPA Stuttgart for their assistance with induction heating microstructural simulation.
- Support staff at The Open University, in particular Courtney and Olivia.
- Dr. Yuki Sakanashi, Dr. Imran Bhamji and Dr. Alex Forsey for assistance with the digital image correlation.
- All my colleagues in the Materials Engineering group for invaluable discussions and support.

Further thanks to Dr. Anna Paradowska, Dr. Mike Drew, Dr. Shu-Yan Zhang, Dr. Joe Kelleher and all members of the Bragg Institute at the Australian Nuclear Science and Technology Organisation (ANSTO) for making an enjoyable and fruitful research stay at their institution possible. I would like to express my gratitude to ANSTO, The Armourers & Brasiers Gauntlet Trust and The Open University for their financial support.

Finally, I convey my special acknowledgements to my family and friends (with special mention to Yeli, David, Suyash, Yanouj, Rawshi, Prithee, and Krish) for their continuous support and encouragement.

Preface

This thesis is submitted for the degree of Doctor of Philosophy of The Open University, United Kingdom. The work described in this thesis was carried out in the Department of the Materials Engineering, Faculty of Mathematics, Computing and Technology, between October 2009 and August 2013 under the supervision of Professor Peter John Bouchard, Dr. John Anthony Francis, Dr. Anna Maria Paradowska and Dr. Ahmed Shibli.

Except where clearly referenced, the work is entirely the author's own work. None of this work has been submitted for a degree or qualification at this or other university. Some of the results of this work have been published in an academic journal, conference proceedings and as oral or poster presentations as listed below:

1. **Paddea S**, Francis JA, Paradowska AM, Bouchard PJ, Shibli IA. Residual stress distributions in a P91 steel pipe girth weld before and after post weld heat treatment. Materials Science and Engineering A. 534, pp. 663-672 (2012).

2. Paradowska A M, Tremsin A, Kelleher J, Zhang S Y, **Paddea S**, Burca G, James J A, Ahmed R A, Faisal N H, Grazzi F, Festa G, Andreani C, Civita F, Bouchard P J, Kockelman W, and Fitzpatrick M E. Modern and historical engineering concerns investigated by neutron diffraction on ENGIN-X. *Journal of Solid Mechanics and Materials Engineering*, 6(6), pp. 408–418 (2012).

3. **Paddea S**, Francis JA, Paradowska AM, Bouchard PJ, Shibli IA. Characterisation of residual stresses in a welded P91 steel pipe section using neutron diffraction. In: *8th European Conference on Residual Stresses*, 26-28 June 2010, Riva del Garda, Italy (2010).

4. **Paddea S**, Francis JA, Paradowska AM, Bouchard PJ, Shibli IA. Characterisation of residual stresses in a welded P91 steel pipe section using neutron diffraction. In: 5th International Conference on High Temperature Defect Assessment (HIDA 5), 23-25 June 2010, Surrey, UK (2010).

Table of Contents

List of Figures

List of Tables

Chapter 1

Introduction

1.1 Background

Global energy demand is expected to be about 30 percent higher in 2040 compared to 2010 [1], as economic output more than doubles and prosperity expands across a world whose population will grow to nearly 9 billion people. The world derives its energy from different sources: coal, gas, oil, renewables and nuclear. Although nuclear power seemed like 'the answer to the engineer's prayer', competitive gas prices and government policies may result in a decline in nuclear power generation capacity in the years to come. Following the disaster at the Fukushima nuclear power plant in Japan, many governments have reviewed plans for new nuclear installations. For example, Germany has decided on a complete nuclear phase-out by 2022 followed by Thailand and others who have suspended approvals for new nuclear power plants until a safety review has been completed [2].

The long term impact of the rise in energy demands is not yet foreseeable, but it is reasonable to assume that fossil-fired power stations will continue to be the predominant form of energy generation for decades to come. However, concern has also grown in recent decades about environmental impact. Climate change, as a result of rising greenhouse gas emissions, threatens the stability of the world's climate and economy. In Australia, for example, the recently introduced "carbon tax" [3] is likely to impact the way

Australia produces its electricity in the future. China in particular is investing in renewable energy and plans are in place to build almost 10 times the wind capacity of Germany. But even this will not be able to keep up with demand, meaning fossil fuels will continue to make up the majority of the overall energy mix for the foreseeable future. And when it comes to fossil fuels, coal is the easy winner - it is generally easier and cheaper to mine, and easier to transport using existing infrastructure such as roads and rail, than oil or gas [4].

If the level of electricity generation capacity is to be maintained while doing our duty towards the environment, then there is a need for new, low-emission and cost effective fossil power plants. Significant reductions in CO_2 emissions can be achieved by the use of clean coal technologies [5]. Through the use of advanced boilers, improved turbines and gasifiers, higher temperatures and pressures, a higher efficiency can be achieved as shown in Figure 1-1. Some of these technologies can also be used to retrofit existing (old) power stations.

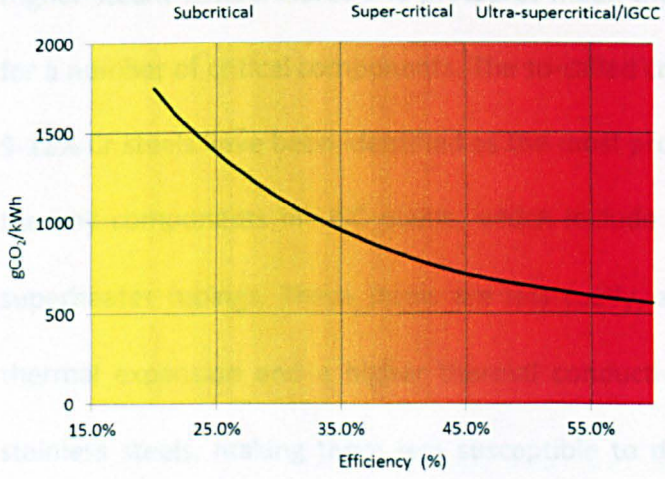

Figure 1-1: Increase in efficiency (in %) and reduction of CO_2 emissions (in gCO_2/kWh) with the introduction of supercritical and ultra-supercritical power plants (adapted from [6]).

In recent years there has been a trend towards the construction of ultra-supercritical (USC) power plants, where the steam pressures can exceed 30 MPa, and where typical service temperatures are in the range of 570–630°C [6,7]. Such power plants can achieve efficiencies in the vicinity of 45% [7], which compares with a typical efficiency for a conventional fossil-fired plant, operating at ~17 MPa and 560°C, of 25–30% [7]. Conventional subcritical units operate at temperatures and pressures such that the water boils before being converted to superheated steam. On the other hand, supercritical (SC) and ultra-supercritical (USC) units operate at conditions above the critical point of water (374°C, 22 MPa), i.e. above the temperature and pressure at which addition of heat and/or pressure does not cause a change of state, and thus, boiling does not occur. Further increases in efficiency can be achieved through the use of Integrated Gasification Combined Cycle (IGCC) which uses a gasifier to convert coal to synthethic gas (a gas mixture that comprises of carbon monoxide, carbon dioxide and hydrogen, also known as syngas), which drives a combined cycle turbine [9].

Higher steam temperatures and pressures mean that superior materials will be required for a number of critical components. The so-called creep strength enhanced ferritic (CSEF) 9-12% Cr steels have been identified as the most promising class of materials for some of the key components in USC plants, which include the main steam pipes, headers and superheater tubings. These steels are less costly, and they have a lower coefficient of thermal expansion and a higher thermal conductivity when compared with austenitic stainless steels, making them less susceptible to degradation through thermal fatigue. One of the first to be developed was ASTM P91 (9Cr–1Mo) steel [10]. The earliest grades of this steel were considerably improved through small additions of V, Nb and N, and now modified P91 steel is recommended for service at temperatures up to 600°C, which

compares well with allowable operating temperatures of up to 560°C for earlier grades such as P22 (2.25Cr–1Mo). Consequently, P91 steel has seen widespread application in fossil fired power plants. More recently 9–12 Cr steels, such as P92, with allowable service temperatures of up to 625°C have been developed [11].

Unfortunately, the potential gains in plant efficiency that were offered by P91 and other 9–12 Cr steels have in practice been restricted by premature failures in welded joints through Type IV cracking [12]; this refers to an enhanced rate of creep degradation in the fine-grained (FGHAZ) or intercritically annealed (ICHAZ) region of the heat-affected zone (HAZ). A great deal of research effort has been directed at understanding the mechanisms that lead to Type IV failures [11–19], although primarily from a microstructural point of view.

1.2 Objectives

The objective of this thesis is to contribute towards an understanding of how Type IV failures manifest in steels that are currently available and are in service operation. Given that significant attention has already been given to the role of microstructure in determining Type IV limited creep life, the focus in this work will be on other aspects that affect the mechanical performance of welded joints as a whole. In particular, areas that are going to be addressed (and which have not been investigated thoroughly to date) include:

- The effects of residual stresses and constraint on the creep performance of P91 welds,
- The influence of residual stress relaxation during post weld heat treatment on cross-weld creep performance, and

- The variability in local tensile and creep properties within P91 welds, as measured by digital image correlation (DIC).

1.3 Outline of thesis

This work commences with a review of the literature. The review is intended to provide the background for research described in later chapters.

Attention is then given to the design of welded specimens in P91 pipe material (chapter 3), and the subsequent measurement of residual stresses over a planar area using neutron diffraction (chapter 4). The results of residual stresses in both the as-welded and post-weld heat treated (PWHT) conditions are presented.

Chapter 5 describes an extensive creep test programme involving cross-weld, FGHAZ simulated, notched FGHAZ simulated and FGHAZ simulated specimens with residual stresses. The influence of residual stress relaxation during post weld heat treatment is also addressed.

Chapter 6 is concerned with the application of digital image correlation to P91 welds in order to spatially resolve tensile and creep properties of different regions of the weldment.

Finally, conclusions and suggestions for future research are presented in chapter 7.

1.4 References

[1] Exxonmobil, "The Outlook for Energy: A view to 2040," Irving, Texas, 2012.

[2] International Energy Agency, "World Energy Outlook," Paris, 2011.

[3] "Carbon Tax Facts," 2012. [Online]. Available: http://www.carbontax.net.au/. [Accessed: 15-Feb-2013].

[4] BBC News, "Coal resurgence calls undermine clean energy commitments," 2012. [Online]. Available: http://www.bbc.co.uk/news/business-20002801. [Accessed: 20-Feb-2013].

[5] T. Lodge, "Clean Coal, A clean, secure and affordable alternative," London, 2007.

[6] International Energy Agency, "Focus on clean coal," Paris, 2006.

[7] R. Viswanathan and W. Bakker, "Materials for ultrasupercritical coal power plants—Turbine materials: Part II," Journal of Materials Engineering and Performance, vol. 10, no. 1, pp. 96–101, 2001.

[8] F. Masuyama, "New Developments in Steels for Power Generation Boilers," in Advanced Heat Resistant Steels for Power Generation, 1999, pp. 33–48.

[9] Geotimes, "Climate Change and the Potential of Coal Gasification," 2006. [Online]. Available: http://www.geotimes.org/sept06/feature_ClimateChange.html. [Accessed: 12-Feb-2013].

[10] V. K. Sikka, C. T. Ward, and K. C. Thomas, "Modified 9Cr–1Mo steel," in Conference on ferritic Steels for High Temperature Applications, 1981, pp. 65–84.

[11] J. A. Francis, W. Mazur, and H. K. D. H. Bhadeshia, "Type IV cracking in ferritic power plant steels," Materials Science and Technology, vol. 22, no. 12, pp. 1387–1395, Dec. 2006.

[12] D. J. Gooch and S. T. Kimmins, "A study of Type IV cracking in 0.5%CrMoV/2.25CrMo weldments," in 3rd International Conference on Creep and Fracture of Engineering Materials and Structures, 1987, pp. 698–703.

[13] Tornado Energy Consultants Inc., "Review of Type IV Cracking in Piping Welds," Palo Alto, 1997.

[14] P. Mayr and H. Cerjak, "Transactions of The Indian Institute of Metals The impact of welding on the creep properties of advanced 9-12 % Cr steels," vol. 29, pp. 5–10, 2010.

[15] S. Tsukamoto, M. Kondo, M. Tabuchi, T. Shirane, and F. Abe, "Suppression of Type IV Failure in High Cr Heat Resistant Steel Welded Joint," pp. 1–9.

[16] M. Kondo, M. Tabuchi, S. Tsukamoto, F. Yin, and F. Abe, "Suppressing Type IV failure via modification of heat affected zone microstructures using high boron content in 9Cr heat resistant steel welded joints," Science and Technology of Welding and Joining, vol. 11, no. 2, pp. 216–223, Mar. 2006.

[17] S. Albert, M. Matsui, T. Watanabe, H. Hongo, K. Kubo, and M. Tabuchi, "Variation in the Type IV cracking behaviour of a high Cr steel weld with post weld heat

treatment," International Journal of Pressure Vessels and Piping, vol. 80, no. 6, pp. 405–413, Jun. 2003.

[18] Y. Hasegawa, T. Muraki, and M. Ohgami, "Metallurgical investigation of a Type IV damage at the heat affected zone of weld for tungsten containing martensitic heat resistant steels," in Experience with creep-strength enhanced ferritic steels and new and emerging computational methods, 2004.

[19] K. Laha, K. S. Chandravathi, P. Parameswaran, and K. Bhanu Sankara Rao, "Type IV Cracking Susceptibility in Weld Joints of Different Grades of Cr-Mo Ferritic Steel," Metallurgical and Materials Transactions A, vol. 40, no. 2, pp. 386–397, Dec. 2008.

Chapter 2

Literature Review

2.1 Material Requirements in the Fossil-Fired Power Industry

The power generation industry has to cope with two major challenges: increasing plant efficiency and reducing CO_2 emissions. Both of these can be achieved by improving the technologies and materials used in power plants, which are increasingly subjected to higher operating stresses and temperatures. There is also enormous pressure to produce materials at a low cost, which are easy to fabricate, and which achieve good environmental properties. The main considerations for material developments in power plants are [1]:

- Mechanical strength (0.2 % proof stress)
- Ductility at service temperature
- 100,000 hour creep strength
- Fatigue resistance (high and low cycles)
- Corrosion resistance
- Oxidation resistance
- Thermal fatigue resistance
- Wear resistance

The material selection procedure is dependent on such factors as the operational duty (stress, temperature, time and environment), likely failure mechanisms, maintenance possibilities and the overall cost. Many components operate below the creep range, so time independent properties can be used. At temperatures up to 340°C, the yield point can still be used as a design criterion for mild steel [1], but at higher temperatures, the time dependence of properties is the main consideration.

Boiler components

The various components of a boiler are employed over a wide range of temperatures, pressures, corrosive atmospheres, and oxidation conditions. The range of alloys necessary to best meet the design demands includes carbon manganese (CMn) steels, low alloy steels, advanced low alloy steels (T23, T24), the 9-12% Cr martensitic family, and the austenitic range with chromium contents varying from 18 to in excess of 25 wt. % [2]. Carbon manganese steels are utilised at lower temperatures, such as for the reheater inlet, but as component temperature increases, it is necessary to move to low alloy steels such as T22, T23 and T24 [2].

Superheater and reheater (SH/RH) tubing applications call for high creep strength, thermal fatigue strength, weldability, resistance to fireside corrosion/erosion and resistance to steamside oxidation. Thermal fatigue resistance and cost will be the most important factors when considering the use of ferritic/martensitic steels [3]. However, the limiting temperature for optimum use of 9-12% Cr steels appears to be approximately 595°C, with austenitic materials being required for higher temperature applications.

Headers and steam pipes

Headers and steam pipes are situated outside the furnace, so fireside corrosion is not a factor in material selection. However, steam oxidation on the bore must still be considered [4]. Development of steels such as P91, P92 led to increases in the pressures and temperatures that can be accommodated, but the operating temperature is still limited to 600-610°C due to steam oxidation [4]. Attempts to improve steam oxidation resistance through the addition of chromium (11-12%) for example to P122 and NF12 have suffered due to the formation of Cr-V-Nb-N rich Z-phase [5] which is regarded as being detrimental to creep strength.

In addition to creep strength, the choice of materials for heavy-section components is governed by thermal fatigue and fracture toughness. Ferritic/martensitic steels such as the 9-12% Cr steels are preferred because of their lower coefficient of thermal expansion and higher thermal conductivity, which can be of benefit during thermal transients such as those experienced during plant shut-downs. A potential disadvantage of such steels in general is their susceptibility to Type IV cracking [6] (cracking in the fine-grained/inter-critical heat affected zone) in welded joints.

For higher temperatures and pressures, nickel alloys such as Inconel 740, or Inconel 617, will generally be required. However, these materials are significantly more expensive than their ferritic and austenitic counterparts. Significant improvements in plant efficiency need to be realised to make such a choice economically viable [4].

Steam turbines

The most critical components in steam turbines are the valve chests and turbine casings (operating under high internal steam pressures) and the turbine rotors and blading

(operating under high centrifugal load). Steam turbines for advanced super-critical steam conditions require the application of advanced alloy steels for the HP and IP turbines, and for the main and reheat steam admission valves, with nickel-based alloys or high-strength austenitic steels being required only for the early stages of blading [2].

Rotor forgings are based on 9-12% CrMoVNbN steels. Valve chests and cylinder casings use similar alloys, but due to the complexity of the shapes, castings or multiple forgings are required. Blading alloys are similar to the rotor forging alloys. Meeting the requirements of bolts operating at the very highest temperatures has frequently required the exploitation of Ni-based alloys such as Nimonic 80A or Refractalloy 26 [4].

2.2 Creep Degradation in Power Plant Materials

2.2.1 Nature of creep deformation

When a material (metals and alloys) is subjected to a stress that is greater than or equal to its yield stress, the material deforms plastically. However, if the temperature is relatively high, plastic deformation can occur even when the stress is lower than the yield stress [7]. High temperature in this context is defined as greater than about 0.4 T_m where T_m is the absolute melting point (Actual temperature (in K)/Melting point (in K)). This ratio is also known as the homologous temperature. At these temperatures, the atoms become sufficiently mobile to allow time-dependent rearrangement of the structure [8].

Classical creep deformation of metals can be split into 3 different stages: Primary, secondary and tertiary creep. These stages are shown on a typical creep curve which is represented schematically in Figure 2-1. Primary creep is the initial stage of creep after load has been applied in which the creep resistance increases with strain and is characterised by rapid hardening of the material. During this stage, the dislocation

density increases rapidly, which strengthens the material. In some materials, the primary stage may sometimes be absent and with some types of creep, such as solute drag, an "inverted" primary occurs where the strain-rate increases with strain [9]. Secondary creep or steady state creep as it is commonly referred to, is a period of constant strain rate as there is a balance between work hardening and recovery (process by which deformed grains can reduce some of their stored internal strain) processes. The material undergoes significant microstructural changes during this period. Existing precipitates coarsen and can chemically change to form other precipitates. Changes to the dislocation structures will also be occurring. Finally, the tertiary stage is characterised by an accelerating creep rate, which eventually leads to fracture. The extent of the tertiary stage may be limited in brittle materials and extensive in ductile materials [8]. Although several processes can cause or contribute to the acceleration in creep rate during the tertiary stage, it is usually the development of microcracks (coalescence of voids) which leads to creep fracture [8].

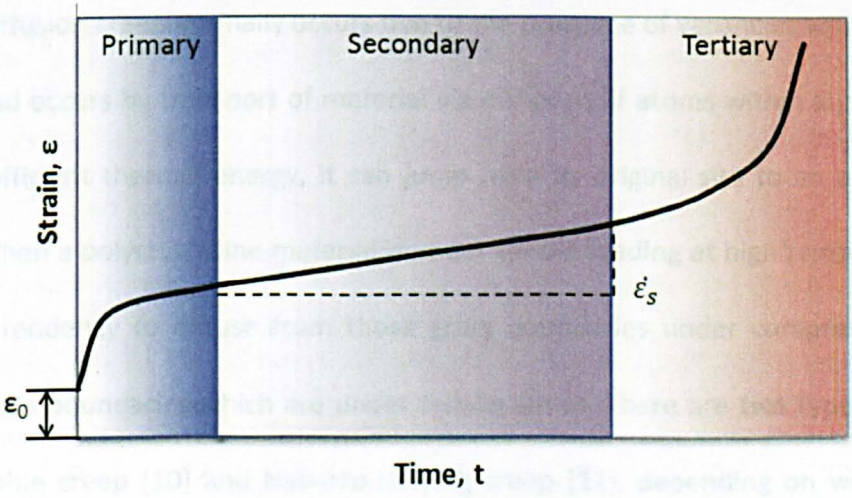

Figure 2-1: Schematic representation of a high temperature creep curve (adapted from [8]).

2.2.2 *Creep Mechanisms*

During the secondary stage, creep takes place by two different mechanisms: diffusion creep and dislocation creep. These are illustrated in Figure 2-2. These depend on the material composition, microstructure and the creep conditions (stress and temperature).

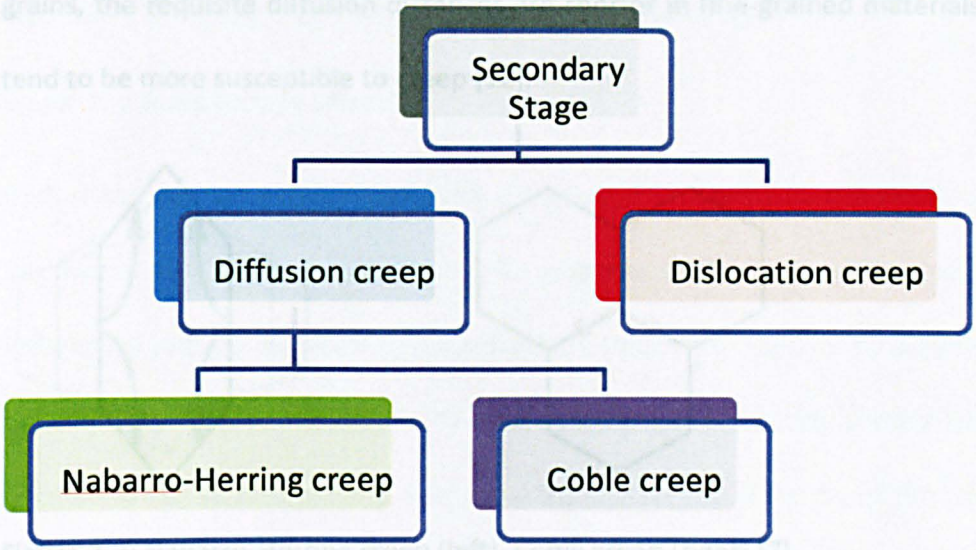

Figure 2-2: Different mechanisms occurring during secondary stage creep.

Diffusion Creep

Diffusion creep normally occurs due to the presence of vacancies within the crystal lattice and occurs by transport of material via diffusion of atoms within a grain. If an atom has sufficient thermal energy, it can jump from its original site to an adjacent vacancy [8]. When a polycrystalline material is under tensile loading at high temperature, atoms have a tendency to diffuse from those grain boundaries under compressive stress towards grain boundaries which are under tensile stress. There are two types of diffusion creep: Coble creep [10] and Nabarro-Herring creep [11], depending on whether the diffusion paths are predominantly along the grain boundaries or within the grains themselves (Figure 2-3) [7]. At high temperatures (T > 0.5Tm), lattice diffusion controls the creep rate; the resulting flow is known as Nabarro-Herring creep [11]. At lower temperatures (T

< $0.5T_m$), atomic diffusion in the lattice becomes progressively more difficult. On the other hand, atoms at grain boundaries are less closely packed than elsewhere and vacancies exist along the boundaries which allow grain-boundary diffusion to take place [10]. The flow is then called Coble creep. Since these occur on the scale of the individual grains, the requisite diffusion distances are shorter in fine-grained materials, which thus tend to be more susceptible to creep [12].

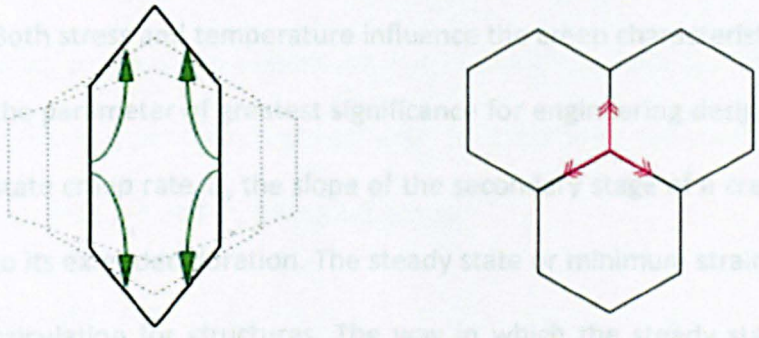

Figure 2-3: Nabarro-Herring creep (left), Coble creep (right) [7].

Dislocation Creep

Dislocation creep or Power Law creep is a mechanism involving motion of dislocations by both dislocation gliding and climbing as shown schematically in Figure 2-4. At high stresses, dislocations in crystalline materials are activated to glide whereby a dislocation line moves parallel to its Burgers vector [13]. It requires only a small displacement without transfer of matter. If the gliding dislocations are stopped by obstacles, then dislocation climbing helps to surmount the obstacles and continue their gliding. Dislocation climbing involves movement perpendicular to their Burgers vector. This process will get repeated the next time it meets an obstacle [14]. The glide motion contributes most of the strain but the strain rate is controlled by the climb step. This process requires diffusion of vacancies or interstitials. Thus, the main rate controlling process is atomic diffusion [15].

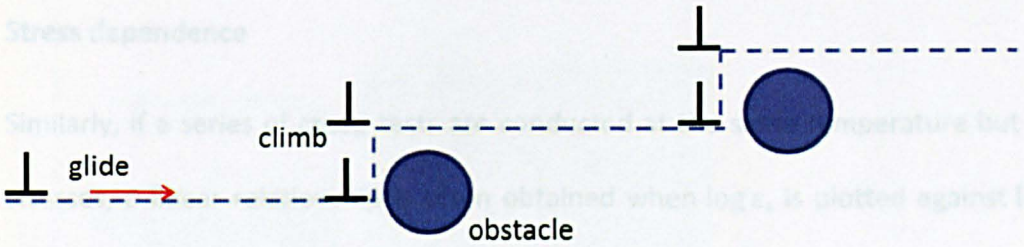

Figure 2-4: Schematic representation of dislocation glide and climb

Stress and temperature effects

Both stress and temperature influence the creep characteristics. It is widely assumed that the parameter of greatest significance for engineering design is the secondary or steady-state creep rate, ε_s the slope of the secondary stage of a creep curve (Equation 2-3), due to its extended duration. The steady state or minimum strain rate is often used in the life calculation for structures. The way in which the steady state creep rate, ε_s varies with both stress and temperature can be defined as [8],

$$\varepsilon_s = u\ \sigma\ \cdot v(T) \qquad \textbf{Equation 2-1}$$

Where the function $u\ \sigma$ describes the variation of $\varepsilon_s$with stress and the function $v(T)$ describes variation with time.

Temperature dependence

When the secondary creep rates are measured in creep tests carried out at the same stress but different temperatures, it is usually found that a linear relationship is obtained by plotting $\ln \varepsilon_s$ against (1/T). The gradient of such a plot yields – (Qc/R), where Qc is the activation energy for creep and R is the universal gas constant. Therefore, it can be inferred that creep obeys Arrhenius's Law [16], such that

$$\varepsilon_s \propto \exp - \frac{Q_c}{RT} \qquad \textbf{Equation 2-2}$$

Stress dependence

Similarly, if a series of creep tests are conducted at the same temperature but different stresses, a linear relationship is often obtained when $\log \varepsilon_s$ is plotted against $\log \sigma$ with gradient n (the stress exponent), indicating Norton's Law [17] behaviour,

$$\varepsilon_s \propto \sigma^n \qquad \textbf{Equation 2-3}$$

Power Law Representation

Since we have expressions for $u\ \sigma$ and $v(T)$ individually, their product will give the way ε_s varies with both stress and temperature. Substituting for $u\ \sigma$ and $v(T)$ using Equation 2-2 and Equation 2-3 gives,

$$\varepsilon_s = A\sigma^n \exp - \frac{Q_c}{RT} \qquad \textbf{Equation 2-4}$$

where A is a constant.

Power Law Breakdown

Figure 2-5 shows the influence of stress on creep strain rate. Power-law creep occupies the intermediate region of stress. At low stresses, a linear dependence on stress is observed known as Harper-Dorn creep [18]. It is believed to be due to climb-controlled creep under conditions where the dislocation density does not change with stress [14]. At higher stresses, the power law breaks down. This process is a transition from climb-controlled to glide-controlled flow [19].

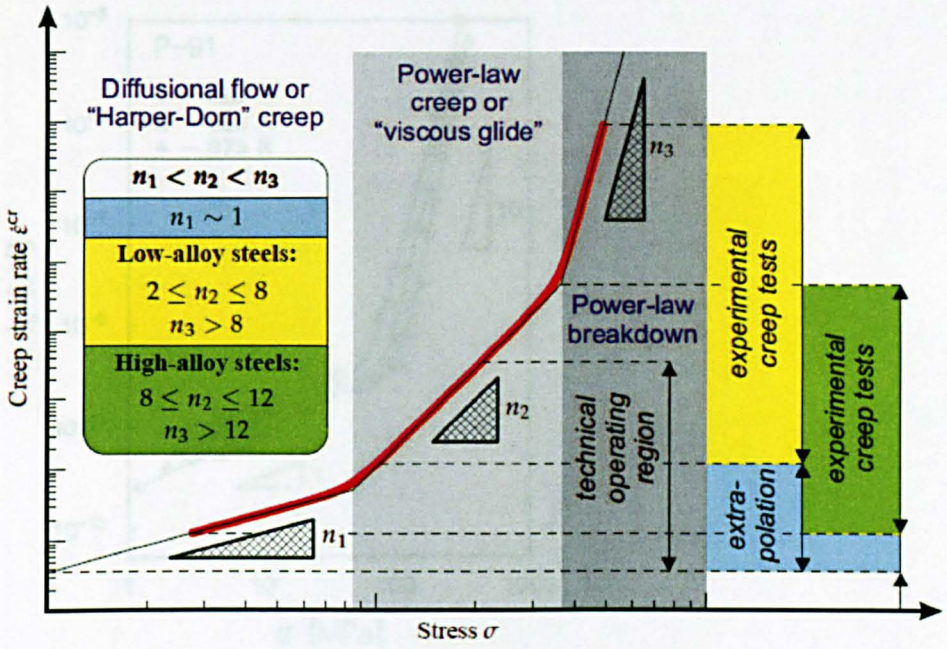

Figure 2-5: Schematic illustration of influence of stress on creep strain rate [20].

Under 'power-law breakdown' conditions, a different expression is normally used for $u\ \sigma$ in Equation 2-4. In general, at very high stresses, ε_s is usually considered to depend exponentially on stress [8]. A change in the dominant creep mechanism is accompanied by a change in the values of n and Qc. An example of the change in the value of n in P91 steel is shown in Figure 2-6 [21]. Steady state creep rates are proportional to applied stress up to about 100 MPa at 600°C, after which a distinct break in the curve is evident. At low stresses, the dominant mechanism is diffusion with an n value of unity. At higher stresses, viscous creep is replaced by power-law creep (dislocation creep dominant) having a stress exponent of about 10. To account for these changes, it has been suggested [10, 11] that the effective stress changes with test conditions due to changes in an 'internal back stress' which represents a resisting force arising from a variety of microstructural factors including dislocation configurations, precipitate dispersion and solid-solution effects.

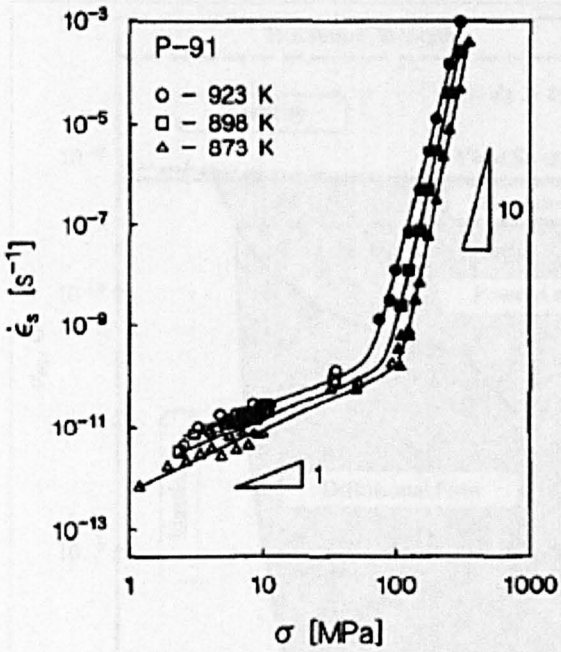

Figure 2-6: Stress dependence of the steady state creep rate in both power law and viscous creep regimes [21].

Deformation mechanism map

Since the creep behaviour of materials is both stress and temperature dependent, the dominant creep mechanism can change. The range of dominance of each of the mechanisms can be identified from a deformation mechanism map specific to the polycrystalline material of interest [19], [24]. A schematic illustration of such a map is shown in Figure 2-7 [20], [24]. Contours of constant strain rates are presented as functions of the normalised equivalent stress σ_{eq}/G and the homologous temperature T/Tm, where G is the shear modulus and Tm is the melting temperature. For a given stress and temperature, the dominant creep mechanism and the strain rate can thus be identified. However, it should be noted that such a diagram differs for different materials. Even for the same material, the boundaries between adjacent creep regimes can be dependent on such microstructural variables as the mean grain diameter [8].

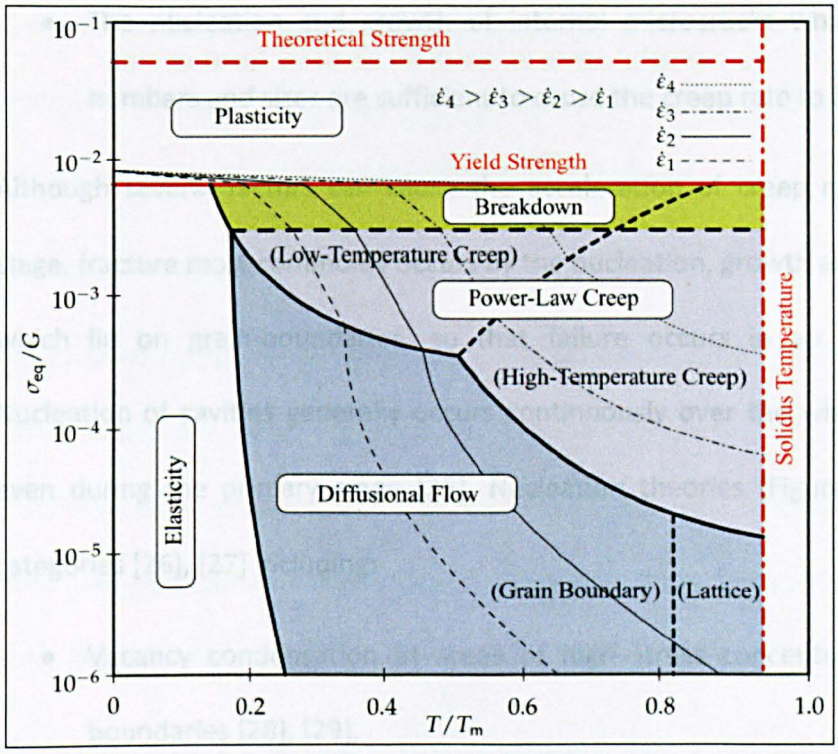

Figure 2-7: Schematic illustration of a typical deformation mechanism map [20]. The y-axis corresponds to the normalised equivalent stress, $\boldsymbol{\sigma_{eq}/G}$ and the x-axis corresponds to the homologous temperature T/Tm.

2.2.3 Creep fracture

The tertiary stage is characterised by an accelerating creep rate, which eventually leads to fracture. Tertiary creep may be caused by [8]:

- Mechanical instability, such as necking which results in localised reduction of the cross-sectional area.
- Microstructural instability, including grain growth or recrystallization with single-phase materials, or the gradual loss of creep strength as overageing occurs during creep of precipitation-hardened alloys.

- The nucleation and growth of internal microcracks which develop until their numbers and sizes are sufficient to cause the creep rate to increase.

Although several factors can cause the acceleration of creep rate during the tertiary stage, fracture most commonly occurs by the nucleation, growth and coalescence of voids which lie on grain-boundaries, so that failure occurs in an intergranular manner. Nucleation of cavities generally occurs continuously over the whole creep life; possibly even during the primary stage [25]. Nucleation theories (Figure 2-8) fall into several categories [26], [27] including:

- Vacancy condensation at areas of high stress concentration, usually at grain boundaries [28], [29],
- Cavity formation at the head of a dislocation pile-up (Zener-Stroh mechanism [30]), and
- Grain boundary sliding leading to voids at triple-point grain junctions or the formation of voids by "tensile" grain boundary ledges, or the creation of voids at second phase particles [26].

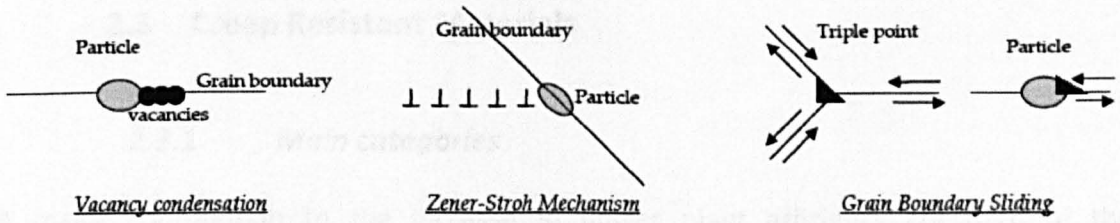

Figure 2-8: Schematic representations of different mechanisms of cavity nucleation [31]

There are a number of mechanisms by which cavities can grow during the creep life of a component, for example plastic deformation, diffusion-controlled and constrained cavity growth [32], [33]. When diffusion is involved, the voids grow on grain-boundaries, but

when power-law creep is dominant, they may grow within the grains as well. At any instant in time, a particular growth mechanism dominates [27]. Cavity coalescence is the last step in the cavitation process leading up to failure.

Extrapolation procedures

Power plant components are usually designed on the basis that creep failure should not occur under the operating conditions imposed during planned lives of ~100.000 - 250,000h. Thus, extrapolation procedures are frequently used to obtain long-term data from short experiments. Some common methods have been proposed by: Larson-Miller [34], Manson-Haferd [35], Orr-Sherby-Dorn [36] and Wilshire [37].

The Larson-Miller [34] method for example involves the use of a time-temperature compensation parameter, defined as $P = T(C + log\ t_r)$ where T is temperature in Kelvin, C a material dependent constant, t_r the rupture time in hours and P is a parameter that depends on stress and rupture time. Hence, if C is known, one can find P in a single test. From this result, one can find the rupture times at any temperature, as long as the same stress is applied.

2.3 Creep Resistant Materials

2.3.1 Main categories

A major contribution to the increase in power plant efficiency consisted of the development of materials with higher creep strength. The main categories of materials used are: ferritic steels, austenitic steels and nickel-based alloys. These are discussed in more detail below.

Austenitic steels

Austenitic steels represent the largest of the general groups of stainless steels and have austenite (face centred cubic crystal) as their primary phase. This class of alloys is structured around the composition of AISI Grade 304 stainless steel, which is based on iron with 18 wt.% chromium and 8 wt.% nickel. During production of such steels, it is necessary to preserve the austenite structure at room temperature and this is achieved by adding elements such as nickel which promote austenite in large quantities (>8 wt.%) [15]. Higher nickel contents favour better ductility. Other austenite promoting elements include carbon, nitrogen and copper. Carbon also imparts high temperature strength.

Austenitic steels are primarily used in areas where, oxidation resistance and fireside corrosion become important in addition to creep strength. The various stages in the evolution of these steels is well described by Mayer and Masuyama [38]. In brief, the Ti and Nb contents were optimised to stabilise the steels from a corrosion point of view and promote creep strength. This was followed by Cu additions for increased precipitation strengthening by fine precipitation of a Cu rich phase, and further improvements have included austenite stabilisation using 0.2% nitrogen as well as W addition for solid solution strengthening [2].

The well-known AISI Grade 316 stainless steel [39] is a modification of the basic stainless steels (18% Cr-8% Ni). Molybdenum (2-3%) is present, which substantially improves the general corrosion (pitting and crevice) resistance of the alloy. Consequently more nickel is also required to help retain the austenitic structure of the alloy [38]. The carbon content within this alloy is also adjusted to produce 316L (low carbon) and 316H (high carbon) grades. While a low carbon content is desirable for welding applications and reducing the

formation of carbides and hence mitigating intergranular corrosion, a higher carbon content results in the improvement of high temperature creep properties.

Ferritic/martensitic steels

Low alloy steels, such as the classical 2.25Cr1Mo or 1CrMoV alloys have formed the backbone of the power generation and petrochemical industries for at least five decades, for operating temperatures up to 565°C [40]. These steels are usually called "ferritic" steels because on cooling from austenitising temperatures they transform to a body centred cubic lattice structure, which includes bainitic structures [41].

One of the key microstructures in most modern creep resistant steels is martensite which develops when austenitised iron-carbon alloys are rapidly cooled to room temperature [40]. It is in the interest of the designer of power plant components to have steels with a martensitic microstructure. Martensitic microstructures are generally very fine with a high dislocation density, and they are effective in inhibiting dislocation motion at typical operating stresses. Martensite is a non-equilibrium phase and when exposed for extended times to high operating temperatures leads to the progressive recovery of the microstructure [42]. The chemical compositions for some prominent ferritic steels are listed in Table 2-1.

Table 2-1: Typical chemical compositions for various ferritic steels in wt.% [43].

Steels	Typical chemical composition, wt-%										
	C	N	Si	Mn	Cr	Mo	V	Nb	W	Co	Cu
ASME P/T22	0·12	–	0·3	0·45	2·25	1·0	–	–	–	–	–
ASME T9	0·12	–	0·6	0·45	9·0	1·0	–	–	–	–	–
HCM9M	0·07	–	0·3	0·45	9·0	2·0	–	–	–	–	–
EM12	0·10	–	0·4	0·10	9·0	2·0	0·30	0·40	–	–	–
X20CrMoV-12-1	0·20	–	0·4	0·60	12·0	1·0	0·25	–	–	–	–
ASME P/T91	0·10	0·05	0·4	0·45	9·0	1·0	0·20	0·08	–	–	–
HCM12	0·10	0·03	0·3	0·55	12·0	1·0	0·25	0·05	1·0	–	–
GX12CrMoWVNbN-10-1-1	0·13	0·05	0·3	0·60	10·5	1·0	0·23	0·08	1·0	–	–
NF616 (ASME P/T92)	0·07	0·06	0·1	0·45	9·0	0·5	0·20	0·05	1·8	–	–
HCM12A (ASME P/T122)	0·11	0·06	0·1	0·60	12·0	0·4	0·20	0·05	2·0	–	1·0
SAVE12	0·10	0·04	0·3	0·20	11·0	–	0·20	0·07	3·0	3·0	–

One of the main problems in the power generation industry is exposure to cyclic stresses created by spatial thermal gradients and time dependent temperature fields caused by two-shifting operations (the process of shutting-down a power plant during periods of low system demand, such as overnight and re-starting it when demand increases). To mitigate these effects, a low coefficient of thermal expansion, low elastic modulus and high thermal conductivity are desirable.

Ferritic/martensitic steels are more favoured than austenitic steels for thick section components owing to their lower thermal expansion coefficient and higher thermal conductivity. The coefficient of thermal expansion (CTE) generally increases with increasing bond energy, which depends on the nature of the interaction between atoms forming the solid and the bond length. BCC ferritic/martensitic steels are less dense than FCC austenitic steels; hence they possess a lower CTE. On the other hand, the thermal conductivity is determined by the number density and mobility of the mobile electrons. In principle, austenitic steels should have a higher thermal conductivity than ferritic/martensitic steels as they are denser structures. However, owing to the smaller inter-atomic distance, the attraction between the nuclei and the electrons is stronger and this leads to lower mobility of mobile electrons. This effect outweighs the effect of the

number density of mobile electrons and therefore the thermal conductivity of ferritic/martensitic steels is higher than that of austenitic steels [44].

Nickel-based alloys

Nickel-based alloys possess excellent high temperature strength and oxidation resistance. Many are metallurgically related to austenitic stainless steels but are much more highly alloyed, particularly with nickel, chromium and molybdenum in order to enhance their corrosion resistance [45]. Due to the alloying additions and in some cases complex manufacturing techniques, they are much more expensive than ferritic and austenitic steels. As such, they are only used in safety-critical applications, for example the hot sections of gas turbine engines.

Nickel-based alloys are sparingly used in power plants except for turbine components, for example as a bolting material (Nimonic 80A or Refractalloy 26) [4] and in some cases as blading material. Research and development activities are currently being carried out (for example see AD700-2 [46] and various COST actions [47]) with the aim of increasing steam temperatures to 700°C and even higher. The higher process temperatures will require a shift in construction materials from ferritic, martensitic and austenitic steels to more creep resistant nickel-based alloys as shown in the chart in Figure 2-9.

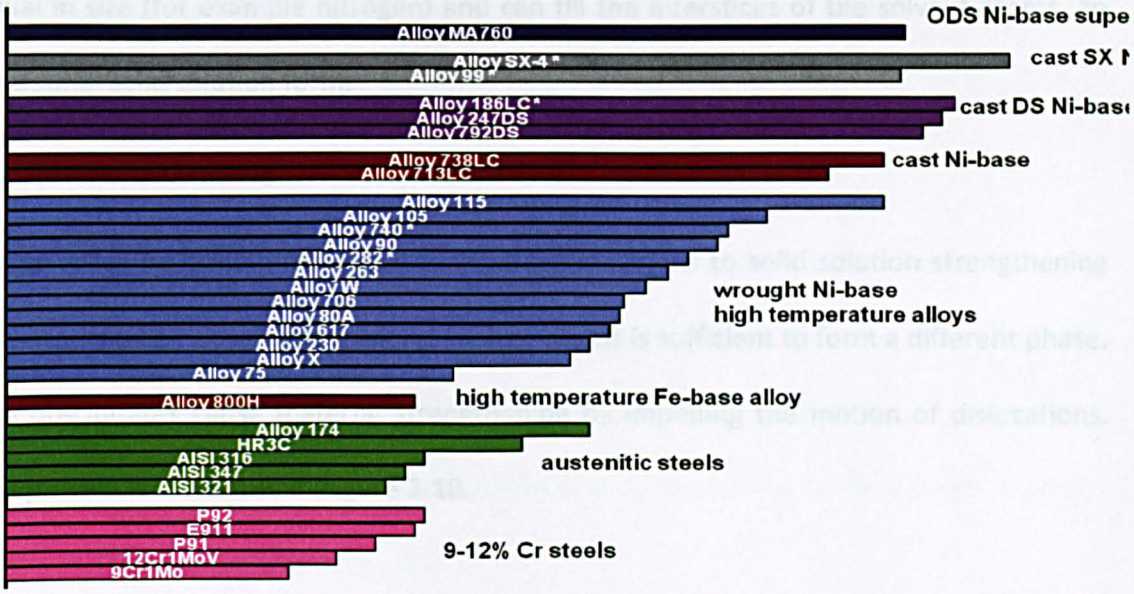

Figure 2-9: Maximum service temperature for candidate alloys based on 100 MPa/100 000 h rupture strength criterion [47].

2.3.2 Creep Strengthening Mechanisms

Plastic deformation occurs as a result of the movement of dislocations. Thus, changes in the microstructure that impede the motion of dislocations will strengthen the material. Some of the basic ways in which creep-resistant steels are strengthened are: solid solution strengthening, precipitation hardening and dislocation hardening. These mechanisms are discussed below.

Solid solution strengthening

This process occurs when atoms of one element (solute) is added to a base element (solvent). The solute dissolves in the matrix of the base element forming a solid solution. If the solute atoms are large enough that they can replace solvent atoms, this results in substitutional solid solution. Mo and W are good examples of substitutional solute atoms in both ferritic and austenitic steels. On the other hand, if the solute atoms are smaller or

equal in size (for example nitrogen) and can fill the interstices of the solvent atoms, an interstitial solid solution forms.

Precipitation hardening

Precipitation hardening can be considered as analogous to solid solution strengthening and occurs when the concentration of solute atoms is sufficient to form a different phase. The precipitates cause material strengthening by impeding the motion of dislocations. The process is illustrated in Figure 2-10.

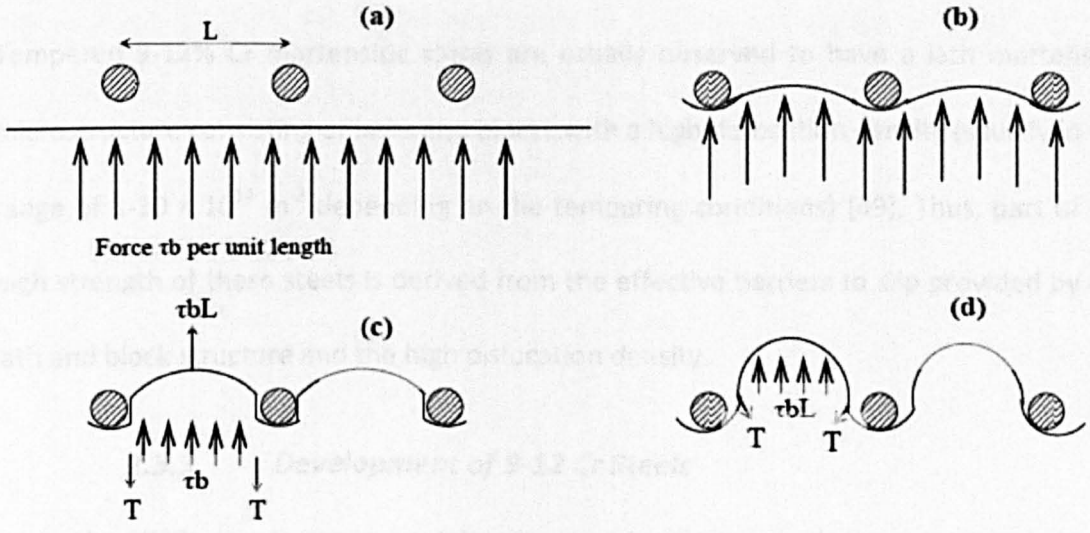

Figure 2-10: Precipitation strengthening (a) approach situation (b) sub-critical situation (c) critical situation (d) escape situation [48].

Creep-resistant steels usually contain different types of precipitates in the matrix and at grain boundaries. Some of the most common ones are carbides and carbonitrides such as $M_{23}C_6$, M_6C, M_7C_3, MX and M_2X, where M denotes the metallic elements, C are the carbon atoms and X denotes that carbon and nitrogen atoms are interchangeable. Other precipitates include intermetallic compounds such as $Fe_2(Mo,W)$ Laves phase, Fe_7W_6 μ-

phase, χ-phase etc. [49]. In some cases, dispersion of alloy oxides such as Y_2O_3 in the matrix form the so-called oxide dispersion strengthened (ODS) steels.

Dislocation hardening

Dislocation hardening occurs as a result of interactions between dislocations in such a way that their further motion is hindered. Some of the mechanisms associated with dislocation hardening are: interaction of stress fields of dislocations, interactions which produce sessile locks, and interpenetration of one slip system by another which results in the formation of dislocation jogs [14].

Tempered 9-12% Cr martensitic steels are usually observed to have a lath martensitic microstructure consisting of laths and blocks with a high dislocation density (usually in the range of 1-10 × 10^{14} m^{-2} depending on the tempering conditions) [49]. Thus, part of the high strength of these steels is derived from the effective barriers to slip provided by the lath and block structure and the high dislocation density.

2.3.3 Development of 9-12 Cr Steels

Up to the 1920s, it was general practice to use non-alloyed steels for components in the steam admission zone exposed to maximum temperatures of 350°C and pressures of about 15 bar. At the beginning of the 1920s, increases in steam temperatures and pressures to approximately 450°C and 35 bar called for the development of low-alloy heat resistant steels [38]. The first of the low alloy steels to be developed was 0.5Mo and since then, creep strengths have improved progressively through introducing new alloying elements and new microstructures. One of the well-known Cr-Mo steels is 2¼Cr-1Mo steel, designated as ASTM Grade 22 [50], which is still widely used today. Higher creep strengths relative to that of T22 were obtained by additions of tungsten, vanadium and

niobium in steel T23, and titanium and vanadium in steel T24. The T23 and T24 steels had the advantage that they did not require PWHT due to the lower carbon content of these steels.

For operations at even higher temperatures (i.e. above 568°C) the use of new high strength austenitic steels could have offered a solution but this was not feasible because these steels are prone to thermal fatigue, are more expensive, and are difficult to inspect by non-destructive examination (NDE) methods. Attention therefore turned to the 9Cr1Mo and 12Cr steels in the search for ferritic steels for superheater and steam pipework components that could withstand operation at up to 600°C and beyond [51]. The systematic development of the 9-12% Cr steels has been well presented by Masuyama [52] and is summarised in Figure 2-11.

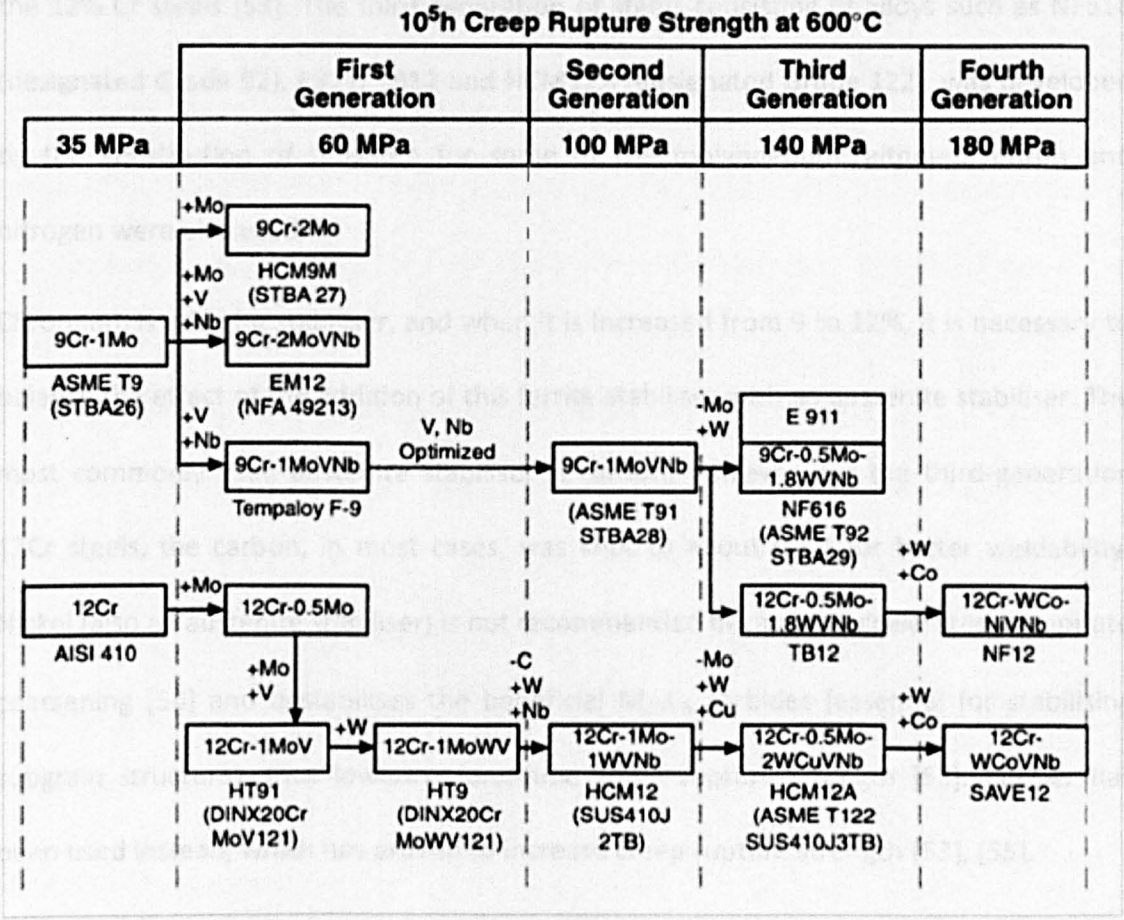

Figure 2-11: Systematic development of 9-12% Cr steels [52].

The first generation consists of alloys such as EM12, HT9 and HT91. These steels feature additions of vanadium and niobium which are carbide formers and thus provide precipitate strengthening. EM12 had a duplex microstructure (tempered martensite and δ-ferrite), giving poor impact toughness [5]. Through the optimisation of the carbon, niobium and vanadium contents, and addition of nitrogen, the second generation of steels was developed. Some examples include HCM12, T91 and HCM2S. Of these steels, T91 has been most extensively used around the world [53].

The microstructures of the 9-12% Cr steels are designed to produce 100% austenite during austenitisation and 100% martensite after an air cooling or quenching treatment,

although a small amount of δ-ferrite (<1%) may be present in some cases, especially in the 12% Cr steels [53]. The third generation of steels consisting of alloys such as NF616 (designated Grade 92), E911, TB12 and HCM12A (designated Grade 122), was developed by the substitution of tungsten for some of the molybdenum, although boron and nitrogen were also used.

Chromium is a ferrite stabiliser, and when it is increased from 9 to 12%, it is necessary to balance the effect of the addition of this ferrite stabiliser with an austenite stabiliser. The most commonly used austenite stabiliser is carbon, however, for the third-generation 12Cr steels, the carbon, in most cases, was kept to about 0.1% for better weldability. Nickel (also an austenite stabiliser) is not recommended because it accelerates precipitate coarsening [54] and destabilises the beneficial $M_{23}C_6$ carbides (essential for stabilising subgrain structure), thus lowering long-time creep rupture strength [53]. Copper has been used instead, which has proved to increase creep rupture strength [53], [55].

The fourth generation of high-chromium martensitic steels consists of two 12% Cr steels, designated NF12 and SAVE12. The main feature of these steels is the reduction of molybdenum and the increase in tungsten content. Instead of nickel, cobalt has been used as an austenite stabiliser as it doesn't lower the Ac_1 temperature. SAVE 12 also contains minor amounts of Ta and Nb and these elements contribute to strengthening by producing fine and stable nitride precipitates [56].

The Japanese MARBN steel [57] is another 9% Cr steel alloyed with boron and nitrogen. It is a fairly recent development (but not yet in service), hence does not feature in Figure 2-11. It was found that the addition of boron and nitrogen improves the long-term creep rupture strength. Boron enriches the $M_{23}C_6$ carbides along grain boundaries and thus

stabilises the lath martensitic structure and nitrogen enhances precipitation of fine MX precipitates.

2.3.4 Modified P91 Steel

Modified 9Cr-1Mo steel was developed jointly by Oak Ridge National Laboratory (ORNL) and Combustion Engineering, Inc. based on the 9Cr-1Mo steel [58]. By optimisation of the alloy with small amounts of V, Nb, and N the creep strength was considerably improved and the steel was eventually approved for tubing by ASTM as A213, Grade T91 and by ASTM and ASME as A/SA-335, Grade P91 in 1984. Grade 91 steel variations are designated as T91 for tubing, P91 for piping, and F91 for forgings. The first large scale application of P91 steel at Ultra Supercritical (USC) steam conditions occurred in the Kawagoe plants in Japan, commissioned in 1988, with operating parameters of 31 MPa at 556°C [3].

Effects of alloying elements

The chemical composition of Grade 91 steel is given in Table 2-2 and the roles of the different alloying additions are discussed below.

Table 2-2: Chemical composition of Grade 91 steel in wt.% [59].

Element	T/P91	
	Min	Max
C	0.08	0.12
Mn	0.3	0.6
P		0.02
S		0.01
Si	0.2	0.5
Cr	8	9.5
Mo	0.85	1.05
V	0.18	0.25
Nb	0.06	0.1
N	0.03	0.07
Al		0.04
Ni		0.4

Carbon

Carbon is an interstitial atom and is present in all steels. It is a strong austenite stabiliser with a relatively low solubility in ferrite, which contributes to the formation of carbides and carbonitrides [53]. Generally the carbon content in steels is restricted to approximately 0.1 wt. % for better weldability. The carbon content is kept even lower in steels such as T23 and T24 (0.04-0.1 wt. %), which significantly reduces the hardness of the as-welded structure and thus eliminates the need for post weld heat treatment in some cases.

Chromium

Chromium is the main alloying element in P91 steel. It is a ferrite stabilising element that is generally added to steels for oxidation and corrosion resistance. Chromium reacts with carbon to form carbides and in the case of P91; the chromium-rich $M_{23}C_6$ carbide

dominates [53]. These help in pinning dislocations and grain boundaries, thus providing solid solution strengthening. In 9-12 Cr steels, chromium plays an even bigger role. It retards the transformation from austenite in reasonable times, so that on cooling martensite becomes the predominant structure.

Molybdenum

Molybdenum is a ferrite stabiliser and improves the creep properties of P91 by solid solution strengthening [60]. Molybdenum does not form carbides or nitrides in 9-12% Cr steels, although Mo_2C has been reported in low alloyed steels such as P22 [61]. In steels that have superseded P91 for example E911, P92 and P122, tungsten was added or substituted for some of the Mo. A molybdenum equivalent, Mo_{eq}, defined as Mo+0.5W (concentrations in wt. %) in solid solution has been established [54] and a value of about 1% is desirable because exposure of the 9–12% Cr steels with a $Mo_{eq} \geq 1$ at 600–650°C has been shown to result in the precipitation of Laves-phase [54], [62]. Although, the two elements (Mo and W) provide relatively high solid-solution strengthening, tungsten diffuses more slowly than molybdenum, which slows recovery and the formation of Laves phase [53].

Vanadium and niobium

V and Nb are added to steels to promote the formation of carbides, nitrides and carbonitrides. In P91, they are expected to form MX, where M is enriched in either V or Nb, and X is either carbon, nitrogen, or a combination of the two, resulting in carbides (MC), nitrides (MN), or carbonitrides [M(C,N)] [63]. These particles are necessary in maintaining a fine subgrain structure and improving creep strength [64].

Nitrogen

Nitrogen, like carbon is a strong austenite stabiliser with a relatively large solubility in austenite and a very low solubility in ferrite, which gives rise to the formation of nitrides and carbonitrides [53].

Nickel and manganese

Nickel and manganese are austenite stabilisers. The addition of nickel enables the austenitic loop to greatly expand such that 100% austenite forms (no δ-ferrite) during austenitisation treatments, thereby ensuring 100% martensite when cooled; the latter being very important in the 12% Cr steels. Nickel does not promote the formation of carbides or intermetallics although it can influence precipitation reactions [65]. It is a good solid solution strengthener and improves toughness in both ferritic and martensitic grades [53].

Although nickel has been the element most often used to prevent δ-ferrite, indications are that it accelerates precipitate coarsening, thus lowering long-time creep strength [53]. Nickel promotes the formation of M_6C, thus destabilising the $M_{23}C_6$, which stabilises the subgrain structure. The combined content of nickel and manganese is usually controlled to a maximum of 1.5%. While further addition is beneficial in improving the toughness, limitations arise due to the influence of Ni on reducing the Ac_1 temperature and on the degradation of creep properties. For example, with excess Ni the Ac_1 temperature can be reduced below the PWHT temperature, so that austenite reformation occurs during tempering or PWHT, which leads to the formation of fresh untempered martensite upon cooling.

Metallurgy of P91 steel

The performance of P91 steel is critically dependent upon obtaining the correct microstructure of tempered martensite and creep-strengthening precipitates. The desired microstructure and satisfactory properties are obtained by precise control of the normalising and tempering heat treatment, or quenching and tempering in the case of thick-section components.

As can be inferred from the Fe-Cr constitutional diagram in Figure 2-12 [66], there is an extensive austenitic region from 820 to 1200°C at compositions near 9% Cr, but most importantly the two-phase region (shaded region) between the austenite and ferrite regions has a very narrow temperature range. Thus, it is possible to produce a fully martensitic structure, with minimal amounts, if any, of delta ferrite, which is generally regarded as detrimental for impact toughness and creep rupture properties [66].

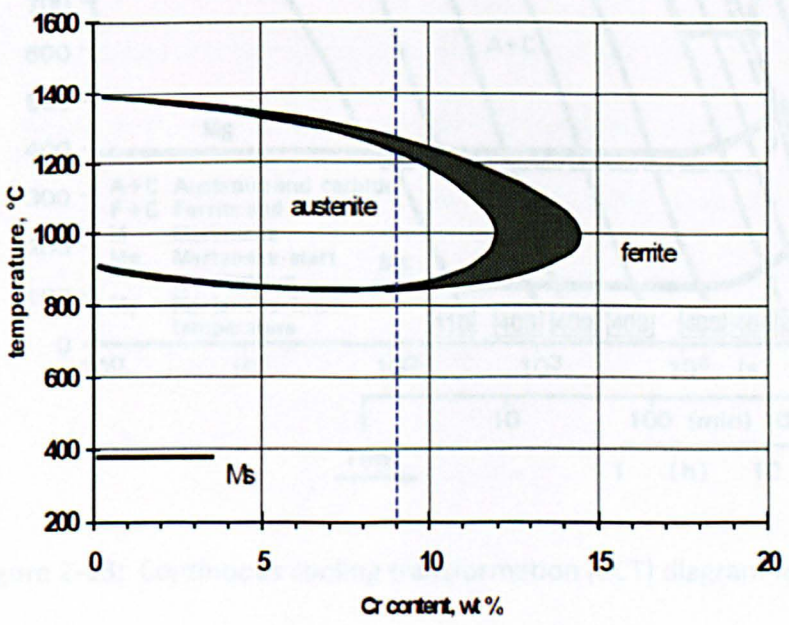

Figure 2-12: Fe-Cr constitutional diagram (adapted from [66]).

P91 steel is supplied in the normalised and tempered condition. During normalising, the steel is heated to well above the Ac_3 temperature and allowed to stabilise to ensure full transformation from ferrite to austenite. Normalising at 1040-1080°C provides for dissolution of most carbides without significant grain growth [59]. After homogenisation has occurred, the material is allowed to cool to room temperature.

On cooling, a martensitic structure is obtained for a wide range of cooling rates as can be inferred from the CCT diagram in Figure 2-13. In general, air cooling is sufficient to obtain 100% martensite. However, the formation of a ferrite-rich microstructure is possible for much slower cooling rates, for example in thick-section components (>75 mm thick) in which case, quenching from the austenitizing temperature is required [50].

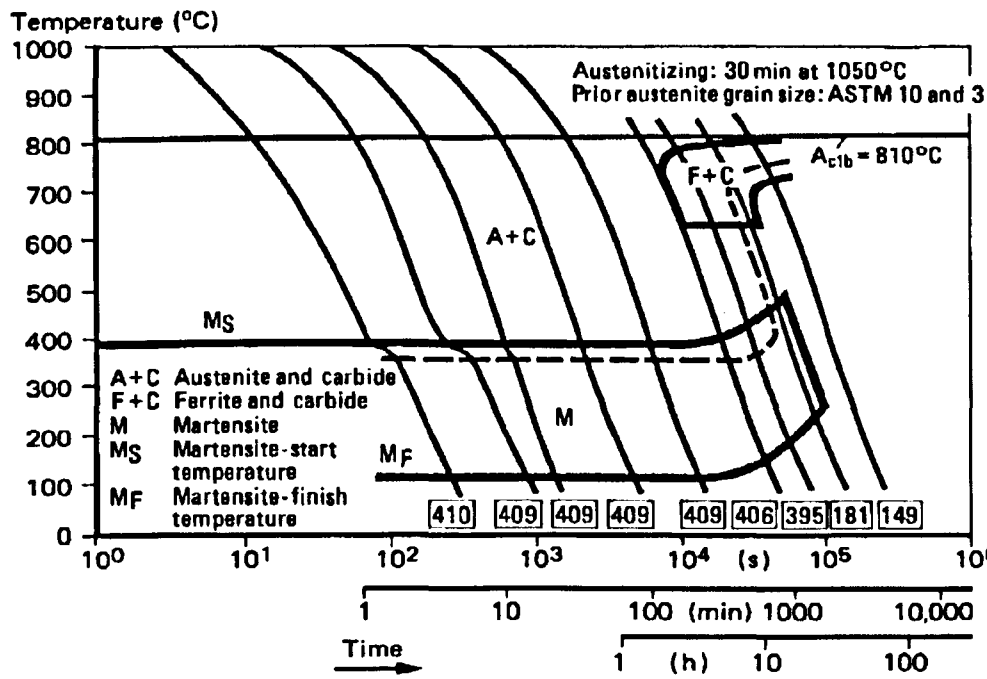

Figure 2-13: Continuous cooling transformation (CCT) diagram for T91/P91 steel [59].

In Figure 2-13, the as-cooled hardness level is also shown for the various cooling rates. Martensite, in addition to being very hard (400-410 HV), is very brittle. Consequently, a tempering heat treatment at 750-780°C is carried out prior to service, which results in the

formation of tempered martensite by diffusional processes. The tempering treatment allows carbides to precipitate homogeneously within the martensitic structure [59] and provides for relief of thermally introduced residual stresses that may have been imparted upon cooling from normalising temperatures. It also increases toughness and ductility.

It is important that the normalising and tempering temperatures are tightly controlled. For example, the upper range of tempering temperature is specified to minimise the risk of reduction in creep strength that can occur when heating above the Ac_1 temperature (800-830°C [59]). Materials mistakenly heated above or below the specified range (i.e. to the intercritical temperature range) will exhibit lower creep rupture strength. Over-tempering can cause coarsening of precipitates and hence loss of precipitation strengthening influence and on the other hand, under-tempering can result in precipitates that are insufficient in size to stabilise the structure or even the absence of precipitates.

A typical microstructure for P91 in the normalised and tempered condition consists of tempered martensite laths, blocks and packets, which have high dislocation densities and fine $M_{23}C_6$ and MX precipitates. The MX precipitates are distributed within the laths while $M_{23}C_6$ are distributed along laths, blocks, packets and prior austenite grain boundaries [67] as shown in Figure 2-14.

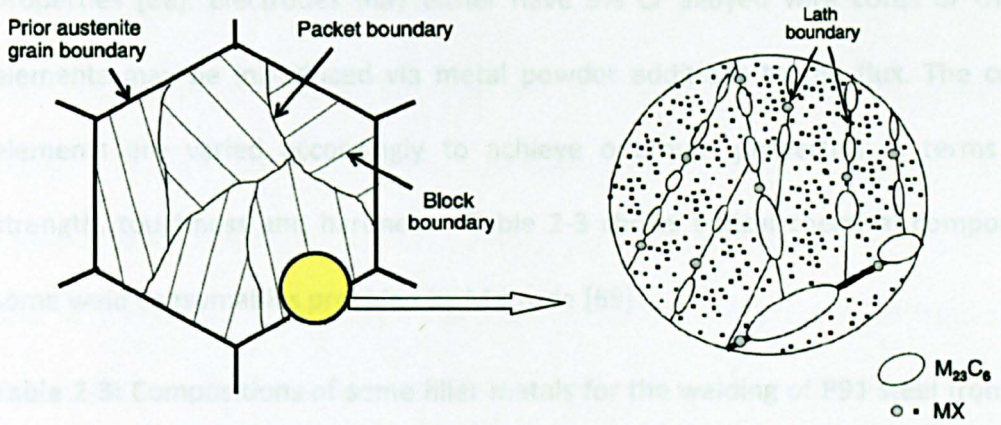

Figure 2-14: Illustration of martensitic 9Cr steel after tempering: subgrain structure (left), distribution of $M_{23}C_6$ and MX precipitates (right) [67].

2.4 Performance of Welds in Ferritic Creep Resistant Steels

2.4.1 Welding of P91

Welding is an essential fabrication process for power plant components. The predominant welding procedure used in power plants is tube-to-tube butt welds to form the complex systems needed in power boilers. However for the construction of water walls, longitudinal welds are also required [41]. More complex welds appear where tubes are joined to thicker sections such as headers. P91 steel can be successfully welded using most of the available welding techniques. However, the choice of welding process will depend on a number of factors such as size and thickness of components, and whether the weld is to be a shop fabrication or site repair.

Welding consumables

For similar-to-similar welding of P91 steels, it is general practice to match the welding consumables to the parent material. The term matching is not directly related to the chemical composition but more specifically to the design-based tensile and creep rupture

properties [68]. Electrodes may either have 9% Cr alloyed wire cores or the alloying elements may be introduced via metal powder additions to the flux. The constituent elements are varied accordingly to achieve optimum properties in terms of creep strength, toughness and hardness. Table 2-3 shows typical chemical compositions for some weld consumables provided by Metrode [69].

Table 2-3: Compositions of some filler metals for the welding of P91 steel from Metrode [69].

Element	P91 base metal range		GTAW wire	GTAW deposit	FCAW Supercore	SAW
	Min	Max	9CrMo-N	9CrMo-V-N	F91	9CrMoV-N + LA492
C	0.07	0.12	0.1	0.08	0.1	0.08
Mn	0.3	0.6	0.6	0.6	0.8	0.5
Si	-	0.5	0.25	0.24	0.25	0.3
Cr	8	9.5	8.7	8.5	9	8.3
Ni	-	0.4	0.7	0.7	0.5	0.6
Mo	0.85	1.05	1	1	1	1
V	0.18	0.25	0.2	0.18	0.2	0.16
Nb	0.04	0.09	0.05	0.04	0.04	0.05
N	0.03	0.07	0.04	0.04	0.05	0.05

Niobium has an adverse effect on weld metal toughness but in order not to compromise the creep strength, an optimum Nb content of 0.04% [59] is usually used. The combined content of Ni and Mn is controlled to a maximum of 1.5% [59]. While Ni is beneficial in improving toughness through improving the response to tempering and reducing the tendency for the formation of δ ferrite, an excessive Ni + Mn content can reduce the Ac_1 temperature below the post weld heat treatment (PWHT) temperature [70], which reduces the tolerance to a temperature overshoot during PWHT. Nitrogen is the other essential element in the filler metal as it contributes to the formation of carbonitrides, which have an important influence on creep rupture strength [69].

Pre-heating, post heating and PWHT

Strict adherence to preheat, interpass and post weld heat treatment temperatures is required to eliminate weld defects and conserve mechanical properties. Figure 2-15 shows a typical heating cycle before, during and after welding. Pre-heating is essential to prevent hydrogen cracking and is normally carried out at 200°C but fabricators go as low as 150°C for root passes involving TIG due to low hydrogen potential. The interpass temperature is usually kept to a maximum of 300°C to prevent hot cracking due to the silicon and niobium content of the weld metal and also to ensure that each bead transforms to martensite [69].

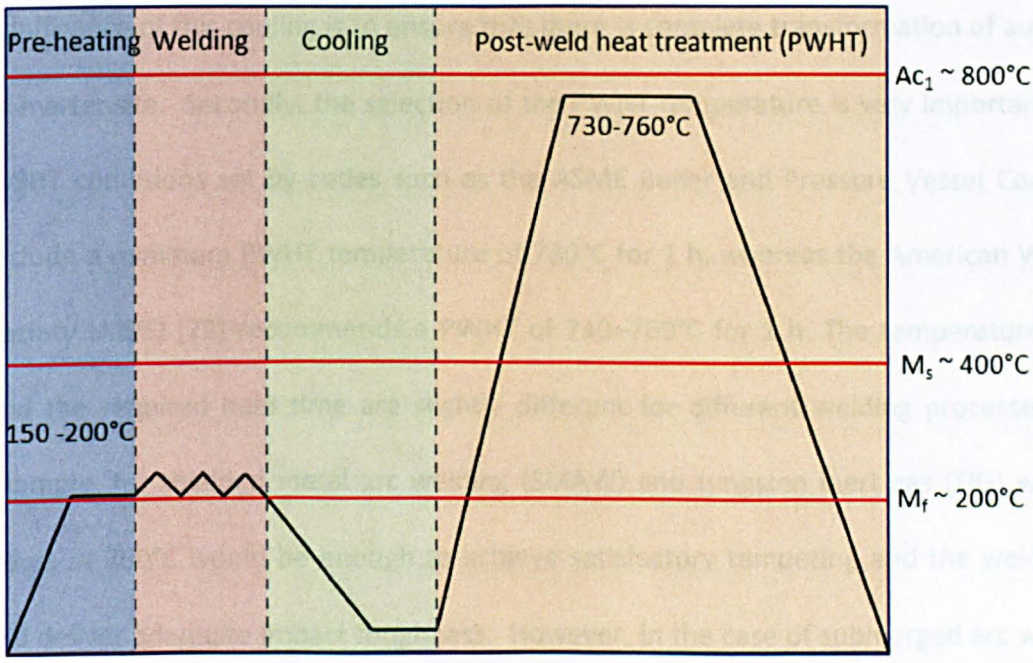

Figure 2-15: Typical heating cycle before, during and after welding. The martensite start (M_s), martensite finish and the lower transformation temperature (Ac_1) is also shown.

Post heating is sometimes carried out when it is not feasible to post weld heat treat the pipe immediately after welding. This practice is very important especially for thick sections and is performed by maintaining the preheat temperature for an extended

period of time after joint completion. This process facilitates hydrogen diffusion from the weldments, thus minimising inadvertent contamination and reduce the risk of stress corrosion cracking (SCC).

PWHT is one of the most important steps in producing satisfactory weldments. It is carried out to temper the microstructure, allows carbides to precipitate homogeneously within the structure, provides relief to residual stresses that may have been imparted during welding and enhances toughness and ductility.

There are two important aspects of PWHT for P91 steel. Firstly, after completion of welding, it is important to let the joint cool to below 100°C before PWHT and the significance of this cooling is to ensure that there is complete transformation of austenite to martensite. Secondly, the selection of the PWHT temperature is very important. The PWHT conditions set by codes such as the ASME Boiler and Pressure Vessel Code [71] include a minimum PWHT temperature of 730°C for 1 h, whereas the American Welding Society (AWS) [72] recommends a PWHT of 730–760°C for 1 h. The temperature range and the required hold time are slightly different for different welding processes. For example, for shielded metal arc welding (SMAW) and tungsten inert gas (TIG) welds, 2 hours at 760°C would be enough to achieve satisfactory tempering and the weld metal will deliver adequate impact toughness. However, in the case of submerged arc welding, a 4 h holding is desirable for obtaining good and consistent ambient toughness. This is attributed to the fact that SAW welds are coarser-grained than welds made with other arc welding processes [73].

With regards to the maximum temperature that can be used, care should be taken not to exceed the Ac_1 temperature which is about 800-830°C [59], where there may be the risk of austenite formation. As mentioned earlier, the Ni and Mn content of the filler metal

have a strong effect on the Ac_1 temperature, so the PWHT temperature and time need to be carefully chosen. If the material has been mistakenly heated above the Ac_1 temperature during PWHT, normalising and tempering should be carried out.

As for the heating rate during PWHT, Metrode recommends < 100°C/hour [69]. This is because a large proportion of piping components made from P91 material have thick wall sections, and in the fabrication of these large pipes, the restraint around the welded joints is normally quite high. A relatively slow heating rate helps to achieve a stable and uniform temperature increase.

Microstructural zones within the weld

Regardless of the primary solidification structure, the fusion zone in 9-12% Cr steels transforms to austenite at a temperature not far from the solidification point and then undergoes a solid state transformation to a structure that will depend on both the hardenability of the alloy and the cooling rate [74]. Adjacent to the fusion zone is the heat affected zone (HAZ); a region that is not heated sufficiently to cause melting, but nevertheless is altered by the welding thermal cycle. The HAZ can be subdivided according to the extent to which grain growth and austenitisation occur [74]; into a coarse grained zone (CGHAZ), a fine grained zone (FGHAZ), an intercritical zone (ICHAZ) and over tempered base metal. The basic influences of the welding process on the metallurgy of the HAZ are shown and compared to the calculated equilibrium phase diagram for P91 steel in Figure 2-16 [75].

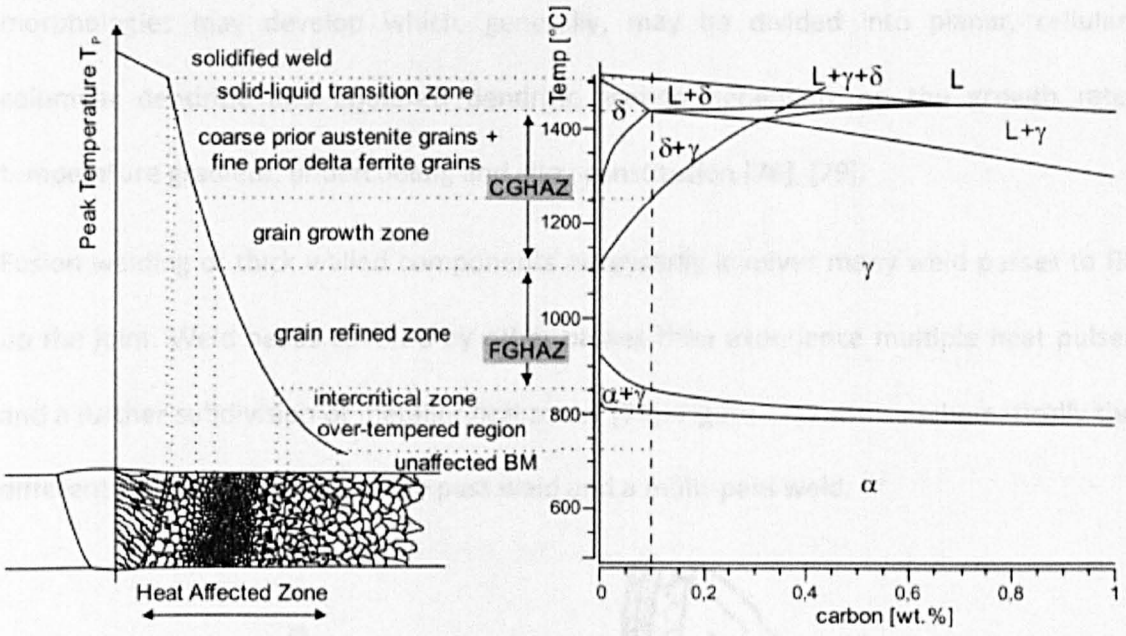

Figure 2-16: Schematic of the sub-zones of the HAZ in relation to the calculated equilibrium phase diagram of P91 steel [75].

The fusion zone

The fusion zone is the region that was heated above the liquidus temperature. Upon cooling to room temperature, the microstructural products that form depend on the cooling rate and the alloy composition. When a filler metal is employed in making the weld, the structure and composition, and thus the properties of the fusion zone can be radically different than the base material; depending on the composition of the filler metal and the amount of dilution [76].

Away from the fusion line, the grain structure is dominated by a mechanism known as competitive growth [77]. During weld metal solidification, grains tend to grow in the direction perpendicular to the pool boundary as this is the direction of the maximum temperature gradient and hence maximum heat extraction. However, columnar dendrites or cells within each grain tend to grow in the easy-growth direction which is <100> for body-centred-cubic and face-centred-cubic crystal structures [77]. Several structural

morphologies may develop which, generally, may be divided into planar, cellular, columnar dendritic and equiaxed dendritic growth depending on the growth rate, temperature gradient, undercooling and alloy constitution [78], [79].

Fusion welding of thick walled components necessarily involves many weld passes to fill up the joint. Weld beads covered by other passes then experience multiple heat pulses and a further subdivision of metallurgical zones [74]. Figure 2-17 shows schematically the different sub zones within a single pass weld and a multi-pass weld.

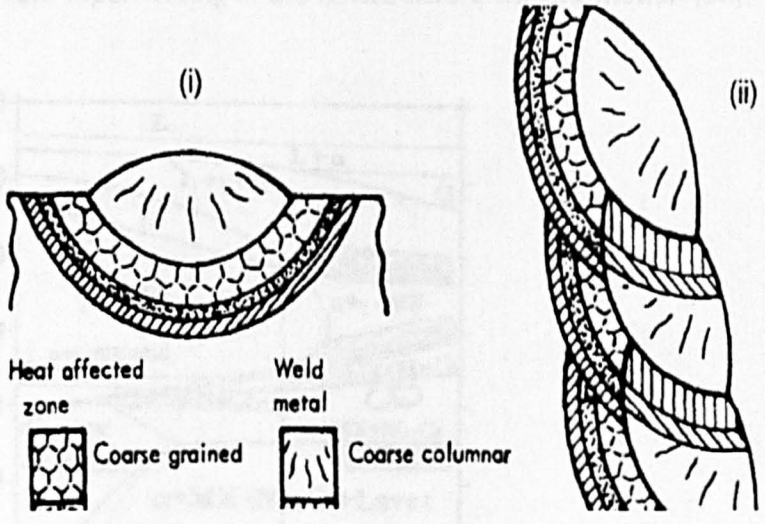

Figure 2-17: Schematic diagram of the various subzones within (i) a single pass and (ii) a multi-pass weld [80].

The heat affected zone (HAZ)

The heat affected zone (HAZ) is part of the parent material that has not melted during welding but in which the microstructure and mechanical properties have been altered [81]. The resulting microstructure is governed by the heating rate of the weld thermal cycle, the peak temperature experienced, the dwell time, the cooling rate, the effect of multipass welding and finally by the post weld heat treatment (PWHT) parameters.

The phase diagram provided by Igarashi *et al.* [82] is useful in interpreting the microstructural variations across the HAZ (Figure 2-18). The solvus temperatures for MX and $M_{23}C_6$ carbides are also shown on the same diagram. However it should be noted that the heating rate in arc welding processes can be as high as 200-300 Ks^{-1} which may result in significantly higher transformation temperatures than predicted in an equilibrium phase diagram. For example, ferrite transforms to austenite at about 100 K higher than the equilibrium temperature at a heating rate of 100 Ks^{-1}, resulting in considerable superheating of the ferrite before transformation [68].

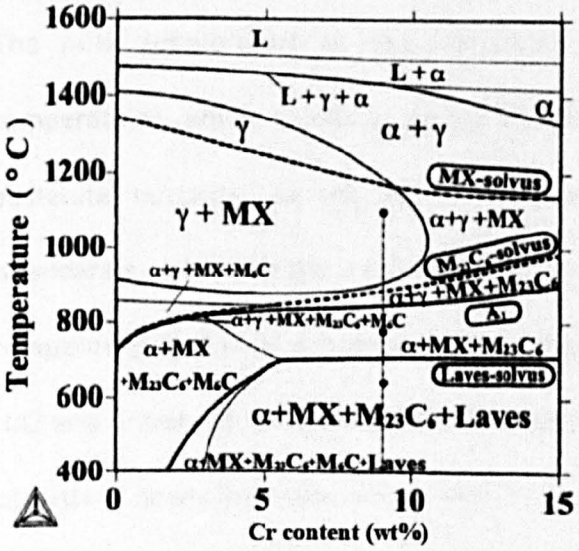

Figure 2-18: Phase diagram for martensitic stainless steels [82].

Coarse grain region (CGHAZ)

The coarse grain HAZ is adjacent to the fusion line and thus experiences peak temperatures well above Ac_3. Precipitates, which obstruct growth of austenite grains at lower temperatures, dissolve, resulting in coarse grains of austenite [83] with almost no grain boundary precipitation. The CGHAZ features the highest hardness of the HAZ and

generally low toughness values are expected [68]. On cooling, a coarse grained martensitic microstructure is formed.

Fine grain region (FGHAZ)

In the FGHAZ, the peak temperature experienced during welding is lower than in the CGHAZ but still above Ac_3. This peak temperature is not sufficiently high to completely dissolve existing precipitates, which results in the formation of small grains of austenite due to recrystallization. On cooling, a fine-grained martensitic microstructure is formed.

Intercritical region (ICHAZ)

The peak temperature in the intercritical region lies between the Ac_1 and Ac_3 temperatures, which results in partial transformation of α into γ on heating. The new austenite nucleates at the prior austenite grain boundaries and martensite lath boundaries, whereas the remainder of the microstructure (remaining α) is simply tempered [68]. Partial dissolution of precipitates can be experienced in this part of the HAZ and coarsening of undissolved precipitates can occur. On cooling, the microstructure consists of newly formed virgin martensite and an over-tempered original microstructure. This region exhibits the lowest hardness of the HAZ.

Over tempered region

With peak temperatures below the Ac_1 temperature, the original microstructure does not undergo any phase transformations but undergoes further tempering which result in coarsening of precipitates.

2.4.2 Nature of Weld Failures

In the past, parent materials have been known to fail due to manufacturing faults, little understood metallurgical effects at that time and/or non-safe operating conditions

(usually out of control temperature and/or steam pressure excursions). However, today these situations occur very infrequently, largely due to high quality steel manufacturing, a good understanding of long-term metallurgical changes and well-controlled and monitored parameters of operation within the power plants.

Therefore, it is more often the integrity and strength of the welded joints that ultimately determine the overall plant performance, structural integrity and life of the steam pressure system. Welded joints are subjected to not only the pressure and temperature of the steam, which generates the hoop stresses within the tubes and pipes, but also to several other stress patterns caused by additional end loads and system stresses, which are exacerbated by the complexity of the mechanical structure and temperature variations, which, nowadays tend to be cyclical [41].

The types of cracking associated with weldments of heat-resistant steels have been well categorised by Schuller *et al.* [84] depending on their location and orientation as shown in Figure 2-19. Type I cracks initiate and remain in the weld metal and run both transverse and longitudinal to the weld. Type II cracks are similar to Type I cracks but extend in the HAZ and sometimes in the parent metal. Both Type I and Type II cracks are rarely associated with creep damage but more commonly related to weld defects or stress relief during PWHT. Type III damage initiates in the coarse-grained HAZ and propagates parallel and close to the fusion line and can also extend into the parent material. One of the possible mechanisms of Type III cracking is stress relaxation during PWHT whereby the local ductility is exceeded such that creep cavitation and eventually cracking occurs on the prior austenite grain boundaries. This form of cracking is also referred to as reheat cracking but it should be noted that the latter can occur in the weld metal as well. A further type of cracking has been found quite recently, and is designated Type IIIa [85].

This mode of cracking occurs close to the weld fusion line in HAZ material that has been fully grain refined by the welding process. It was designated as Type IIIa to distinguish cracks in such fine grained structures from reheat cracking in coarser grained structures at the same location, which would be classified as Type III cracking. Type IIIa cracking has been found to occur in 0.5%CrMoV pipework after about 80 000h of service [86]. Finally, Type IV cracking refers to cracks formed in the fine-grained or intercritical HAZ.

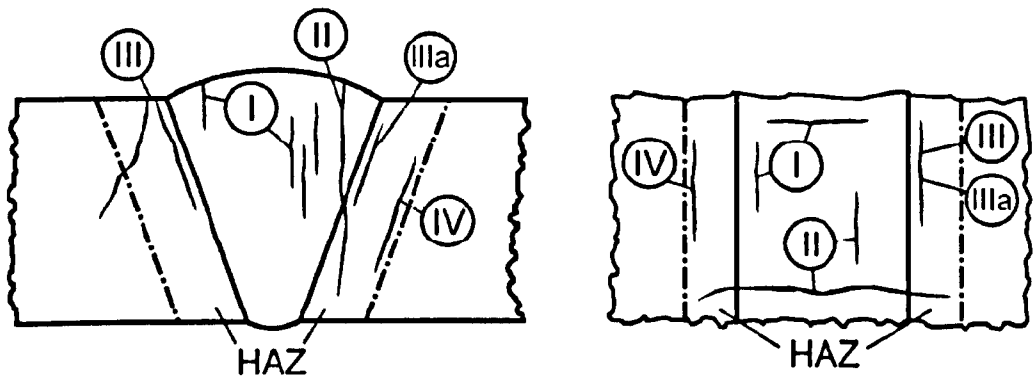

Figure 2-19: Schematic of cracking modes in weldments in heat resistant steels [75], [84].

2.4.3 Type IV Cracking Phenomenon

This form of cracking is very time-dependent and was discovered in the late 1970s [51]. Type IV cracking (Figure 2-20) has been observed in low alloy ferritic/bainitic steels (½CrMoV, 1CrMo, 1CrMoV, 1¼Cr0.5Mo, 2CrMo, T/P22, T/P23, T/P24), as well as in ferritic/martensitic 9-12% Cr steels (P91, X20CrMoV121, P92, P122, E911) [41], [51], [68], [87], [88]. Traditionally, Type IV creep cracking has been associated with the intercritical HAZ in low alloy ferritic steels. The behaviour of martensitic steels is somewhat different and Type IV cracks are typically found in the fine grained HAZ [51]. Nevertheless, some authors [89], [90] have reported failures in the intercritical HAZ in P91 but this may be related to the difficulty in differentiating between the fine grained and intercritical HAZ due to similar features in both regions.

Figure 2-20: Type IV cracking observed in a P91 weldment (courtesy of European Technology Development).

After normalising and tempering heat treatments, 9-12% Cr steels have a tempered martensitic microstructure that consists of laths and blocks of martensite with a high dislocation density, and fine carbonitride particles dispersed along the lath and block boundaries as well as in the matrix. During welding, the microstructure and mechanical properties of the parent material adjacent to the weld are altered by the weld thermal cycle. The lath-block martensitic structure is absent in the FGHAZ region which suggests that boundary and sub-boundary hardening is significantly reduced, making it more vulnerable to cracking and failure [91].

The peak temperature in the FGHAZ is just above the Ac_3 temperature, which is not sufficiently high to completely dissolve existing precipitates. On cooling, precipitation on retained large particles, such as $M_{23}C_6$ is favoured instead of fine re-precipitation on grain boundaries in order to decrease the interfacial energy of the microstructure [92]. During PWHT, this results in severe coarsening which minimises the precipitation strength of the

material and the large particles act as preferred nucleation sites for creep cavitation. The formation of small grains due to recrystallization also results in a high proportion of grain boundary surface area per unit volume of material, which suggests that grain boundary sliding is significant in the FGHAZ region, which tends to reduce the creep strength [93].

2.4.4 Previous Studies on Type IV Failure in Welds

Type IV cracking has plagued the power generation industry for over 30 years now, but plant operators may be reluctant to discuss cracking incidents/failures. After a few years of confidentiality, information on some of these failures has now been published [51], [94]. Most of the reported P91 failures have occurred very early in life (~50,000 h of service), with some only after 20,000 h in service. This is in spite the fact that the service temperature was only a modest 568°C compared to the design temperature of 600°C [94]. Type IV cracking is thus a matter of great concern and has spurred a lot of research interest worldwide. Good overviews of Type IV cracking are given in papers by Middleton and Metcalfe [95], Ellis [96] and Francis *et al.* [97].

It is now very well established that the creep strength of welded joints in 9-12% Cr steels is much lower than that of parent metal due to Type IV cracking. The microstructural features discussed in the previous section, together with a small grain size that enables faster diffusion, result in lower long-term creep resistance in the FGHAZ. Figure 2-21 shows the difference in creep strength of P91 welded joints compared to P91 parent material at different temperatures. Clearly, the base material strength exceeds the cross-weld (joint) strength at all the investigated temperatures. Interestingly, in short-term tests (high stress levels); we note that the cross-weld specimens perform better than the parent material.

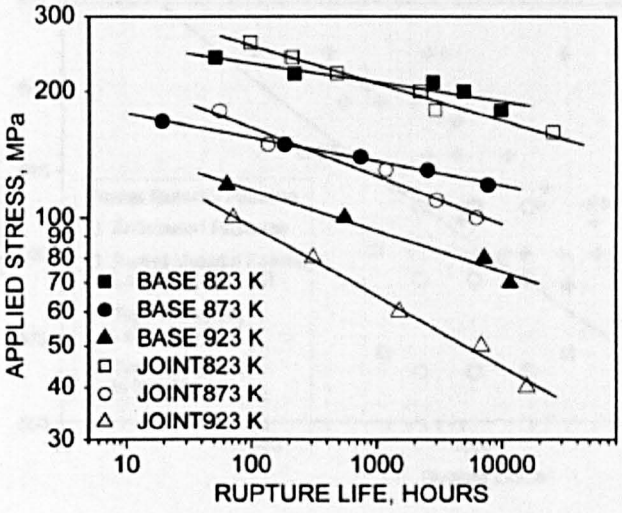

Figure 2-21: Creep rupture data for P91 welded joint [98].

In a cross-weld creep test, the sample fails either in the parent metal, weld metal, or the HAZ. From the literature, it emerges that when tests are conducted at high stress levels, failures take place randomly. For lower stress levels, failures are confined to the FGHAZ or the intercritical region in low alloy steels. The shift in fracture location depends on both stress and temperature, with stress being of greater influence [59]. An analysis of published data on cross-weld creep strength of 9-12% Cr steel reveals that the transition stress for Type IV failures is 100 MPa [97], [99]. A weld failure prediction diagram (Figure 2-22) has been produced by EPRI to show a line of demarcation in which Type IV failure would occur at different test temperatures. These observations provide useful information to take into account when planning a creep test programme.

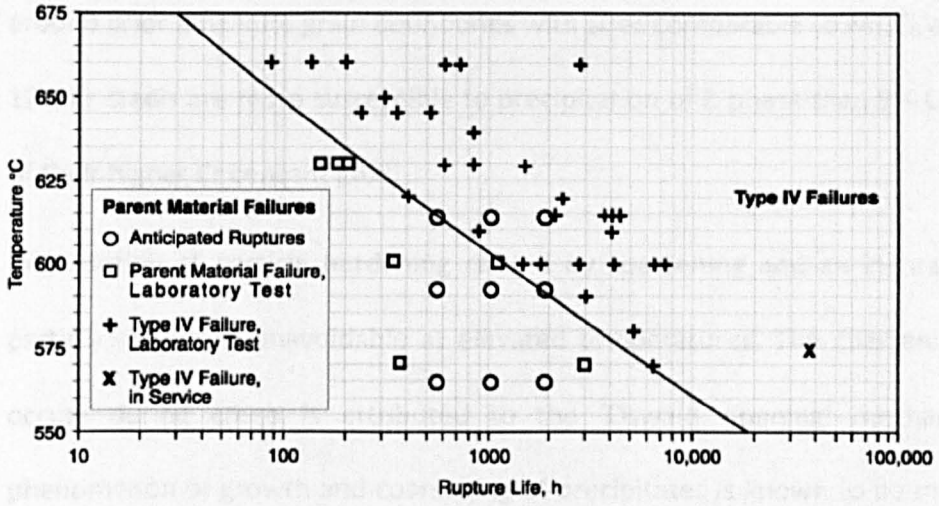

Figure 2-22: Predicted failure locations for P91 at different temperatures [100].

A significant amount of work has been carried out towards understanding the microstructural changes that occur during creep in 9-12% Cr martensitic steels [54], [62], [75], [79], [101], [102], [103], [104]. When exposed to creep conditions, a significant reduction in dislocation density occurs along with coarsening of $M_{23}C_6$ and MX precipitates allowing the martensite laths to transform to more equiaxed subgrains to reduce the free energy of the crystal. The subgrain size and shape is sensitive to the applied stress level and duration of exposure to high temperatures [105], [106], [107]. At low stresses, lath recovery occurs preferentially in the vicinity of prior austenite grain boundaries, resulting in premature creep failure.

During creep, grain boundary phases emerge such as; Laves phase Fe_2 (W, Mo), M_6X carbonitrides and Cr-V-Nb-N rich Z-phase [5], [49]. Laves phase is an intermetallic compound found to precipitate on grain and subgrain boundaries during exposure to high temperatures. The precipitation of Laves phase decreases solute strengthening but can also increase the precipitation strengthening when the precipitates are fine [39]. Z-phase [5] is regarded as being detrimental to creep strength because it consumes the fine MX carbonitride particles, which are the main strengthening elements [49]. Z-phase forms

around prior austenite grain boundaries with sizes comparable to $M_{23}C_6$ and Laves phase. 12% Cr steels are more susceptible to precipitation of Z-phase than 9% Cr steels because of their higher Cr content [108].

Degradation of particle hardening caused by coarsening and an increase in the mean particle spacing is unavoidable at elevated temperatures. The coarsening process that occurs during creep is attributed to the 'Oswald ripening' mechanism [61]. The phenomenon of growth and coarsening of precipitates is known to be more prevalent in the FGHAZ. Li *et al.* [109] proposed that since the grain size in the FGHAZ region is smallest compared to other regions of the weldment, grain boundary diffusion is much faster than diffusion within the grain. Thus, it can be considered that the small grain size provides more diffusion routes for boundary diffusion which lead to larger precipitates [109].

Sawada *et al.* [103] have studied the microstructural changes during creep in E911 steel welded joints. Before creep, equiaxed subgrains were observed in the FGHAZ. Some of the $M_{23}C_6$ particles in this region do not dissolve during welding because the peak temperature is only just above the Ac_3 temperature. As a result, the martensite lath structure that is formed on cooling has a lower carbon content and a lower dislocation density than the base metal and consequently, dislocation re-arrangements and recovery of the FGHAZ structure are possible during PWHT. Figure 2-23 shows the changes that occurred in the equiaxed subgrain structure of the FGHAZ and in the martensite lath structure of the base metal during creep exposure at 600°C. It was observed that $M_{23}C_6$ particles grow faster in the FGHAZ than in the base metal during creep, and a larger number of Z-phase particles were formed in the FGHAZ.

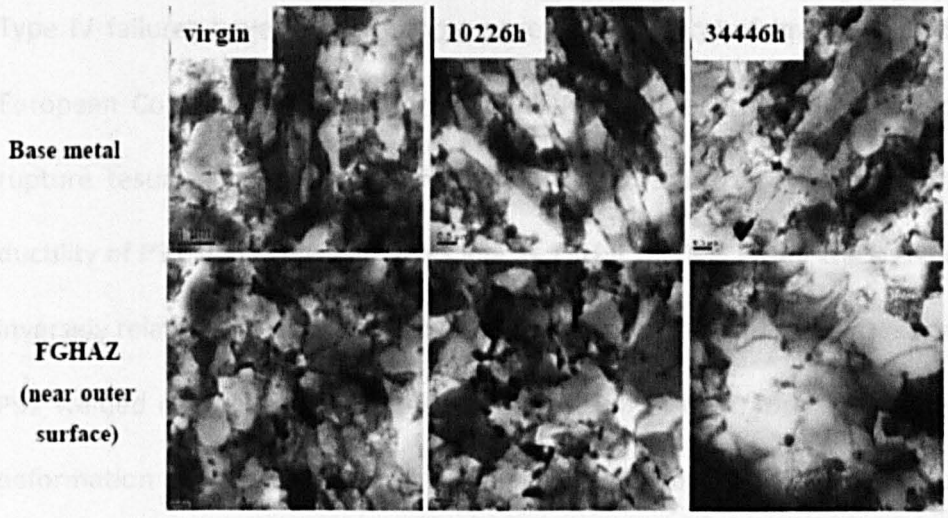

Figure 2-23: Changes in martensitic lath structure of the base metal and equiaxed subgrain structure of the FGHAZ during creep exposure [103].

Parker and Stratford [110] have studied the effects of PWHT on creep fracture in low alloy steels. They studied samples post weld heat treated for 2 hours at 3 different temperatures (700°C, 725°C, and 750°C). Their results showed an increase in creep rupture life with decreasing temperature. Similar results have been reported for P91 steel by Li [111] where weldments were post weld heat treated in the range of 600 to 840°C, for durations of 2 and 8 hours. Longer creep rupture life resulted from samples heat treated at a lower temperature for a shorter time (600°C, 2 hours). However, the room temperature toughness of the heat-affected zone only recovered after a 720°C, 2 hour post-weld heat treatment.

A different story emanates from the work of Albert *et al.* [112] on the effect of PWHT on Type IV cracking. Specimen blanks extracted from a P122 welded joint were post weld heat treated at 1013 K for durations of 0.25, 0.5, 1, 2, 3 and 4 hours with air-cooling in all cases. Their results showed no significant change in rupture time with duration of PWHT, except slightly lower values for specimens subjected to short duration PWHT (15 and 30 min) than those subjected to PWHT for 1 h and above.

Type IV failures have a macroscopic appearance typical of low ductility failures. In the European Commission funded project 'HIDA' [113], a programme of cross-weld creep rupture testing showed that when fracture occurs in the Type IV position, the creep ductility of P91 specimens can be as low as 1% (at 625°C). Creep crack growth is generally inversely related to material creep ductility, so creep crack growth rates could be faster in P91 welded components. However, in the region of the Type IV zone, significant creep deformation has been measured by Parker and Parsons [114]. In their study, specimens with a surface grid of microhardness indents were used and strains were calculated by measuring the spacing between the indents before and after testing. Strains in the order of 20% were measured in the Type IV zone with much less strain accumulation elsewhere. In another study by the same author, strains of similar magnitudes were estimated from measurements of the grains' dimensions [115]. Similar results have been reported for 2.25Cr-1Mo steel by Laha *et al.* [116]. These results suggest that enhanced creep cavitation and thus Type IV cracking may be related to the high strain localisation in the HAZ.

The stress state in a pipe weld is multiaxial because of the complex weld geometry and the influence of the internal pressure and piping-system loads. Because creep rupture life is dependent on the stress state, application of uniaxial creep rupture data to complex welds can affect the accuracy of life predictions [23]. Several experiments have been conducted mainly in Germany (MPA Stuttgart) on internal pressure creep tests [117], [118], [119], [120]. Due to the constraint on deformation capacity, the sensitivity to creep cavity evolution is promoted [119] and multiaxially loaded components show shorter times to failure for comparable equivalent stresses (von Mises criterion). This effect is

also shown in Figure 2-24. Thus, it is recommended to consider a Multiaxiality Factor in the design in order to prevent premature failure and to establish safety margins.

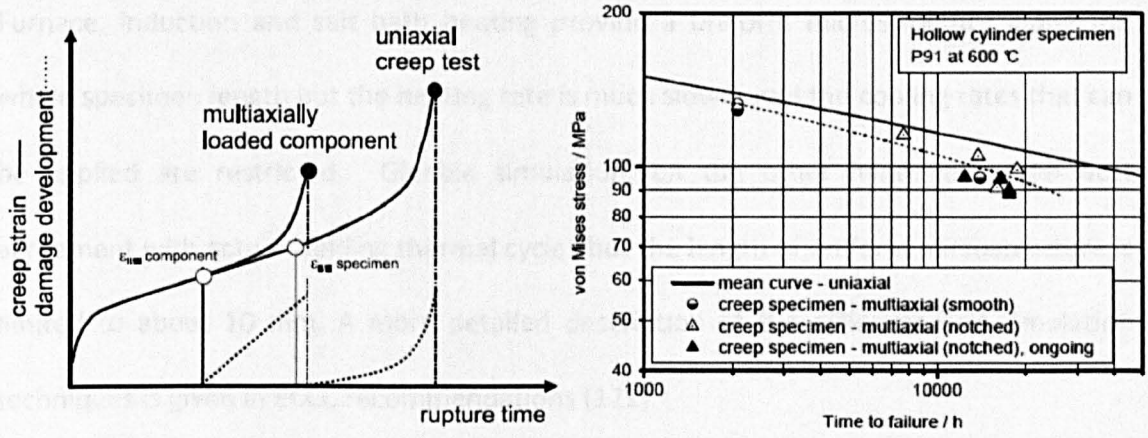

Figure 2-24: Effect of multiaxial stress state on creep strain (left) and creep rupture behaviour (right) of P91 parent material [119].

2.4.5 HAZ Simulation Studies

In a welded joint, the HAZ is typically only a few mm in width, which makes extracting specimens from a single metallurgical zone difficult and thus, the properties of the different zones are difficult to derive from cross-weld creep test results. Simulated HAZ specimens are usually used to characterise the behaviour of each sub-zone of the HAZ. The microstructure and mechanical properties of the HAZ are dependent on the peak temperature, transformation kinetics, and cooling rate. Microstructural simulation is a useful technique because it enables the experimenter to isolate the contributions of specific influences on creep performance.

Simulated HAZ specimens can be prepared by:

- Furnace heating
- Induction heating

- Gleeble weld simulation
- Salt bath heating

Furnace, induction and salt bath heating provide a uniform microstructure along the whole specimen length but the heating rate is much slower and the cooling rates that can be applied are restricted. Gleeble simulation, on the other hand, gives the best agreement with actual welding thermal cycles but the length of uniform microstructure is limited to about 10 mm. A more detailed description of the different HAZ simulation techniques is given in ECCC recommendations [121].

Albert *et al.* [122] used both furnace and Gleeble simulation to look at the performance of P122 specimens heated to peak temperatures varying from 750 to 1200°C. The specimens heated just above the Ac_3 temperature (i.e. the FGHAZ) showed minimum time to rupture and the two methods were in reasonable agreement (Figure 2-25), except for high peak temperatures (1000 and 1200°C). Furthermore, fracture always occurred in the region where creep strength was at a minimum. For the 1000 and 1200°C simulated specimens, the creep strength of the simulated zone (~10 mm in the centre of the specimen) was high and thus failure occured outside the simulated zone (but still in the gauge length), which was not desirable. Thus, furnace heat treatment showed to be more practical for the complete range of peak temperatures.

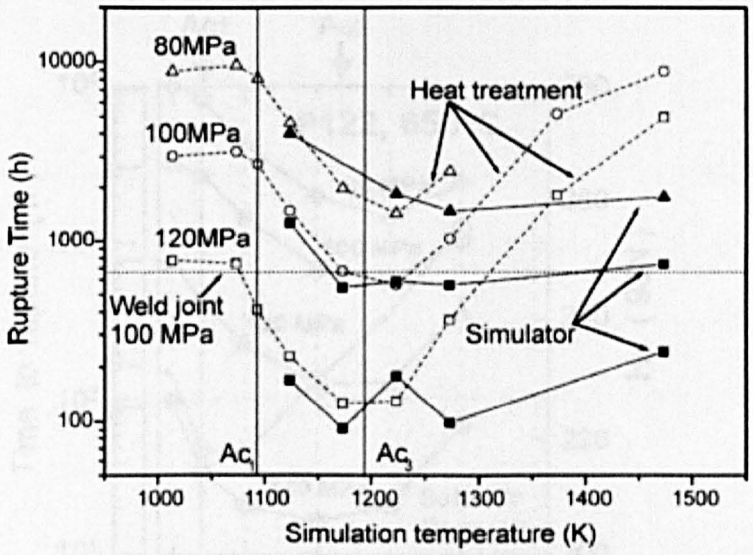

Figure 2-25: Variation of creep rupture time with simulation temperature and stress in ASME-P122 steel [122].

Abe and Tabuchi [101] also studied P122 HAZ simulated specimens using furnace heat treatments. The creep rupture time had its minimum after heating the specimens to a temperature near the Ac_3 temperature, whereas the hardness evaluation showed a minimum after heating to a temperature near the Ac_1 temperature (Figure 2-26). The softening produced by Ac_1 heating therefore does not explain the minimum time to rupture. Interestingly, at high stresses (140 and 120 MPa), the minimum time to rupture corresponds to specimens heat treated below the Ac_3 temperature (ICHAZ). When the stress was reduced, specimens heated to above the Ac_3 temperature (FGHAZ) exhibited the minimum time to rupture.

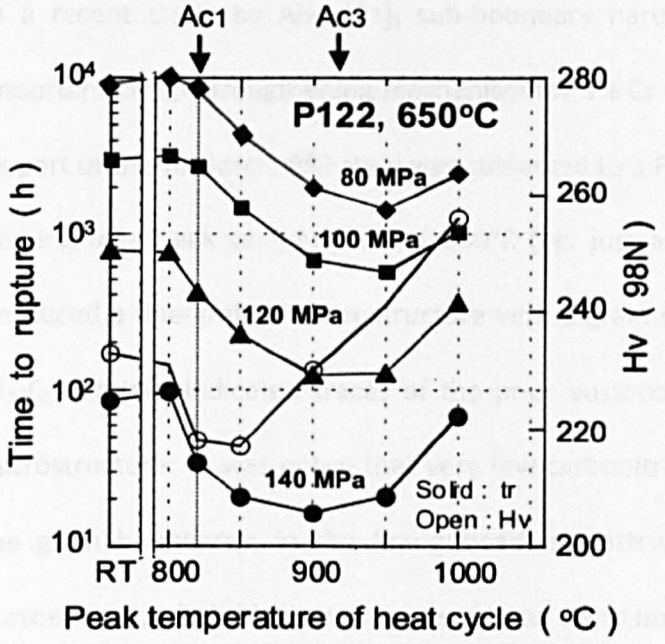

Figure 2-26: Rupture times for furnace heat treated HAZ simulation specimens in ASME-P122 steel at 650°C [101].

An alternative approach to simulated HAZ specimens is to conduct creep tests on small samples machined directly from different locations within the weld. The creep properties of a P91 welded joint were investigated in this way by Spigarelli and Quadrini [123]. Their results indicated high values of minimum strain rate in the FGHAZ while the base metal and weld metal exhibited an intermediate behaviour. Extracting small specimens accurately from the different regions of the weldment is very challenging and poses constraints on the type of creep testing methods that can be used. Very often, small specimen testing methods such as small-scale "conventional", small punch and impression creep testing need to be employed [124], [125]. Such methods are widely used in industries on in-service materials whereby a non-invasive material sampling technique is used to extract a small sample of appropriate size from the operating plant components, without jeopardising its integrity. Miniature specimen tests are then conducted for determination of residual service life of the operating components.

In a recent study by Abe [91], sub-boundary hardening was identified as the most important creep-strengthening mechanism for 9% Cr steel base metal and welded joints. As part of this research, P92 steel was subjected to a FGHAZ simulation heat treatment by heating to a peak temperature of 950°C (i.e. just above the Ac_3 temperature), which produced a fine-grained microstructure with a grain size less than 10μm. Rows of large $M_{23}C_6$ carbides indicated traces of the prior austenite grain boundaries of the original microstructure. It was noted that very few carbonitride precipitates were formed along the grain boundaries in the fine-grained microstructure during PWHT (Figure 2-27). Furthermore, a lath-block martensite structure was not evident in the fine-grained region. These observations suggested that boundary and sub-boundary hardening were significantly reduced in the simulated FGHAZ material compared to the base metal. Creep rupture testing of simulated HAZ structures confirmed that the simulated FGHAZ material had the shortest creep rupture lifetime.

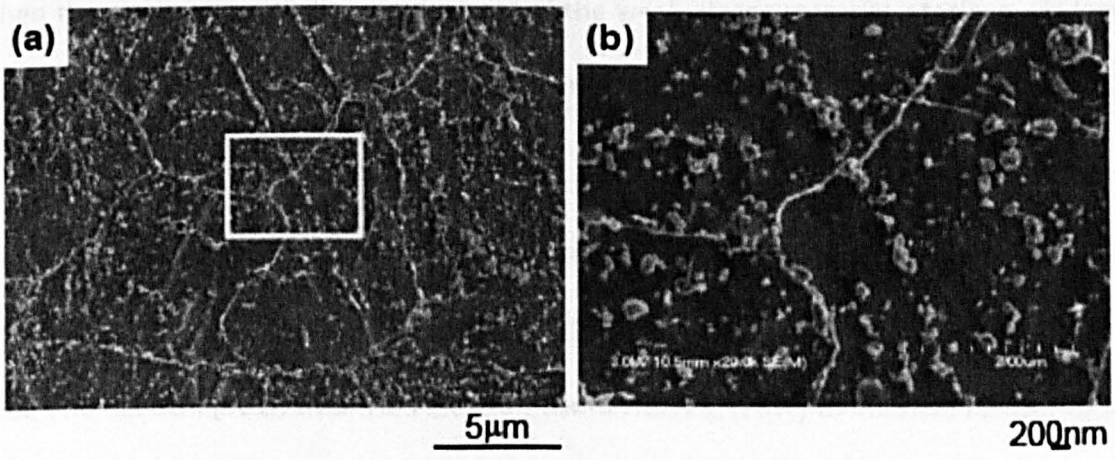

Figure 2-27: Microstructure of simulated FGHAZ of P92 steel, after heating to a peak temperature of 950°C [91].

2.4.6 *Influence of constraint on creep of weldments*

Because of the gradients in microstructure within a weldment, there are corresponding gradients in the creep properties. Simplifying the load condition to plain tensile loading of the dissimilar regions within a weldment (parent metal, HAZ, weld metal) in series, the weakest part (HAZ in the case of 9-12% Cr steels) tries to deform transversely under high strains [68]. If this region is sufficiently thin, it is constrained from doing so by the adjacent stronger material. As a result, triaxial stresses develop in the HAZ, which could explain the preferential creep failure of welds in the weak region of the HAZ. A high degree of triaxiality in stress can also reduce the ductility an order of magnitude or more [126].

A number of finite element studies have been conducted to study the behaviour of cross-welds undergoing uniaxial tension [93], [127], [128], [129], [130], [131]. The results showed that when the width of the weak layer is less than the diameter of the specimen, then the strain compatibility requirement of the weak/strong material interface will lead to a significant constraint of the weak material and the strength of the weak material would be close to that of the strong material.

A narrow HAZ can decrease the equivalent strain in the FGHAZ and thus be beneficial in improving resistance to Type IV cracking [129]. This has been shown experimentally by Abe and Tabuchi [101], who used Electron beam welding (EBW) to improve resistance to Type IV cracking by decreasing the width of the HAZ. Indeed, the rupture lives for the EBW joints were about two times longer than those of the GTAW joints (Figure 2-28). At 110 MPa and 650°C, the location of fracture was away from the welded part in EBW joints whereas GTAW joints failed by Type IV cracking. However, the brittle Type IV fracture

persisted even in the EBW welded joints at low stresses (<100 MPa) and long-time conditions.

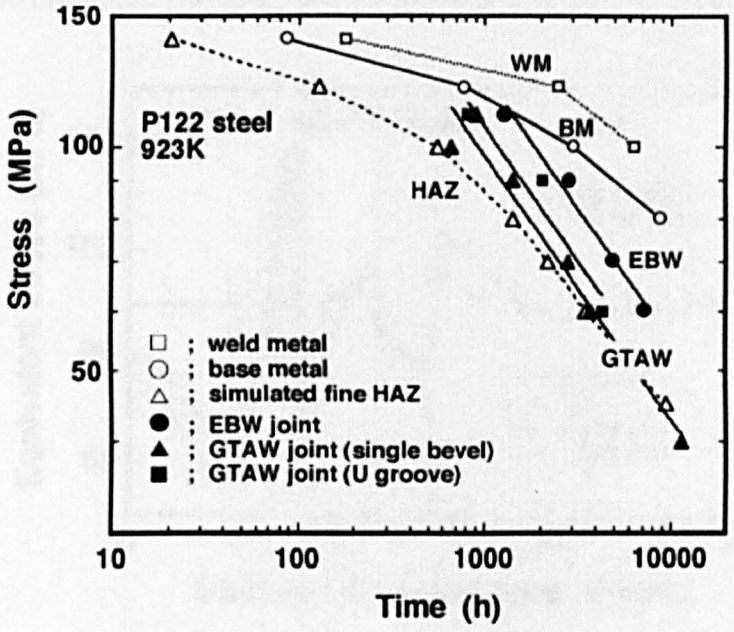

Figure 2-28: Type IV creep rupture data for weld metal, base metal, Ac_3 simulated fine-grained HAZ, GTAW and EB welded joints in ASME-P122 steel at 650°C [101]

Li *et al.* [131] simulated creep behaviour of a P122 weldment based on Norton's law by compiling a model consisting of four regions with different creep properties (weld metal, CGHAZ, FGHAZ and base metal). They showed that a high tensile first principal stress and high tensile hydrostatic stress were generated in the FGHAZ and that the strain focuses in the weaker FGHAZ during the early stages of creep. This phenomenon suggests an important role for equivalent strain on the occurrence of creep voids, which are then encouraged to grow by the strain mismatch and triaxial stresses. The distribution of equivalent stress along the centre-line of the specimen is shown in Figure 2-29. It can be seen that for the CGHAZ/FGHAZ interface the equivalent stress is low in the FGHAZ but high in the CGHAZ region adjacent to the FGHAZ, and for the FGHAZ/BM interface, the equivalent stress is low in the FGHAZ but high in the BM region adjacent to the FGHAZ.

The FGHAZ creeps more easily than the CGHAZ and BM. Thus, when the FGHAZ creeps, the CGHAZ and BM deform less and impose constraints on the FGHAZ to prevent its creep deformation. The constraints lead to high equivalent stress in the CGHAZ and BM.

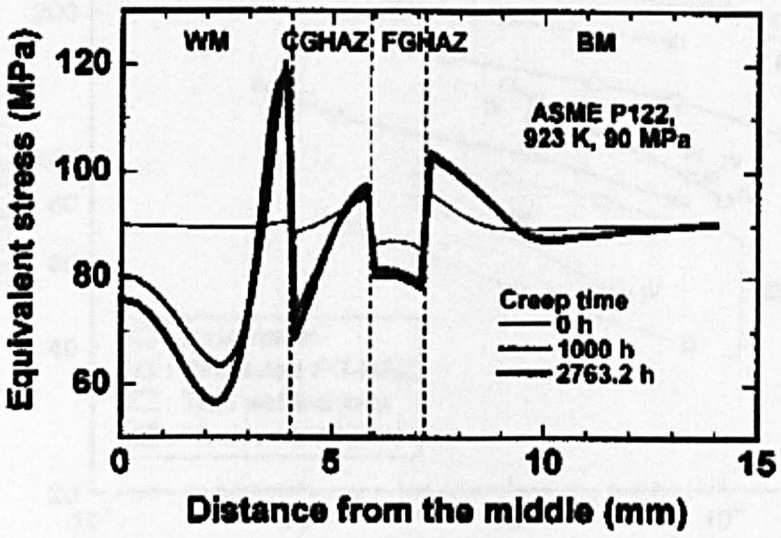

Figure 2-29: Equivalent stress distribution along the centreline of specimen after different creep times [131].

These results are significant because on the one hand, they suggest that a weak FGHAZ sandwiched between stronger parent and weld metal gives rise to significant constraint, which delays failure in the FGHAZ but, on the other hand, the triaxial stress state in the FGHAZ accelerates the growth of creep voids. It is well established that a triaxial stress state (high hydrostatic stresses) accelerates the growth and coalescence of voids into microcracks [122], [132]. Thus, it is reasonable to assume that constraint is both beneficial and detrimental. This is consistent with experimental results. For example, considering the data presented by Li *et al.* [133] in Figure 2-30, the creep performance of welded joints is close to the base metal at high stresses and there is a large difference between the performance of welded joint and FGHAZ simulated specimens. This indicates that constraint (present only in the welded joint) is beneficial and actually delays failure in

the FGHAZ in short term tests. Similar results have been reported by Abe and Tabuchi [101].

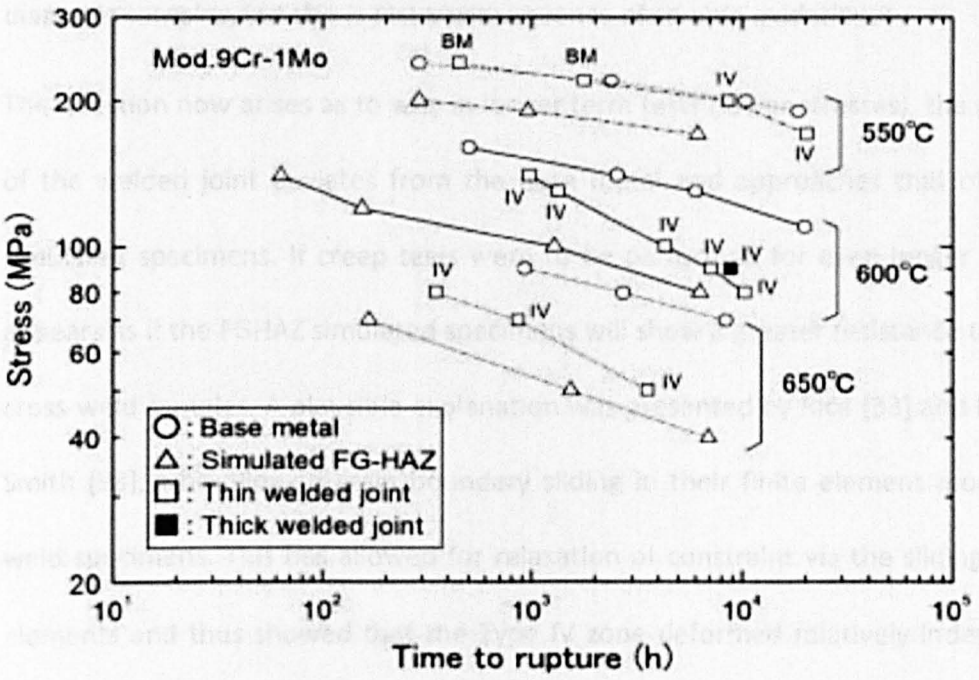

Figure 2-30: Results of creep rupture tests for base metal, simulated fine-grained HAZ, and welded joints of Mod.9Cr–1Mo steel at 550, 600 and 650°C. The subscripts 'BM' and 'IV' on the data plots mean that the fracture location of welded joint is base metal and fine-grained HAZ (Type IV), respectively [133].

In Figure 2-30, an important observation is made regarding specimen size effect. The rupture life of larger specimen was slightly longer than smaller specimen (90 MPa, 600°C, 8853hr vs. 7147 hrs). The effect of constraint can thus, also be used to some extent to explain the increase in life that is normally seen with increasing sample dimensions [134], [135]. For a fixed HAZ width, as the size of the specimen is increased, the impediment to deformation and necking increases which results in an increase in rupture life. The effect of sample size has been well studied by Iwadate *et al.* [134], Prager [136], Parker [137], and Viswanathan and Foulds [138] and it is thus recommended that accelerated tests on

weldments should use large samples which are representative of the weld geometry. For low alloy steels, even homogeneous specimens show an increase in rupture life for larger diameter samples, but this is just a consequence of sample oxidation.

The question now arises as to why in longer term tests (lower stresses), the performance of the welded joint deviates from the base metal and approaches that of the FGHAZ simulated specimens. If creep tests were to be performed for even longer durations, it appears as if the FGHAZ simulated specimens will show a greater resistance to creep than cross-weld samples. A plausible explanation was presented by Rice [33] and Kimmins and Smith [93], who allowed grain boundary sliding in their finite element model of cross-weld specimens. This has allowed for relaxation of constraint via the sliding of adjacent elements and thus showed that the Type IV zone deformed relatively independently of adjacent stronger material. Grain boundary sliding is a major factor in creep deformation and cavity nucleation at high temperatures and relatively low stresses. The influence of this mechanism will be especially pronounced in the FGHAZ region due to the high grain boundary area per unit volume of material. At high stresses matrix deformation plays a greater role and consequently a small grain size may be expected to increase creep strength [128].

2.5 Residual Stresses

Residual stresses are defined as stresses that exist in a structure under uniform temperature conditions in the absence of any externally applied loads, and are those which are not necessary to maintain equilibrium between the structure and its environment. Residual stresses can be introduced by forming, joining, machining, heat treatment, abrasion, impact and many other processes that materials are subjected to

during fabrication [139]. They can be detrimental to the performance of engineering components and thus need to be considered in the same way as external stresses; otherwise, the service life may be greatly affected. They superimpose on in-service stresses and thus add to the stresses caused by the applied load to cause localised yielding, even though the applied load itself may not have been high enough to do so. On the other hand, residual stresses are sometimes deliberately introduced into a component, for example by shot peening, the toughening of glass, and in the manufacture of prestressed concrete.

Residual stresses can be grouped according to the scale over which they act [140], [141]. For instance, macrostresses (Type I) are nearly homogeneous across large areas and equilibrate over a length scale comparable to a macroscopic dimension of the structure. These stresses originate mainly from processing operations such as: shot peening, welding, heat treatment and forming. Type II stresses (microlevel), are usually present in polycrystalline or multiphase materials and vary over a much smaller scale. They self-equilibrate over a length comparable to the grain size. These stresses occur because of some small scale heterogeneity in the material for example mismatch in coefficient of thermal expansion or elastic modulus [142]. Type III stresses is the other term associated with microstresses and these are inhomogeneous across submicroscopic areas of a material varying over distances down to atomic dimensions within the grain. These usually arise from local stress fields around dislocations. Type II and Type III residual stresses are also referred to as intergranular and intragranular stresses respectively. The variation of Type I, II and III residual stresses have been clearly illustrated by Hutchings *et al.* [140] in Figure 2-31.

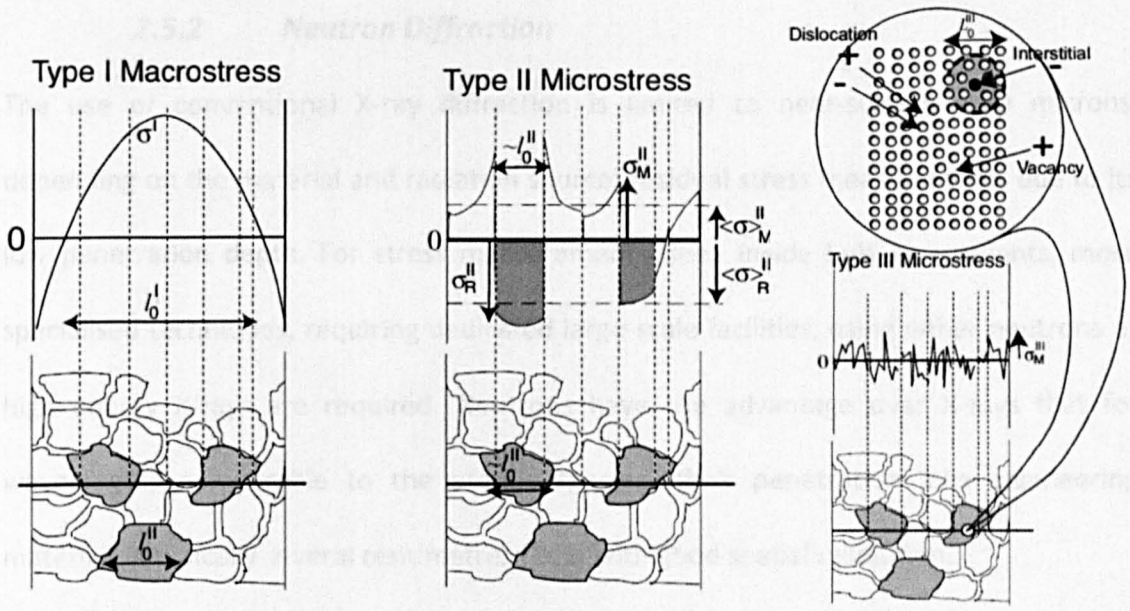

Figure 2-31: Variation of Type I, II, and III stresses in a material [140].

2.5.1 Methods of residual stress measurement

The methods that can be used to measure residual stresses can be classified into two categories: destructive and non-destructive. Destructive stress measurement techniques generally involve material removal from a sample in some way. This is done to cause at least partial relaxation of the residual stress field within the sample, whilst the resulting strain is measured [139]. The residual stress that caused the deformation can then be calculated from measurements of the deformation response. Examples of destructive techniques include hole drilling, slitting and the contour method. Non-destructive methods, as the name implies, are those methods in which the properties and performance of the components are not altered and thus, the components can be reused or tested further. Some examples include diffraction-based, magnetic and ultrasonic techniques.

2.5.2 *Neutron Diffraction*

The use of conventional X-ray diffraction is limited to near-surface (~50 microns, depending on the material and radiation source) residual stress measurements due to its low penetration depth. For stress measurements deep inside bulk components, more specialised techniques, requiring dedicated large-scale facilities, using either neutrons or high energy X-rays are required. Neutrons have the advantage over X-rays that for wavelengths comparable to the atomic spacing, their penetration into engineering materials is typically several centimetres [141] with good spatial resolution.

There are two sources for the production of intense neutron beams: reactor sources and accelerator-based spallation sources. In reactor sources, neutrons are generated by the fission of uranium whilst in spallation sources, neutrons are obtained by the bombardment of protons into a heavy nucleus (e.g. Tungsten, Uranium, Tantalum). Examples of reactor sources are: ILL in France, ANSTO in Australia and examples of spallation sources are: PSI in Switzerland and ISIS in UK. Spallation sources are also sometimes referred to as pulsed sources or time-of-flight diffractometer.

The measurement of residual stresses using neutron diffraction is based on Bragg's law of diffraction (Equation 2-5). If neutrons with a wavelength λ are incident on a crystal and are diffracted from lattice planes of spacing dhkl, diffraction peaks will be observed at an angle 2ϑ relative to the incident beam (Figure 2-32). Under an applied tensile (or compressive) stress, the lattice spacing in individual crystallite grains expands (or contracts). This change in the lattice spacing can be detected, at constant wavelength, as a shift ($\Delta\vartheta_{hkl}$) in diffraction peaks.

$$\lambda_{hkl} = 2d_{hkl}\sin\theta \qquad \textbf{Equation 2-5}$$

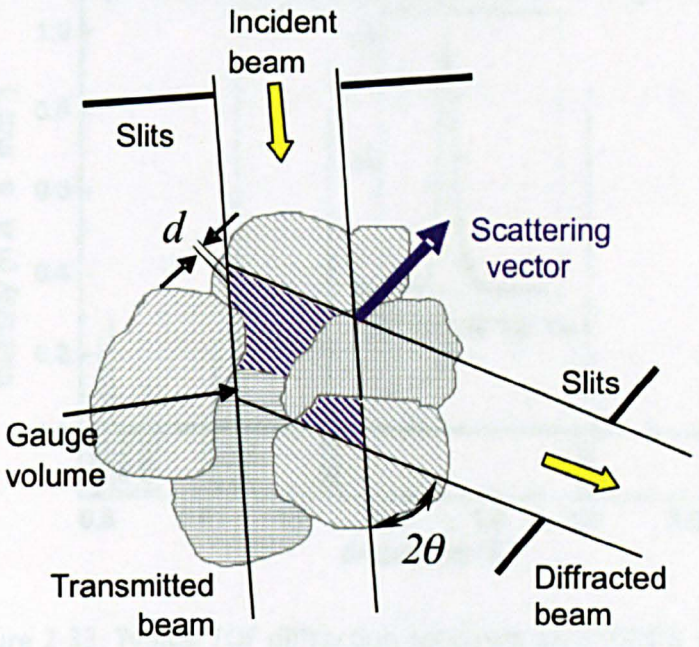

Figure 2-32: Principle of neutron diffraction showing a Bragg reflection from favourably aligned crystal planes. There are normally a large number of grains in the gauge volume, but only a fraction of these will be in the correct orientation to meet the diffraction condition at any time [143].

In a time-of-flight (TOF) diffractometer, the neutrons originating from the moderator have a wide energy range from a few meV up to many eV, which corresponds to wavelengths in the range from 0.1–10 Å. When a pulse of neutrons is directed onto a sample, those with different wavelengths will require different times to reach the sample at a fixed distance from the moderator. Thus if the detected neutron count is plotted as a function of time it will exhibit a series of peaks corresponding to the different d_{hkl} lattice planes in the material as shown in Figure 2-33 [144].

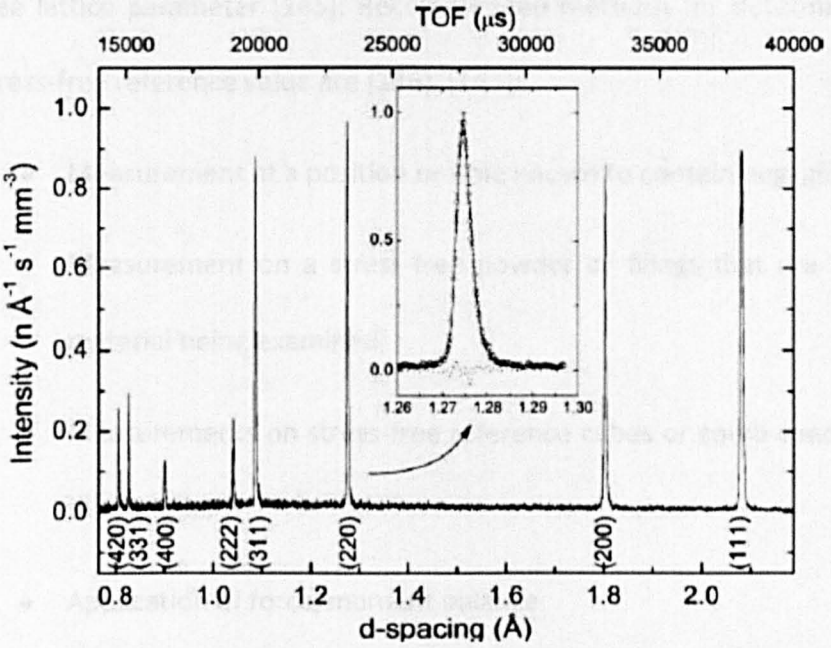

Figure 2-33: Typical TOF diffraction spectrum on ENGIN-X, in this case for a stainless-steel specimen [144].

If one can measure the d-spacing in a stress-free material and a stressed material, the strain can be easily calculated from the change in lattice spacing using Equation 2-6:

$$\varepsilon_{xx} = \frac{d_{xx} - d_{0xx}}{d_{0xx}} \qquad \textbf{Equation 2-6}$$

where ε_{xx} is the strain in the xx direction, d_{xx} is the stressed lattice spacing and d_{0xx} is the stress-free lattice parameter.

Stress-free lattice spacing

The stress-free lattice spacing, d_0, is a critical measured parameter required for determining residual stresses as very small changes in its value can result in large uncertainties. Changes in composition, martensitic phase transformations, changes in temperature and intergranular strains are some of the factors that can affect the stress-

free lattice parameter [145]. Recommended methods for determining a representative stress-free reference value are [146], [147]:

- Measurement at a position or time known to contain negligible stress;
- Measurement on a stress-free powder or filings that are representative of the material being examined;
- Measurements on stress-free reference cubes or comb specimens extracted from the sample;
- Application of force/moment balance
- Imposing a zero stress condition perpendicular to a free surface

Generally cubes are used, but these are difficult to handle and position accurately on the instrument. Furthermore, in some components (for example weldments), there may be gradual changes in stress-free lattice spacings, which calls for an extensive process of extracting cubes accurately from different locations. Combs and matchsticks are becoming increasingly common for measurements of stress-free lattice parameters in such cases.

2.5.3 Residual stresses in welds

Welding residual stresses arise as a consequence of localised plastic deformation in the material. When the weld metal cools and solidifies, contraction occurs which imposes strains on the surrounding material. In the absence of transformation effects, the residual stresses in the weld region are normally tensile. Residual stresses significantly affect the performance of welded structures and can contribute to fatigue crack development, stress corrosion cracking and have been shown to accelerate the onset of creep damage [74], [148], [149].

2.5.4 *Magnitude and Distribution of Residual Stresses*

A reasonable assumption with regard to the magnitude of residual stresses in welds in the as-welded condition is a maximum tensile residual stress equal to the yield strength of the weld or parent material [150]. However, this depends on different factors such as the geometry and stiffness of the parts being joined and the material properties and thus, is only true if the following two conditions are met [151]:

- There is restraint against the free thermal contraction of the heated material.
- The thermal contraction strain from the softening temperature to ambient or pre-heat temperature is greater than the yield strain of the material.

The restraint in a welded joint is the resistance to the free thermal expansion and contraction of the heated material. It is affected by a range of factors, including the geometry of the parts, the use of fabrication aids such as tack-welds, cleats and jigs and the weld pass sequence in the case of multipass welds [151]. The restraint on an assembly during welding must naturally influence the nature and extent of residual stresses [74]. For instance, if bending restraint is applied to resist the angular distortion at the weld caused by the transverse shrinkage of successive weld passes, then a net bending stress can be generated at the weld or, if in-plane or membrane restraint is applied to resist the mean transverse shrinkage at the weld, then net membrane stresses are generated across the weld [151]. The effects of bending and membrane restraint on the transverse residual stresses in a multi-pass butt weld made from austenitic steel are shown in Figure 2-34.

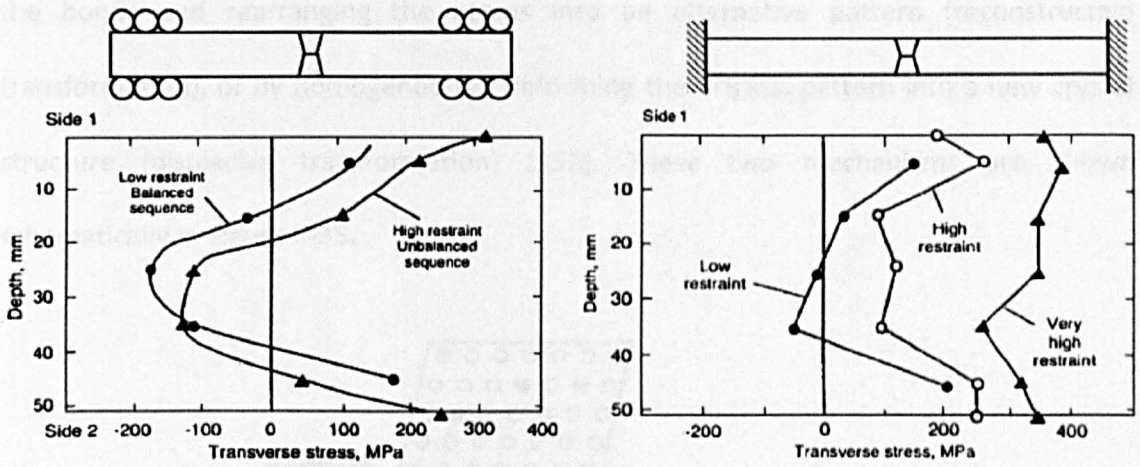

Figure 2-34: Effects of bending restraint (left) and membrane restraint (right) on transverse residual stresses [152].

The thermal contraction can be represented mathematically as:

$$\alpha\ T_s - T_o\ \geq \sigma_Y/E \qquad \textbf{Equation 2-7}$$

where α is the coefficient of thermal expansion; T_s the softening temperature; T_o the ambient or uniform pre-heat temperature; σ_Y the yield strength at ambient or pre-heat temperature and E the Young's modulus. For example, in a simple C-Mn steel, the contraction strain, $\alpha\ T_s - T_o$ is about 0.8 % and the yield strain, σ_Y/E is about 0.17 %. Thus, yield level residual stresses can be expected. In a different material, for example Ti-6Al-4V, due to the high yield strength, the contraction strain (~0.62 %) is less than the yield strain (~0.89 %). In such a case, yield magnitude residual stresses are not expected [151].

Phase transformation

Another feature of ferritic steels that may affect the residual stresses in welded joints is phase transformation, especially when this occurs in the solid-state at low temperatures during cooling. The atomic arrangement in a crystal can be altered by either, breaking all

the bonds and rearranging the atoms into an alternative pattern (reconstructive transformation), or by homogeneously deforming the original pattern into a new crystal structure (displacive transformation) [153]. These two mechanisms are shown schematically in Figure 2-35.

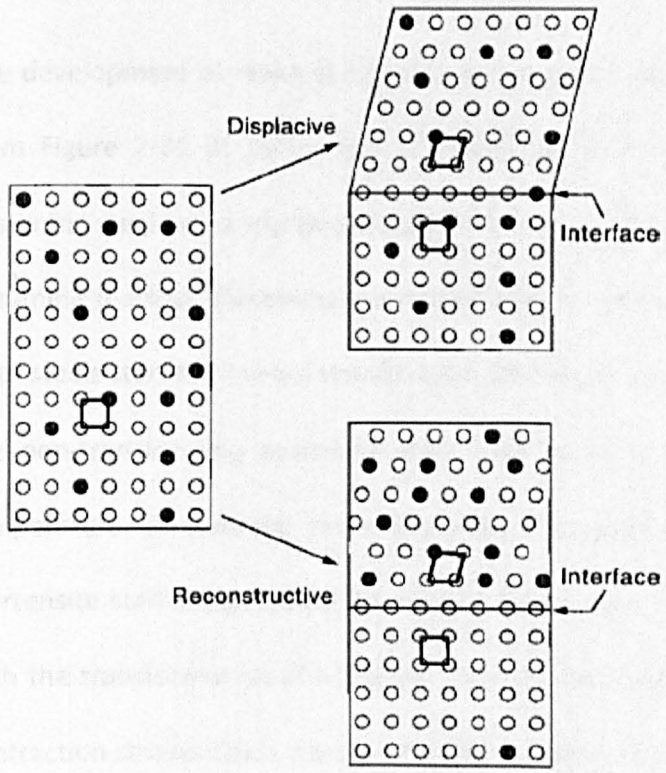

Figure 2-35: Schematic representation of reconstructive and displacive transformation mechanisms [153].

In the reconstructive mechanism, also known as the diffusive mechanism, the diffusion of atoms is required and atoms move randomly over large distances (1-106 interatomic spacings) [13]. The formation of allotriomorphic ferrite, idiomorphic ferrite, massive ferrite and pearlite are all examples of reconstructive transformations [153]. In contrast, the displacive mechanism, also known as a diffusionless, shear or martensitic transformation, occurs at temperatures where diffusion is inconceivable and involves an invariant-plane shape deformation with a large shear component parallel to the invariant

plane, and a dilatational strain normal to the plane [74]. The shape deformation during constrained transformations is accommodated by a combination of elastic and plastic strains in the surrounding matrix. The product phase grows in the form of thin plates to minimise the strains [153]. Widmanstätten ferrite, acicular ferrite, bainite and martensite are all products of displacive transformations [153].

The development of residual stresses during a phase transformation can be interpreted from Figure 2-36. It shows the accumulation of stresses in 2 different materials (an austenitic steel and a martensitic steel) i.e. a non-transforming and a transforming steel. Assuming the test specimens are rigidly held, on cooling from the austenite phase field, both steels start to develop tensile residual stresses due to thermal contraction strains. In the non-transforming austenitic steel, the stress increases monotonically until room temperature. In contrast, the martensitic steel shows a reduction in stress when the martensite start temperature (M_s ~400°C) is reached. At this stage, the strain associated with the transformation of austenite (FCC) to martensite (BCT) overwhelms the thermal contraction strains. Once the martensitic transformation is complete (M_f ~200°C), thermal contraction remains as the only influence on stress, so tensile stresses accumulate once more.

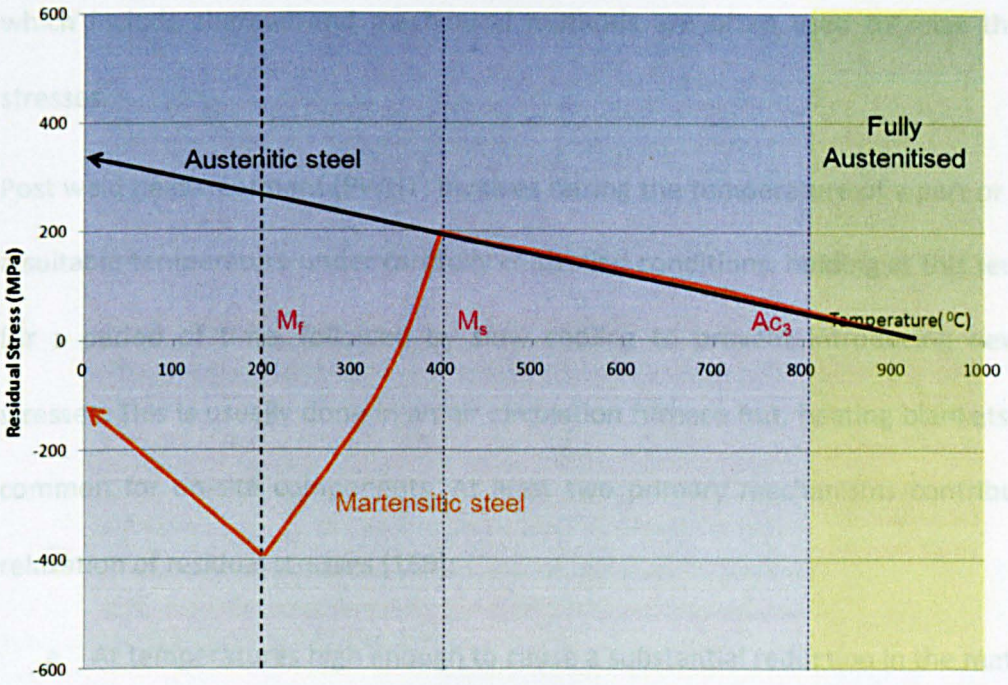

Figure 2-36: Schematic illustration of the development of residual stresses in a transforming (martensitic) and a non-transforming (austenitic) steel test specimen that is rigidly held.

The effects of phase transformations on residual stress development have been well studied by different authors [154], [155], [156] by conducting Satoh tests [157], [158], [159], [160], [161] or dilatometry [162], [163], [164], [165]. If the martensite-start and finish temperatures are well engineered (for example by judicious alloying additions), it is possible to develop filler metals that reduce the residual stresses generated during welding. Ohta *et al.* [166], Wang *et al.* [167] and Shirzadi *et al.* [168], for example, have proposed welding filler metals capable of achieving near zero or compressive residual stresses in the fusion zones of their welds.

2.5.5 Influence of PWHT

Tensile residual stress levels resulting from welding are often too high, which can be detrimental to the integrity and service behaviour of components. Stress relief operations

which include thermal and mechanical methods are often used to relax the residual stresses.

Post weld heat treatment (PWHT) involves raising the temperature of a part or section to a suitable temperature under carefully controlled conditions, holding at this temperature for a period of time, followed by slow cooling to prevent introducing new residual stresses. This is usually done in an air circulation furnace but, heating blankets are more common for on-site components. At least two primary mechanisms contribute to the relaxation of residual stresses [169]:

- At temperatures high enough to cause a substantial reduction in the material yield strength, plasticity mechanisms relieve some of the elastic strain through rapid thermal activation of dislocations.
- At lower temperatures, classical diffusional creep enables the counterbalancing regions of tensile and compressive stresses to contract or expand slightly, and thus stresses to redistribute. Precipitation and ageing effects also cause volume changes that can relax elastic stresses.

PWHT is designed for microstructural optimisation and relief of residual stresses. In the case of 9-12% Cr steels, the choice of temperature is often more important than the time because of the significant microstructural changes that can occur; for example the formation of untempered martensite when heating above the Ac_1 temperature.

Fidler [170], [171] has advocated the use of the Larson-Miller parameter to predict the relaxation rate for stresses in austenitic stainless steels and Cr-Mo steels. The Larson-Miller parameter [34] can be used to relate creep properties at different temperatures

and thus, provide a means of determining appropriate durations for post weld heat treatment [169].

Fidler [172] used finite element method to model the effect of putting a weld into service without PWHT and compared the results with a weld which received PWHT. The results suggested that for a weld, in the as-welded condition, 10,000 hours of service at 565°C was required to reduce the tensile stresses to values that are comparable as those produced by heat treatment. It was also concluded that the mechanism of stress relaxation in service is similar to that occurring during heat treatment and the stresses tend towards equi-biaxiality with time.

2.5.6 Previous studies on residual stress evaluation in ferritic welds

A limited number of studies have been reported on residual stress measurements in ferritic steel welds. For example Smith *et al.* [173] measured residual stress distributions in a butt-welded ferritic steel pipe of wall thickness 84mm using the deep hole drilling method. Hoop and axial measurements were made along the weld centre-line before and after PWHT and their results are shown in Figure 2-37. Before PWHT, the maximum tensile stress occured at the mid-thickness of the pipe in both the axial and hoop directions. After PWHT, there was significant relaxation and redistribution of the residual stresses. Francis *et al.* [74] made an interesting observation from these results, suggesting that only the deviatoric component of stress, and not the hydrostatic component was relieved by PWHT, and suggested that it is possible that the hydrostatic component of stress may only be relieved by long term mechanisms involving diffusion and grain boundary sliding [74], [93].

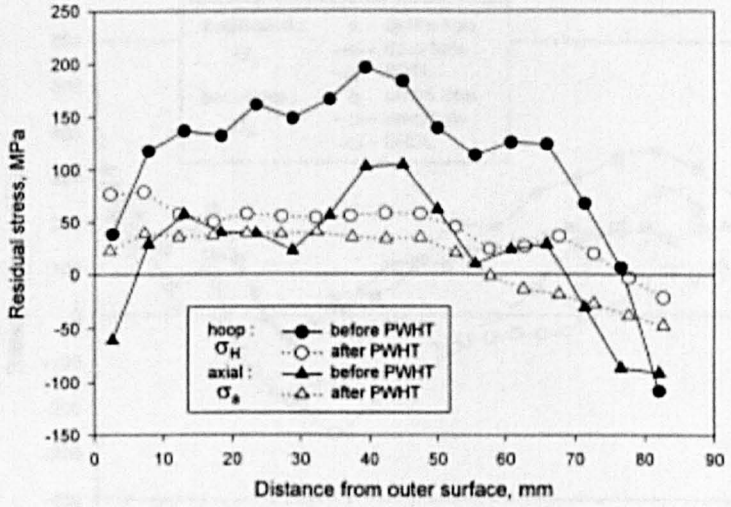

Figure 2-37: Axial and hoop residual stresses along the weld centre-line in a ferritic steel pipe [173].

The very low tensile or even compressive stresses near the outer surface can be explained by the effect of phase transformations on the development of residual stresses. Away from the weld centre-line, for example in the HAZ, the residual stresses would have been significantly different because of the less pronounced effect of phase transformation and high tensile stresses could be expected. Unfortunately, Smith *et al.* [173] did not perform any measurements away from the weld centre-line on this particular component. However, they did perform measurements on a ferritic steel plate at a location 20 mm from the weld centre-line, using several techniques (deep-hole drilling, centre-hole drilling and block removal, splitting and layering (BRSL)). The results are shown in Figure 2-38. The different techniques were in reasonable agreement, but most importantly, we note that the residual stresses were highly tensile near the top and bottom surfaces, whereas compressive stresses were recorded away from the surfaces of the plate.

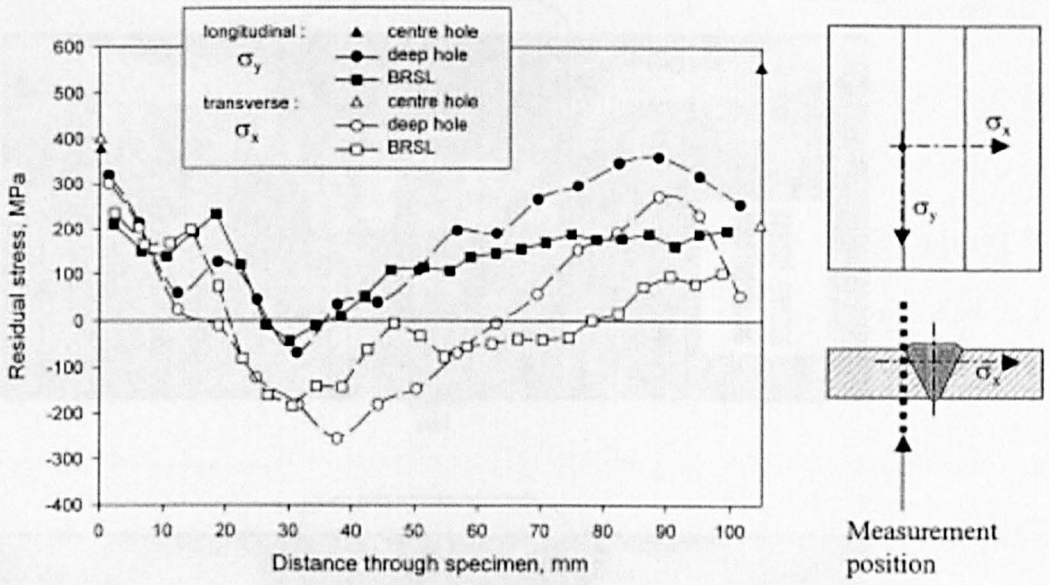

Figure 2-38: Measured residual stresses in a ferritic steel plate 108 mm thick [173]

Finite Element (FE) simulation of welding processes is complex, and the solid-state phase transformations (SSPT) and the thermal cycling that takes place in multipass ferritic welds present even further modelling challenges. Yaghi *et al.* [174], [175], [176] used finite element modelling to predict residual stresses in a multi-pass butt weld in a P91 steel pipe taking the temperature dependence of the material properties into consideration as well as allowing for phase transformations. The PWHT was also numerically modelled, showing how changes in PWHT holding time and material creep constants can affect the predicted residual stress profiles [174]. Their results are shown in Figure 2-39. The residual maximum principal stress, reflecting the superimposed tensile axial and hoop stresses, is tensile and substantial on the outside surface of the welded pipe and in its vicinity [175], [176]. When phase transformations are taken into account, the residual maximum principal stress moderately reduces in magnitude and compressive stresses are found to dominate in the bead corresponding to the last weld pass.

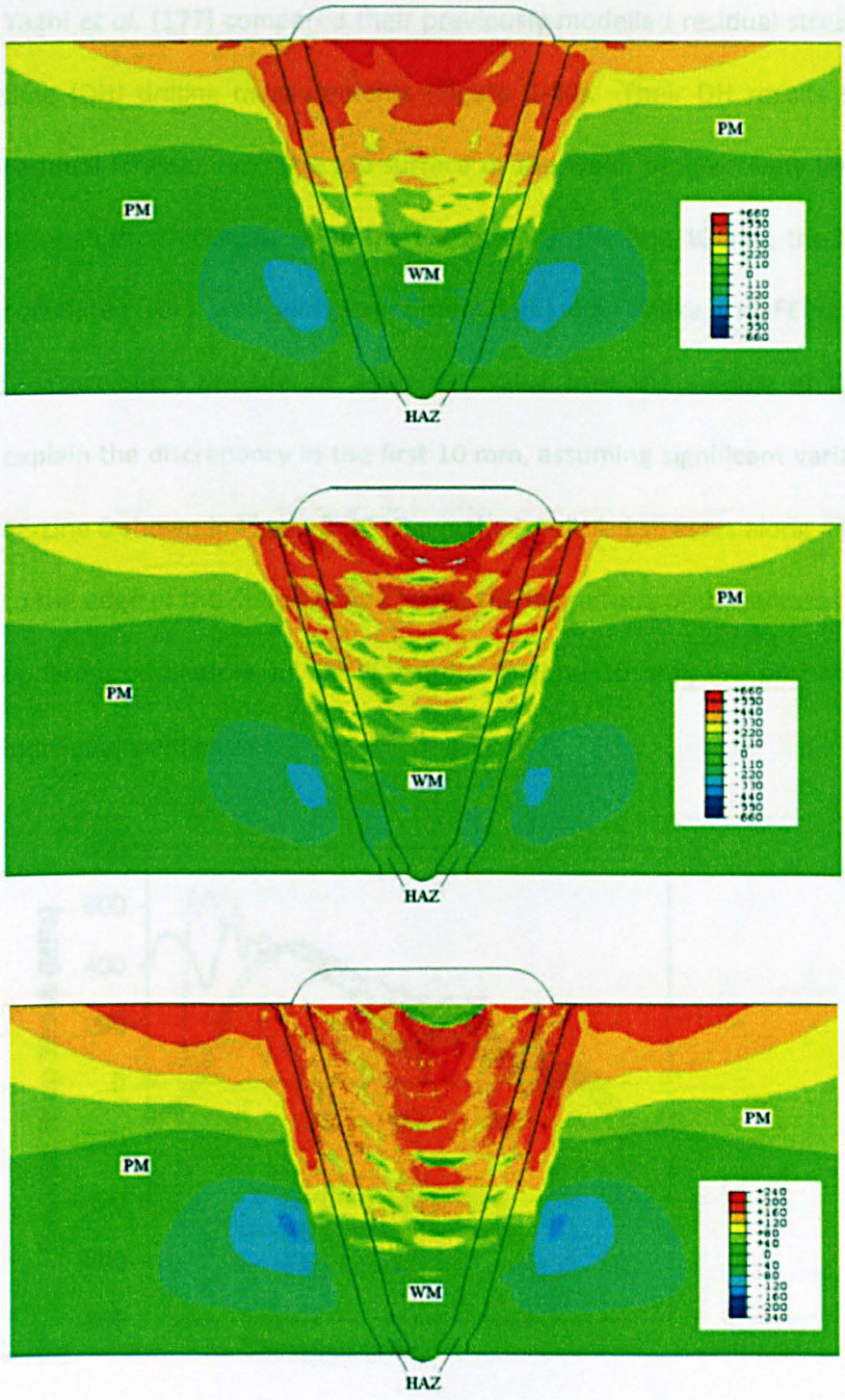

Figure 2-39: Residual maximum principal stress contours in the weld metal region, HAZ and parent metal without allowing for solid-state phase transformations SSPT (top), including the effects of phase transformations (middle) and after PWHT including the effects of phase transformations (bottom) [174].

Yaghi *et al.* [177] compared their previously modelled residual stresses [174] with deep-hole (DH) drilling measurements (Figure 2-40). Their DH results showed compressive residual stresses near the top surface of the weld, progressively becoming more tensile through the thickness. With the exception of the first 10 mm, the finite element results correlated very well with experimental results. Unlike the FE results, the deep-hole measurements provide an 'averaged' value over the volume of the core which could explain the discrepancy in the first 10 mm, assuming significant variation in stresses. The FE-Line 6 shown in Figure 2-40 shows the predicted stresses along a line that corresponds to the edge of the drilled hole. Clearly, the magnitude of the stresses is very different. The apparent oscillations in the FE results, beyond 10 mm, are probably a consequence of individual weld passes.

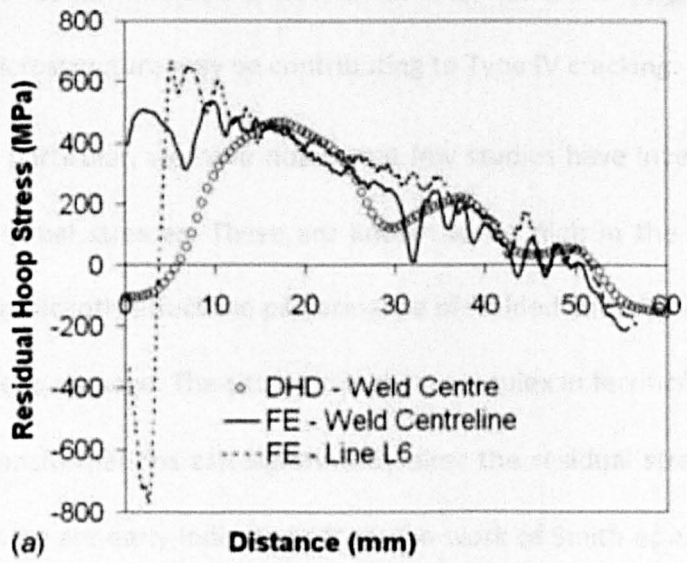

Figure 2-40: Comparison of deep-hole drilling measurements and finite element analysis of hoop residual stress through the wall thickness [177].

More recently, Kundu *et al.* [178] and Kumar *et al.*[179] measured residual stresses in 9 mm thick Grade 91 plates, welded using electron beam (EB) and laser welding respectively. High tensile peaks of the order of 500-600 MPa were observed in the vicinity

of the HAZ/parent material boundary and low tensile or compressive trough in the fusion zone. There was little variation of residual stress through the plate's thickness and the most significant components were in the longitudinal and normal orientations. These observations may be different with multi-pass welds and where component dimensions are significant. Furthermore, there was clear evidence of the effect of phase transformation on the magnitude of residual stresses within the fusion zone.

2.6 Rationale for this work

There are many publications in the literature dealing with microstructural changes that occur during creep in 9-12% Cr martensitic steels. The FGHAZ region is particularly weak in long-term creep, making it more vulnerable to cracking and failure. Nevertheless, there are some interesting results in the literature suggesting that factors other than microstructure may be contributing to Type IV cracking.

In particular, we have noted that few studies have investigated the influence of welding residual stresses. These are known to be high in the vicinity of welds, and this could significantly affect the performance of welded structures and thus accelerate the onset of creep damage. The situation is more complex in ferritic/martensitic steels whereby phase transformations can significantly alter the residual stress distributions and magnitudes. There are early indications from the work of Smith *et al.* [173] and Yaghi *et al.* [174] that residual stresses can be quite high in the vicinity of the HAZ in ferritic steels. Francis *et al.* [97], in their review paper on Type IV cracking, stated that the role of residual stresses arising from welding on the creep performance of 9-12% Cr steels needs to be investigated. It was intended that the current work address this issue.

Quite a few authors have shown (using finite element predictions) that a weak layer of material sandwiched within stronger parent and weld metal give rise to significant constraint, which delays failure in the FGHAZ. On the other hand, triaxial stresses that develop in the HAZ (due to constraint) could explain the preferential creep failure of welds in the weak region of the HAZ. Experimental evidence, for example Abe and Tabuchi [101] and Li *et al.* [133] indicate that the relative performance of cross-weld specimens and simulated HAZ specimens are significantly different in short term tests than in longer term tests. There is, therefore, a need to clarify the effect of constraint/triaxiality on Type IV failures.

During PWHT, undissolved precipitates coarsen and hence lose their ability to restrict dislocation motion. Parker and Stratford [110] and Li [111] have shown that the longest creep rupture life resulted from samples heat treated at a lower temperature for a shorter time. However, the work of Albert *et al.* [112] suggests otherwise; there was no significant change in rupture time with duration of PWHT in their work. On closer examination of the experimental procedures adopted by these authors, it appears that Parker and Stratford [110] and Li [111] have conducted PWHT on the actual welded pipes whereas Albert *et al.* [112] have extracted specimen blanks from the as-welded pipe and then conducted PWHT on the blanks. One of the factors that may have influenced the rupture lives in the case of Parker and Stratford [110] and Li [111] is residual stress relaxation during PWHT, which may have introduced some creep damage. In the work of Albert *et al.* [112], this is not the case, because most of the residual stresses would have relaxed by the machining process and the subsequent PWHT would not have introduced any (or very little) creep damage. The effect of the creep that occurs during PWHT needs to be clarified.

Within the Type IV zone, significant creep deformation has been measured by Parker and Parsons [114], [115] and Laha *et al.* [116] in low alloy steels. Strains of the order of 20% were measured in the Type IV zone with much less strain accumulation elsewhere. These results suggest that enhanced creep cavitation and thus Type IV cracking may be related to the high strain localisation in the HAZ. Similar behaviour is expected for the 9-12% Cr steels. A new high temperature strain measurement system, using Digital Image Correlation (DIC) in order to investigate spatially varying and time dependent deformation during high temperature creep, has been developed at the Open University by Sakanashi [180]. This technique can be applied to 9-12% Cr steel to spatially resolve the local creep deformation properties across the weldment.

2.7 References

[1] P. Alberry, "Power generation materials - EGTM70," Swansea, 2008.

[2] DTI, "Advanced Power Plant Using High Efficiency Boiler / Turbine," Carbon Abatement Technologies Programme, vol. BPB010, 2006.

[3] R. Viswanathan and W. T. Bakker, "Materials for Ultra Supercritical Fossil Power Plants," Palo Alto, 2000.

[4] Materials UK, "Fossil-fuelled power generation," Materials UK Energy Review, Report 2, 2007.

[5] A. Strang and V. Vodarek, "Z phase formation in martensitic 12CrMoVNb steel," Materials Science and Technology, vol. 12, no. 7, pp. 552–556, 1996.

[6] D. J. Gooch and S. T. Kimmins, "A study of Type IV cracking in 0.5%CrMoV/2.25CrMo weldments," in 3rd International Conference on Creep and Fracture of Engineering Materials and Structures, 1987, pp. 698–703.

[7] University of Cambridge, "Creep deformation of metals." [Online]. Available: http://www.doitpoms.ac.uk/tlplib/creep/index.php. [Accessed: 10-Oct-2012].

[8] R. W. Evans and B. Wilshire, Introduction to creep. London: The Institute of Materials, 1993.

[9] M. E. Kassner and T. A. Hayes, "Creep cavitation in metals," International Journal of Plasticity, vol. 19, pp. 1715–1748, Oct. 2003.

[10] R. L. Coble, "A model for boundary diffusion controlled creep in pollycrystalline materials," Journal of Applied Physics, vol. 34, pp. 1679–1684, 1963.

[11] F. R. N. Nabarro, "Report of conference on the strength of solids," Physics Society, p. 75, 1948.

[12] J. Li and a. Dasgupta, "Failure-mechanism models for creep and creep rupture," IEEE Transactions on Reliability, vol. 42, no. 3, pp. 339–353, 1993.

[13] W. J. Evans, "Aerospace Materials Engineering," 2008.

[14] G. E. Dieter, Mechanical Metallurgy. London: McGraw-Hill, 1988.

[15] A. Rao, "Creep and Anelastic Deformation in Austenitic Steels," Ph.D. Thesis. The Open University, 2010.

[16] K. J. Laidler, Chemical Kinetics, 3rd ed. New York: Harper & Row, 1987, p. 42.

[17] F. H. Norton, Creep of steel at high temperatures. New York: McGraw-Hill Book Co, 1929.

[18] J. G. Harper and J. E. Dorn, "Viscous creep of Aluminium near its melting temperature," Acta Metallurgica, vol. 5, no. 11, pp. 654–665, 1957.

[19] H. J. Frost and M. F. Ashby, Deformation-Mechanism Maps (The Plasticity and Creep of Metals and Ceramics). Pergamon Press, 1982.

[20] Y. Gorash, "Development of a creep-damage model for non-isothermal long-term strength analysis of high-temperature components operating in a wide stress range," Martin-Luther-Universitat Halle-Wittenberg, 2008.

[21] L. Kloc and V. Sklenieka, "Transition from power-law to viscous creep behaviour type heat-resistant steel of P-91," Materials Science & Engineering A, vol. A234–236, pp. 962–965, 1997.

[22] B. J. Cane, "The process controlling creep and creep fracture of 2 1/4 Cr-1Mo Steel," CEGB Report RD/LR 1979, 1979.

[23] R. Viswanathan, Damage Mechanisms and Life Assessment of High-Temperature Components. Ohio: ASM International, 1989.

[24] M. F. Ashby, "A first report on deformation-mechanism maps," Acta Metallurgica, vol. 20, no. 7, pp. 887–897, Jul. 1972.

[25] P. J. Bouchard, M. Rist, R. Haigh, J. James, M. Hutchings, J. Moffatt, C. K. Boon, and A. Rao, "Creep Damage Measurement Methods Review," 2010.

[26] H. Riedel, "Cavity nucleation at particles on sliding grain boundaries. A shear crack model for grain boundary sliding in creeping polycrystals," Acta Metallurgica, vol. 32, no. 3, pp. 313–321, 1984.

[27] A. C. F. Cocks and M. F. Ashby, "ON CREEP FRACTURE BY VOID GROWTH," Progress in Materials Science, vol. 27, pp. 189–244, 1982.

[28] J. N. Greenwood, "Intercrystalline cracking of metals," Bulletin of the Institute of Metals, vol. 1, p. 104, 1952.

[29] R. Raj and M. F. Ashby, "Intergranular fracture at elevated temperature," Acta Metallurgica, vol. 23, no. 6, pp. 653–666, 1975.

[30] A. N. Stroh, "The Formation of Cracks in Plastic Flow. II," Proceedings of the Royal Society of London. Series A. Mathematical and Physical Sciences, vol. 232, no. 1191, pp. 548–560, 1955.

[31] V. Gaffard, "Experimental study and modelling of high temperature creep flow and damage behaviour of 9Cr1Mo-NbV steel weldments," Ecole des Mines de Paris, 2004.

[32] B. F. Dyson, "Constraints on diffusional cavity growth rates," Metal Science, vol. 10, no. 10, pp. 349–353, 1976.

[33] J. R. Rice, "Constraints on the diffusive cavitation of isolated grain boundary facets in creeping polycrystals," Acta Metallurgica, vol. 29, no. 4, pp. 675–681, Apr. 1981.

[34] F. R. Larson and J. Miller, "A time-temperature relationship for rupture and creep stress," Transactions ASME, vol. 74, p. 765, 1952.

[35] S. S. Manson and A. M. Haferd, "A linear time-temperature relation for extrapolation of creep and stress rupture data," NACA TN 2890, 1953.

[36] R. L. Orr, O D Sherby, and J. E. Dorn, "Correlation of rupture data for metals at elevated temperatures," Transactions ASME, vol. 46, p. 113, 1954.

[37] B. Wilshire, "New high-precision creep procedures for accurate life extension of plant," International Journal of Pressure Vessels and Piping, vol. 39, no. 1–2, pp. 73–82, 1989.

[38] K. H. Mayer and F. Masuyama, "The development of creep-resistant steels," in in Creep-resistant steels, F. Abe, T.-U. Kern, and R. Viswanathan, Eds. Cambridge, England: Woodhead publishing limited, 2008, pp. 15–77.

[39] H. Cobb, Steel Products Manual - Stainless Steels. Warrendale, PA: Iron and Steel Society, 1999.

[40] H. K. D. H. Bhadeshia, "Mechanical properties of martensite in heat-resistant steels," Ultra Steel 2000, vol. 205–213, 2000.

[41] J. Orr, "A review of low alloy ferritic steels for elevated temperature service," Surrey, 2008.

[42] J. J. Sanchez-Hanton and R. C. Thomson, "Characterization of isothermally aged Grade 91 (9Cr–1Mo–Nb–V) steel by electron backscatter diffraction," Materials Science and Engineering: A, vol. 460–461, pp. 261–267, Jul. 2007.

[43] C. D. Lundin, P. Liu, and Y. Cui, A literature review on characteristics of high temperature ferritic Cr-Mo steels and weldments. New York, USA: Welding Research Council, 2000, pp. 1–36.

[44] Y. Yin and R. G. Faulkner, "Physical and elastic behaviour of creep-resistant steels," in in Creep-resistant steels2, F. Abe, T. U. Kern, and R. Viswanathan, Eds. Cambridge, England: Woodhead publishing limited, 2008, pp. 217–239.

[45] Nickel Institute, "High Nickel Alloys & Superalloys." [Online]. Available: http://www.nickelinstitute.org/en/NickelUseInSociety/MaterialsSelectionAndUse/Ni-ContainingMaterialsProperties/HighNickelAlloysAndSuperalloys.aspx. [Accessed: 01-May-2013].

[46] European Commission, "Phase 2. advanced 700° c pf power plant (AD700-2)," 2002. [Online]. Available: http://cordis.europa.eu/projects/rcn/70779_en.html. [Accessed: 15-Jul-2013].

[47] P. J. Ennis, "A review of Ni-Based Alloys for Elevated Temperature Service," Surrey, 2010.

[48] M. F. Ashby and D. R. H. Jones, Engineering Materials 1: An introduction to their properties & applications, 2nd ed. Oxford: Butterworth-Heinemann, 2002.

[49] F. Abe, "Strengthening mechanisms in steel for creep and creep rupture," in in Creep-resistant steels, F. Abe, T. U. Kern, and R. Viswanathan, Eds. Cambridge, England: Woodhead publishing limited, 2008, pp. 279–301.

[50] ASTM International, "ASTM A335 / A335M - 11 Standard Specification for Seamless Ferritic Alloy-Steel Pipe for High-Temperature Service," 2011.

[51] D. G. Robertson and I. A. Shibli, "A Review of Martensitic 9-12% Chromium Steels for Elevated Temperature Service," Surrey, 2011.

[52] F. Masuyama, "New Developments in Steels for Power Generation Boilers," in Advanced Heat Resistant Steels for Power Generation, 1999, pp. 33–48.

[53] R. L. Klueh, "Elevated-temperature ferritic and martensitic steels and their application to future," Oak Ridge, 2004.

[54] A. Strang and V. Vodarek, "Microstructural Stability of Creep Resistant Alloys for High Temperature Plant Applications," in International Conference on Microstructural Stability of Creep Resistant Alloys for High Temperature Plant Applications, 1998, pp. 117–134.

[55] M. Schwind, M. Hättestrand, and H.-O. Andrén, Microstructural Stability of Creep Resistant Alloys for High Temperature Plant Applications. London: The Institute of Materials, 1998, pp. 197–214.

[56] R. Viswanathan and W. Bakker, "Materials for ultrasupercritical coal power plants—Turbine materials: Part II," Journal of Materials Engineering and Performance, vol. 10, no. 1, pp. 96–101, 2001.

[57] F. Abe, M. Tabuchi, H. Semba, M. Igarashi, M. Yoshizawa, N. Komai, and A. Fujita, "Feasibility of MARBN Steel for Application to Thick Section Boiler Components in USC Power Plant at 650°C," in Fifth international conference on advances in materials technology for fossil power plants, 2007, pp. 92–106.

[58] V. K. Sikka, C. T. Ward, and K. C. Thomas, "Modified 9Cr–1Mo steel," in Conference on ferritic Steels for High Temperature Applications, 1981, pp. 65–84.

[59] K. Haarmann, J. C. Vaillant, B. Vandenberghe, W. Bendick, and A. Arbab, The T91/P91 book, 2nd ed. Vallourec & Mannesmann Tubes, 2002.

[60] R. W. K. Honeycomb and H. K. D. H. Bhadeshia, Steels: Microstructure and Properties. Oxford: Butterworth-Heinemann, 1995.

[61] J. Nutting, "The structural stability of low alloy steels for power generation applications," in in Advanced Heat Resistant Steels for Power Generation, R. Viswanathan and J. Nutting, Eds. London: IOM Communications Ltd, 1999, pp. 12–30.

[62] J. Hald, "Microstructure and long-term creep properties of 9–12% Cr steels," International Journal of Pressure Vessels and Piping, vol. 85, no. 1–2, pp. 30–37, Jan. 2008.

[63] V. Foldyna, J. Purmensky, and Z. Kubon, "Development of advanced 9-12% Cr creep resistant steels with respect to structural stability," in 7th International Conference on Creep and Fracture of Engineering Materials and Structures, 1997, pp. 587–597.

[64] F. Abe, "Coarsening behavior of lath and its effect on creep rates in tempered martensitic 9Cr–W steels," Materials Science and Engineering: A, vol. 387–389, no. 0, pp. 565–569, Dec. 2004.

[65] D. Peckner and I. M. Bernstein, Handbook of Stainless Steels. McGraw Hill, 1977.

[66] P. J. Ennis and A. Czyrska-Filemonowicz, "Recent advances in creep-resistant steels for power plant applications," Sadhana, vol. 28, no. 3 & 4, pp. 709–730, 2003.

[67] F. Abe, M. Taneike, and K. Sawada, "Alloy design of creep resistant 9Cr steel using a dispersion of nano-sized carbonitrides," International Journal of Pressure Vessels and Piping, vol. 84, no. 1–2, pp. 3–12, Jan. 2007.

[68] H. Cerjak and P. Mayr, "Creep strength of welded joints of ferritic steels," in in Creep-resistant steels, F. Abe, T. U. Kern, and R. Viswanathan, Eds. Cambridge, England: Woodhead publishing limited, 2008, pp. 472–503.

[69] Metrode Products Limited, "Welding consumables for P91 steels for the power generation industry," Surrey, 2006.

[70] Z. Zhang, J. C. M. Farrar, and A. M. Barnes, "Weld metals for P91-tough enough?," in Fourth International EPRI Conference on Welding and Repair Technology for Power Plants, 2000.

[71] American Society of Mechanical Engineers, "ASME, Section I, II, IX and B31.1: Boiler and Pressure Vessel Code," 2007.

[72] American Welding Society, "AWS A5.23/A5.23M, Specification for Low-Alloy Steel Electrodes and Rods for Gas Shielded Arc Welding," Miami, Florida, 2007.

[73] "Zhang, Z., 2010. Discussion on different aspects of PWHT in P91. [Email] (Private communication, 15 March 2010)."

[74] J. A. Francis, H. K. D. H. Bhadeshia, and P. J. Withers, "Welding residual stresses in ferritic power plant steels," Materials Science and Technology, vol. 23, no. 9, pp. 1009–1020, Sep. 2007.

[75] P. Mayr, "Evolution of microstructure and mechanical properties of the heat affected zone in B-containing 9 % chromium steels (Doctor of technical sciences)," Graz University of Technology, Austria, 2007.

[76] R. W. J. Messler, Principles of Welding. Weinheim: Wiley-VCH, 2004.

[77] S. Kou, Welding Metallurgy, 2nd ed. New Jersey: John Wiley & Sons, Inc, 2003.

[78] S. A. David and J. M. Vitek, "Correlation between Solidification Parameters and Weld Microstructures," International Materials Reviews, vol. 34, pp. 213–245, 1989.

[79] Y. Zhang, "Changes in Microstructure and Mechanical Properties of P91 Weld Metal during Creep," Ph.D. University of Nottingham, 2009.

[80] M. C. Coleman, "The Structure of Weldments and its Relevance to High Temperature Failure," in in Weldments: Physical Metallurgy and Failure Phenomena, R. J. Christoffel, E. F. Nippes, and H. D. Solomon, Eds. London Central Electricity Generating Board, 1979, pp. 409–420.

[81] ASM International, "Welding, Brazing and Soldering," ASM Handbook, vol. 6, 1983.

[82] M. Igarashi, S. Muneki, and F. Abe, "Microstructure control of martensite phase matrix in advanced ferritic steels for USC boilers to achieve long term stability," in Materials for advanced power engineering - 6th Liege Conference, 1998, pp. 637–646.

[83] P. Mayr, I. Holzer, and H. Cerjak, "Evolution of precipitate structure in the heat-affected zone of a martensitic 9 wt.% Cr steel during welding and post-weld heat treatment," Welding in the World, vol. 55, no. 5–6, pp. 70–77, 2011.

[84] H. J. Schuller, L. Hagn, and A. Woltscheck, "Risse im Schweissnachberricht von Formstucken aus Heissdampfleitungen," Werkstoffuntersuchungen VGB Kraftwerkstech, vol. 54, 1974.

[85] S. J. Brett, "Type IIIa cracking in 1/2CrMoV steam pipework systems," Science and Technology of Welding and Joining, vol. 9, no. 1, pp. 41–45, 2004.

[86] S. J. Brett, "In-service Cracking Mechanisms affecting 2CrMo Welds in 0.5%CrMoV Steam Pipework Systems," in Conf Integrity of High Temperature Welds, 1998, p. 3.

[87] C. D. Lundin and M. Prager, "A new approach to investigation into Type IV cracking susceptibility," in Int conf Fitness-for Service Evaluations in Petroleum and Fossil Power Plants, 1998.

[88] N. Komai and F. Masuyama, "Microstructural Degradation of the HAZ in 11Cr – 0 . 4Mo – 2W – V – Nb – Cu Steel (P122) during Creep," ISIJ International, vol. 42, no. 12, pp. 1364–1370, 2002.

[89] J. Besson, S. Leclercq, V. Gaffard, and a.-F. Gourgues-Lorenzon, "Analysis of creep lifetime of a ASME Grade 91 welded pipe," Engineering Fracture Mechanics, vol. 76, no. 10, pp. 1460–1473, Jul. 2009.

[90] V. Gaffard, a. F. Gourgues-Lorenzon, and J. Besson, "High Temperature Creep Flow and Damage Properties of the Weakest Area of 9Cr1Mo-NbV Martensitic Steel Weldments," ISIJ International, vol. 45, no. 12, pp. 1915–1924, 2005.

[91] F. Abe, "Boundary and sub-boundary hardening in high-Cr ferritic steels during long-term creep at 650°C," in 34th MPA Seminar "Materials and Components Behaviour in Energy & Plant Technology," 2008.

[92] Y. Hasegawa, T. Muraki, and M. Ohgami, "Metallurgical investigation of a Type IV damage at the heat affected zone of weld for tungsten containing martensitic heat resistant steels," in Experience with creep-strength enhanced ferritic steels and new and emerging computational methods, 2004.

[93] S. T. Kimmins and D. J. Smith, "On the relaxation of interface stresses during creep of ferritic steel weldments," The Journal of Strain Analysis for Engineering Design, vol. 33, no. 3, pp. 195–206, Jan. 1998.

[94] A. Shibli and F. Starr, "Some aspects of plant and research experience in the use of new high strength martensitic steel P91," International Journal of Pressure Vessels and Piping, vol. 84, no. 1–2, pp. 114–122, Jan. 2007.

[95] C. J. Middleton and E. Metcalfe, "A review of laboratory Type IV cracking data in high chromium ferritic steels," in International Conference Steam Plants for the 1990's, 1990.

[96] F. V Ellis, "Review of Type IV Cracking in Piping Welds - Final Report," Palo Alto, 1997.

[97] J. A. Francis, W. Mazur, and H. K. D. H. Bhadeshia, "Review Type IV cracking in ferritic power plant steels," Materials Science and Technology, vol. 22, no. 12, pp. 1387–1395, Dec. 2006.

[98] K. Laha, K. S. Chandravathi, P. Parameswaran, K. B. S. Rao, and S. L. Mannan, "Characterization of Microstructures across the Heat-Affected Zone of the Modified 9Cr-1Mo Weld Joint to Understand Its Role in Promoting Type IV Cracking," Metallurgical and Materials Transactions A, vol. 38, no. 1, pp. 58–68, Jan. 2007.

[99] J. A. Francis and W. Mazur, "Welding Procedures and Type IV Phenomena," in Trends in Welding Research: Proceedings of the 7th International Conference, 2006, pp. 737–742.

[100] EPRI, "Optimal Hardness of P91 Weldments - Interim Report," Palo Alto, 2003.

[101] F. Abe and M. Tabuchi, "Microstructure and creep strength of welds in advanced ferritic power plant steels," Science and Technology of Welding and Joining, vol. 9, no. 1, pp. 22–30, Feb. 2004.

[102] M. E. A. El-azim, A. M. Nasreldin, G. Zies, and A. Klenk, "Microstructural instability of a welded joint in P91 steel during creep at 600uC," vol. 21, no. 7, pp. 779–790, 2005.

[103] K. Sawada, M. Bauer, F. Kauffmann, P. Mayr, and a. Klenk, "Microstructural change of 9% Cr-welded joints after long-term creep," Materials Science and Engineering: A, vol. 527, no. 6, pp. 1417–1426, Mar. 2010.

[104] M. Tabuchi, H. Hongo, Y. Li, T. Watanabe, and Y. Takahashi, "Evaluation of Microstructures and Creep Damages in the HAZ of P91 Steel Weldment," Journal of Pressure Vessel Technology, vol. 131, no. 2, p. 021406, 2009.

[105] A. Orlová, J. Buršík, K. Kuchařová, and V. Sklenička, "Evolution of Microstructure in P91-Type Steel in High Temperature Creep," in in Microstructural Stability of Creep Resistant Alloys for High Plant Temperature Applications, C. and G. Strang, Ed. IOM, 1998, p. 93.

[106] A. Orlová, J. Buršík, K. Kuchařová, and V. Sklenička, "Evolution of Creep in P91-Type Steel in High Temperature Creep," in in Microstructural Stability of Creep Resistant Alloys for High Plant Temperature Applications, A. Strang, J. Cawley, and G. W. Greenwood, Eds. 1998, pp. 89–105.

[107] A. Orlová, J. Buršík, K. Kuchařová, and V. Sklenička, "Microstructural Development During High Temperature Creep of 9% Steel," Materials Science & Engineering, vol. A245, pp. 38–48, 1998.

[108] H. K. Danielsen and J. Hald, "Behaviour of Z phase in 9-12%Cr Steels," Energy Materials, vol. 1, pp. 49–57, 2006.

[109] D. Li, K. Shinozaki, H. Harada, and K. Ohishi, "Investigation of Precipitation Behavior in a Weld Deposit of 11Cr-2W Ferritic Steel," Metallurgical and Materials Transactions A, vol. 36A, no. January, pp. 107–115, 2005.

[110] D. Parker and G. C. Stratford, "Effect of heat treatment on creep and fracture behaviour of 1.25Cr-O.5Mo steel," Materials Science and Technology, vol. 11, pp. 1267–1273, 1995.

[111] L. Li, "Effect of Post-Weld Heat Treatment on Creep Rupture Properties of Grade 91 Steel Heavy Section Welds," Utah, 2012.

[112] S. Albert, M. Matsui, T. Watanabe, H. Hongo, K. Kubo, and M. Tabuchi, "Variation in the Type IV cracking behaviour of a high Cr steel weld with post weld heat treatment," International Journal of Pressure Vessels and Piping, vol. 80, no. 6, pp. 405–413, Jun. 2003.

[113] I. A. Shibli, "Overview of the HIDA project," in 2nd International HIDA Conference on "Advances in Defect Assessment in High Temperature Plant," 2000.

[114] J. D. Parker and A. W. J. Parsons, "High temperature deformation and fracture processes in 2 1/4Cr1/2Mo1/2Cr1/2Mo1/4V weldments," vol. 0161, no. 94, pp. 45–54, 1995.

[115] J. D. Parker and G. C. Stratford, "Strain localization in creep testing of samples with heterogeneous microstructures," International Journal of Pressure Vessels and Piping, vol. 68, no. 2, pp. 135–143, Sep. 1996.

[116] K. Laha, K. Rao, and S. L. Mannan, "Creep behaviour of post weld heat treated 2.25CrMo ferritic steel base weld metal weldments," Material Science and Engineering, vol. A129, pp. 183–195, 1990.

[117] K. Maile, D. Thelen, and S. Sheng, "A New experimental approach to multiaxial creep and creep fatigue," Journal of Nuclear Materials, vol. 171, no. 1, pp. 108–112, Apr. 1990.

[118] "Influence of stress state on creep damage development in components A. Klenk, M. Rauch, K. Maile, MPA University of Stuttgart," pp. 1–9.

[119] M. Rauch, K. Maile, and M. Ringel, "Numerical Calculation and Experimental Validation of Damage Development in 9 Cr Steels," pp. 1–19, 2004.

[120] S. Sheng, "Anwendung von Festigkeitshypothesen im Kriechbereich bei mehrachsigen Spannungs-Formänderungszuständen," Universität Stuttgart, 1992.

[121] ECCC, "Data acceptability criteria and data generation: Creep data for welds," vol. 3 Part II, no. 3, 2004.

[122] S. . Albert, M. Matsui, H. Hongo, T. Watanabe, K. Kubo, and M. Tabuchi, "Creep rupture properties of HAZs of a high Cr ferritic steel simulated by a weld simulator," International Journal of Pressure Vessels and Piping, vol. 81, no. 3, pp. 221–234, Mar. 2004.

[123] S. Spigarelli and E. Quadrini, "Analysis of the creep behaviour of modified P91 (9Cr–1Mo–NbV) welds," Materials & Design, vol. 23, no. 6, pp. 547–552, Sep. 2002.

[124] ECCC Recommendations, "Recommendations for creep testing of PE (ex-service) materials," vol. 3, Part II, 2005.

[125] ECCC Recommendations, "Data acceptability criteria and data generation: Recommendations for creep testing of post-exposed (ex-service) materials," vol. 3, Part II, no. 14, 1999.

[126] J. R. Rice and D. M. Tracey, "On the ductile enlargement of voids in triaxial stress fields," Journal of the Mechanics and Physics of Solids, vol. 17, pp. 201–217, 1969.

[127] D. M. Rodrigues, L. F. Menezes, A. Loureiro, and J. V Fernandes, "Numerical study of the plastic behaviour in tension of welds in high strength steels," International Journal of Plasticity, vol. 20, pp. 1–18, 2004.

[128] S. T. Kimmins, D. J. Smith, and N. J. Walker, "Creep deformation and rupture of low alloy ferritic weldments under shear loading," Journal of Strain Analysis, vol. 31, no. 2, pp. 125–133, 1996.

[129] R. E. Craine and T. D. Hawkes, "On the creep of ferritic weldments containing multiple zones in plates under uniaxial loading," The Journal of Strain Analysis for Engineering Design, vol. 28, no. 4, pp. 303–309, 1993.

[130] J. Storesund, "Prediction of creep cracks in low alloy steel pipe welds by use of the continuum damage mechanics approach," in in Ageing of Materials and Methods for teh Assessment of Lifetimes of Engineering Plant, R. K. Penny, Ed. Netherlands: Balkema, 1997, pp. 129–144.

[131] D. Li, K. Shinozaki, and H. Kuroki, "Stress-strain analysis of creep deterioration in heat affected weld zone in high Cr ferritic heat resistant steel," Materials Science and Technology, vol. 19, pp. 1253–1260, Sep. 2003.

[132] T. Watanabe, M. Tabuchi, M. Yamazaki, H. Hongo, and T. Tanabe, "Creep damage evaluation of 9Cr–1Mo–V–Nb steel welded joints showing Type IV fracture," International Journal of Pressure Vessels and Piping, vol. 83, no. 1, pp. 63–71, Jan. 2006.

[133] Y. Li, H. Hongo, M. Tabuchi, Y. Takahashi, and Y. Monma, "Evaluation of creep damage in heat affected zone of thick welded joint for Mod.9Cr–1Mo steel," International Journal of Pressure Vessels and Piping, vol. 86, no. 9, pp. 585–592, Sep. 2009.

[134] T. Iwadate, M. Prager, and M. J. Humphries, "Reliability of New and Older Chrome-Moly Steels for Hydrogen Processing Vessels: Part II: Enhanced Performance," in in New Alloys For Pressure Vessels and Piping, New York: ASME, 1990, pp. 38–47.

[135] J. D. Parker, "The creep and fracture behaviour of thick-section, multi-pass weldments," in International Conference on "Integrity of High-Temperature Welds," 1998, pp. 143–152.

[136] M. Prager, "Issues in Life Assessment of Chrome-Moly Welds," in Serviceability of petroleum, process and power equipment: Pressure Vessels and Piping Conference, 1992, vol. 239, pp. 253–265.

[137] J. D. Parker, "The effect of specimen size on creep behaviour," Welding in the World, vol. 37, no. 5, pp. 233–241, 1996.

[138] R. Viswanathan and J. Foulds, "Accelerated Stress Rupture Testing for Creep Life Prediction—Its Value and Limitations," Journal of Pressure Vessel Technology, vol. 120, no. 2, pp. 105–115, May 1998.

[139] The Open University, Structural Integrity: Designing against failure. Stress Analysis (T357: Block 1 Part 7). Milton Keynes: The Open University, 2007.

[140] M. T. Hutchings, P. J. Withers, T. M. Holden, and T. Lorentzen, Introduction to the characterization of residual stress by neutron diffraction. Florida, USA: Taylor & Francis, 2005.

[141] P. J. Withers and H. K. D. H. Bhadeshia, "Residual stress Part 1 – Measurement techniques," Materials Science and Technology, vol. 17, pp. 355–365, 2001.

[142] M. E. Fitzpatrick, M. T. Hutchings, and P. J. Withers, "Separation of macroscopic, elastic mismatch and thermal expansion misfit stresses in metal matrix composite quenched plates from neutron diffraction measurements," Acta Materialia, vol. 45, no. 12, pp. 4867–4876, Dec. 1997.

[143] A. M. Paradowska, "Investigation of Residual Stress in Welds Using Neutron and Synchrotron Diffraction," Ph.D. Thesis. Monash University, Australia, 2007.

[144] J. R. Santisteban, M. R. Daymond, J. A. James, and L. Edwards, "ENGIN-X: a third-generation neutron strain scanner," Journal of Applied Crystallography, vol. 39, no. 6, pp. 812–825, Nov. 2006.

[145] P. J. Withers, M. Preuss, A. Steuwer, and J. W. L. Pang, "Methods for obtaining the strain-free lattice parameter when using diffraction to determine residual stress," Journal of Applied Crystallography, vol. 40, no. 5, pp. 891–904, Sep. 2007.

[146] G. A. Webster, A. G. Youtsos, C. Ohms, and R. C. Wimpory, "Draft Standard for the Measurement of Residual Stresses by Neutron Diffraction," in in Recent Advances in Experimental Mechanics SE - 44, E. Gdoutos, Ed. Springer Netherlands, 2004, pp. 467–476.

[147] G. A. Webster, "Polycrystalline Materials – Determinations of Residual Stresses by Neutron Diffraction," ISO/TTA3 Technology Trends Assessment, 2001.

[148] M. Turski, P. J. Bouchard, a. Steuwer, and P. J. Withers, "Residual stress driven creep cracking in AISI Type 316 stainless steel," Acta Materialia, vol. 56, no. 14, pp. 3598–3612, Aug. 2008.

[149] P. J. Bouchard, P. J. Withers, S. a. McDonald, and R. K. Heenan, "Quantification of creep cavitation damage around a crack in a stainless steel pressure vessel," Acta Materialia, vol. 52, no. 1, pp. 23–34, Jan. 2004.

[150] British Standards Institution, "BS7910 - Guide to methods for assessing the acceptability of flaws in metallic structures," 2005.

[151] R. H. Leggatt, "Residual stresses in welded structures," International Journal of Pressure Vessels and Piping, vol. 85, no. 3, pp. 144–151, Mar. 2008.

[152] R. H. Leggatt, "Residual stresses and distortion in multipass butt welded joints in type 316 stainless steel," Residual Stresses Science Technology, vol. 2, pp. 997–1004, 1986.

[153] H. K. D. H. Bhadeshia, "Some phase transformations in steels," Materials Science and Technology, vol. 15, pp. 22–29, 1999.

[154] H. Dai, J. A. Francis, H. J. Stone, H. K. D. H. Bhadeshia, and P. J. Withers, "Characterizing Phase Transformations and Their Effects on Ferritic Weld Residual Stresses with X-Rays and Neutrons," Metallurgical and Materials Transactions A, vol. 39, no. 13, pp. 3070–3078, Jul. 2008.

[155] W. K. C. Jones and P. J. Alberry, "Ferritic steels for fast reactor steam generators," in Ferritic steels for fast reactor steam generators, 1977, pp. 1–4.

[156] W. K. C. Jones and P. J. Alberry, "Residual stresses in welded constructions," in Residual stresses in welded constructions, 1977.

[157] K. Satoh, "Thermal Stresses Developed in High-Strength Steels Subjected to Thermal Cycles Simulating Weld Heat-Affected Zone," Transactions of the Japan Welding Society, vol. 3, no. 1, pp. 135–142, 1972.

[158] K. Satoh, "Transient Thermal Stresses of Weld Heat-Affected Zone by Both-Ends-Fixed Bar Analogy," Transactions of the Japan Welding Society, vol. 3, no. 1, pp. 125–134, 1972.

[159] J. A. Francis, H. J. Stone, S. Kundu, R. B. Rogge, H. K. D. H. Bhadeshia, P. J. Withers, and L. Karlsson, "The Effects of Filler Metal Transformation Temperature on Residual Stresses in a High Strength Steel Weld," Transactions of the ASME, Journal of Pressure Vessels Technology, vol. 131, no. 4, pp. 1–21, 2009.

[160] R. J. Moat, H. J. Stone, A. A. Shirzadi, J. A. Francis, S. Kundu, A. F. Mark, H. K. D. H. Bhadeshia, L. Karlsson, and P. J. Withers, "Design of weld fillers for mitigation of residual stresses in ferritic and austenitic steel welds," Science and Technology of Welding & Joining, vol. 16, no. 3, pp. 279–284, Apr. 2011.

[161] A. A. Shirzadi and H. K. D. H. Bhadeshia, "Accumulation of stress in constrained assemblies: novel Satoh test configuration," Science and Technology of Welding and Joining, vol. 15, no. 6, pp. 497–499, Aug. 2010.

[162] G. K. Prior, "The Role of Dilatometry in Characterisation of Steels," Materials Forum, vol. 18, pp. 265–276, 1994.

[163] J. A. Farrar and Z. Zhang, "No Title," Journal of Materials Science Letters, vol. 12, p. 1606, 1993.

[164] S. Sulaiman, "Structure of properties of the heat affected zone of P91 creep resistant steel," Ph.D. Thesis. University of Wollongong, 2007.

[165] S. Kumar, a. Kundu, K. a. Venkata, a. Evans, C. E. Truman, J. a. Francis, K. Bhanumurthy, P. J. Bouchard, and G. K. Dey, "Residual Stresses in Laser Welded ASTM A387 Grade 91 Steel Plates," Materials Science and Engineering: A, vol. 575, pp. 160–168, Mar. 2013.

[166] A. Ohta, K. Matsuoka, N. T. Nguyen, Y. Maeda, and N. Suzuki, "Fatigue strength improvement of lap joints of thin steel plate using low-transformation-temperature welding wire," Welding Journal, vol. 82, no. 4, p. 78S–83S, 2003.

[167] W. X. Wang, L. X. Huo, Y. F. Zhang, D. P. Wang, and H. Y. Jing, "New developed welding electrode for improving the fatigue strength of welded joints," Journal of Materials Science and Technology, vol. 18, no. 6, pp. 527–531, 2002.

[168] A. A. Shirzadi, H. K. D. H. Bhadeshia, L. Karlsson, and P. J. Withers, "Stainless steel weld metal designed to mitigate residual stresses," Science and Technology of Welding and Joining, vol. 14, no. 6, pp. 559–565, Aug. 2009.

[169] M. R. James, "Relaxation of Residual Stresses: An Overview," Advances in Surface Treatments: technology-applications-effects, vol. 4, pp. 349–365, 1987.

[170] R. Fidler, "Residual stresses in a CrMoV-2CrMo pipe weld: Part 1—The as-welded condition," International Journal of Pressure Vessels and Piping, vol. 14, no. 1, pp. 35–62, 1983.

[171] R. Fidler, "Residual stresses in a CrMoV-2CrMo pipe weld: Part 2—The heat treated condition," International Journal of Pressure Vessels and Piping, vol. 14, no. 3, pp. 181–195, 1983.

[172] R. Fidler, "The relaxation of as-welded residual stresses in a CrMoV-2CrMo pipe weld during service, TPRD/M/1283/N82, CEGB," 1983.

[173] D. J. Smith, P. J. Bouchard, and D. George, "Measurement and prediction of residual stresses in thick-section steel welds," Journal of Strain Analysis, vol. 35, no. 4, pp. 287–305, 2000.

[174] A. H. Yaghi, T. H. Hyde, A. A. Becker, and W. Sun, "Finite element simulation of welding and residual stresses in a P91 steel pipe incorporating solid-state phase

transformation and post-weld heat treatment," The Journal of Strain Analysis for Engineering Design, vol. 43, no. 5, pp. 275–293, May 2008.

[175] A. Yaghi, T. H. Hyde, A. A. Becker, W. Sun, J. A. Williams, and B. Pathiraj, "Simulation of Residual Stresses in Welded P91 Pipes," in 5th International Conference on Mechanics and Materials in Design, 2006.

[176] A. H. Yaghi, T. H. Hyde, A. A. Becker, and W. Sun, "Numerical simulation of P91 pipe welding including the effects of solid-state phase transformation on residual stresses," Proceedings of the Institution of Mechanical Engineers, Part I: Journal of Materials: Design and Applications, vol. 221, pp. 213–224, Jan. 2007.

[177] A. H. Yaghi, T. H. Hyde, A. A. Becker, W. Sun, G. Hilson, S. Simandjuntak, P. E. J. Flewitt, M. J. Pavier, and D. J. Smith, "A Comparison Between Measured and Modeled Residual Stresses in a Circumferentially Butt-Welded P91 Steel Pipe," Journal of Pressure Vessel Technology, vol. 132, no. 1, pp. 1–10, 2010.

[178] A. Kundu, P. J. Bouchard, S. Kumar, K. A. Venkata, J. A. Francis, A. Paradowska, G. K. Dey, and C. E. Truman, "Residual stresses in P91 steel electron beam welds," Science and Technology of Welding & Joining, vol. 18, no. 1, pp. 70–75, Jan. 2013.

[179] S. Kumar, A. Kundu, K. A. Venkata, A. Evans, C. E. Truman, J. A. Francis, K. Bhanumurthy, P. J. Bouchard, and G. K. Dey, "Residual stresses in laser welded ASTM A387 Grade 91 steel plates," Materials Science and Engineering: A, vol. 575, pp. 160–168, Jul. 2013.

[180] Y. Sakanashi, "Measurement of Creep Deformation in Weldments," Ph.D. Thesis. The Open University, UK, 2013.

Chapter 3

Welding and Material Characterisation

3.1 Introduction

This chapter describes the material used in the current work and some of the early material characterisation work that was performed. The base material used was a seamless P91 pipe, out of which, four nominally identical pipe girth welds were made. Two of the joints were kept in the as-welded condition and the other two were post weld heat treated. One of the pipes in each condition was ear-marked for neutron diffraction residual stress measurements. The remaining two pipes were reserved for destructive contour method residual stress measurements, and these pipes would also provide cross-weld material for creep test specimens. Simulated FGHAZ specimens were also produced using an induction heating and oil quenching method. Finally, attention is given to some of the early materials characterisation work that was carried out, which includes optical and scanning electron microscopy, hardness and tensile testing. The results from these tests were used in later chapters to interpret the measured residual stresses and the results of creep testing.

3.2 Materials

The base material used in this study was a seamless hot finished P91 pipe with an outer diameter of 324 mm and a wall thickness of 25.4 mm, and it was supplied by Sumitomo

Metal Industries, now Nippon Steel & Sumitomo Metal, Japan. The pipe was manufactured using an extrusion process and was supplied in the normalised (1040°C for 5 min) and tempered (780°C for 30 min) condition in accordance with ASTM standard A335/A 335M [1]. The dimensions of the pipe were carefully chosen to achieve an appropriate balance between, on the one hand, producing a weld configuration that would be substantial enough to be of relevance to power plant integrity, while at the same time not having dimensions that would make residual stress measurements with neutron diffraction impractical. The composition, as given in the batch certificate provided by the manufacturer of the pipe (ladle analysis) is listed in Table 3-1 along with the ASME material specification.

Table 3-1: Nominal composition of P91 pipe in wt. % compared with ASME P91 material specification [2].

Element	P91	ASME Spec	
		Min	Max
C	0.09	0.08	0.12
Mn	0.36	0.3	0.6
P	0.01		0.02
Si	0.27	0.2	0.5
Cr	8.15	8	9.5
Mo	0.88	0.85	1.05
V	0.19	0.18	0.25
Nb	0.06	0.06	0.1
N	0.05	0.03	0.07
Al	0		0.04
Ni	0.06		0.4

3.3 Welding

Four nominally identical pipe girth welds were made, using the manual gas-tungsten arc (GTAW) welding process for the root and hot passes, and semi-automatic submerged arc welding (SAW) for the filling passes at TWI, UK. Each weld joined two pieces of P91 pipes that were each 170 mm long when measured on the outer surface, using a single-Vee joint preparation as illustrated in Figure 3-1.

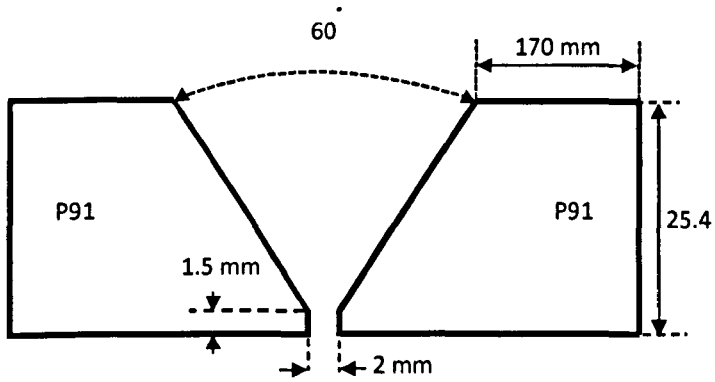

Figure 3-1: Schematic diagram of joint preparation.

The weld procedure specification (WPS) used is a modified version of Metrode WPS No: SAW 9CrMoVN-01 [3]. The nominal welding parameters that were used in making the joints are summarised in Table 3-2.

Table 3-2: Nominal welding parameters.

Preheat Temperature	200°C
Interpass Temperature	200-300°C
GTAW (Root and hot passes)	Nos. 1 - 15
SAW (Filling passes)	Nos. 16 - 24
Heat Input (GTAW)	1.2 kJ/mm
Heat Input (SAW)	1.8 kJ/mm

After the two pieces of pipe to be welded together were positioned as required, tack welds were used as a temporary means of holding the components in the required location, and in alignment, and at a distance apart as shown in Figure 3-2. A preheat temperature of 200°C and an interpass temperature of 250 - 300°C were used for both welding processes in accordance with BS 2633 [4]. These were maintained by using ceramic resistance heating mats which were wrapped around the entire circumference of the pipe as shown in Figure 3-2.

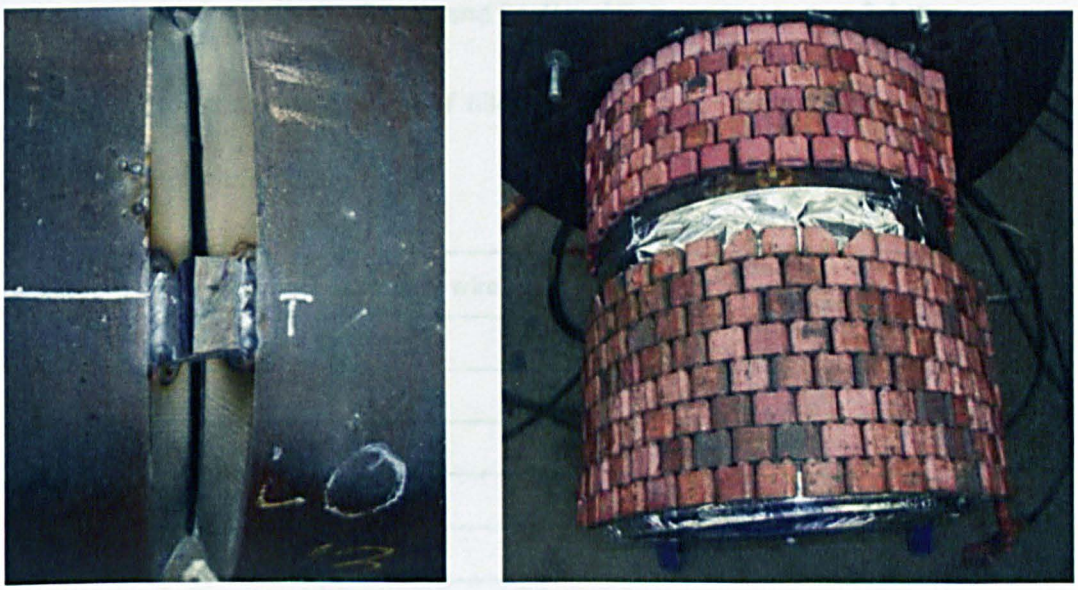

Figure 3-2: Tack-welded pipes (left) and ceramic resistance heating mats for maintaining preheat and interpass temperatures (right).

3.3.1 Filler metals

The filler metals used for both welding processes were of the 9CrMoV-N type, and were intended to match the composition and properties of the parent material (PM). The filler metals were supplied by Metrode, UK as solid wires and, for the SAW filling passes; a fluoride agglomerated welding flux (Metrode-LA491) was used. The chemical compositions of the filler metals, as given by the manufacturer, are given in Table 3-3 and

they are compared to the base metal composition where information is available. In national standards, solid wire classifications are based on wire analysis. As can be seen from Table 3-3, the deposit analysis will be slightly different from the certified wire composition. Owing to the nature of the GTAW process, very little loss of the alloying elements is seen, with the most noticeable loss being C which tends to be about 0.01-0.02% lower in the deposit than the wire [3]. The deposit analysis for the 9CrMoV-N wire combined with LA491 flux is inevitably different owing to the influence of the flux. The filler metal size for both the GTAW and SAW welding processes was 2.4 mm.

Table 3-3: Nominal composition of filler metal [3] and the P91 pipe material in wt.% as given by the manufacturers.

Element	P91	9CrMoV-N wire	9CrMoV-N Deposit	9CrMoV-N + LA491 Deposit
C	0.09	0.1	0.08	0.08
Mn	0.36	0.6	0.6	0.6
P	0.01	0.005	0.005	0.007
Si	0.27	0.3	0.3	0.35
Cr	8.15	9	8.5	8.5
Mo	0.88	1	1	1
V	0.19	0.2	0.18	0.16
Nb	0.06	0.05	0.05	0.04
N	0.05	0.04	0.04	0.04
Al	0			
Ni	0.06	0.7	0.7	0.7
S		0.005	0.005	0.005
O		0.003	0.005	0.04

An analysis of the 9CrMoV-N wire revealed that it generally conforms to the AWS A5.23/ASME SFA 5.28 [5], [6] and BS EN 12070 [7] standards. The wire-flux combination for the SAW process conforms to the AWS A5.23 standard [5]. As can be noted from Table

3-3, the Ni + Mn content is approximately 1.3 wt. % which complies with the maximum level specified by the ASME Boiler and Pressure Vessel Code [8]. While nickel is beneficial in improving toughness through improving the response to tempering and reducing the tendency for the formation of δ ferrite, an excessive Ni + Mn content can reduce the Ac_1 temperature below the PWHT temperature, which could lead to the formation of untempered martensite on cooling after PWHT [9].

3.3.2 Gas-tungsten arc welding (GTAW)

During the GTAW process, welding grade argon was used as the shielding gas. However, this was only required for the root pass. The filler wire was manually fed to the weld pool with the pipe constantly rotating as shown in Figure 3-3.

Figure 3-3: Pipe during Gas-tungsten arc welding.

3.3.3 Submerged arc welding (SAW)

Figure 3-4 shows the pipe during submerged arc welding, and the completed joint. The addition of the flux generates protective gases and slag, and adds alloying elements to the weld pool. Unmelted flux was recovered and recycled while remaining fused slag

layers were removed by light chipping. The starts/stops were staggered within ¼ of the circumference so that measurement of residual stresses and machining of specimens could be carried out elsewhere along the circumference (i.e. away from start/stop locations). It has previously been demonstrated that starts and stops can affect residual stress magnitudes and distributions [10], [11].

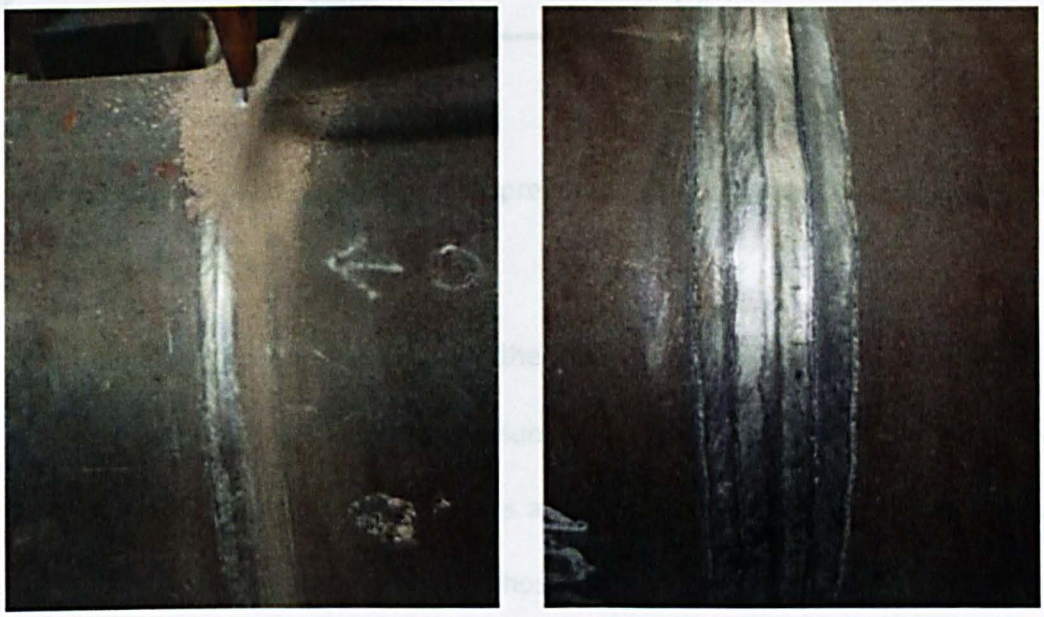

Figure 3-4: Pipe during submerged arc welding (left) and completed joint (right).

The total length of the finished piece was approximately 375 mm with the weld being at the mid-length position. The welding pass sequence is illustrated in Figure 3-5. As will be seen later, this information was used to interpret measured residual stresses. Weld beads covered by subsequent passes will experience multiple heat pulses, which will affect the residual stress distribution within the joint.

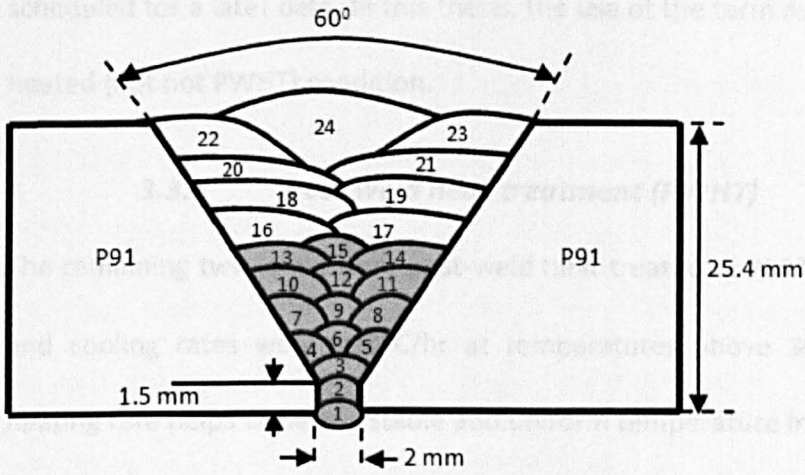

Figure 3-5: Schematic diagram of joint preparation showing sequence of weld passes, TIG (1–15), SAW (16–24).

Three more joints were welded using the same processes and weld pass sequence, and these joints were all subjected to ultrasonic inspection. The inspection report revealed a large defect in the first joint which was attributed to root undercut/excess penetration. The other joints had minor defects whose positions have been clearly marked so that these regions could be avoided during the measurement of residual stresses, and when extracting specimens for creep testing.

3.3.4 Post heating

Following welding, all the joints were allowed to cool to below 100°C. The significance of this cooling is to ensure complete transformation of austenite to martensite. Two of the four welded joints were then post heated (hydrogen bake-out) at 200°C for 3 hours. This process facilitates hydrogen diffusion from the weldments, thus minimising inadvertent contamination and reducing the risk of stress corrosion cracking (SCC). This step was necessary because the measurement of residual stresses on the as-welded pipe was

scheduled for a later date. In this thesis, the use of the term as-welded refers to the post heated (but not PWHT) condition.

3.3.5 Post weld heat treatment (PWHT)

The remaining two joints were post-weld heat treated at 750°C for 4 hours. The heating and cooling rates were ~90°C/hr at temperatures above 300°C. This relatively slow heating rate helps achieve a stable and uniform temperature increase. The temperature-time aspect of the PWHT was in accordance with BS EN 1599 [12]. The PWHT conditions set by other codes, such as the ASME Boiler and Pressure Vessel Code [8] include a minimum PWHT temperature of 730°C for 1 hour, whereas the American Welding Society (AWS) [13] recommends a PWHT of 730-760°C for 1 hour. To achieve appropriate weld toughness, a Larson-Miller parameter, P, for the heat treatment ≥ 21 [9] is desirable, where P is given by:

$$P = K(\log t + C) \times 10^{-3} \qquad \textbf{Equation 3-1}$$

and where K is the soak temperature in Kelvin, t is the holding time in hours and C is a material specific constant. This corresponds to a PWHT of 755°C for 2-3 hours assuming C = 21 [9]. From an industrial perspective, the 1 hour hold specified by both the ASME [8] and AWS [13] standards is considered insufficiently long and instead a hold time of 4 hours is often used to suit the coarse grain structures that are produced with SAW [9], [14].

3.4 Simulated FGHAZ specimens

Microstructural simulation is a useful technique because it enables the experimenter to reproduce the microstructure of sub-zones of the HAZ in a larger volume of material that

is easier to characterise. In chapter 2, it was seen that in 9-12% Cr steels, Type IV cracking occurs in the FGHAZ. In order to characterise the behaviour of this potentially weak zone, simulated FGHAZ samples were produced using induction heating and oil quenching at MPA Stuttgart, Germany. This method was chosen because, although Gleeble simulation gives the best agreement with an actual weld thermal cycle, the length of uniform microstructure is limited to about 10 mm [15]. This is an important consideration for the present work as there may be constraint effects arising in simulation specimens made using a Gleeble.

3.4.1 Choice of simulation parameters

The most widely used procedure to predict the welding thermal cycle is the standardised cooling time concept according to the German standard SEW088 [16], based on the analytical solution proposed by Rosenthal [17], which was later simplified by Rykalin [18]. The welding thermal cycle is characterised by the peak temperature, t_p, which depends on the distance from the fusion line and the cooling time between 800 and 500°C (t8/5). From the literature, it was noted that the thermal cycle corresponding to the weakest HAZ (FGHAZ) in 9-12% Cr steels is characterised by a peak temperature $Ac_3 < t_p < 1100°C$. The value of the Ac_3 temperature given by Haarmann *et al.* is 890-940°C [2]. Therefore, a peak temperature of 950°C was chosen. The dwell time at this peak temperature was ~2s and the cooling parameter $t_{8/5}$ was chosen to be 10 s based on previous experiments on similar steels at MPA Stuttgart.

3.4.2 Induction heating and oil quenching

The HAZ simulation, as applied in the current work, was performed by inductive overheating. Round bars, 180 mm long with a diameter of 20 mm were machined from a

section of as-received P91 parent material. A small hole (1 mm diameter and 1.5 mm deep) was drilled at the centre of each specimen in which Type R thermocouples were fitted and covered with a thick paste of sodium silicate. At above ~100°C, sodium silicate loses water molecules and forms a glass seal which provides resistance to the direct heat from the induction coil and thus it ensured that the thermocouples were reading the specimen temperature at all times.

The specimen was located within the central section of the induction coil and was mounted at the end of a vertical bar, which was secured at the other end onto an electromagnet as shown in Figure 3-6. After heating up to 950°C and holding at the peak temperature for 2 seconds, the electromagnet was deactivated and the vertical bar dropped into an oil bath, which was maintained at a suitable temperature, in this case 75°C. The oil temperature governs the cooling parameter, $t_{8/5}$. A circular guide, as shown in Figure 3-6, ensured that the bar dropped vertically to avoid specimen distortion upon quenching.

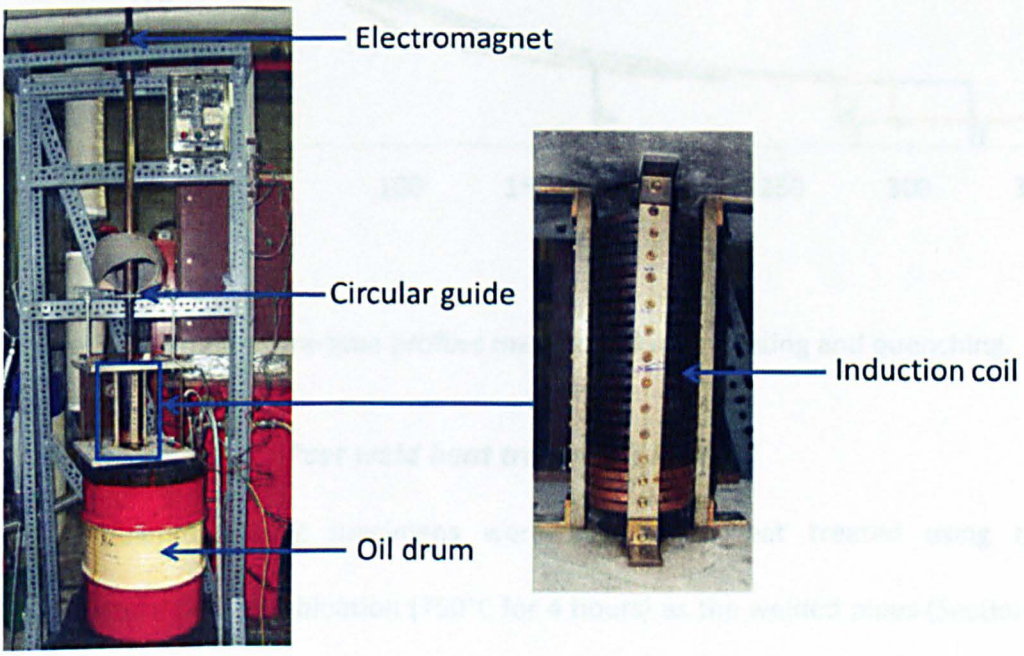

Figure 3-6: Induction heating and quenching equipment at MPA Stuttgart.

The measured temperature-time profiles for the simulated specimens are shown in Figure 3-7. The repeatability of the simulation was adequate with the peak temperature kept to within ±2°C of the set temperature (950°C). Specimens 1, 2 and 3 are not shown because these were used for trials, to optimise the simulation procedure. In some cases, for example specimen 4 (black line), we note a sudden drop in temperature at about 175 s. This was due to loss of contact between the thermocouple and the specimen in the oil bath. However, this occurred well after the temperatures of interest and thus was not considered to be an issue.

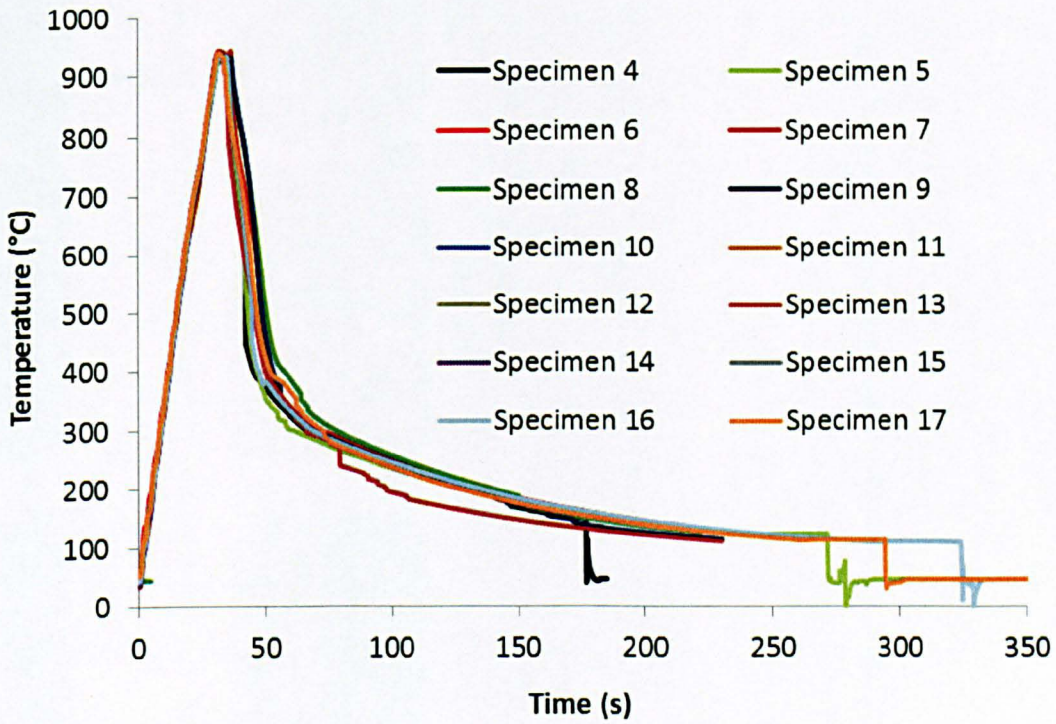

Figure 3-7: Temperature-time profiles measured during heating and quenching.

3.4.3 Post weld heat treatment (PWHT)

The simulated FGHAZ specimens were post weld heat treated using the same temperature-time combination (750°C for 4 hours) as the welded pipes (Section 3.2.5). It may be argued that that the 4 hours hold time in this case may have been far too long for

cylindrical samples with a diameter of 20 mm. However, a decision was taken to keep the number of variables to a minimum.

3.5 Materials Characterisation

Before embarking on a description of the various materials characterisation work that was carried out, it will be useful to summarise the materials described so far in this work and their processing history. Figure 3-8 shows a schematic illustration of the welded pipes, and FGHAZ simulated specimens, and their respective heat treatments.

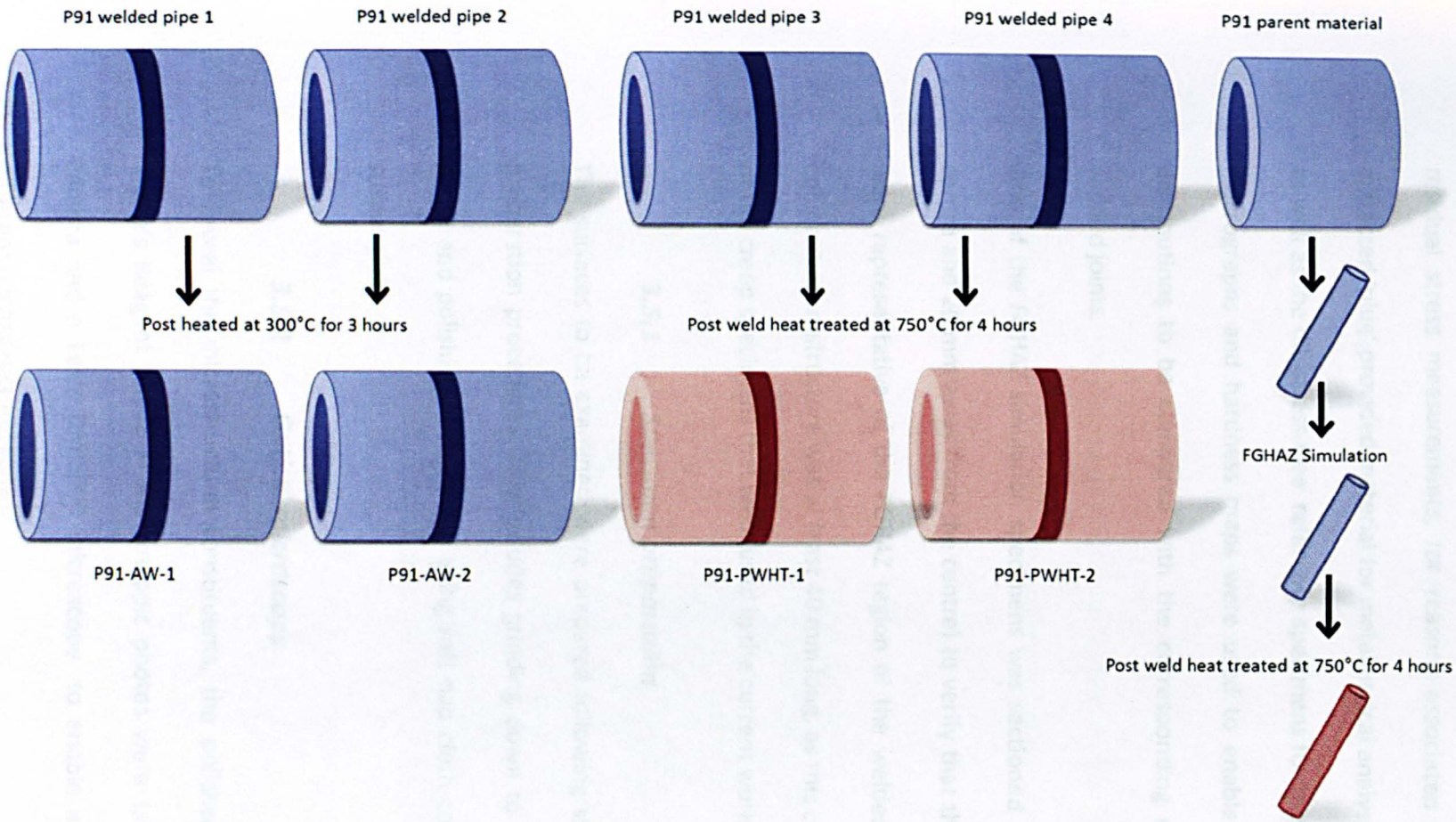

Figure 3-8: Schematic illustration of materials used (as-welded and PWHT pipes, and FGHAZ simulated specimens).

As will be described later, in chapter 4, it was necessary to machine a slot (or window) measuring 60 mm x 60 mm in the pipes that were reserved for neutron diffraction residual stress measurements, for reasons associated with beam attenuation. The extracted 'plug' provided material for metallurgical analysis and hardness measurements, as well as the d0 'stress-free' reference specimens for the diffraction measurements. The macrographs and hardness maps were used to enable the measured residual stress distributions to be compared with the corresponding metallurgical zones across the welded joints.

One of the FGHAZ simulation specimens was sectioned at two different locations (the centre and 20 mm away from the centre) to verify that the microstructure and hardness were representative of the FGHAZ region of the welded pipe, and that the length of constant microstructure was at least 40 mm long, as this corresponds to the gauge length of the creep specimens that were used in the current work.

3.5.1 Specimen preparation

The surfaces to be examined were prepared following standard metallographic sample preparation procedures. This includes grinding down to 4000 grit using silicon carbide paper and polishing in two steps using soft nap cloth coated with 3μ and 1μ diamond suspension.

3.5.2 Optical microscopy

To reveal the microstructural constituents, the polished surfaces were etched using Villela's Reagent for 15 s. Macroscopic photos were taken using a Nikon Digital SLR camera and a Leica DMI5000 microscope, to enable a detailed investigation of the different microstructural zones.

Figure 3-9 shows a macrograph of the as-welded P91 pipe weld. The width of the HAZ was approximately 2-3 mm. The weld beads deposited with submerged arc weld passes were significantly larger than for the GTAW passes, and the associated HAZ also seems to be larger. The letters a through to e, which are marked on the macrograph, correspond to the positions for the optical micrographs that are presented in Figure 3-10 through to Figure 3-14 respectively. The microstructural regions represented are, in order of decreasing peak temperature experienced during the welding thermal cycle; the weld metal (WM); the coarse-grained HAZ (CGHAZ); the fine-grained HAZ (FGHAZ); the intercritical HAZ (ICHAZ); and finally unaffected parent metal (PM).

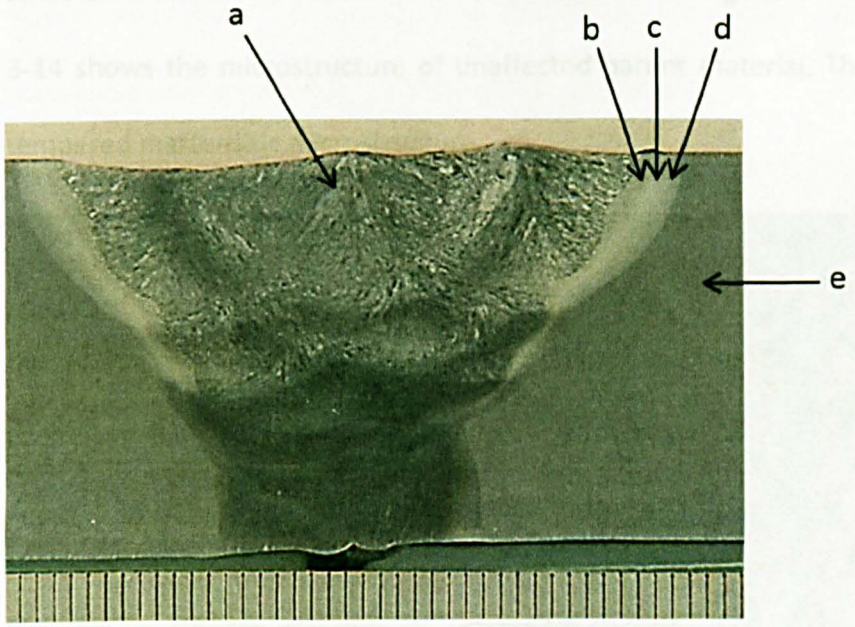

Figure 3-9: Macrograph from the as-welded pipe showing locations where optical micrographs in Figure 3-10 through to Figure 3-14 were captured.

In the as-welded condition, P91 steel has a martensitic microstructure. Figure 3-10 was captured in the weld metal region in the last weld pass. It is possible to identify the plate-like structure of the martensite with a columnar prior-austenite grain structure. Plate-like martensite can also be seen in the CGHAZ region (Figure 3-11), which shows that the prior

austenite grains were typically between 20 and 50 μm in size. The CGHAZ did not reveal many austenite grains of a size much larger than this, which may be attributable to the role that niobium can play in pinning grain boundaries and thus retarding grain growth [19]. Figure 3-12 shows the FGHAZ with prior-austenite grains being in the order of 10 μm across, or perhaps somewhat less. The ICHAZ, which is shown in Figure 3-13, is the region that is only partially austenitised on heating, so it often exhibits lighter regions of ferrite (i.e. overtempered martensite) and darker regions, which were austenitised during the welding thermal cycle, and which subsequently transformed to martensite on cooling. The ICHAZ is characterised by a small grain size (similar to those in the FGHAZ) and thus a strict differentiation between the ICHAZ and FGHAZ is generally difficult. Finally, Figure 3-14 shows the microstructure of unaffected parent material. This is a normalised and tempered martensitic microstructure.

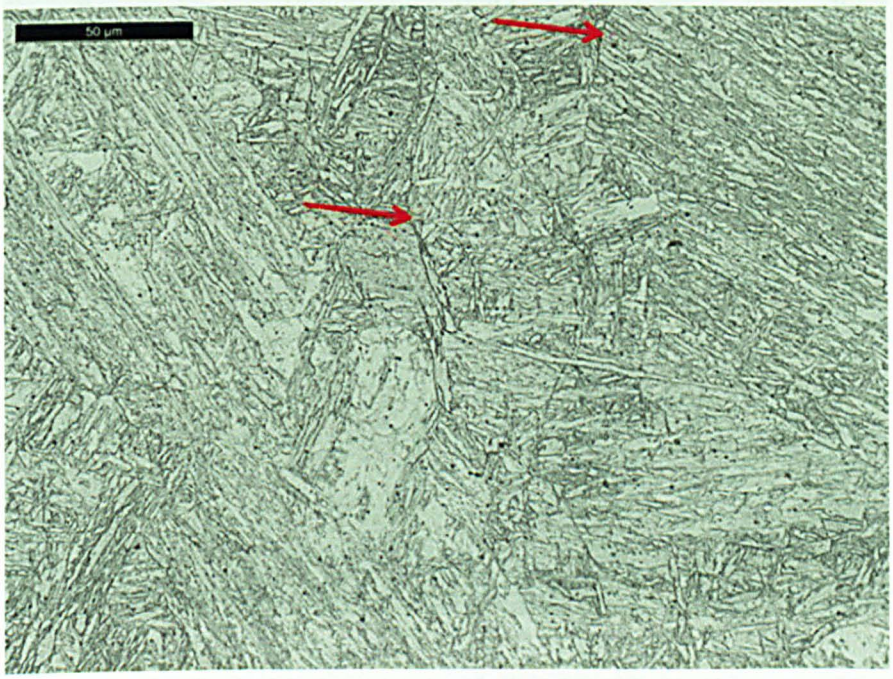

Figure 3-10: Optical micrograph of the weld metal in the as-welded condition. Arrows highlight examples of prior austenite grain boundaries.

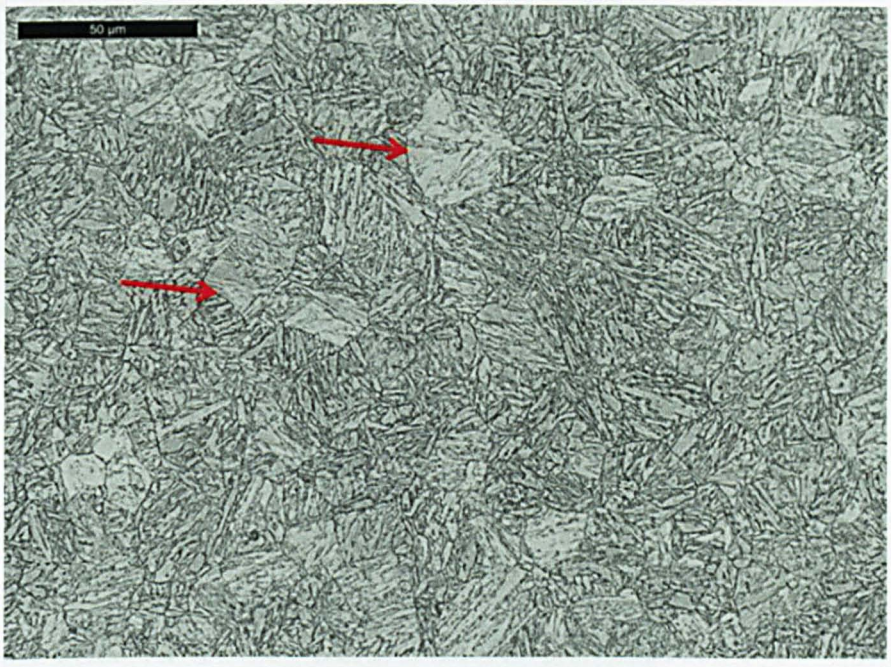

Figure 3-11: Optical micrograph of the CGHAZ in the as-welded condition. Arrows highlight examples of prior austenite grain boundaries.

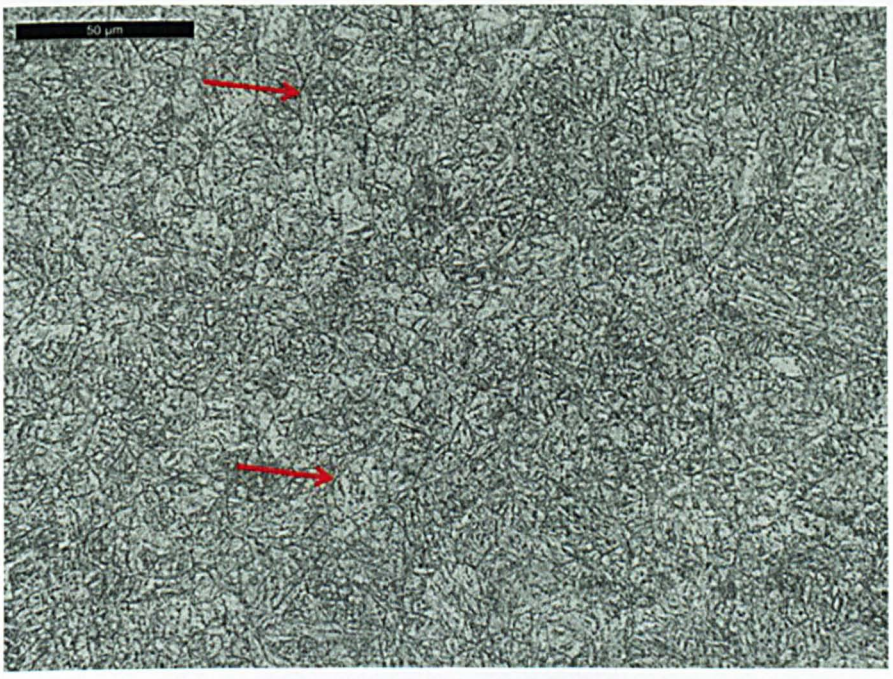

Figure 3-12: Optical micrograph of the FGHAZ in the as-welded condition. Arrows highlight examples of prior austenite grain boundaries.

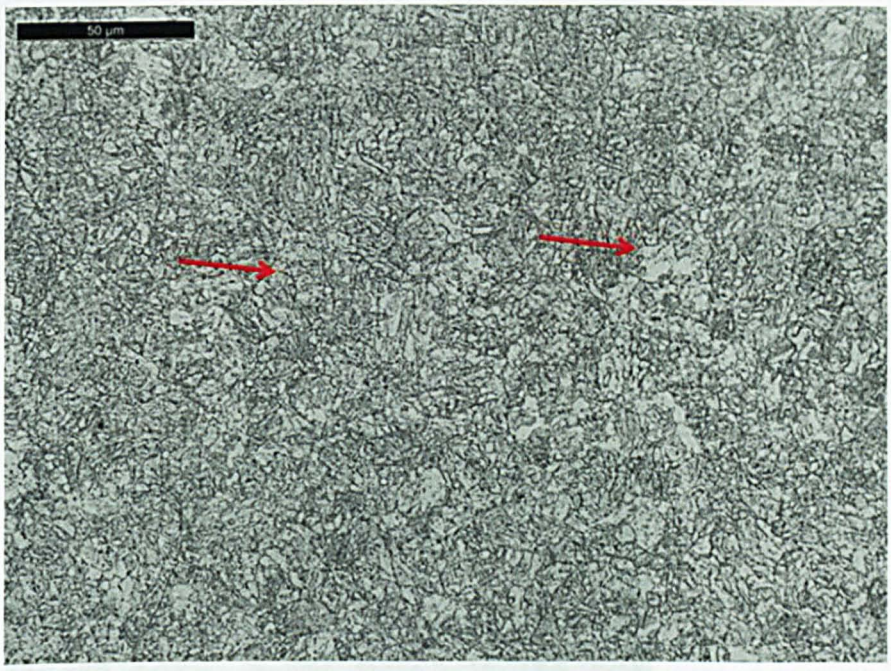

Figure 3-13: Optical micrograph of the ICHAZ in the as-welded condition. Arrows highlight examples of prior austenite grain boundaries.

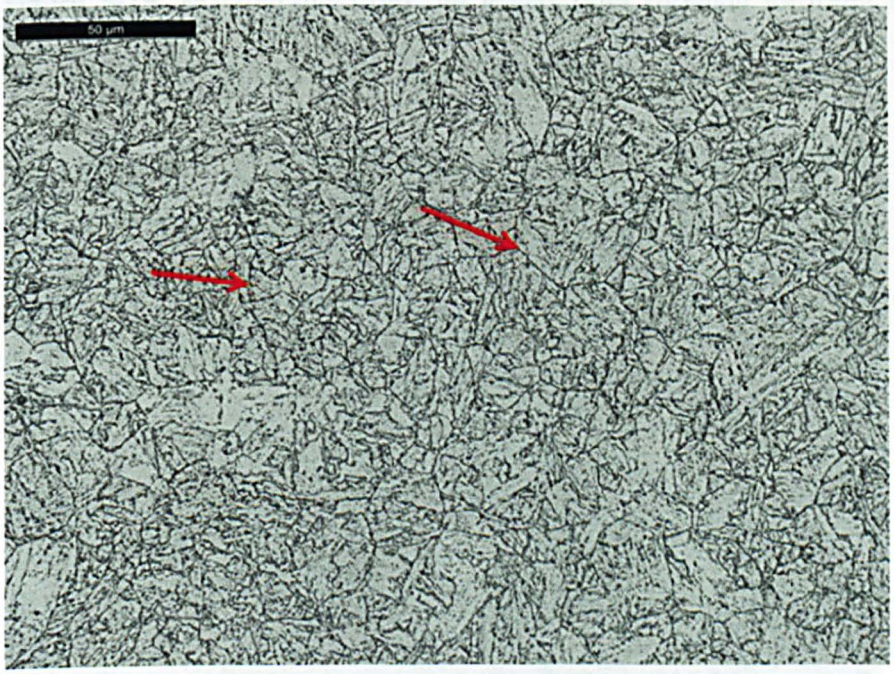

Figure 3-14: Optical micrograph of the parent metal in the as-welded condition. Arrows highlight examples of prior austenite grain boundaries.

Figure 3-15 shows a macrograph of the pipe that was subjected to PWHT for 4 hours at 750°C. Micrographs were taken at similar locations as for those described for the as-welded pipe. The letters a through to e, which marked on the macrograph, correspond to micrographs presented in Figure 3-16 through to Figure 3-20 respectively.

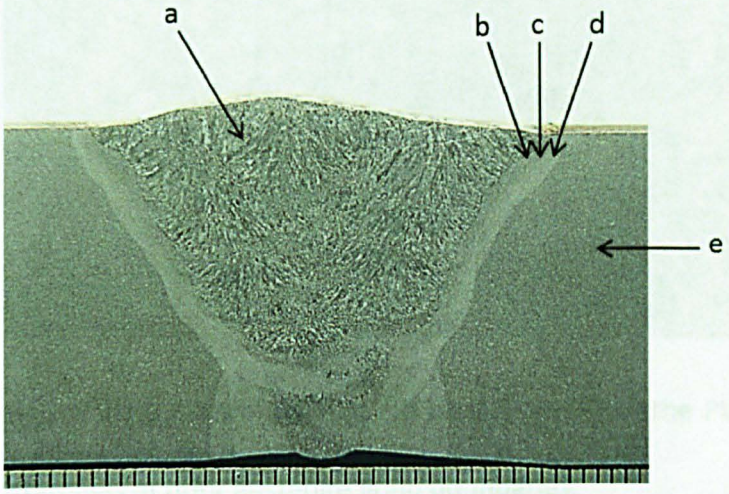

Figure 3-15: Macrograph from the PWHT pipe showing locations from which optical micrographs in Figure 3-16 through to Figure 3-20 were obtained.

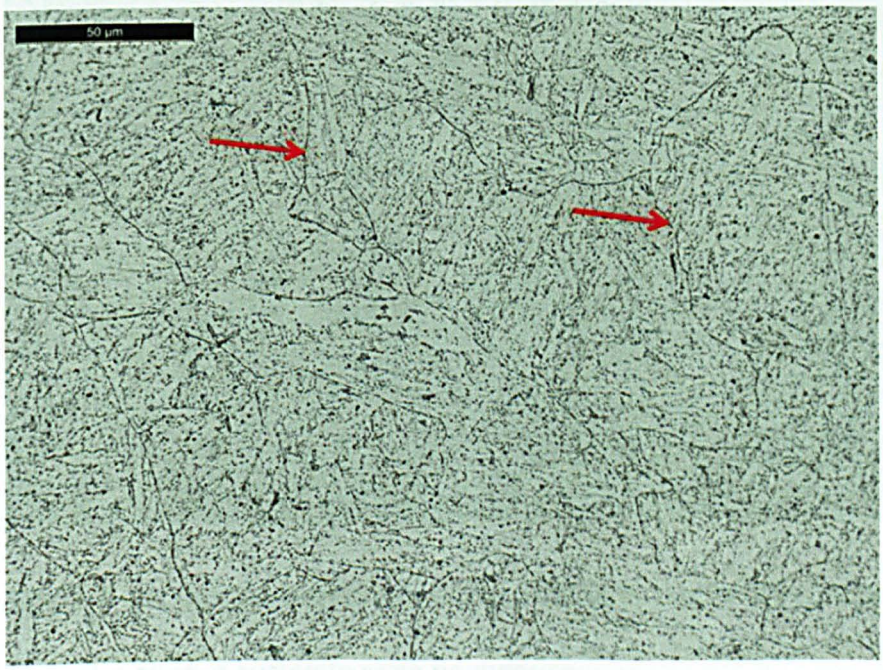

Figure 3-16: Optical micrograph of the weld metal in the PWHT condition. Arrows highlight examples of prior austenite grain boundaries.

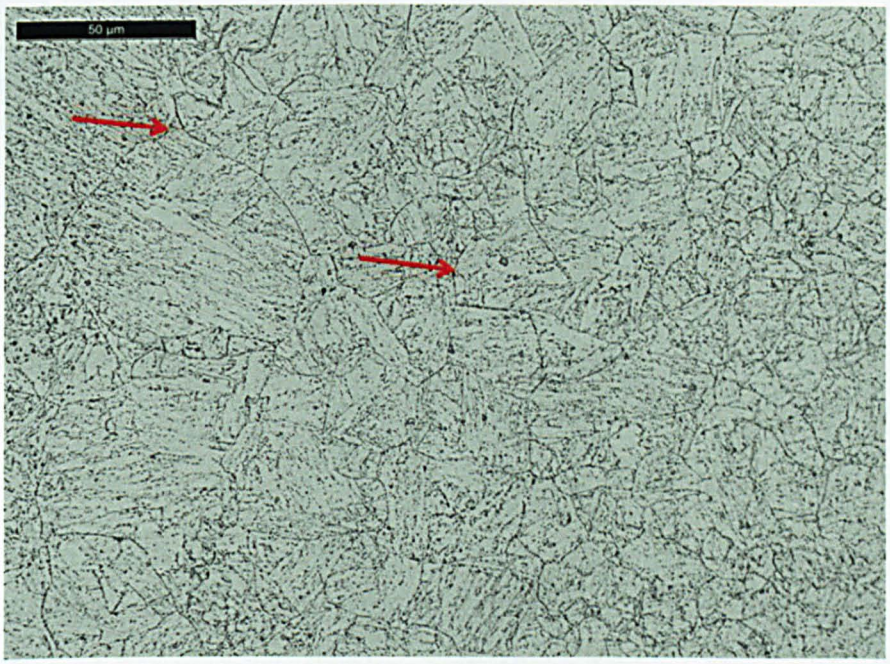

Figure 3-17: Optical micrograph of the CGHAZ in the PWHT condition. Arrows highlight examples of prior austenite grain boundaries.

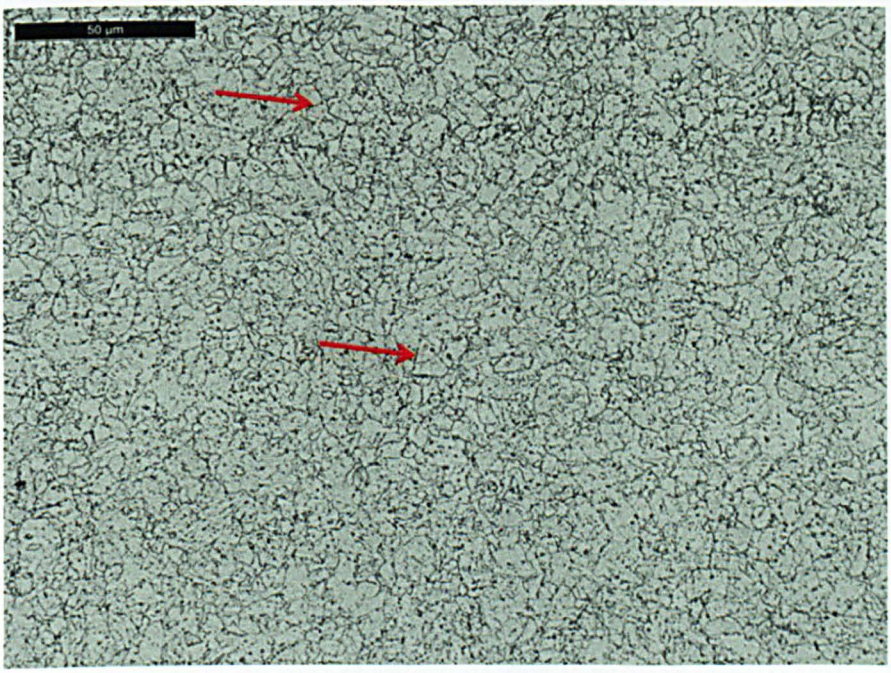

Figure 3-18: Optical micrograph of the FGHAZ in the PWHT condition. Arrows highlight examples of prior austenite grain boundaries.

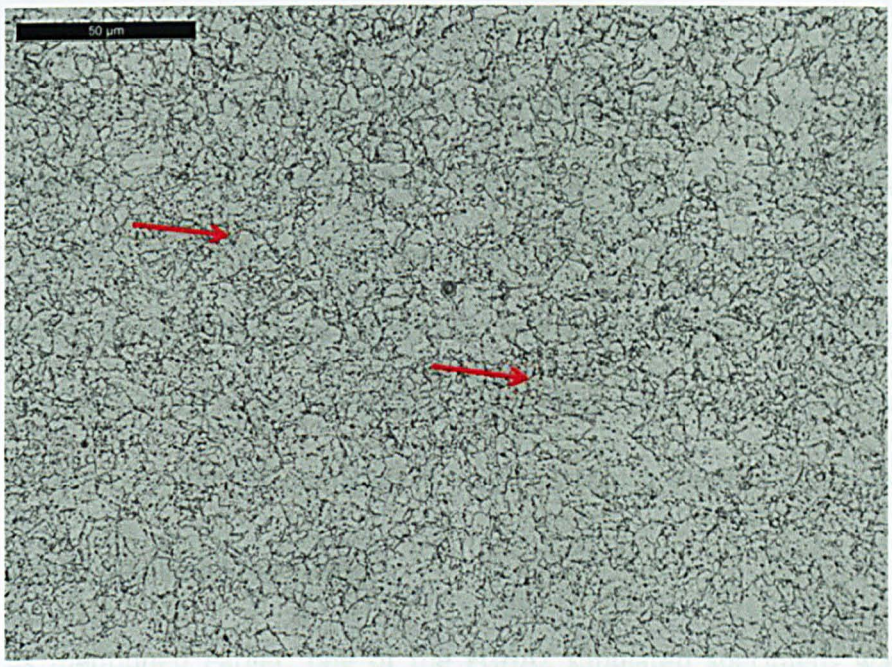

Figure 3-19: Optical micrograph of the ICHAZ in the PWHT condition. Arrows highlight examples of prior austenite grain boundaries.

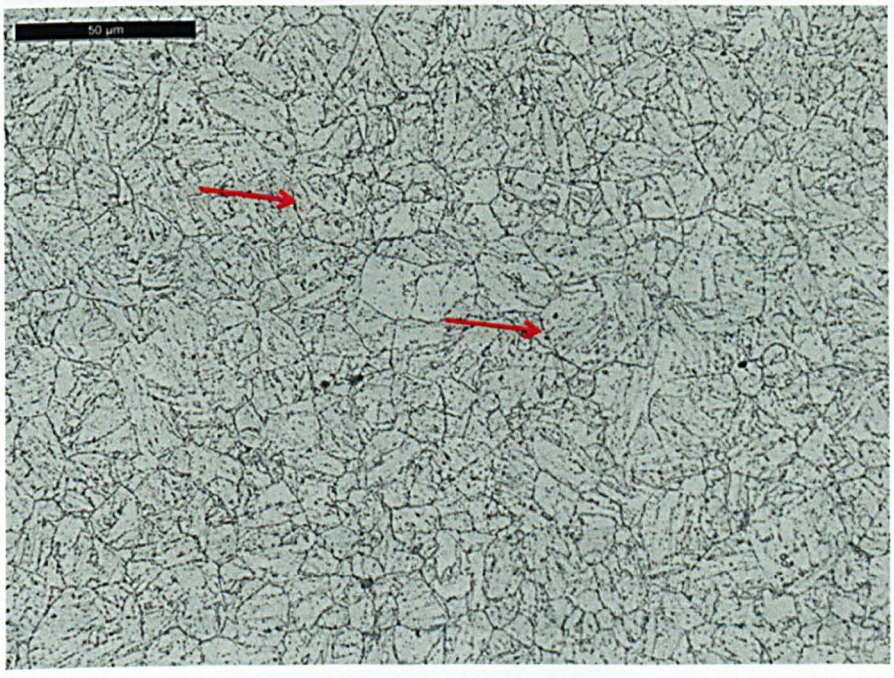

Figure 3-20: Optical micrograph of the parent metal in the PWHT condition. Arrows highlight examples of prior austenite grain boundaries.

The micrographs presented for the PWHT material show very similar features to those observed in the as-welded material with more or less the same grain structure and size. The martensite that would have formed upon cooling after welding will have been tempered by the post weld heat treatment to produce a microstructure comprising a ferrite matrix with $M_{23}C_6$ carbides on lath boundaries and MX precipitates both on lath boundaries and within each lath. These features cannot be identified on the optical micrographs and require higher resolution scanning electron microscopy.

FGHAZ Simulated specimens

As mentioned earlier, one of the FGHAZ simulated specimens was sectioned at two different locations (A and B as shown in Figure 3-21) to verify that the microstructure was representative of the FGHAZ region of the PWHT pipe i.e. the micrograph presented in Figure 3-18.

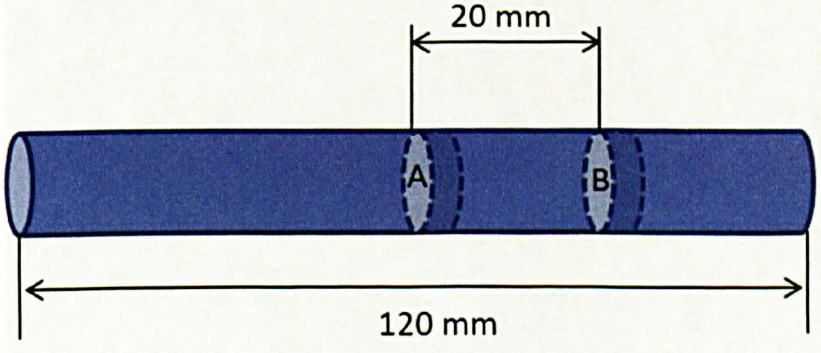

Figure 3-21: Schematic diagram of the FGHAZ simulated bar showing locations where optical micrographs were taken and hardness measurements carried out (A and B).

Figure 3-22 and Figure 3-23 show the optical micrographs taken at locations A and B respectively. Clearly both microstructures are very similar to the one presented for the FGHAZ in the PWHT pipe, with typical prior-austenite grains being in the order of 10 μm across.

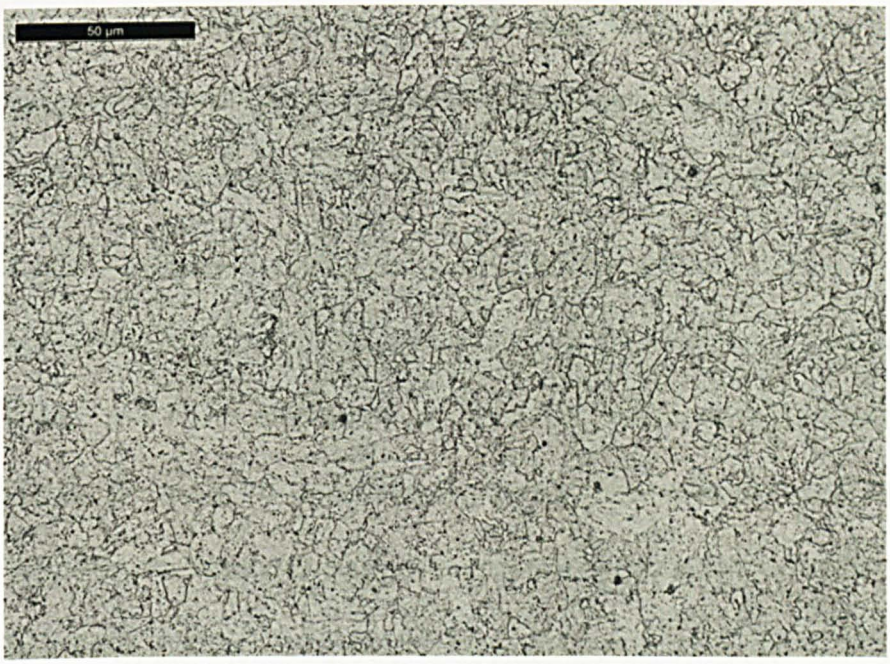

Figure 3-22: Optical micrograph taken at location A of the FGHAZ simulated bar.

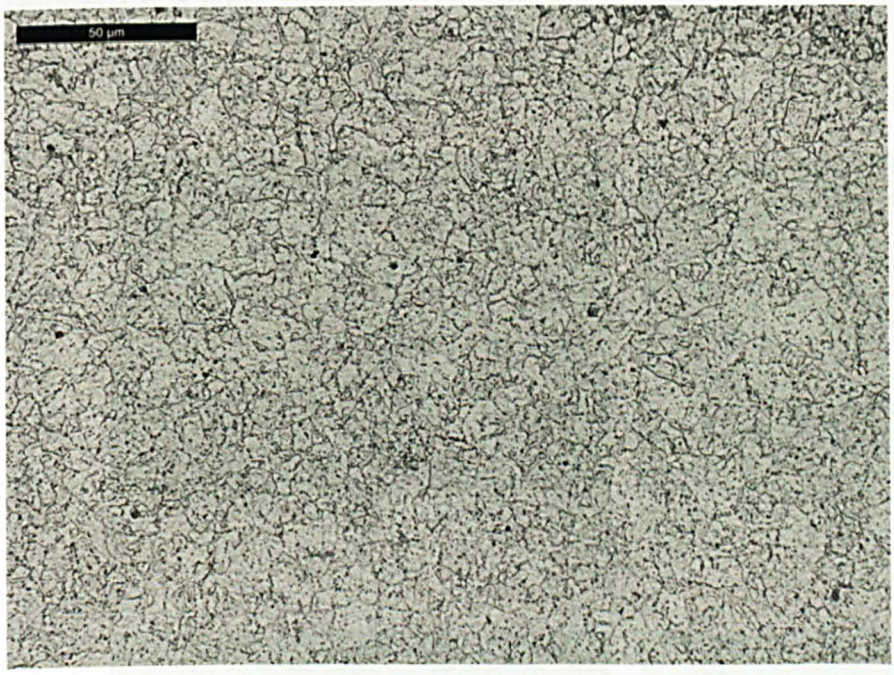

Figure 3-23: Optical micrograph taken at location B of the FGHAZ simulated bar.

3.5.3 Scanning electron microscopy

Scanning electron microscopy was used to study in more detail the changes that occurred after PWHT. The as-welded and PWHT sections were examined using a Zeiss Supra 55VP

Scanning Electron Microscope. Images were taken in secondary electron (SE) mode, which provide information concerning the topography and surface structure of the sample. The working distance was ~10 mm with an accelerating voltage of 5 kV.

Figure 3-24 shows scanning electron micrographs of the different microstructural regions as represented in the optical micrographs, i.e. the weld metal; the CGHAZ; the FGHAZ; the ICHAZ; and finally unaffected parent metal from both the as-welded and PWHT pipe welds. Arrows in these micrographs highlight examples of PAGBs. Chromium rich $M_{23}C_6$ carbides were identified on prior austenite grain boundaries (PAGBs) and lath boundaries (using EDX analysis). On the other hand, MX precipitates which tend to be vanadium rich nitrides (VN) and/or niobium rich carbo-nitrides Nb(C, N) [20] were too small to be resolved using SEM.

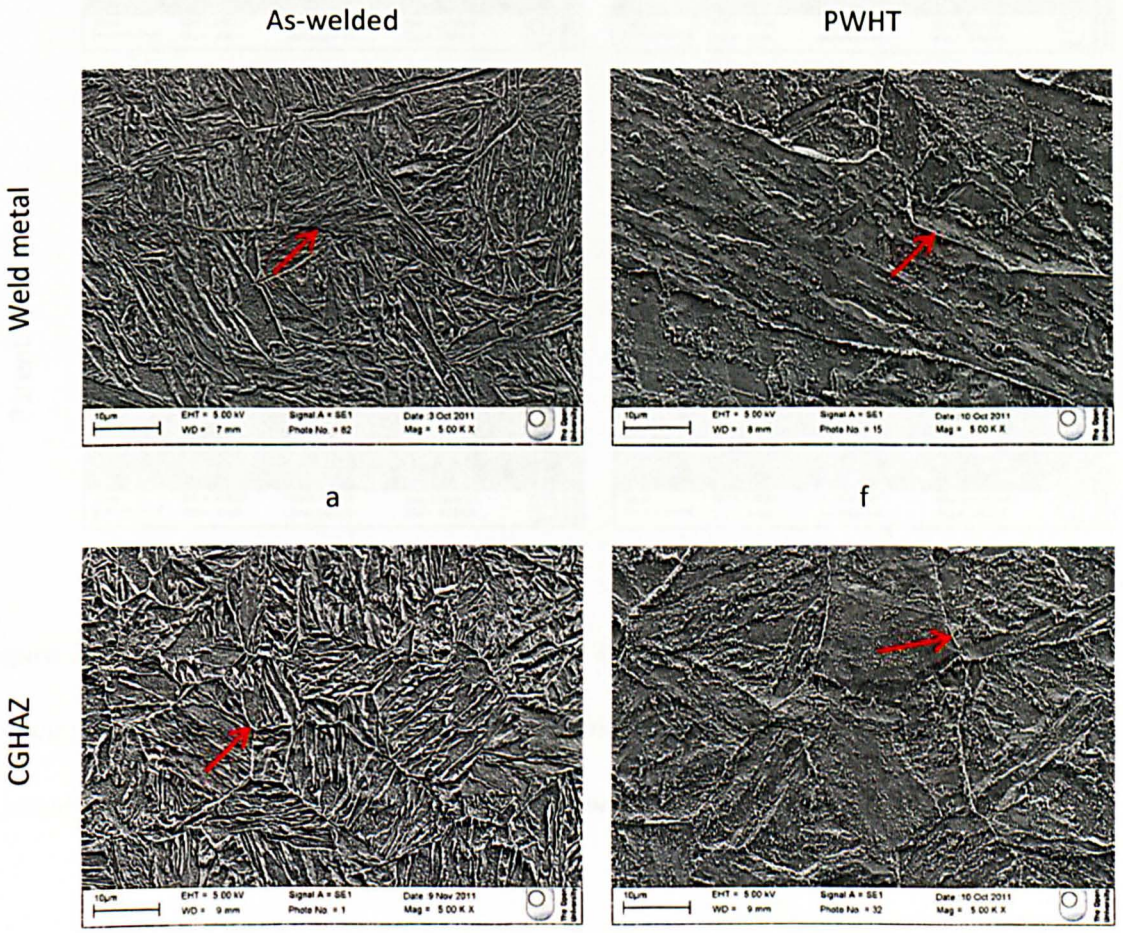

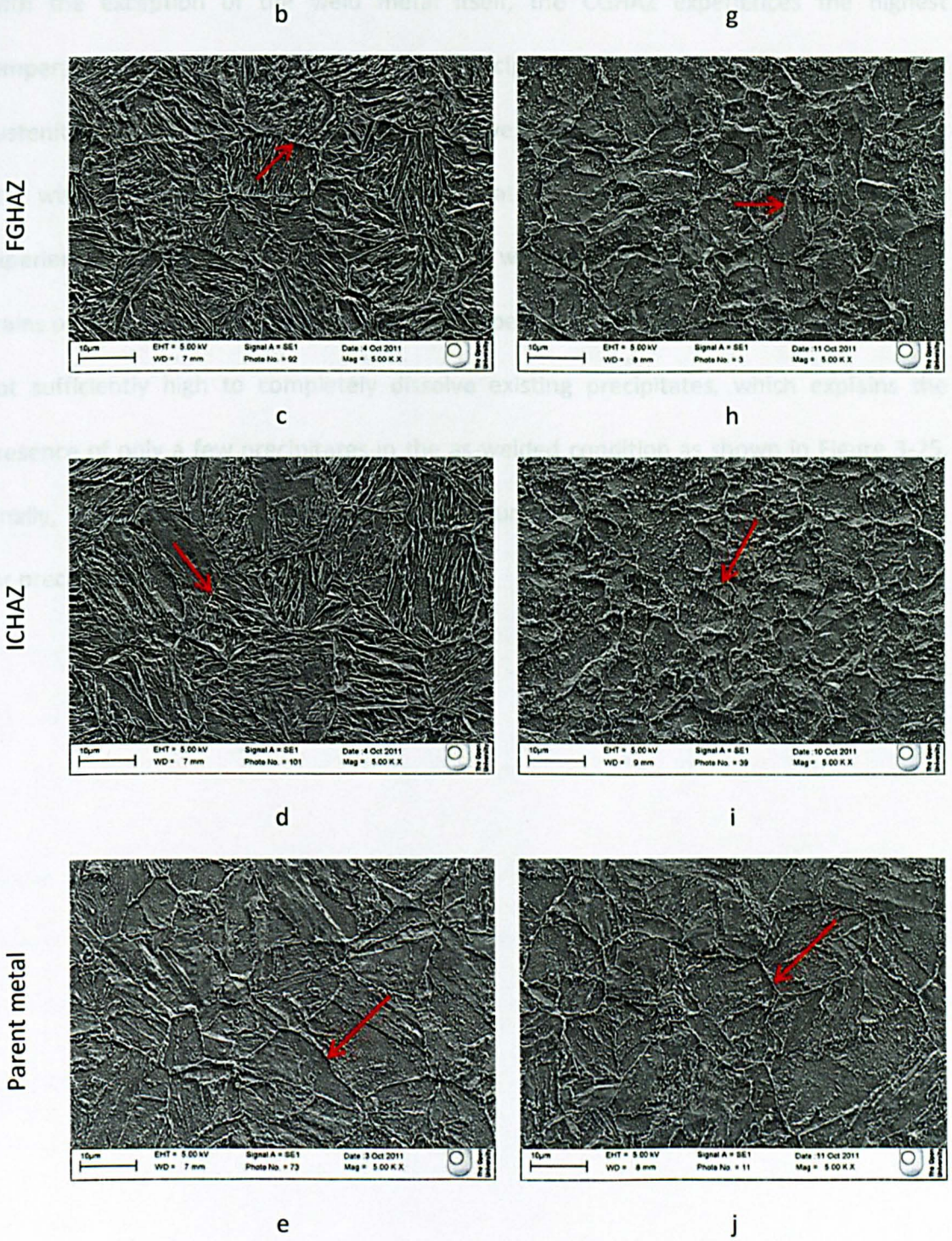

Figure 3-24: Scanning electron micrographs of as-welded (left) and PWHT (right) pipes showing WM, CGHAZ, FGHAZ, ICHAZ and unaffected parent material. Examples of prior austenite grain boundaries are highlighted (arrows).

With the exception of the weld metal itself, the CGHAZ experiences the highest temperature during welding ($T_p >> Ac_3$). Precipitates, which obstruct the growth of austenite grains at lower temperatures, dissolve, resulting in coarse grains of austenite [21] with almost no grain boundary precipitation. In the FGHAZ, the temperature experienced during welding is around 950°C, which results in the formation of small grains of austenite due to recrystallisation. The peak temperature reached in this region is not sufficiently high to completely dissolve existing precipitates, which explains the presence of only a few precipitates in the as-welded condition as shown in Figure 3-25. Finally, in the parent metal the peak temperatures during welding are not high enough for precipitate dissolution to occur.

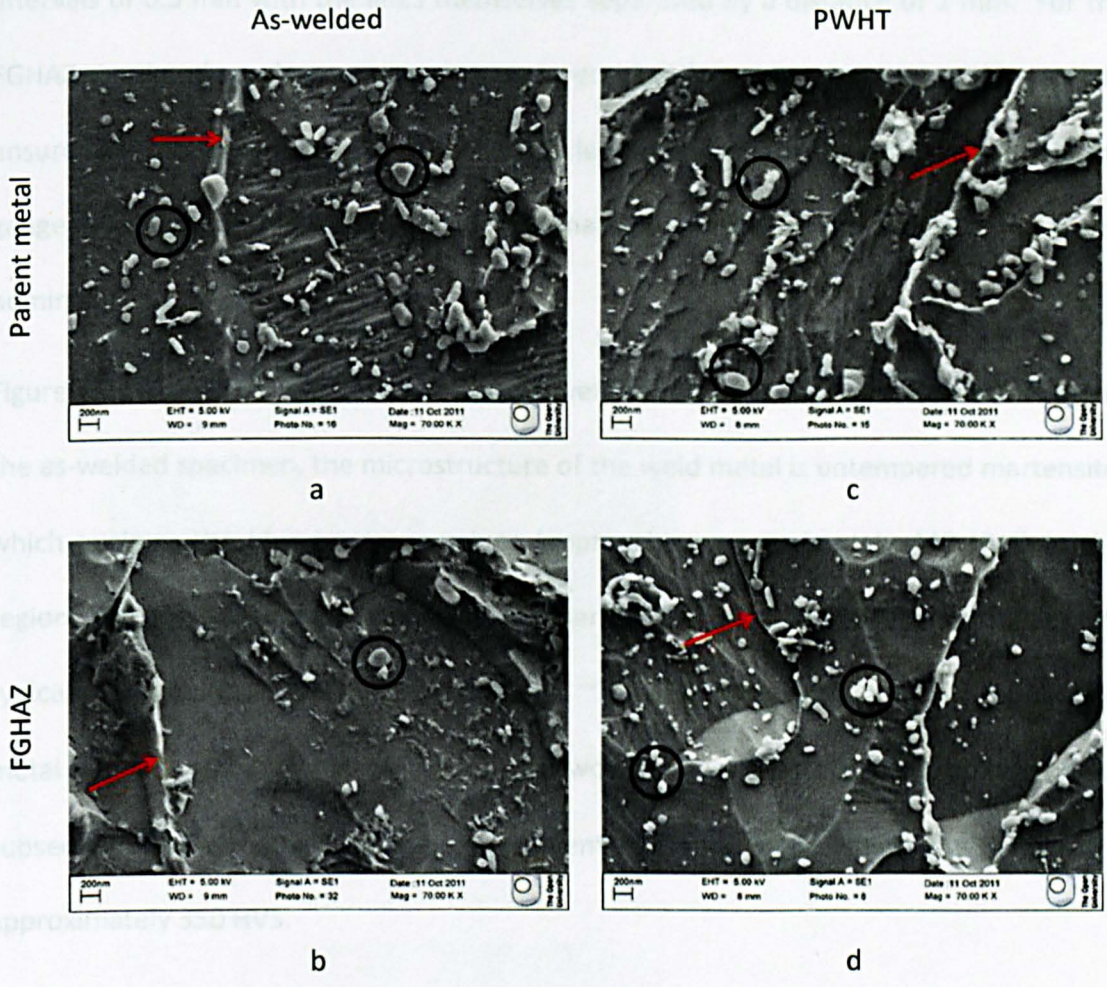

Figure 3-25: Scanning electron micrographs of as-welded (left) and PWHT (right) pipes showing parent metal and FGHAZ at high magnification. Examples of prior austenite grain boundaries (arrows) and $M_{23}C_6$ carbides (circles) are highlighted.

After PWHT, the nucleation of new precipitates is discernible in all the microstructures that are presented. The average size of the $M_{23}C_6$ carbides was found to be around 300 nm.

3.5.4 Hardness testing

Hardness measurements were carried out using a Vickers (HV) indenter, with a load of 5 kg, using an automated Struers Duramin-A-300 hardness tester. In the case of the as-welded and PWHT sections, measurements were taken on several straight lines at

intervals of 0.5 mm with the lines themselves separated by a distance of 1 mm. For the FGHAZ simulated specimen, measurements were distributed in a square grid. This was to ensure that the hardness within a central circle 8 mm in diameter, which represents the gauge diameter of the creep specimens that were used in the current work, was nominally uniform.

Figure 3-26 shows hardness maps for the as-welded and post-weld heat treated joints. In the as-welded specimen, the microstructure of the weld metal is untempered martensite, which explains the high hardness values (approaching approximately 440 HV5) in this region. Moving towards the parent metal, there is a marked decrease in hardness, with typical values being ~300 HV5 in the HAZ, and ~215 HV5 in the parent metal. In the weld metal region, some of the weld passes would have been partially tempered by subsequent passes. These regions are evident in Figure 3-26a where the hardness is approximately 350 HV5.

The PWHT operation results in a considerable decrease in hardness in the weld metal region, with typical values after PWHT being ~240 HV5. It is well established [9, 22, 23] that in this class of steel, there is a tendency to form a soft zone in the intercritical ICHAZ and over-tempered HAZ after PWHT. Indeed, this is where we see the lowest hardness values, being approximately 170 HV5 in this region. The ICHAZ is only partially austenitised during welding, and the remaining ferritic (or tempered martensitic) structure is over-aged during the welding thermal cycle and subsequent PWHT operation, producing a relatively soft microstructure which lacks the carbo-nitride strengthening that is essential for creep resistance [9]. Meanwhile, in the FGHAZ, the peak temperature experienced during welding falls within the range $Ac_3 < T_p < 1100°C$. While, on the one hand, the material in the FGHAZ is completely austenitised on heating, the peak

temperature is also high enough for much of the carbon and nitrogen go into solution, so the FGHAZ still experiences some degree of softening. Finally, the hardness in the parent material is not affected by the PWHT and values of hardness are relatively constant at 215 HV5.

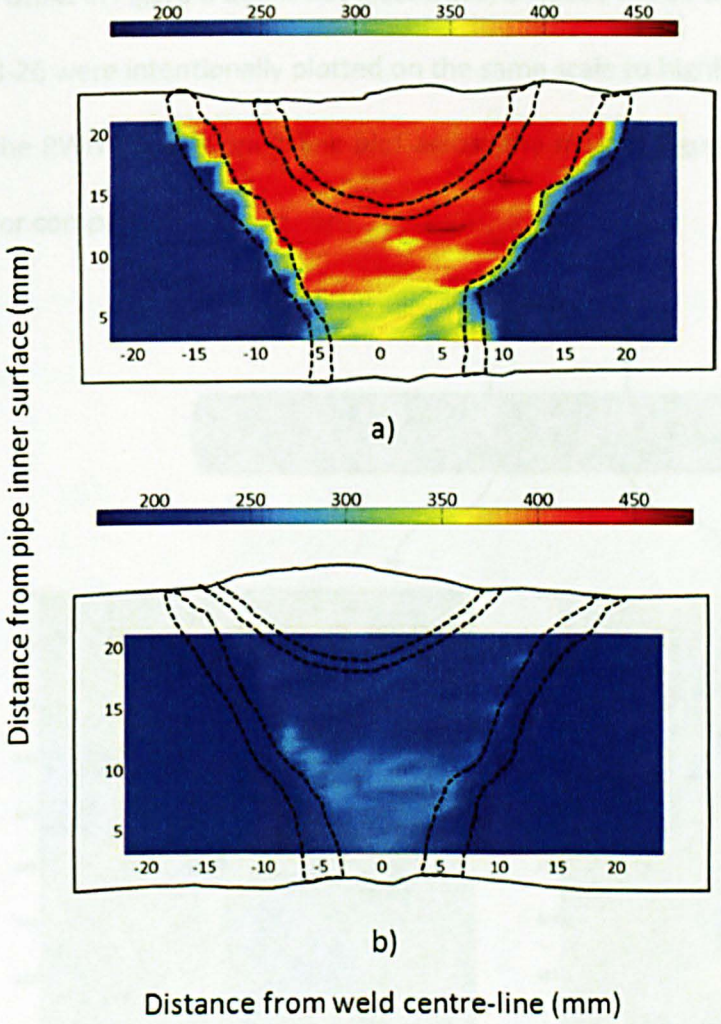

Figure 3-26: Vickers hardness (HV5) maps on a plane orientated transversely to the welding direction for (a) the as-welded condition and (b) the PWHT condition, embedded in outlines of the respective macrographs. Dotted lines highlight the fusion line/HAZ region for the last weld pass and the weld as a whole.

The hardness measurements on the FGHAZ simulation specimens at the two different locations (the mid-length position and 20 mm away from the mid-length position of the simulated bar) are shown in Figure 3-27. The hardness varied between 196 and 203 HV5 giving an average hardness of 199 HV5. A comparison of this value to the hardness of the FGHAZ in Figure 3-26b is not illustrative, because the as-welded and PWHT maps in Figure 3-26 were intentionally plotted on the same scale to highlight the tempering effect during the PWHT operation. A line plot across the map in Figure 3-26b is shown in Figure 3-28 for comparison.

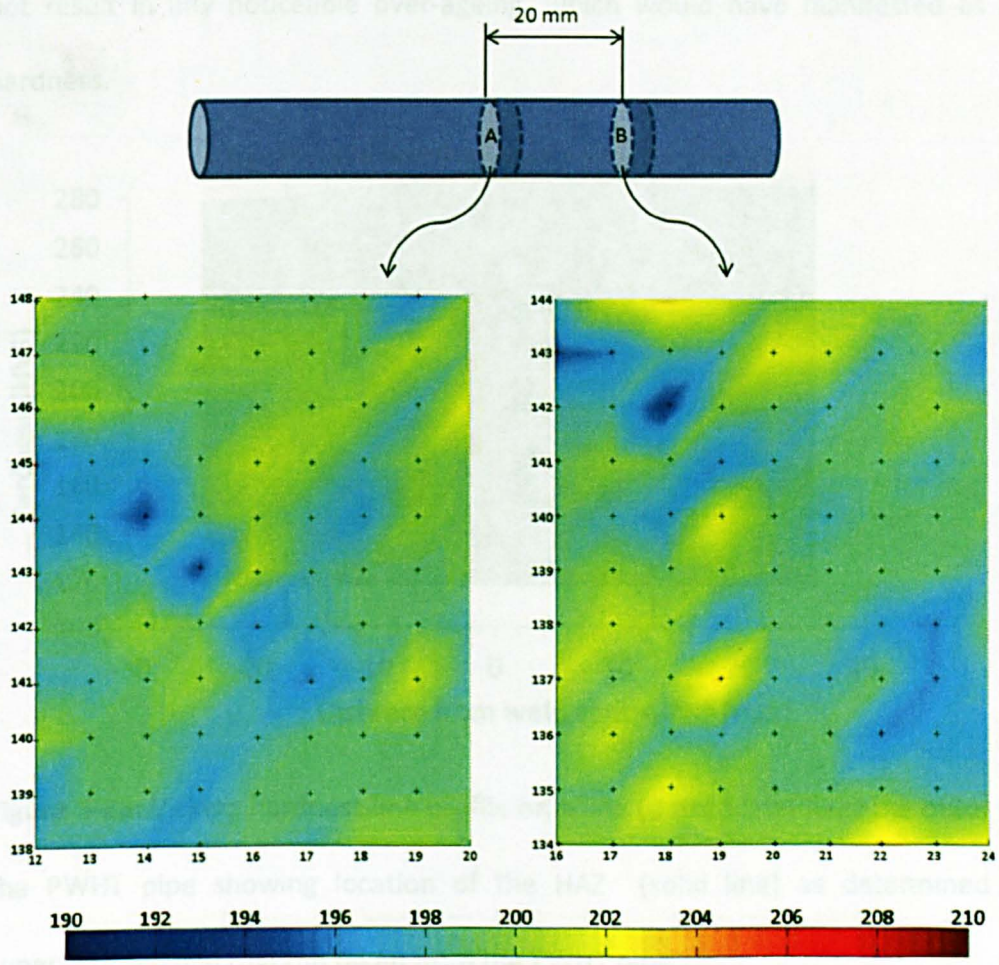

Figure 3-27: Vickers hardness (HV5) maps at the centre (left) and 20 mm away from the centre (right) of the simulated FGHAZ bar.

The hardness results presented in Figure 3-28 were taken at a location close to the pipe's outer surface (dotted line) such that the effects of subsequent welding passes were minimised. The solid lines represent the extent of the heat affected zone as obtained from the superimposed macrograph taken from the PWHT pipe. Assuming that the FGHAZ region lies approximately in the centre of the HAZ, It can be confirmed that the hardness in the FGHAZ location is approximately 204 HV5, which correlates well with the measured hardness of 199 HV5 in the FGHAZ simulated specimens. Furthermore, these results suggest that the PWHT of the FGHAZ simulated specimens at 750°C for 4 hours did not result in any noticeable over-ageing, which would have manifested as a drop in hardness.

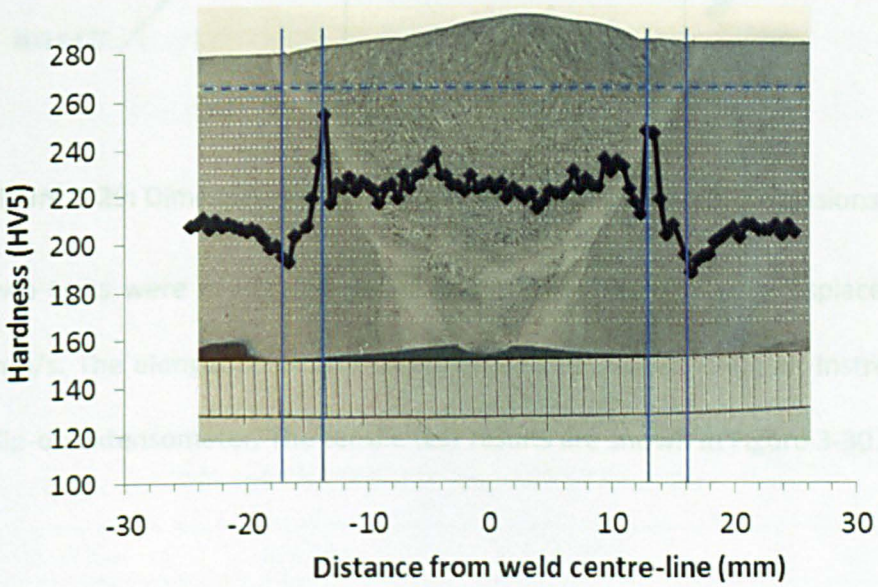

Figure 3-28: Vickers hardness line profile on a line (dotted line) near the outer surface of the PWHT pipe showing location of the HAZ (solid line) as determined from the superimposed macrograph taken from the PWHT pipe.

3.5.5 *Tensile testing*

Tensile properties of the P91 base material in the pipe axial direction at ambient temperature were conducted using an Instron servo-electric testing machine with a capacity of 100 kN. Standard cylindrical tensile test specimens were machined and tested according to ASTM E8/E8M-08: Standard Test Methods for Tension Testing of Metallic Materials [24]. The specimen dimensions are given in Figure 3-29.

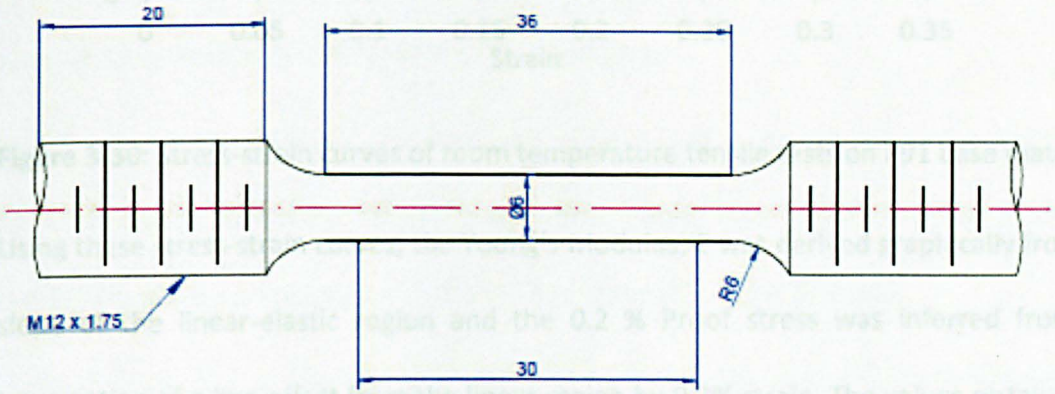

Figure 3-29: Dimensions of round tensile test specimen. All dimensions in mm.

Two tests were conducted under displacement control at a displacement rate of 0.01 mm/s. The elongation of the specimen was measured using an Instron 2630-100 series clip-on extensometer. The tensile test results are shown in Figure 3-30.

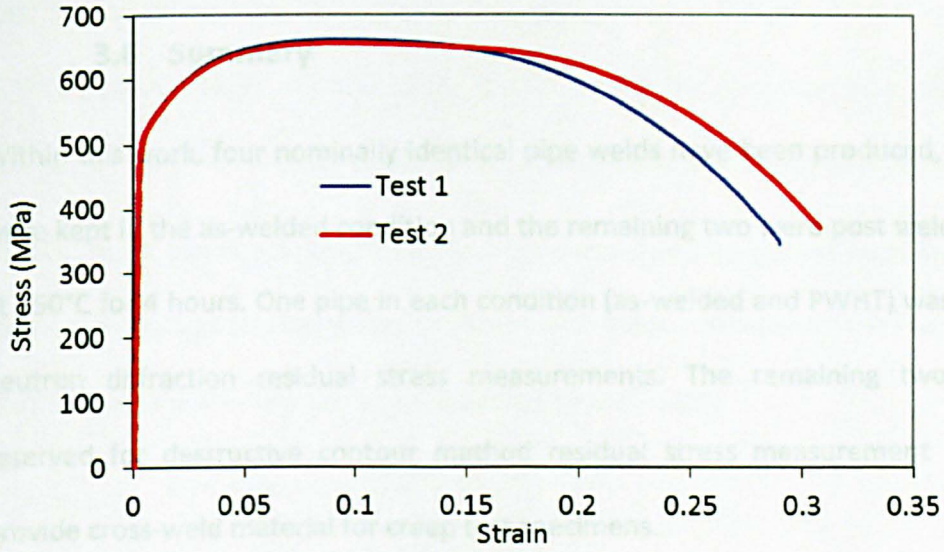

Figure 3-30: Stress-strain curves of room temperature tensile tests on P91 base material.

Using these stress-strain curves, the Young's Modulus, E was derived graphically from the slope of the linear-elastic region and the 0.2 % Proof stress was inferred from the intersection of a line offset from the linear region by 0.2% strain. The values obtained are given in Table 3-4 along with the ASME specification for comparison.

Table 3-4: Mechanical properties of the P91 parent metal obtained from room temperature tensile tests. ASME material specification was obtained from [2].

	0.2% Proof Stress (MPa)	Young's Modulus (GPa)	Ultimate Tensile Strength (MPa)
ASME Spec	Min 415	218*	Min 585
Test 1	502	213	656
Test 2	498	215	660
Average	500	214	658

*From Vallourec and Mannesmann [2]

3.6 Summary

Within this work, four nominally identical pipe welds have been produced, two of which were kept in the as-welded condition and the remaining two were post weld heat treated at 750°C for 4 hours. One pipe in each condition (as-welded and PWHT) was allocated for neutron diffraction residual stress measurements. The remaining two pipes were reserved for destructive contour method residual stress measurement trials, and to provide cross-weld material for creep test specimens.

Simulated FGHAZ samples were produced using induction heating and oil quenching at MPA Stuttgart, Germany. These were post weld heat treated using the same temperature-time combination as the welded pipes (750°C for 4 hours).

Optical micrographs were taken at different locations across the weld in both the as-welded and PWHT pipes. A martensitic plate-like structure was clearly identified in the weld metal, CGHAZ and in the parent metal. The prior austenite grain sizes in the FGHAZ and the ICHAZ were very similar (10 μm across), thus a strict differentiation between these two regions was difficult. Micrographs were also taken from the FGHAZ simulation specimen and these exhibited very similar features as the FGHAZ in the PWHT pipe.

Scanning electron micrographs showed that significant changes occurred to the precipitate distribution after PWHT, which were not discernible in the optical micrographs. In general, the as-welded microstructures did not reveal many precipitates along grain or lath boundaries. After PWHT, the nucleation of new precipitates was discernible in all the microstructural regions.

Hardness measurements were carried out on the as-welded and PWHT sections. The PWHT operation resulted in a considerable decrease in hardness in the weld metal region,

with typical values after PWHT being ~240 HV5. The lowest hardness was measured in the ICHAZ (typical values of ~190 HV5). In the FGHAZ the hardness was ~200 HV5 which correlated very well with hardness values of the FGHAZ simulated specimens.

Finally, room temperature tensile tests conducted on P91 parent material showed that the mechanical properties were consistent with those provided by the manufacturer and that they met the minimum values specified by the ASME.

3.7 References

[1] ASTM International, "ASTM A335 / A335M - 11 Standard Specification for Seamless Ferritic Alloy-Steel Pipe for High-Temperature Service," 2011.

[2] K. Haarmann, J. C. Vaillant, B. Vandenberghe, W. Bendick, and A. Arbab, The T91/P91 book, 2nd ed. Vallourec & Mannesmann Tubes, 2002.

[3] Metrode Products Limited, "Welding consumables for P91 steels for the power generation industry," Surrey, 2006.

[4] British Standards Institution, "BS2633 - Class I Arc Welding of Ferritic Steel Pipework for Carrying Fluids," London, 1987.

[5] American Welding Society, "AWS A5.23/A5.23M, Specification for Low-Alloy Steel Electrodes and Rods for Gas Shielded Arc Welding," Miami, Florida, 2007.

[6] American Society of Mechanical Engineers, "ASME SFA 5.28, Nuclear Components: Boiler & Pressure Vessel Code," New York, 2007.

[7] B. S. Institution, "BS EN 12070, Welding Consumables, Wire Electrodes, Wires and Rods for Arc Welding of Creep-resisting Steels.," London, 2000.

[8] American Society of Mechanical Engineers, "ASME, Section I, II, IX and B31.1: Boiler and Pressure Vessel Code," 2007.

[9] Z. Zhang, J. C. M. Farrar, and A. M. Barnes, "Weld metals for P91-tough enough?," in Fourth International EPRI Conference on Welding and Repair Technology for Power Plants, 2000.

[10] M. Turski, J. A. Francis, P. R. Hurrell, S. K. Bate, S. Hiller, and P. J. Withers, "Effects of stop–start features on residual stresses in a multipass austenitic stainless steel weld," International Journal of Pressure Vessels and Piping, vol. 89, no. 0, pp. 9–18, Jan. 2012.

[11] P. J. Bouchard, J. R. Santisteban, L. Edwards, M. Turski, J. James, S. Pratihar, and P. J. Withers, "Residual Stress Measurements Revealing Weld Bead Start and Stop Effects in Single and Multi-Pass Weld-Runs," in ASME 2005 Pressure Vessels and Piping Conference, 2005, pp. 853–860.

[12] British Standards Institution, "BS EN 1599, Welding Consumables. Covered Electrodes for Manual Metal Arc Welding of Creep-resisting Steels," London, 1997.

[13] American Welding Society, "AWS D10.10, Recommended Practices for Local Heating of Welds in Piping and Tubing," Miami, Florida, 2009.

[14] J. C. Vaillant, B. Vandenberghe, B. Hahn, H. Heuser, and C. Jochum, "T/P23, 24, 911 and 92: New grades for advanced coal-fired power plants - Properties and experience," International Journal of Pressure Vessels and Piping, vol. 85, no. 1–2, pp. 38–46, Jan. 2008.

[15] ECCC, "Data acceptability criteria and data generation: Creep data for welds," vol. 3 Part II, no. 3, 2004.

[16] SEW088, "Weldable Fine Grained Steels; Guidelines For Processing, Particular For Fusion Welding," 1993.

[17] D. Rosenthal, "Mathematical theory of heat distribution during welding and cutting," Welding Journal, vol. 20, no. 5, pp. 220–234, 1941.

[18] N. N. Rykalin, "Berechnung der Wärmevorgänge beim Schweißen," Berlin, 1957.

[19] L. M. Fu, H. R. Wang, W. Wang, and a D. Shan, "Austenite grain growth prediction coupling with drag and pinning effects in low carbon Nb microalloyed steels," Materials Science and Technology, vol. 27, no. 6, pp. 996–1001, Jun. 2011.

[20] F. Abe and M. Tabuchi, "Microstructure and creep strength of welds in advanced ferritic power plant steels," Science and Technology of Welding and Joining, vol. 9, no. 1, pp. 22–30, Feb. 2004.

[21] P. Mayr, I. Holzer, and H. Cerjak, "Evolution of precipitate structure in the heat-affected zone of a martensitic 9 wt.% Cr steel during welding and post-weld heat treatment," Welding in the World, vol. 55, no. 5–6, pp. 70–77, 2011.

[22] H. Cerjak and E. Letofsky, "The effect of welding on the properties of advanced 9–12%Cr steels," Science and Technology of Welding and Joining, vol. 1, no. 1, pp. 36–42, Feb. 1996.

[23] K. Laha, K. S. Chandravathi, P. Parameswaran, K. B. S. Rao, and S. L. Mannan, "Characterization of Microstructures across the Heat-Affected Zone of the Modified 9Cr-1Mo Weld Joint to Understand Its Role in Promoting Type IV Cracking," Metallurgical and Materials Transactions A, vol. 38, no. 1, pp. 58–68, Jan. 2007.

[24] ASTM International, "ASTM E8/E8M-08: Standard Test Methods for Tension Testing of Metallic Materials."

Chapter 4

Residual Stress Measurements

4.1 Introduction

Welding residual stresses arise as a consequence of localised plastic deformation in the material. When the weld metal cools and solidifies, contraction occurs which imposes strains on the surrounding material. Residual stresses significantly affect the performance of welded structures and can contribute to fatigue crack development, stress corrosion cracking, and they have also been shown to accelerate the onset of creep damage [1], [2], [3]. In a recent review by Francis *et al.* [4] the role of residual stresses arising from welding has been highlighted as a potential contributing factor for Type IV failures in ferritic/martensitic steels.

This chapter deals with the measurement of residual stresses in welded P91 steel pipes, in the as-welded and post weld heat treated conditions, over a planar area that includes the heat affected zones of these welds, where premature Type IV failures occur. The results arising from this chapter have been published in a peer reviewed paper [5]. While it is possible that the effects of residual stress on creep life are reduced by PWHT, the stresses remaining after PWHT may still be significant in comparison to typical loads experienced in service. It was intended for these measurements to establish the stress levels that would later be used in simpler experiments, in which the effects of residual stresses and stress relaxation on creep damage would be investigated (chapter 5).

4.2 Experimental setup

The measurement of residual stresses using neutron diffraction is based on Bragg's law of diffraction, which states that:

$$\lambda = 2d \sin\theta \qquad \text{Equation 4-1}$$

where λ is the de Broglie wavelength of the incident neutron, and d is the spacing between the crystallographic planes for which neutrons with a de Broglie wavelength of λ constructively interfere at a diffraction angle of 2θ. In a time-of-flight neutron source, a neutron beam with a distribution of wavelengths is incident upon the sample and the detectors are fixed so the diffraction angle is nominally 90°. The time-of-flight for a given neutron is then used to determine its de Broglie wavelength leaving d as the only unknown in Equation 4-1. Since the neutron beam is polychromatic, it is possible to obtain diffraction peaks for several crystallographic planes (d_{hkl}) simultaneously. An estimate for the lattice parameter, a, is then obtained, using the calculated values of d for several crystallographic planes.

4.2.1 Instrument

Neutron diffraction measurements were made at the ENGIN-X beam line [6] at ISIS, which is part of the Rutherford-Appleton Laboratory in the United Kingdom. ISIS is a time-of-flight spallation source, where neutrons are produced by the periodic bombardment of a heavy metal target by high-energy protons. ENGIN-X is a dedicated strain scanning instrument, sitting on a curved 'supermirror' neutron guide with a 50 m flight path. This optimum length maximises strain resolution through a combination of high intensity and good wavelength resolution [7]. A plan view of the instrument is illustrated in Figure 4-1.

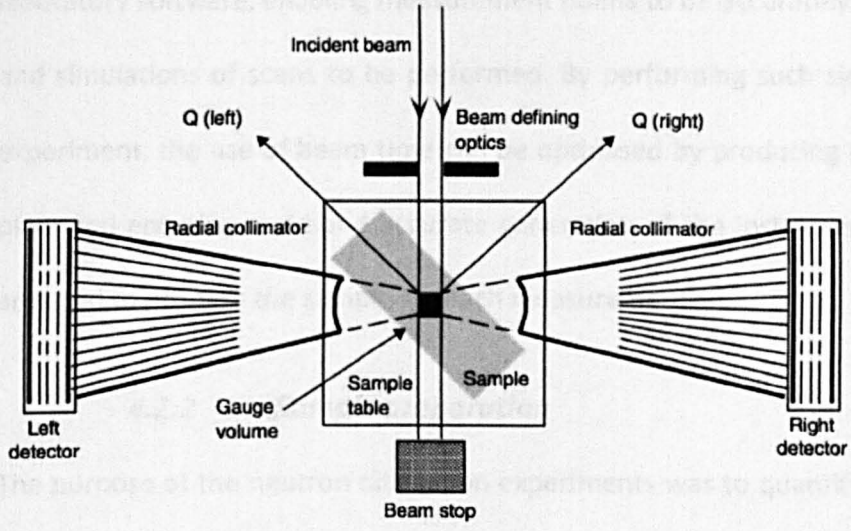

Figure 4-1: Plan view of the ENGIN-X instrument [8]. The arrows marked 'Q' indicate the directions in which strain is measured by the two detectors.

Neutrons originate from a liquid methane moderator in short pulses (of between 5 and 50 μs) and travel to the sample where they scatter into 2 banks of detectors situated at an angle of ±2θ to the trasmitted beam. The incident beam is defined in area by a pair of motorised slits made from sintered boron carbide. The aperture can be varied between 0.2 and 10 mm wide and between 0.2 and 30 mm high. The outgoing beam dimensions are defined by interchangeable radial collimators, located in front of the detectors. Four sizes of collimator, defining gauge lengths of 0.5, 1, 2 and 4 mm are available. The sample table (positioner) is motorised and programmable for its x, y, z and ω movements and can hold samples up to 1.5 tonnes in weight. Samples are accurately aligned using the positioner and optical theodolites, which sit at nominal angles of ±45° to the incident beam.

An important part of the development of ENGIN-X has been the development of SScanSS (Strain Scanning Simulation Software) [9], a software tool for the planning and execution of neutron diffraction experiments. A laser scanner is used to scan the surfaces of a component to create a 3D model that can be manipulated in the SScanSS virtual

laboratory software, enabling measurement points to be accurately defined in the sample and simulations of scans to be performed. By performing such simulations prior to the experiment, the use of beam time can be optimised by producing a viable measurement plan, and ensuring rapid and accurate generation of the instrument control scripts that are used to position the sample for each measurement.

4.2.2 Sample preparation

The purpose of the neutron diffraction experiments was to quantify the residual stresses in the welded P91 steel pipes, in the as-welded condition and after PWHT. While it was desirable to conduct measurements on the same pipe before and after PWHT, after consideration was give to the manner in which neutron beamtime is allocated and the fact that welded P91 steel pipes cannot be kept in the as-welded condition for prolonged periods of time, a decision was made to conduct measurements on two different pipes (one as-welded and one PWHT). It was shown in Chapter 3 that the welding parameters (heat input, weld pass sequence, etc.) were nominally the same for all of the pipes produced in this work. The measurement locations and the number of measurement points were also kept the same for both pipes in order to make meaningful comparisons.

Measurements in some sample orientations can be difficult, particularly if both the incident and scattered beams travel a significant distance through the sample. Beam attenuation causes an exponential decrease in the diffracted intensity which means that the time to acquire a given integrated peak count also increases exponentially, and sometimes the background level can limit the depth to which practical measurements can be made [7]. To enable measurements in the hoop orientation to be made with an acceptable attenuation a slot (or window), measuring 60mm x 60 mm, was machined so that the beam passed through the thickness of the pipes once only (Figure 4-2).

Measurements of the lattice parameter were made at a circumferential position on the girth weld that was thought to be a sufficient distance from the slot (approximately 300 mm around the circumference) for the effects of any relaxation or redistribution of stresses to be insignificant, for example see Bouchard *et al.* [10].

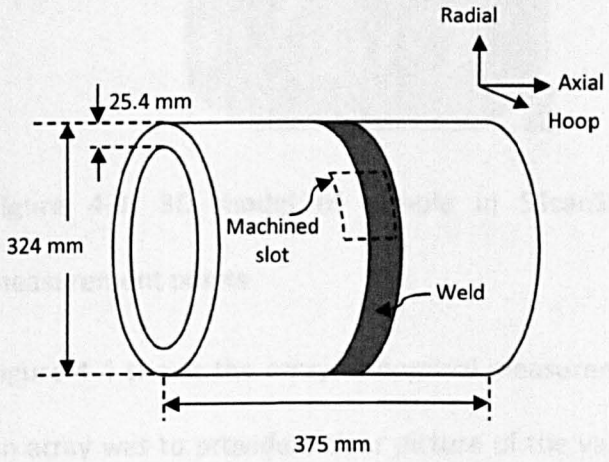

Figure 4-2: Schematic representation of welded pipe showing position of machined slot to facilitate neutron diffraction experiments. Hoop, axial and normal orientations are highlighted.

Prior to the experiment, fiducial points (ball bearings) were glued to the pipes at locations away from the measurement positions. These fiducial points, as will be described later, serve as reference locations for the alignment of the sample. A 3D model of the sample was then created by laser scanning, and this model was imported into SScanSS as shown in Figure 4-3. The measurement points and strain components are defined by the graphical intersection of planes and lines within the 3D model.

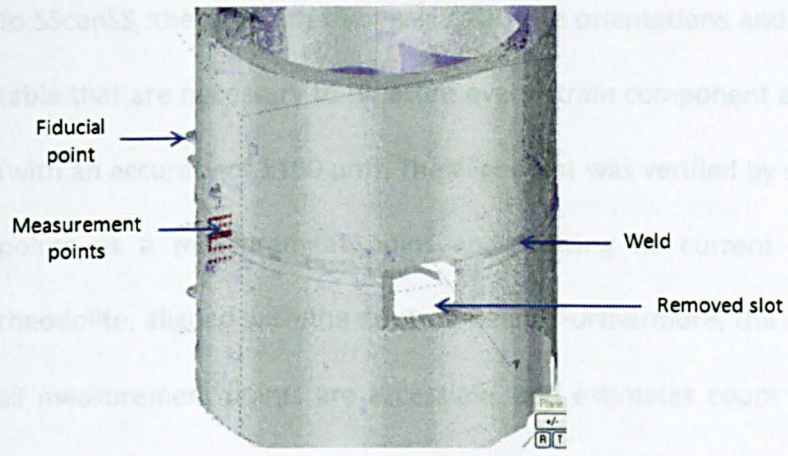

Figure 4-3: 3D model of sample in SScanSS showing the viewing window and measurement points.

Figure 4-4 shows the array of nominal measurement positions. The objective with such an array was to provide a clear picture of the variation in the inter-atomic plane spacing (and hence the residual strains) over a planar area in the weld metal, HAZ and parent metal. The density of measurement points was increased at distances of 15 mm and 18.5 mm from the weld centreline as these measurement lines intersect the FGHAZ and ICHAZ (i.e. the Type IV region).

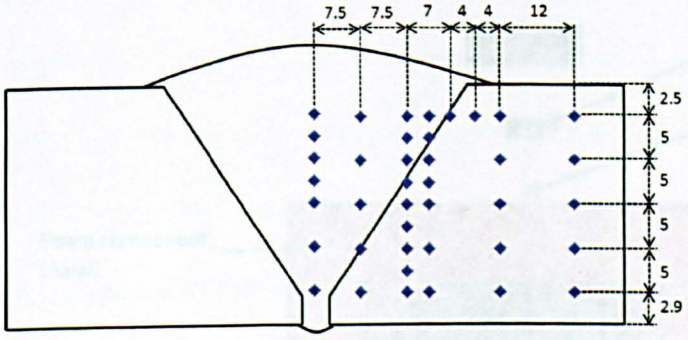

Figure 4-4: Array of nominal measurement points with respect to the welded joint.

At this stage, the pipe can be positioned and secured onto the sample table. A laser touch probe (located inside the experimental hutch) is then used to find the coordinates of the fiducial points by taking a minimum of 6 random measurements of their surfaces. Using these coordinates and the current position of the sample table (x, y, z, and ω) as input in

to SScanSS, the program then calculates the orientations and translations of the sample table that are necessary to measure every strain component at each measurement point (with an accuracy of ±100 μm). The alignment was verified by selecting one of the fiducial points as a measurement point and viewing its current position using an optical theodolite, aligned with the neutron beam. Furthermore, the software also determines if all measurement points are accessible, and estimates count times and path lengths. A script is automatically generated at the end of the simulation, essentially containing the coordinates (x, y, z, and ω) of the sample table for each measurement point and strain component. An example of the output from a SScanSS simulation for the measurement of the radial and axial components of strain is shown in Figure 4-5. It should be noted that for measurements in the hoop direction, the pipe needs to be manually repositioned (upright) and the laser touch probe measurements and SScanSS simulation repeated. For smaller samples (up to 20 kg in weight), ENGIN-X also has a high capacity robot (Cybaman Manipulator), which can be used in conjunction with SScanSS to automatically orient a sample so that any strain component can be measured in one set-up.

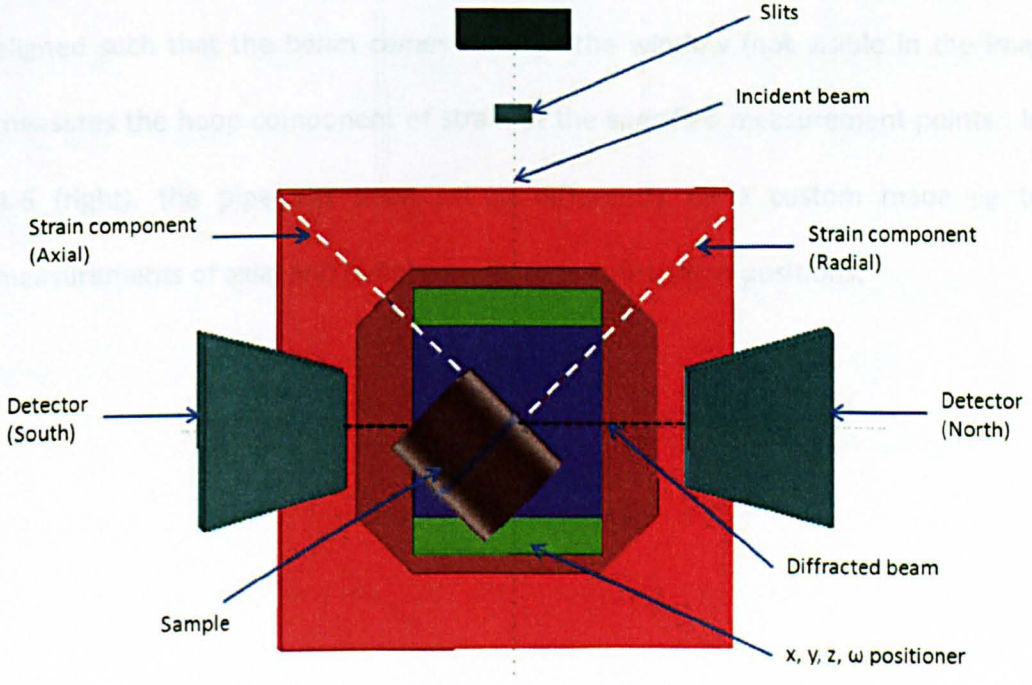

Figure 4-5: SScanSS simulation showing measurement of radial (North detector) and axial (South detector) components of strain.

4.2.3 Lattice parameter measurements

Measurements of the lattice parameter were made in three orientations: namely the hoop, axial and radial orientations. The nominal gauge volume for the measurements of the hoop orientation was 3 × 3 × 3 mm^3 but for the axial and radial orientations, this was relaxed in the direction that was tangential to the pipe, so that the gauge volume was 3 x 3 x 4.5 mm^3. It was thought that, over distances of 3 to 5 mm, the lattice parameter could be assumed to remain constant when moving in a direction tangential to a pipe with a diameter of 324 mm. Thus, the gauge volume was increased in the belief that there would not be an effect on the measured lattice parameter but, at the same time, the count times for measurements would be reduced. In the present work, data acquisition times were chosen to ensure that the diffraction peaks were clearly defined and that the fitting uncertainties did not exceed 100 microstrain.

Figure 4-6 shows the welded pipe on the sample table. In Figure 4-6 (left), the pipe is aligned such that the beam comes through the window (not visible in the image) and measures the hoop component of strain at the specified measurement points. In Figure 4-6 (right), the pipe has been set-up differently on a custom made jig to make measurements of axial and radial components at the same positions.

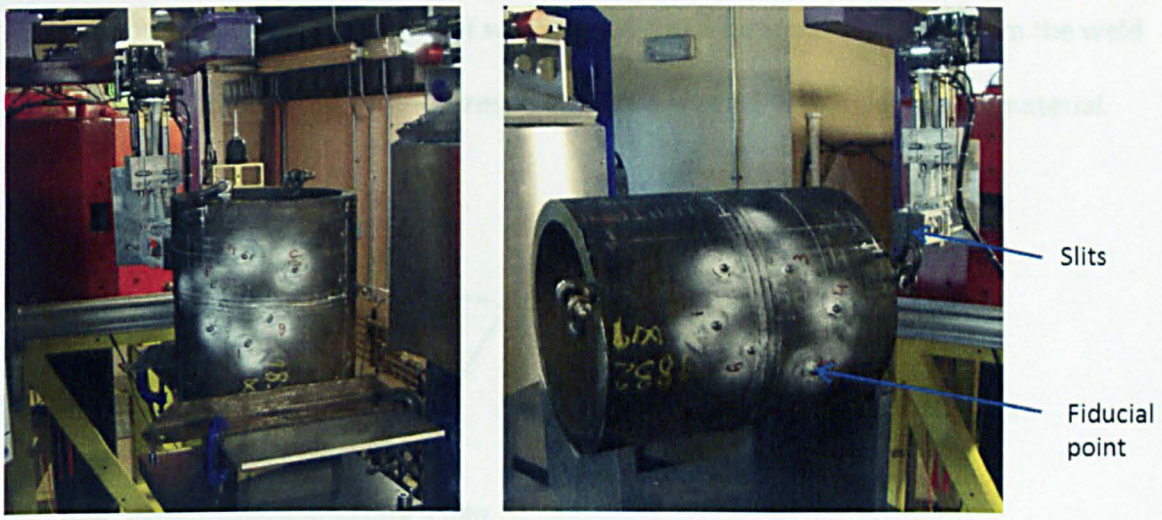

Figure 4-6: Pipe on sample stage measuring hoop (left) and axial components (right). An example of a fiducial point and the position of the slits are also highlighted.

4.2.4 Stress-free lattice parameter

In order to determine strains at each position, it is necessary to have values for the strain free lattice parameter, a0. Since welds introduce changes in composition [11] and gradients in both microstructure and strain history [12], large changes in lattice spacing can result and thus it is necessary to measure the strain-free lattice spacing at different positions. In this case, values across the weld metal, HAZ and parent metal regions were required. A comb specimen was cut from the welded joint (using the plug of material that was removed to create the slot) by electro-discharge machining (Figure 4-7). The dimensions of the comb teeth were 33 x 5 x 5 mm^3 to allow a 3 x 3 x 3 mm^3 gauge volume to be fully immersed within the sample. A partially-filled gauge volume may lead to the generation of errors or pseudo-strains as a result of an apparent shift in the position of the diffraction peak [8]. The long axis of the teeth was aligned parallel to the axial direction of the pipe so that measurements could be made at varying distances from the weld centreline by moving the position of the gauge volume along one of the comb teeth.

Furthermore, a pin, 5mm in diameter was extracted at a distance of 40 mm from the weld centreline to obtain values for the stress-free lattice spacing within the parent material.

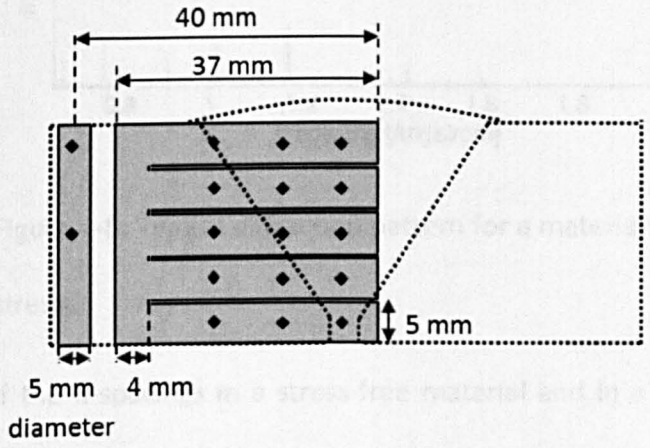

Figure 4-7: Schematic diagram showing the location and orientation of the stress-free reference comb and pin specimens (both shaded) with respect to the welded joint (dotted outline). The locations at which stress-free lattice parameter measurements were made are shown (black diamonds).

4.2.5 Data analysis

If the detected neutron count is plotted as a function of time, it will exhibit a series of peaks corresponding to the different d_{hkl} lattice planes in the material, as shown in Figure 4-8. These can be used individually (single peak fitting) or, as is more common, in combination (Rietveld or Pawley-Rietveld approach [13]) for determining a precise value of d. In the present work, the data analysis was performed using in-house analysis software EX-SBA (written in Open GENIE) which uses the computer package GSAS [14] for automatic Rietveld refinement of the diffraction spectra.

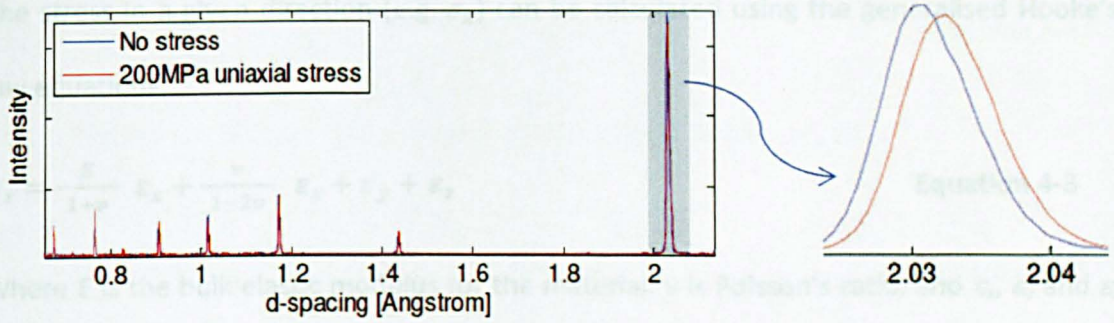

Figure 4-8: Typical diffraction pattern for a material under no stress and 200 MPa uniaxial stress.

If the d-spacings in a stress-free material and in a stressed material are measured, the change in lattice spacing can be used to calculate strain using the equation:

$$\varepsilon_{xx} = \frac{d_{xx} - d_{0xx}}{d_{0xx}} \qquad \textbf{Equation 4-2}$$

where ε_{xx} is the strain in the xx direction, d_{xx} is the measured lattice parameter and d_{0xx} is the stress-free lattice parameter. For points in the weld metal or HAZ, position-dependent values for the stress-free lattice parameter (a_0) were used, whereas a single value corresponding to the parent material was used for all other locations.

In general, because stress is a tensor, measurements are required in at least six orientations to completely determine the stress state at a point (averaged over the gauge volume). However, in many cases symmetry considerations enable assumptions to be made about the directions of the principal stresses, in which case only three orthogonal principal strain components need to be measured. It should be noted that any three measured orthogonal strain components can form the basis for calculating the corresponding three orthogonal components of stress, without any knowledge of the shear strains and shear stresses. Thus, these three orthogonal stress components can be determined from the corresponding orthogonal strains, irrespective of whether they correspond to principal directions or not [7].

The stress in a given direction (e.g. σ_x) can be calculated using the generalised Hooke's law equations:

$$\sigma_x = \frac{E}{1+v}\ \varepsilon_x + \frac{v}{1-2v}\ \varepsilon_x + \varepsilon_y + \varepsilon_z \qquad \textbf{Equation 4-3}$$

Where E is the bulk elastic modulus for the material, v is Poisson's ratio, and ε_x, ε_y and ε_z are the measured strains in three orthogonal orientations x, y and z, respectively. In determining stresses it was assumed that the material was isotropic, with a bulk Young's modulus of 218 GPa and a Poisson's ratio of 0.3 [15].

Experimental uncertainties

There are a number of possible contributions to uncertainties in stressed and un-stressed lattice parameter measurements. The most easily quantified, is the error in the fitting of the diffraction peaks, which is generally an output from the peak fitting routines and is dependent on the counting times. Other sources of experimental uncertainties may arise from thermal, grain size, and texture effects, or partially filled gauge volumes and uncertainties in the positioning of the sample. These uncertainties are less easily quantified.

The uncertainties reported in this chapter were derived using an error propagation method, of the form [16][17]:

$$\Delta z = \sqrt{\left(\frac{\delta z}{\delta x}\Delta x\right)^2 + \left(\frac{\delta z}{\delta y}\Delta y\right)^2} \qquad \textbf{Equation 4-4}$$

where z is a function of x and y and Δx and Δy are the uncertainties in x and y. The uncertainty in a strain component, for example ε_{xx} is therefore:

$$\Delta\varepsilon_{xx} = \sqrt{\left(\frac{\delta\varepsilon_{xx}}{\delta d_{xx}}\Delta d_{xx}\right)^2 + \left(\frac{\delta\varepsilon_{xx}}{\delta d_0}\Delta d_0\right)^2} \qquad \textbf{Equation 4-5}$$

which, according to Equation 4-2 may be written;

$$\Delta\varepsilon_{xx} = \frac{d_{xx}}{d_0}\sqrt{\left(\frac{\Delta d_{xx}}{d_{xx}}\right)^2 + \left(\frac{\Delta d_0}{d_0}\right)^2} \qquad \textbf{Equation 4-6}$$

The uncertainty in a stress component (e.g. σ_x) is similarly derived, i.e.

$$\Delta\sigma_{xx} = \sqrt{\left(\frac{\delta\sigma_{xx}}{\delta\varepsilon_{xx}}\Delta\varepsilon_{xx}\right)^2 + \left(\frac{\delta\sigma_{xx}}{\delta\varepsilon_{yy}}\Delta\varepsilon_{yy}\right)^2 + \left(\frac{\delta\sigma_{xx}}{\delta\varepsilon_{zz}}\Delta\varepsilon_{zz}\right)^2} \qquad \textbf{Equation 4-7}$$

which, according to Equation 4-3 gives;

$$\Delta\sigma_{xx} = \frac{E}{1+V\ 1-2V}\sqrt{1-V\ ^2\Delta^2\varepsilon_{xx} + v^2\Delta^2\varepsilon_{yy} + v^2\Delta^2\varepsilon_{zz}} \qquad \textbf{Equation 4-8}$$

Equation 4-8 therefore relates the uncertainty in the calculated strains and stresses to the uncertainty in the measured stressed and un-stressed d-spacings, Δd and Δd_0 respectively.

4.2.6 Satoh tests

Satoh tests [18], [19], [20] were carried out on the P91 base material to illustrate the effects that solid-state phase transformations can have on the development of residual stresses upon cooling under the influence of restraint. During a test, an unconstrained round bar test specimen 6 mm in diameter and 58.5 mm long was first heated to 950°C at a rate of 10°C s^{-1} in a Gleeble 3500 thermo-mechanical simulator, as shown in Figure 4-9. After holding at this temperature for 10 s, the sample was allowed to cool at the same rate with its ends rigidly restrained whilst the stress was monitored. A further test was performed using a peak temperature of 780°C. These peak temperatures were chosen because they are slightly above and slightly below the Ac_3 and Ac_1 temperatures respectively [15]. As such, they simulate the response of material that, on the one hand, is within the fine-grained HAZ of a weld (which undergoes full austenitisation upon heating) and, on the other, is immediately outside the region of the HAZ that undergoes any austenitisation on heating.

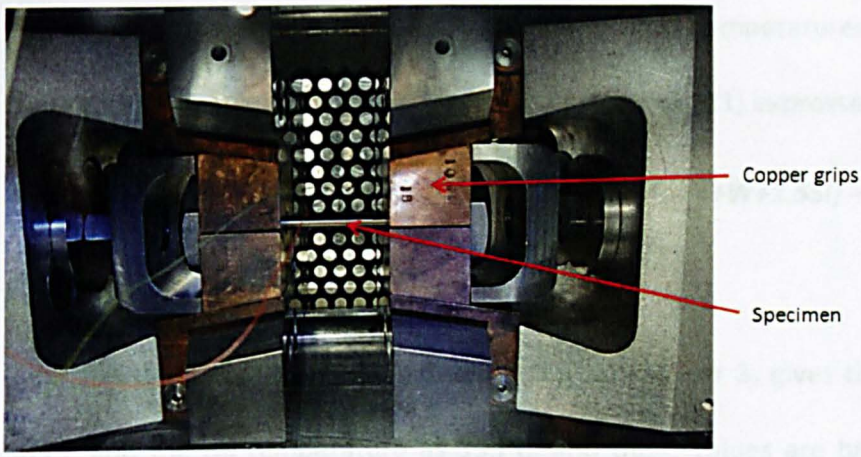

Figure 4-9: Satoh test showing round bar test specimen in a Gleeble 3500 thermo-mechanical simulator.

4.3 Results

4.3.1 Satoh tests

The results of the Satoh tests on the base metal are shown in Figure 4-10. In the case of the specimen that was heated to 780°C before restraint was applied, the stress simply increased monotonically on cooling with decreasing temperature, due to the accumulation of thermal contraction strains. The residual stress at room temperature was comparable to the room temperature yield stress (~480 MPa). On the other hand, the specimen that was heated to 950°C (i.e. above the Ac_3 temperature) behaved differently. At 950°C, the specimen would have been completely austenitised and, upon cooling, the stress increased until a temperature of approximately 500°C was reached. At this temperature, a phase transformation commenced and the transformation strain associated with the decomposition of austenite (fcc) to martensite (bct) will have overwhelmed the thermal contraction strains, resulting in a decrease in overall stress. After the transformation had exhausted, tensile stresses started to accumulate again, due to thermal contraction, until room temperature was reached.

The martensite start (M_s) and martensite finish (M_f) temperatures for P91 steel can be estimated using relationships proposed by Beres *et al.* [21] expressed as,

$$M_s = 454 - 210C + 4.2/C - 27Ni - 7.8\,Mn - 9.5(Cr+Mo+V+W+1.5Si) - 21Cu$$ **Equation 4-9**

$$M_f = (M_s - 190) +/- 10$$ **Equation 4-10**

Substituting the values given in Table 3-1 from chapter 3, gives the M_s temperature as 385°C and the M_f temperature as 195°C, and these values are broadly consistent with data provided by Vallourec & Mannesmann (M_s = 400 and M_f >150°C) [15]. However, from the Satoh test results, it appears that the transformation started at ~500°C and exhausted at ~350°C. This discrepancy may be attributed in part to the fact that the transformation start temperature is likely to increase in the presence of stress [12]. However, it is also important to appreciate that the specimens were heated using resistance heating, and this will have resulted in a temperature gradient along each specimen. The thermocouples that were attached to each specimen were monitoring the temperature at the centre of the specimen, which will have been the position at which the temperature was highest. Thus, upon cooling, material located some distance from the thermocouples may have started transforming well before material at the centre of the specimen. This is consistent with the data in Figure 4-10 which shows a change in slope during the transformation with a more dramatic effect, i.e. a steeper reduction in stress, at a temperature closer to 400°C.

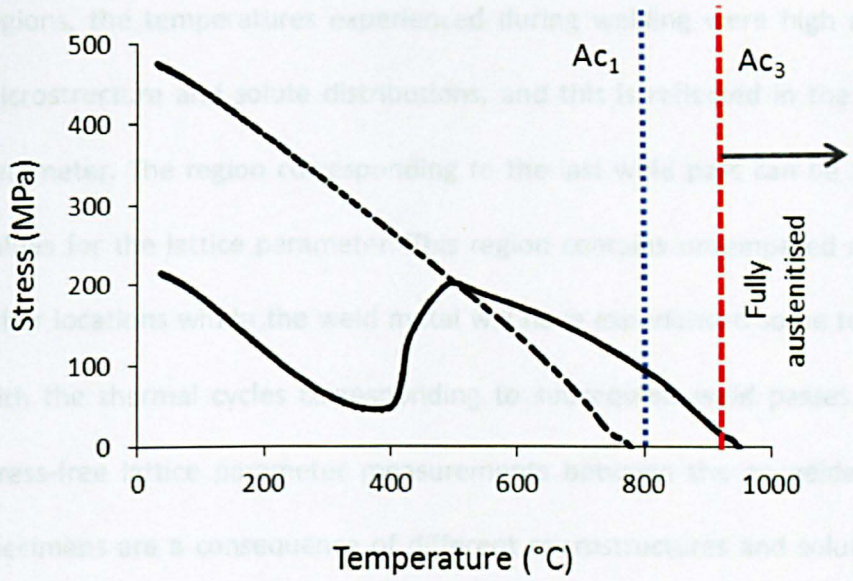

Figure 4-10: Accumulation of stress in restrained P91 test coupons upon cooling from different initial temperatures - 780°C (dotted) and 950°C (solid). Note the reduction in stress that occurs at approximately 450°C on cooling for the coupon that was heated above the austenitisation temperature. The Ac_1 and Ac_3 temperatures are also shown.

The most significant observation arising from the Satoh test results is that a coupon of P91 steel that was heated to 950°C was left with a lower residual stress at room temperature than a coupon heated to 780°C, despite the fact that thermal contraction strains will have accumulated over a larger temperature range in the 950°C specimen. Indeed, the results illustrate that the strains associated with solid-state phase transformations can compensate for thermal contraction strains to a significant extent in P91 steel.

4.3.2 Stress-free lattice parameter

The stress-free lattice parameter measurements on the as-welded and PWHT comb specimens were used to create contour maps using the commercial software "MATLAB" [22] (Figure 4-11). The measurements on the pins (unaffected parent material) in both conditions are also shown on the same figure for comparison. In the weld metal and HAZ

regions, the temperatures experienced during welding were high enough to alter the microstructure and solute distributions, and this is reflected in the variations in lattice parameter. The region corresponding to the last weld pass can be seen to have higher values for the lattice parameter. This region contains untempered martensite, whereas other locations within the weld metal will have experienced some tempering associated with the thermal cycles corresponding to subsequent weld passes. The differences in stress-free lattice parameter measurements between the as-welded and PWHT comb specimens are a consequence of different microstructures and solute distributions. The stress-free lattice parameter measurements in both pins (parent material) were very similar.

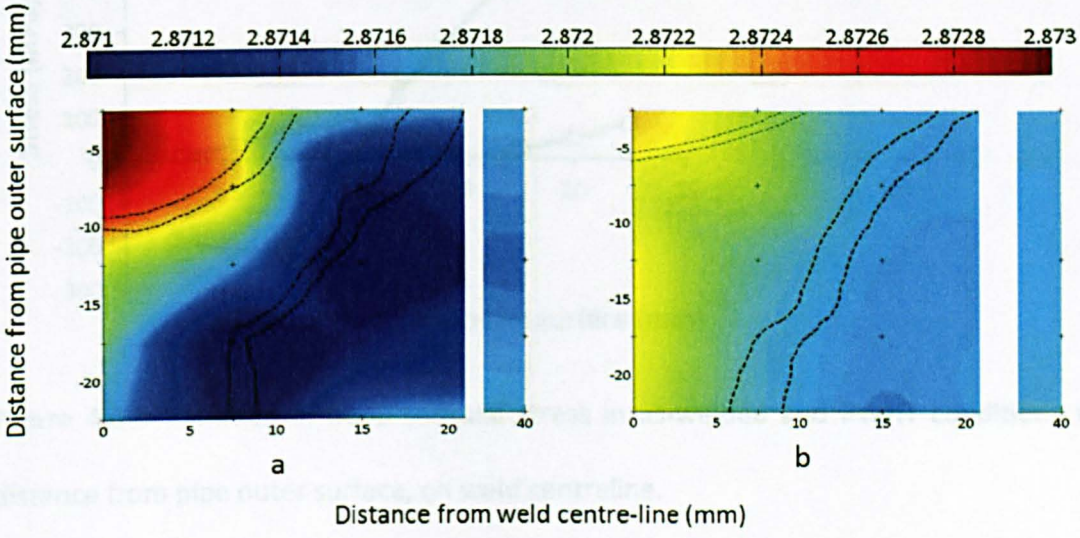

Figure 4-11: Variation of d-spacing in stress-free comb and pin reference samples from (a) the as-welded pipe (see Figure 4-7) and (b) the post-weld heat treated pipe. Measurement locations are marked on the diagrams (black crosses); along with the location of the last weld pass and HAZ as determined by metallography (dotted lines).

4.3.3 *Residual stress distributions*

Figure 4-12 shows the hoop residual stresses acting on the weld centre-line, as a function of distance from the outer surface of the pipe, for the pipes in the as-welded and PWHT conditions. Throughout this work, the position of "the outer surface of the pipe" refers to the nominal radial position that would have intersected the outer surface of the pipe, on the weld centre-line, had a joint preparation not been machined beforehand, and it excludes any deviations in the position of the outer surface of the pipe resulting from the deposition of weld beads.

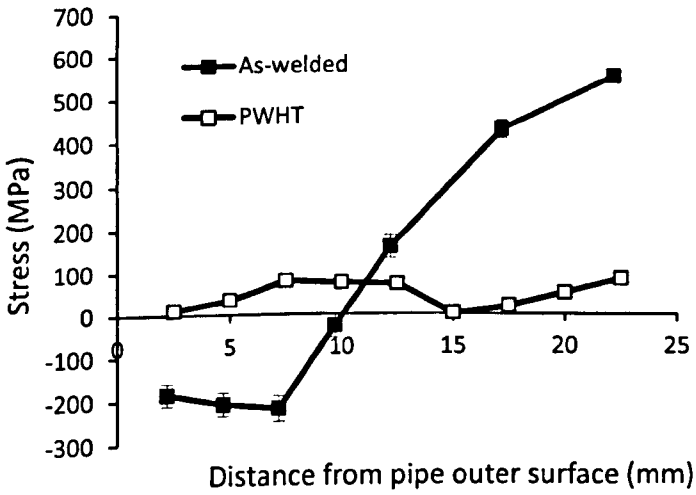

Figure 4-12: Variation in hoop residual stress in as-welded and PWHT conditions with distance from pipe outer surface, on weld centreline.

In both welds the last submerged arc welding (SAW) weld pass was approximately aligned with the weld centre-line (see chapter 3). In the as-welded pipe, the hoop stresses towards the outer surface on the weld centre-line are compressive, but they become progressively more tensile when moving through the weld metal towards the inner surface. The peak tensile stresses exceed the yield stress of the parent material (~480 MPa), reaching a magnitude of ~600 ± 15 MPa near the weld root. A von Mises equivalent stress of approximately 470 MPa was found to exist in the vicinity of the weld root, which

would suggest that the measured stresses are realistic. Furthermore, it can be appreciated from the hardness maps presented in chapter 3 that the yield stress (YS) of the weld metal in the as-welded condition is significantly higher than that of unaffected parent material. Figure 4-12 clearly shows that, after PWHT, the residual stresses are substantially relaxed and the maximum stress is only about 100 ± 10 MPa. In general, the uncertainties in the estimated stresses in the as-welded condition were no greater than ± 30 MPa, while for the PWHT stresses they did not exceed ± 20 MPa maximum, to the point that the error bars do not extend beyond the data point markers.

The hoop stresses acting on a line 15 mm from the weld centre-line are shown in Figure 4-13. The stresses along this measurement line were all tensile, with peak stresses in the vicinity of ~600 ± 15 MPa near the mid-thickness in a position corresponding approximately to the HAZ. Again, the stresses after PWHT show that significant relaxation took place, since the maximum tensile stress after PWHT was in the vicinity of ~100 ± 15 MPa.

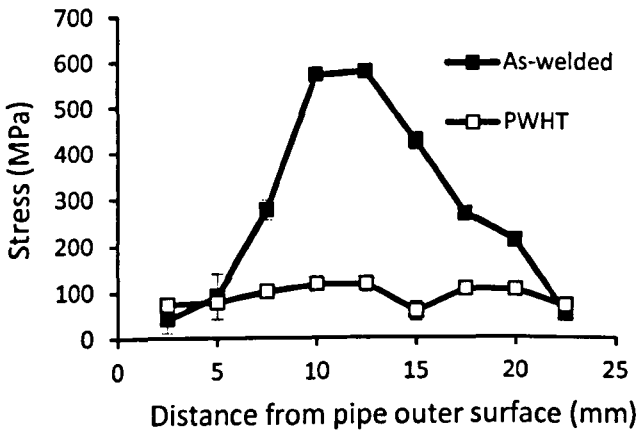

Figure 4-13: Variation in hoop residual stress in as-welded and PWHT condition with distance from pipe outer surface 15 mm from weld centre-line.

In the axial orientation on the same measurement line (Figure 4-14), the stresses are slightly compressive (~ -25 ± 25 MPa) in the weld near the outer surface of the pipe. The

highest tensile stresses again correspond to locations in the vicinity of the HAZ, i.e. between 10 and 15 mm from the outer surface of the pipe. Another important feature of this particular plot is that the stresses appear to balance approximately across the thickness of the pipe. (Note that stresses have not been extrapolated to the pipe surfaces). This is reassuring since, assuming a steady-state welding condition was achieved; one would expect the axial stresses to balance through the wall thickness.

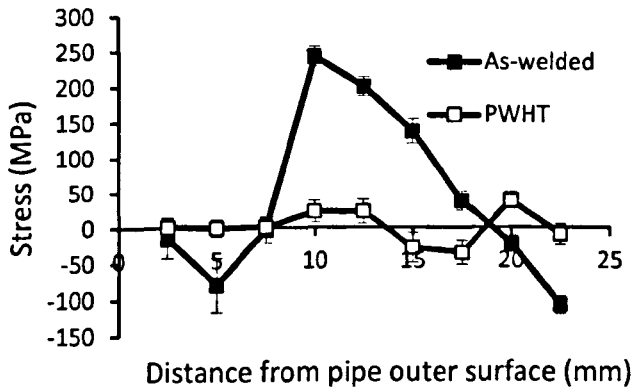

Figure 4-14: Variation in axial residual stress in as-welded and PWHT condition with distance from pipe outer surface 15 mm from weld centre-line.

The measured stresses were used to create contour maps (Figure 4-15) in order to obtain an overall impression of the residual stress distributions. While contour maps make for a convenient presentation of the data, care must be taken to avoid drawing inferences based on extrapolated data. The black cross markers on the contour plots indicate the measurement positions, while the dotted lines show the location of the last weld pass and HAZ regions, as determined from the macrographs that were obtained from each pipe sample. Note that it was not feasible to use the same colour scale for all the contour maps due to the significant differences in the stress magnitudes. The calculated hoop, axial and radial stress components for the as-welded and PWHT pipes are included in Appendix 1 respectively.

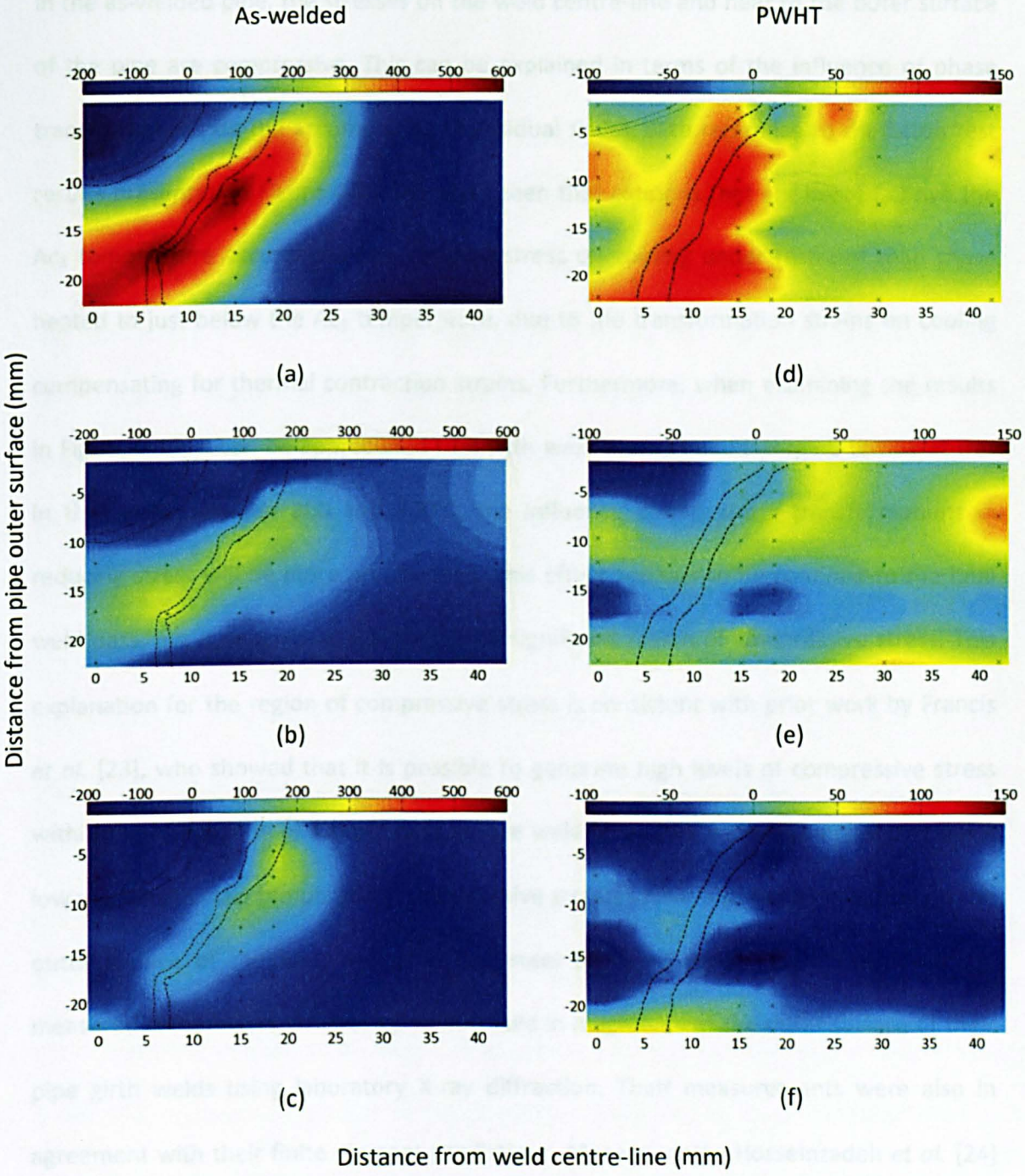

Figure 4-15: Contour maps for hoop (a, d), axial (b, e) and radial (c, f) components of residual stress, as measured by neutron diffraction in the as-welded (left) and PWHT (right) conditions. Measurement locations are marked on the diagram (black crosses, along with the location of the last weld pass and HAZ as determined by metallography (dotted lines).

In the as-welded pipe, the stresses on the weld centre-line and near to the outer surface of the pipe are compressive. This can be explained in terms of the influence of phase transformations on the accumulation of residual stress, with reference to the Satoh test results presented in Figure 4-10. We have seen that coupons that are heated above the Ac_3 temperature accumulate less residual stress on cooling under restraint than those heated to just below the Ac_1 temperature, due to the transformation strains on cooling compensating for thermal contraction strains. Furthermore, when examining the results in Figure 4-10, it can be appreciated that with weld preheat and interpass temperatures in the range between 200 and 300°C, the influence of the phase transformations in reducing stress will be more pronounced. This effect appears to be confined to the final weld pass, but it nevertheless introduces a significant region of compressive stress. This explanation for the region of compressive stress is consistent with prior work by Francis *et al.* [23], who showed that it is possible to generate high levels of compressive stress within the fusion zone of a single pass groove weld by using a weld filler metal that has a low martensite start temperature. Compressive stresses have also been measured on the outer surface of multipass welds in P91 steel by Yaghi *et al.* [25] . These workers measured compressive stresses up to 400 MPa in magnitude at the outer surface of their pipe girth welds using laboratory X-ray diffraction. Their measurements were also in agreement with their finite element predictions. More recently, Hosseinzadeh *et al.* [24] have measured compressive stresses of the order of -217 MPa on an almost identical P91 welded pipe, which correlates well with the -220 MPa measured in the present work.

Moving along the weld centre-line, towards the weld root, the stresses become progressively more tensile. This may be a response to the successive introduction of compressive misfit strains near to the outer surface of the pipe during the final weld passes, but there is also a requirement for the residual stresses to balance over the plane

that is shown. Interestingly, the overall pattern for the axial and normal stresses appears to be similar, despite the magnitudes for these components of stress being lower.

The highest tensile stresses in each orientation appear to reside in regions that coincide with the outer boundary of the HAZ, and the weld root region. The hoop orientation gives rise to the highest tensile stresses overall, with values in the vicinity of 600 MPa (120% of the yield strength of the PM) being measured. It was shown that, in Satoh tests on P91 test coupons, residual stresses comparable to the yield stress will develop when the coupon is heated to a temperature of 780°C, since significant thermal contraction strains will develop and there will be no compensation associated with solid-state phase transformations during cooling. This will be the case immediately outside the HAZ boundary. One might expect, therefore, that tensile residual stresses of near-yield magnitude will develop. The stresses appear to be higher than the yield stress of the parent material. This is feasible in situations where there is significant restraint and where hydrostatic stresses develop. Another contributing factor might be an increase in the local yield stress, either through transformation hardening within the HAZ or through cyclic strain hardening immediately outside the HAZ boundary.

When assessing residual stress data, it is important to check that the stresses acting in a direction that is normal to a free surface are zero at that surface. On the contour plots in Figure 4-15c and Figure 4-15f, it is clear that the radial stresses are generally very close to zero near the free surfaces. Small stress magnitudes can be explained by the fact that the nearest measurement positions are located at a distance of ~2.5 mm from the free surfaces. In the weld itself, this distance was closer to 4 mm, since there was a surplus of filler material, which led to a cambered reinforcement profile at the outer surface. This might explain why higher compressive stresses are shown in this region in the normal orientation.

The contour maps for the PWHT stresses reveal that significant stress relaxation has taken place. Nevertheless, some features of the as-welded residual stresses persist. In the hoop direction, the highest tensile stresses are ~120± 20 MPa which is roughly 24% of the YS of the PM and they occur just outside the HAZ. Indeed, the stresses in the HAZ are still generally in the order of 100 ± 20 MPa (20 % of the PM YS). Interestingly, these stresses are considerably higher than those recently presented by Yaghi *et al.* [25] who, for a 3 hour post-weld heat treatment at 760°C, predicted that the as-welded stresses would be reduced by a factor of 40. Meanwhile, the stresses in the weld are still compressive for the last weld pass, whereas they are close to zero at other locations.

Hydrostatic and von Mises stress

Figure 4-16 and Figure 4-17 show contour maps for the hydrostatic and von Mises components of stress respectively in both the as-welded and PWHT pipes. In the as-welded pipe, compressive hydrostatic stresses manifest near the outer surface of the weld on the weld centre-line across a region corresponding to the last weld bead, while tensile hydrostatic stresses in excess of 400 MPa are present in the vicinity of the HAZ. In the PWHT pipe, the hydrostatic stresses have relaxed significantly, but tensile stresses in the range of 50 MPa still exist both at and just outside the HAZ boundary. It has previously been reported [26] that high levels of plastic deformation can facilitate nucleation of voids at grain boundaries while high hydrostatic stresses influence their growth and coalescence into microcracks [27]. While the high levels of tensile hydrostatic stress that develop in the as-welded condition are largely relieved by PWHT, the hydrostatic stresses after PWHT are still in the order of 50 MPa, which is likely to be larger than the nominal service stress in a power plant. As such, these hydrostatic stresses may be significant in terms of growth rates for creep voids.

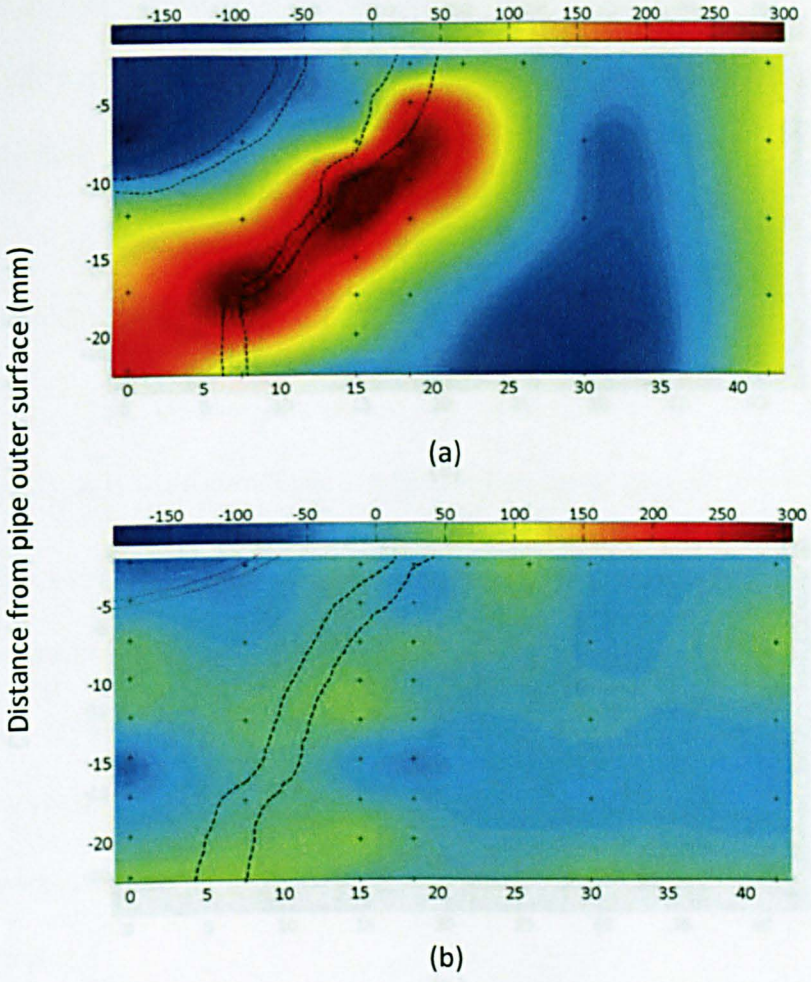

Figure 4-16: Contour maps for hydrostatic stress in the as-welded (a) and PWHT (b) conditions. Measurement locations are marked on the diagram (black crosses); along with the location of the last weld pass and HAZ as determined by metallography (dotted lines).

Figure 4-17a also shows that the locations in which the highest von Mises stresses were measured correspond to the weld root region. The maximum von Mises stresses appear to be approximately 470 MPa in tension, which is comparable to the yield stress of the as received parent material. This would suggest that the residual stresses that have been presented are plausible.

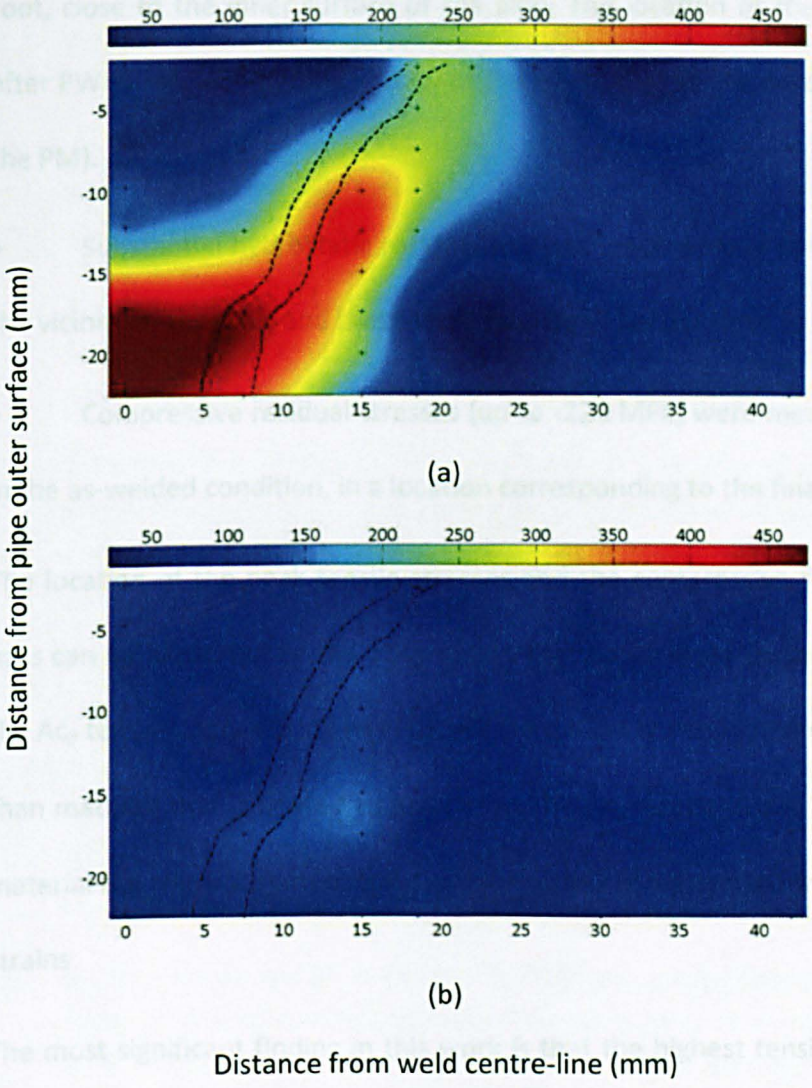

Figure 4-17: Contour maps for von Mises stress in the as-welded (a) and PWHT (b) conditions. Measurement locations are marked on the diagram (black crosses); along with the location of the last weld pass and HAZ as determined by metallography (dotted lines).

4.4 Conclusions

The residual stresses in a pipe girth weld in P91 steel have been measured in both the as-welded and PWHT conditions using neutron diffraction, and correlated with the different metallurgical zones across each weld. The following observations were made:

- In the as-welded condition the highest tensile residual stresses (~ 600 MPa) were found at the boundary between the HAZ and adjacent parent material, and at the weld

root, close to the inner surface of the pipe. The location of the highest tensile stresses after PWHT remained in the vicinity of the HAZ, being in the order of 120 MPa (24% YS of the PM).

- Substantial hydrostatic residual stresses (~400 MPa in tension) were generated in the vicinity of the HAZ, and these were relaxed to levels closer to 50 MPa after PWHT.

- Compressive residual stresses (up to -220 MPa) were measured in the weld metal in the as-welded condition, in a location corresponding to the final weld pass.

The location of the peak tensile stresses and the compressive stresses in the final weld pass can be explained by the observation that constrained material that is heated above the Ac_3 temperature during welding will have a lower residual stress at room temperature than material that is heated to just below the Ac_1 temperature, since in the austenitised material the transformation strain on cooling will compensate for the thermal contraction strains.

The most significant finding in this work is that the highest tensile residual stresses (and significant hydrostatic stresses) coincided with the HAZ boundary and the microstructural region that is prone to Type IV cracking in these welds, in both as-welded and PWHT conditions. Further work, especially with regard to the influence of residual stress on creep performance, will be required to establish whether tensile residual stresses are contributing to premature failure in welds through Type IV cracking.

4.5 References

[1] M. Turski, P. J. Bouchard, A. Steuwer, and P. J. Withers, "Residual stress driven creep cracking in AISI Type 316 stainless steel," Acta Materialia, vol. 56, no. 14, pp. 3598–3612, Aug. 2008.

[2] P. J. Bouchard, P. J. Withers, S. a. McDonald, and R. K. Heenan, "Quantification of creep cavitation damage around a crack in a stainless steel pressure vessel," Acta Materialia, vol. 52, no. 1, pp. 23–34, Jan. 2004.

[3] J. A. Francis, H. K. D. H. Bhadeshia, and P. J. Withers, "Welding residual stresses in ferritic power plant steels," Materials Science and Technology, vol. 23, no. 9, pp. 1009–1020, Sep. 2007.

[4] J. A. Francis, W. Mazur, and H. K. D. H. Bhadeshia, "Review Type IV cracking in ferritic power plant steels," Materials Science and Technology, vol. 22, no. 12, pp. 1387–1395, Dec. 2006.

[5] S. Paddea, J. A. Francis, A. M. Paradowska, P. J. Bouchard, and I. A. Shibli, "Residual stress distributions in a P91 steel-pipe girth weld before and after post weld heat treatment," Materials Science and Engineering: A, vol. 534, no. 0, pp. 663–672, Feb. 2012.

[6] J. R. Santisteban, M. R. Daymond, J. A. James, and L. Edwards, "ENGIN-X: a third-generation neutron strain scanner," Journal of Applied Crystallography, vol. 39, no. 6, pp. 812–825, Nov. 2006.

[7] M. T. Hutchings, P. J. Withers, T. M. Holden, and T. Lorentzen, Introduction to the characterization of residual stress by neutron diffraction. Florida, USA: Taylor & Francis, 2005.

[8] M. W. Johnson and M. R. Daymond, "Neutron pulsed source instrumentation," in in Analysis of residual stress by diffraction using neutron and synchrotron radiation, M. E. Fitzpatrick and A. Lodini, Eds. London: Taylor & Francis, 2003, pp. 146–169.

[9] J. . James, J. R. Santisteban, L. Edwards, and M. R. Daymond, "A virtual laboratory for neutron and synchrotron strain scanning," Physica B: Condensed Matter, vol. 350, no. 1–3, pp. E743–E746, Jul. 2004.

[10] P. J. Bouchard, D. George, J. R. Santisteban, G. Bruno, M. Dutta, L. Edwards, E. Kingston, and D. J. Smith, "Measurement of the residual stresses in a stainless steel pipe girth weld containing long and short repairs," International Journal of Pressure Vessels and Piping, vol. 82, no. 4, pp. 299–310, Apr. 2005.

[11] P. J. Withers, M. Preuss, A. Steuwer, and J. W. L. Pang, "Methods for obtaining the strain-free lattice parameter when using diffraction to determine residual stress," Journal of Applied Crystallography, vol. 40, no. 5, pp. 891–904, Sep. 2007.

[12] J. A. Francis, M. Turski, and P. J. Withers, "Measured residual stress distributions for low and high heat input single weld beads deposited on to SA508 steel," Materials Science and Technology, vol. 25, no. 3, pp. 325–334, Mar. 2009.

[13] M. R. Daymond, M. a. M. Bourke, R. B. Von Dreele, B. Clausen, and T. Lorentzen, "Use of Rietveld refinement for elastic macrostrain determination and for

evaluation of plastic strain history from diffraction spectra," Journal of Applied Physics, vol. 82, no. 4, p. 1554, 1997.

[14] A. C. Larson and R. B. V Dreele, "General Structure Analysis System (GSAS). Los Alamos National Laboratory Report LAUR," 2000.

[15] K. Haarmann, J. C. Vaillant, B. Vandenberghe, W. Bendick, and A. Arbab, The T91/P91 book, 2nd ed. Vallourec & Mannesmann Tubes, 2002.

[16] J. R. Taylor, An introduction to error analysis. Oxford: Oxford University Press, 1982.

[17] J. A. James, "Measurement of Residual Stress in a Welded CT Specimen by Neutron Diffraction. OU/MatsEng/001," Milton Keynes, 2009.

[18] K. Satoh, "Transient Thermal Stresses of Weld Heat-Affected Zone by Both-Ends-Fixed Bar Analogy," Transactions of the Japan Welding Society, vol. 3, no. 1, pp. 125–134, 1972.

[19] K. Satoh, "Thermal Stresses Developed in High-Strength Steels Subjected to Thermal Cycles Simulating Weld Heat-Affected Zone," Transactions of the Japan Welding Society, vol. 3, no. 1, pp. 135–142, 1972.

[20] A. A. Shirzadi and H. K. D. H. Bhadeshia, "Accumulation of stress in constrained assemblies: novel Satoh test configuration," Science and Technology of Welding and Joining, vol. 15, no. 6, pp. 497–499, Aug. 2010.

[21] L. Beres, A. Balogh, and W. Irmer, "Welding of martensitic creep resistant steels," Welding Journal, vol. supplement, 2001.

[22] The Mathworks Inc., "MATLAB version 7.10.0.499 (R2010a)," Natick, Massachusetts, 2010.

[23] J. A. Francis, H. J. Stone, S. Kundu, R. B. Rogge, H. K. D. H. Bhadeshia, P. J. Withers, and L. Karlsson, "The Effects of Filler Metal Transformation Temperature on Residual Stresses in a High Strength Steel Weld," Transactions of the ASME, Journal of Pressure Vessels Technology, vol. 131, no. 4, pp. 1–21, 2009.

[24] F. Hosseinzadeh and P. J. Bouchard, "Mapping Multiple Components of the Residual Stress Tensor in a Large P91 Steel Pipe Girth Weld Using a Single Contour Cut," Experimental Mechanics, vol. 53, no. 2, pp. 171–181, May 2012.

[25] A. H. Yaghi, T. H. Hyde, A. A. Becker, W. Sun, G. Hilson, S. Simandjuntak, P. E. J. Flewitt, M. J. Pavier, and D. J. Smith, "A Comparison Between Measured and Modeled Residual Stresses in a Circumferentially Butt-Welded P91 Steel Pipe," Journal of Pressure Vessel Technology, vol. 132, no. 1, pp. 1–10, 2010.

[26] A. C. F. Cocks and M. F. Ashby, "ON CREEP FRACTURE BY VOID GROWTH," Progress in Materials Science, vol. 27, pp. 189–244, 1982.

[27] H. Riedel, "Cavity nucleation at particles on sliding grain boundaries. A shear crack model for grain boundary sliding in creeping polycrystals," Acta Metallurgica, vol. 32, no. 3, pp. 313–321, 1984.

Chapter 5

Creep Testing

5.1 Introduction

Creep and creep fracture properties can be measured by conducting stress rupture, constant load and constant stress creep testing, and constant strain rate tests [1]. Stress rupture testing involves applying a known tensile load to a specimen held at a fixed temperature until it fails. The only data derived from such a test is the time to failure (t_f) and strain to failure (ε_f).

If a full creep curve is required, then constant load or constant stress creep tests need to be carried out. During such tests, the changes in specimen gauge length are continuously monitored over the whole creep life. A creep test therefore provides not only the values of t_f and ε_f but also a full strain-time record at a fixed stress and temperature [1]. In a constant load creep test, the creep properties are defined in terms of the initial stress on the specimen. As creep continues, the specimen elongates and the cross-sectional area decreases, which leads to an increase in the axial stress. Different methods have been developed to compensate for this change in dimensions, so that the creep tests are carried out under constant stress conditions. When the latter is conducted, it is usually found that the onset of tertiary creep is greatly delayed [2]. In engineering applications, it is usually the load and not the stress that is maintained constant, so that a constant load creep test is more relevant, although fundamental mechanisms of creep should be studied under constant stress conditions [2].

All the creep tests in the present work were conducted in uniaxial tension under constant load at The Open University, in accordance with ASTM E139-11: Standard Test Methods for Conducting Creep, Creep-Rupture, and Stress-Rupture Tests of Metallic Materials [3]. Two further tests were conducted at the Institute for Materials Engineering, ANSTO, Australia.

Equipment details

A schematic diagram of the equipment used to conduct the creep tests is shown in Figure 5-1. The specimen is located within the uniform hot zone of a furnace controlled at the required creep temperature. The force on the specimen is applied through a loading lever arm and the ratio of the distances between the knife edges determines the amplification of the force applied. Universal couplings ensure that the load is applied axially to the specimen, thus avoiding bending stresses. When applying the load, it is essential that the lever arm remains horizontal. This is achieved by an automatic levelling mechanism which moves the pull rod up and down accordingly when the lever arm deviates from its horizontal position.

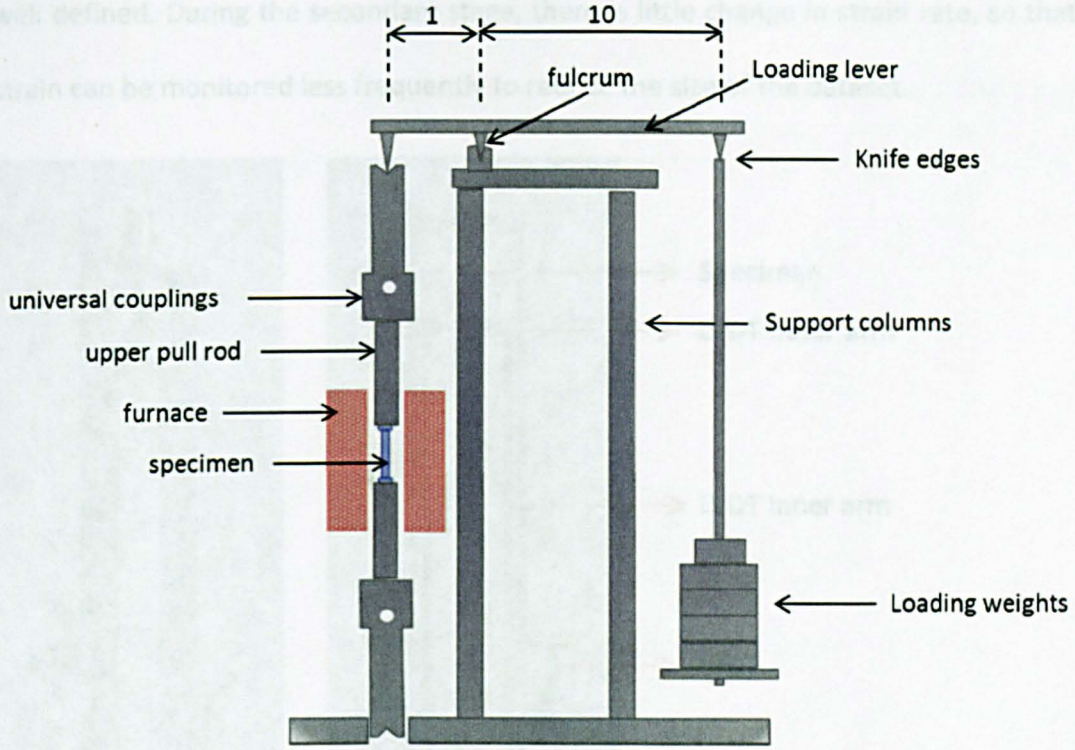

Figure 5-1: Schematic illustration of the constant load creep rig used in the present work, adapted from [1].

Strain Monitoring

For calculation of strain, the change in specimen length (extension) and the initial specimen length are required. The extension was measured using a pair of Linear Variable Differential Transformers (LVDTs), mounted in frames as shown in Figure 5-2. The frames are attached onto the specimen shoulder using screws. During creep testing, the specimen elongates and the outer arms move upwards relative to the inner arms. This upward movement which is the specimen extension is recorded by LVDTs. By having one LVDT on either side, a check can be made on alignment, as each LVDT should record the same displacement. The sampling rate is user defined and is often varied during the course of a test. For instance, it is good practice to have a high sampling rate in the initial and final stages of the test so that the primary and tertiary stages of the creep curve are

well defined. During the secondary stage, there is little change in strain rate, so that the strain can be monitored less frequently to reduce the size of the dataset.

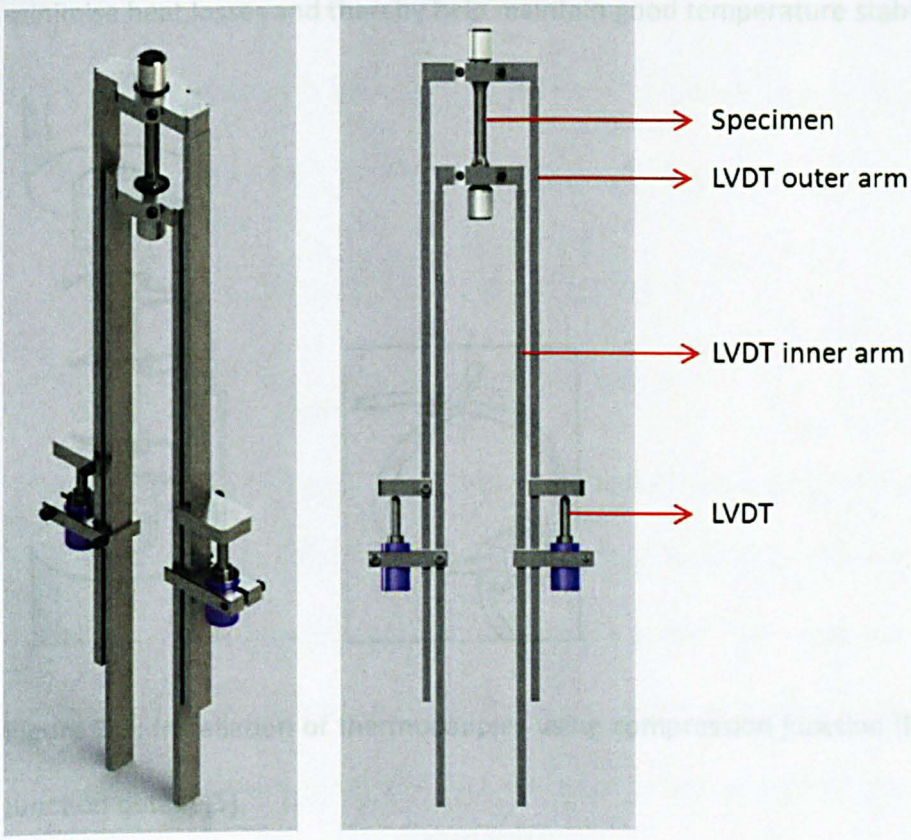

Figure 5-2: Schematic diagram showing LVDT frames, fitted onto the shoulders of a cylindrical test-piece.

Temperature Monitoring

The creep frames used in the present work are equipped with their own dedicated furnaces. These have three heating zones (top, middle, and bottom) each controlled individually using PID (Proportional Integral Derivative) controllers. Testing standards for example BS EN ISO 204:2009(E) [4] prescribe a thermal gradient less than 4°C across the gauge length and the sample temperature should be within ±4°C of the required temperature. Three N-type thermocouples were attached to the sample gauge length (top, middle and bottom) in a way similar to that depicted in Figure 5-3. This method (in accordance with ASTM E633-00 [5]) ensures that the thermocouple measuring junction

will attain thermal equilibrium with the test specimen at the attachment point. Ceramic plugs and high temperature insulation wool were used at the ends of the furnace tube to minimise heat losses and thereby help maintain good temperature stability.

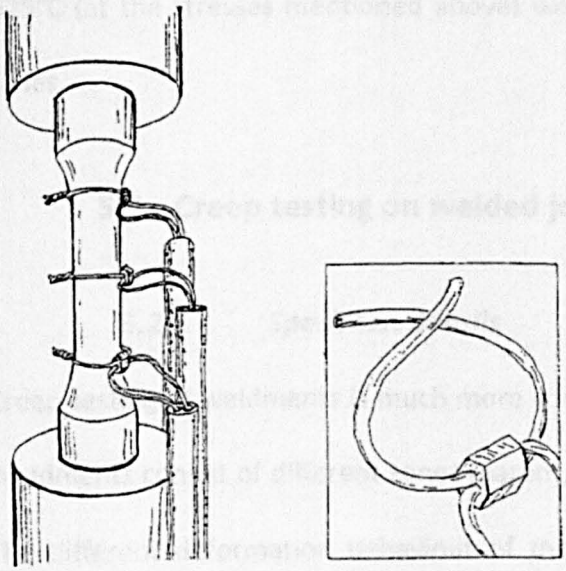

Figure 5-3: Installation of thermocouples using compression junction (Inset: compression junction detail) [5].

Selection of testing conditions

The choice of stress and temperature for the creep tests in the present work was strongly weighted towards obtaining Type IV failures in reasonable times in the cross-weld specimens. The same conditions were then used for tests involving FGHAZ simulated specimens, for comparison purposes. There is evidence in the literature, for example see Laha *et al.* [6], that when cross-weld creep tests are conducted at relatively high stresses, failures occur randomly in the parent metal, weld metal or HAZ. An analysis of published data on cross-weld creep strength of 9-12% Cr steel has revealed that the transition stress for promoting Type IV failures is 100 MPa [7], [8]. Thus, 100 MPa was chosen as the highest stress level, with 85, 75 and 65 MPa as lower stress levels in the present test programme.

As far as the temperature is concerned, 625°C was chosen, as this represents a temperature not far from service temperatures. Furthermore, the weld failure prediction diagram produced by EPRI [9] and data published by Tabuchi *et al.* [10] showed that 625°C (at the stresses mentioned above) would produce Type IV failures in reasonable times.

5.2 Creep testing on welded joints

5.2.1 Specimen details

Creep testing of weldments is much more complex than testing homogeneous materials. Weldments consist of different zones (parent, HAZ, weld) with different creep properties. The different deformation behaviour of these zones may yield stress redistributions, which may cause size and shape dependence of the test results [11]. Therefore, much attention needs to be paid to the design of a cross-weld test-piece and the sampling strategy. The recommendations produced by the European Creep Collaborative Committee (ECCC) on 'Data Acceptability Criteria and Data Generation: Creep Data for Welds' [11] were followed in this work. The main considerations were:

- The gauge length of a cross-weld test piece must contain at least one half of the joint, i.e. weld metal, heat affected zones and parent metal on one side of the joint.
- Test pieces may be sampled with their axes perpendicular to the weld axis (centre-line) or perpendicular to the fusion line. The latter is more complex to machine.
- A minimum diameter (d_0) of 8 mm is necessary to ensure cross weld specimen deformation behaviour is representative of the welded joint.

- A minimum gauge length of at least 5d0 ensures that there is no influence on stress rupture time.
- In order to cater for the possibility of failure in the parent metal, the test piece gauge length must contain a considerable length of parent metal. High deformation in the FGHAZ may cause stress redistribution in the parent metal in the direct vicinity of the HAZ.

To characterise the creep behaviour of the welded joint, test specimens containing all the different zones (i.e. weld metal, HAZ and parent metal on both sides of the weld) were machined at mid-thickness from the post-weld heat-treated pipe as illustrated in Figure 5-4. It should be noted that the sampled region of the weld was found to contain weld passes from the SAW process only.

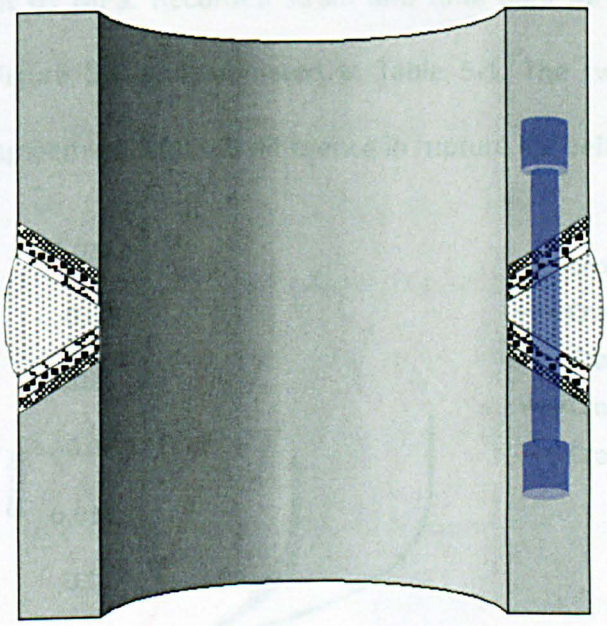

Figure 5-4: Specimen sampling location.

The dimensions of the specimen are given in Figure 5-5. Five creep tests were conducted at 625°C at 4 different stresses: 100, 85, 75 and 65 MPa with 1 repeat test at 85 MPa.

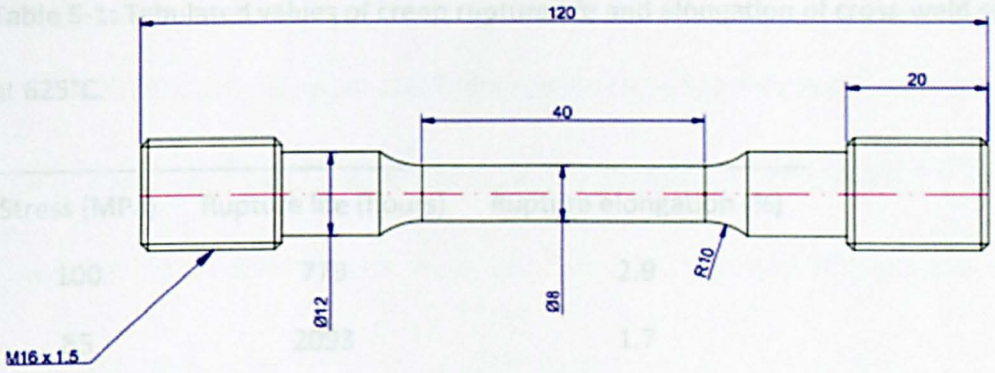

Figure 5-5: Creep specimen dimensions.

5.2.2 Results

All the cross-weld specimens ruptured in the HAZ. The precise location was investigated by optical microscopy and hardness measurements and is discussed later in this chapter. The longest test duration achieved was 7972 hours corresponding to the specimen tested at 65 MPa. Recorded strain and time data for all the stress levels are summarised in Figure 5-6 and tabulated in Table 5-1. The two tests at 85 MPa were in very good agreement with the difference in rupture life being of the order of 60 hours.

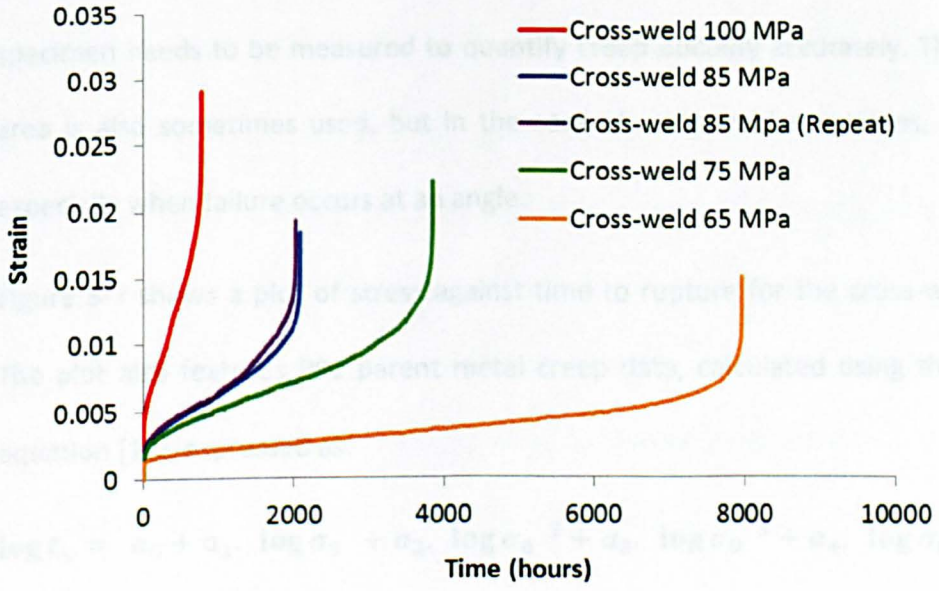

Figure 5-6: Creep curves for cross-weld tests extracted from PWHT pipe at different stresses.

Table 5-1: Tabulated values of creep rupture life and elongation of cross-weld specimens at 625°C.

Stress (MPa)	Rupture life (hours)	Rupture elongation (%)
100	779	2.9
85	2093	1.7
85 Repeat	2030	1.9
75	3864	2.1
65	7972	1.5

The strain at failure appears to be very low (of the order of 1.5 - 3%) and generally decreased with decreasing stress levels. Type IV failures are known to be low ductility failures and for P91 steel, creep ductility as low as 1% has been reported in the European Commission project 'HIDA' [12]. However, it should be noted that the strain at failure recorded by LVDTs is dependent on the sampling rate and thus, is not an accurate measure of creep ductility/rupture elongation. The gauge length of the fractured specimen needs to be measured to quantify creep ductility accurately. The reduction of area is also sometimes used, but in the case of cross-weld specimens, this is difficult, especially when failure occurs at an angle.

Figure 5-7 shows a plot of stress against time to rupture for the cross-weld specimens. The plot also features P91 parent metal creep data, calculated using the ECCC master equation [13], expressed as:

$$\log t_u = a_0 + a_1 . \log \sigma_0 + a_2 . \log \sigma_0{}^2 + a_3 . \log \sigma_0{}^3 + a_4 . \log \sigma_0{}^4 . T - T_a + 17.5 \qquad \textbf{Equation 5-1}$$

where t_u is the predicted rupture time in hrs, T is the absolute temperature in K, σ_0 is the stress in MPa, a_0, a_1, a_2, a_3, a_4 and T_a are constants with the following values:

a_0 = -0.86363, a_1 = 1.8227, a_2 = -1.4795, a_3 = 0.53004, a_4 = -0.071486 and T_a = 550

The lower and upper bounds were calculated by factoring the stresses by ± 20%.

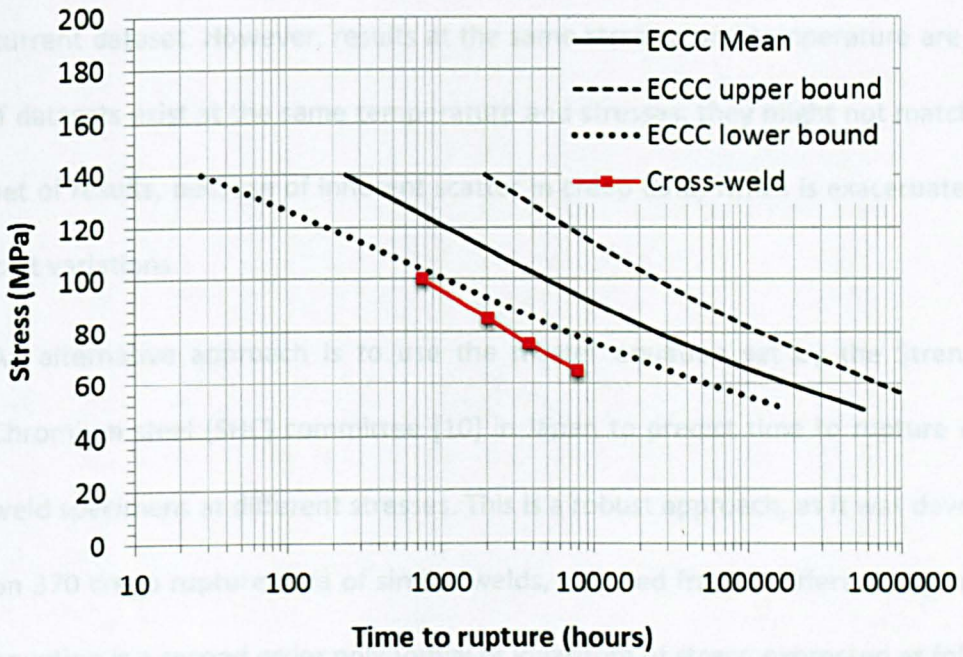

Figure 5-7: Comparison of cross-weld creep rupture strength with ECCC predicted mean values for P91 base material. The ± 20% scatter bands are also shown.

It is clear from Figure 5-7, that the creep strengths of the cross-weld specimens were lower than that of parent material and outside of the base material scatter band. This is due to premature failure of cross-weld specimens by Type IV cracking. It is noticeable that the differences in creep rupture strength became larger as the stress was reduced. However, it also appears that if tests were conducted at stresses higher than 100 MPa, the data points would lie within the parent metal scatter band or at least coincide with the lower bound properties.

The ECCC master equation predicts the time to rupture for base material only. It will be useful to compare the cross-weld creep rupture strengths in the current work with other cross-weld creep results reported in the literature. This is particularly useful in the current work because repeat tests were not conducted for all the stress levels and thus, comparison with other cross-weld creep data will be an indicator of the reliability of the current dataset. However, results at the same stresses and temperature are scarce. Even if datasets exist at the same temperature and stresses, they might not match the current set of results, because of inherent scatter in creep data, which is exacerbated by cast-to-cast variations.

An alternative approach is to use the master equation set by the Strength of High-Chromium steel (SHC) committee [10] in Japan to predict time to rupture of P91 cross-weld specimens at different stresses. This is a robust approach, as it was developed based on 370 creep rupture data of similar welds, supplied from 7 different organisations. The equation is a second order polynomial of logarithm of stress, expressed as follows [10]:

$$LMP = T + 273 \quad C + \log t_r = a_0 + a_1 \log \sigma + a_2 \log \sigma^{\,2} \qquad \textbf{Equation 5-2}$$

where LMP is the Larson-Miller parameter, T is the temperature in °C, t_r is the time to rupture in hours, σ is the stress in MPa, and C, a_0, a_1, and a_2 are the constants. The SHC committee has provided different values for these constants based on:

- Results of regression for all data on Grade 91 steel welded joints,
- Results of regression for the data that fractured in HAZ,
- Results of regression for selected data, of which conditions are close to structural components, and
- Results of regression for the data that fractured in HAZ but with conditions close to structural components.

In the present work, the values used were: C = 28.8, a_0 = 36.549, a_1 = -2255, a_2 = -880 which fall in the category 'Results of regression for the data that fractured in HAZ'. Figure 5-8 shows the comparison of the present dataset with the predicted time to rupture obtained using Equation 5-2. The ±20% scatter bands are also shown and were calculated in the same manner as for the ECCC parent metal scatter band.

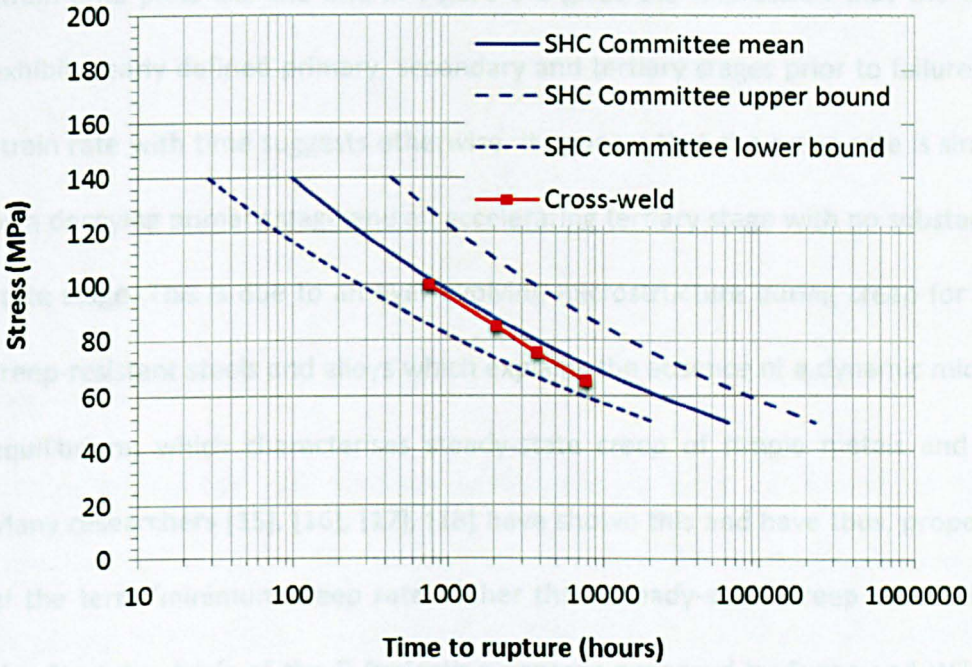

Figure 5-8: Comparison of cross-weld creep rupture strength with predicted P91 cross-weld creep rupture strength, calculated using the SHC committee equation. The ± 20% scatter bands are also shown.

Up to testing durations of 2000 hours, the present dataset is very well aligned with the predicted mean values. For the lower stresses (75 and 65 MPa), there seems to be a small deviation from the mean line, but the results are still well within the scatter band.

Creep strain rate

The creep strain rates can be estimated by drawing a tangent, at different locations of the creep curve, but this is very tedious and likely to be inaccurate for parts of the creep

curve with sharp curvature. The alternative is to use the least squares procedure described by Evans and Wilshire [1]. Least squares straight lines are passed through groups of creep strain points and the resulting gradient, gives a numerical estimate of the creep strain rate at the centre point.

Figure 5-9 shows the variations of creep strain rate (ε) with time. Although conventional strain-time plots like the one in Figure 5-6 gives the impression that the creep curves exhibit clearly defined primary, secondary and tertiary stages prior to failure, the plot of strain rate with time suggests otherwise. It appears that the creep rate is simply defined by a decaying primary stage and an accelerating tertiary stage with no substantial steady-state stage. This is due to an ever-evolving microstructure during creep for engineering creep-resistant steels and alloys which explains the absence of a dynamic microstructural equilibrium, which characterises steady-state creep of simple metals and alloys [14]. Many researchers [15], [16], [17], [18] have shown this and have thus, proposed the use of the term 'minimum creep rate' rather than 'steady-state' creep rate. These findings also form the basis of the θ Projection concept proposed by Evans and Wilshire [1]. By explicitly quantifying the decaying primary and accelerating tertiary components, accurate descriptions of the creep curve shape dependence on stress and temperature can be made, allowing extrapolation of short-term data to provide long-term property estimates [19].

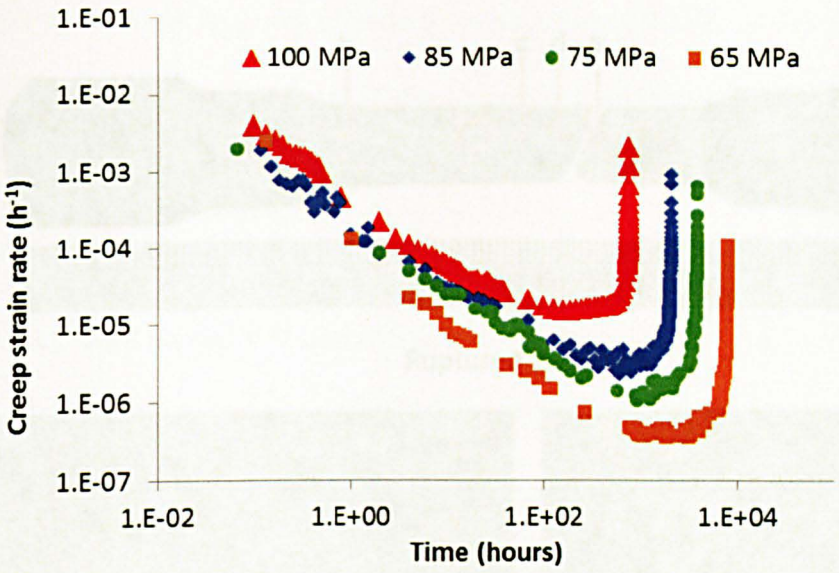

Figure 5-9: Variations of creep strain rates with time for P91 cross-weld creep tests at 625°C at different stresses.

Post-test examination

Optical microscopy and hardness measurements were conducted on the ruptured specimens to determine the exact location of failure. The crept specimens were sectioned along the specimen axis, as shown in Figure 5-10 and the surfaces were prepared following standard metallographic preparation, as described in chapter 3.

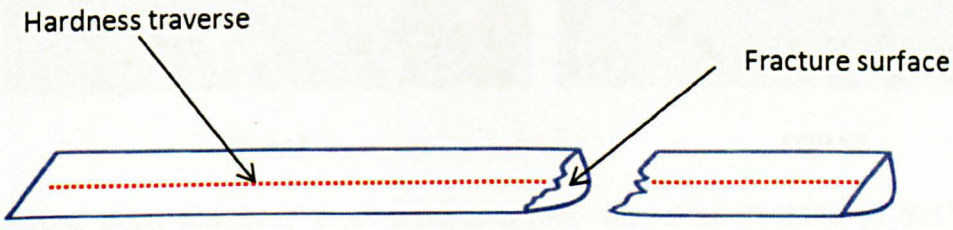

Figure 5-10: Longitudinally sectioned fractured specimen showing location where hardness measurements were taken.

A picture of one of the ruptured specimens is shown in Figure 5-11a. The letters marked b through to e correspond to locations where optical micrographs were taken and correspond to the parent metal (b), weld metal (c), CGHAZ (d) and FGHAZ (e).

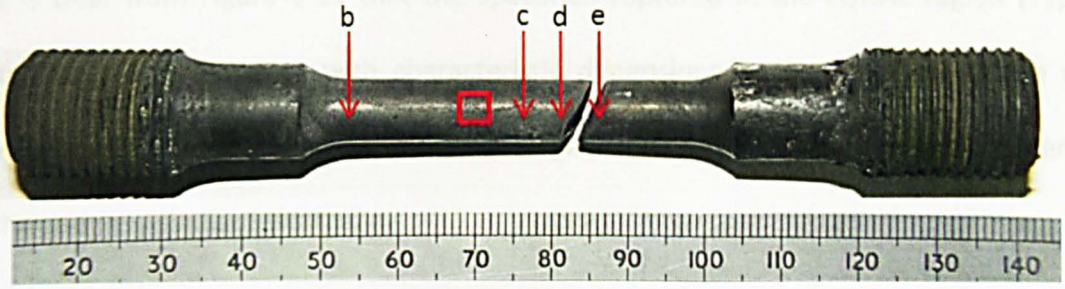

Ruptured specimen

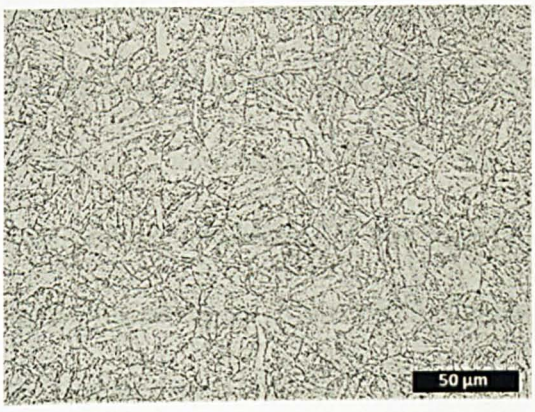

Parent metal

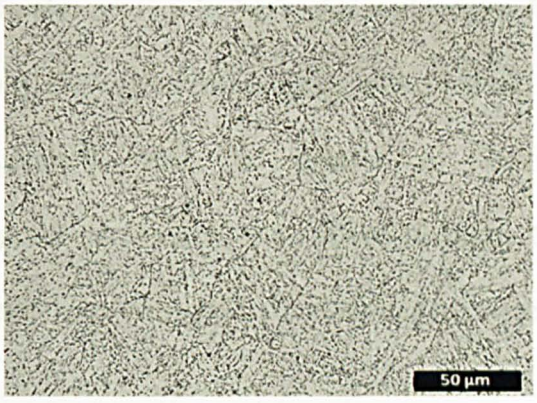

Weld metal

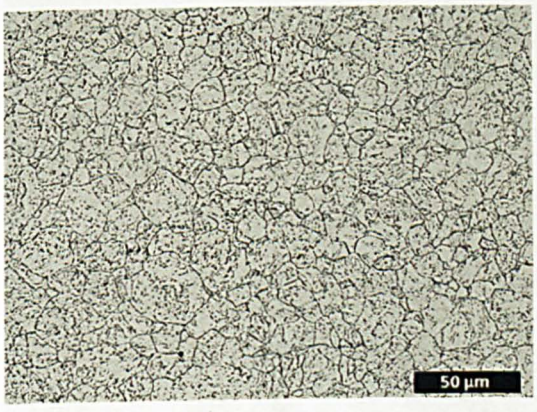

CGHAZ

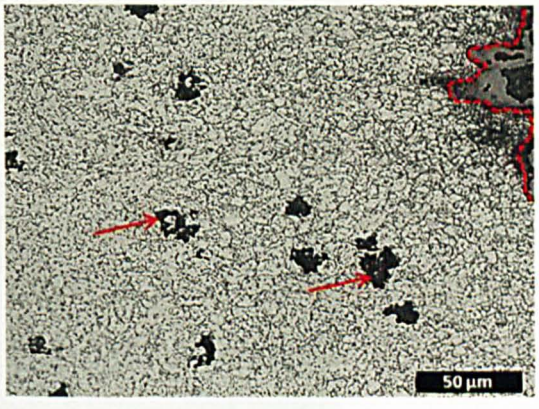

FGHAZ

Figure 5-11: Ruptured cross-weld specimen tested at 75 MPa at 625°C. The letters marked b through to e, correspond to locations where optical micrographs were captured, corresponding to the parent metal, weld metal, CGHAZ and FGHAZ near the failure location respectively. The rectangular box shows the location where the micrograph in Figure 5-12 was taken, corresponding to the 'un-failed' HAZ. Arrows in (e) highlight creep cavities and the dotted line shows the fracture location.

It is clear from Figure 5-11 that the specimen ruptured in the FGHAZ region (Type IV location). Creep cavities with characteristic dimensions in the order of 10 μm were evident in this region. All the cross-weld specimens ruptured in a similar manner and showed very similar features.

Figure 5-12 shows a lower magnification image of the adjacent 'un-failed' HAZ. It is apparent that cavities and micro-cracks were also present in this region and judging from the distance from the fusion line (1.5 - 2 mm), this region corresponds to the FGHAZ. The additional information from the 'unfailed' HAZ is related to damage initiation/accumulation. On the scale of optical microscopy, the cavities in Figure 5-12 were only observed in the mid-thickness region, which suggests that damage initiated in the mid-thickness region.

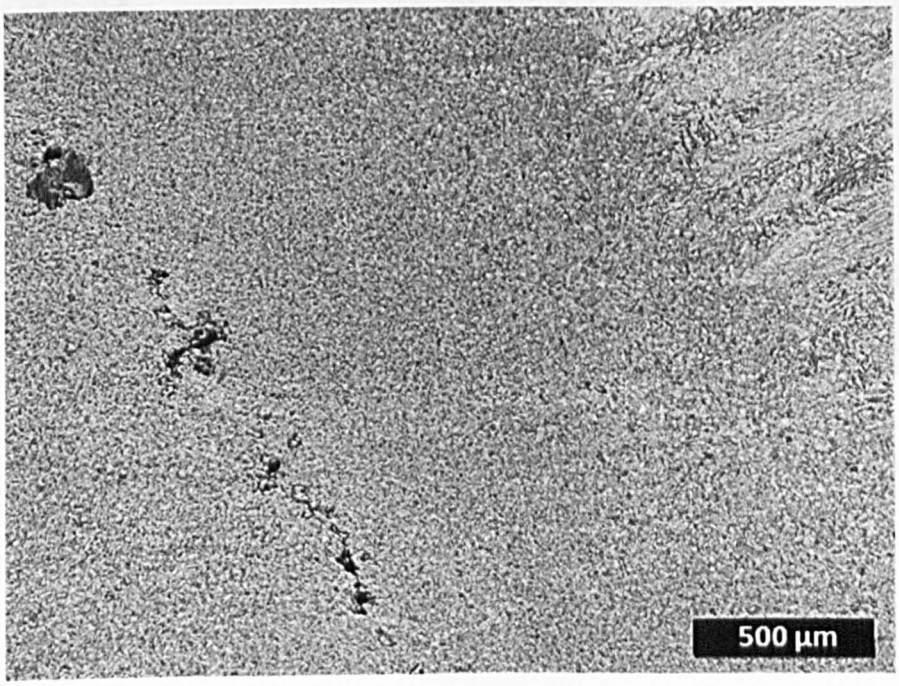

Figure 5-12: Lower magnification image of the adjacent 'un-failed' HAZ.

This is illustrated nicely in Figure 5-13, which was captured from a specimen interrupted very close to failure (>90% creep life). Eventually, in this case, the cavities have linked up to form a macro-crack which was observed at the specimen mid-thickness. Nevertheless,

it is clear that the crack 'width' was much larger in the central section indicating that a larger number of cavities would have formed in this region. The other discernible feature is that the crack path is parallel to the fusion boundary (even following the curvature associated with the fusion boundary), suggesting that creep damage was confined to only 1 region of the HAZ. Several authors [20], [21], [22], [23] have shown similar distribution of creep cavities in P91 weldments and these observations have been attributed to the stress triaxiality factor, which was shown to be higher in the centre of weldments and regions with strong curvatures in the fusion boundary.

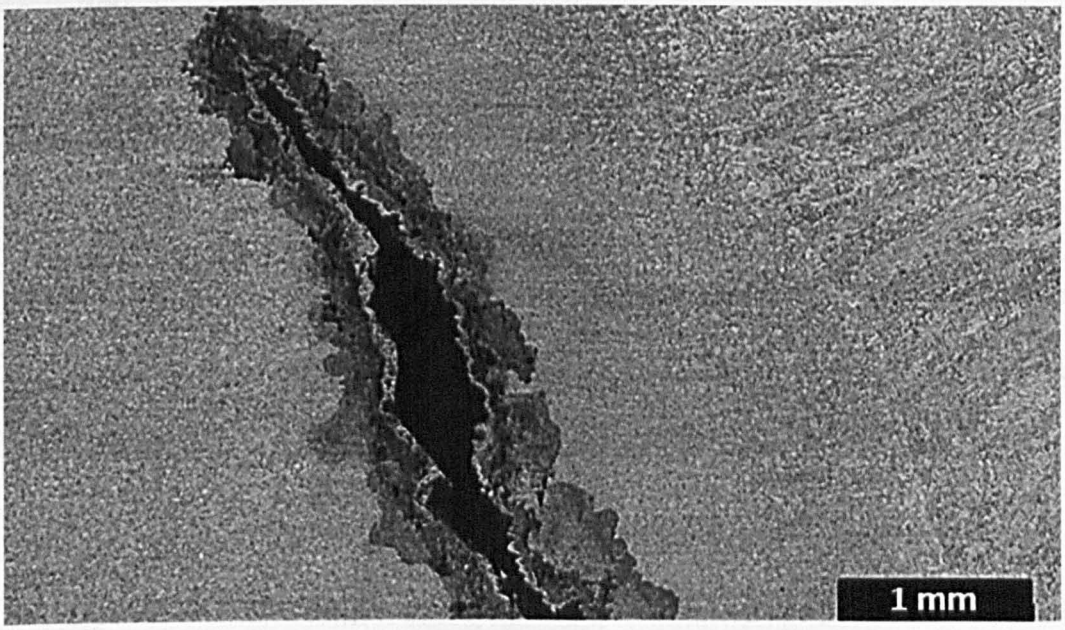

Figure 5-13: Creep crack captured from a specimen interrupted very close to failure (>90% creep life).

The fracture location of the cross-weld specimens was also investigated by conducting hardness measurements along the specimen gauge length as shown in Figure 5-10. This was necessary because it was discussed in chapter 2 that both the FGHAZ and the ICHAZ exhibit very similar features and thus a clear distinction is often difficult. Hardness measurements were taken on one straight line at mid-thickness at intervals of 0.75 mm

using a Vickers (HV) indenter with a load of 5 kg. The hardness result for the specimen shown earlier (Figure 5-11), is given in Figure 5-14.

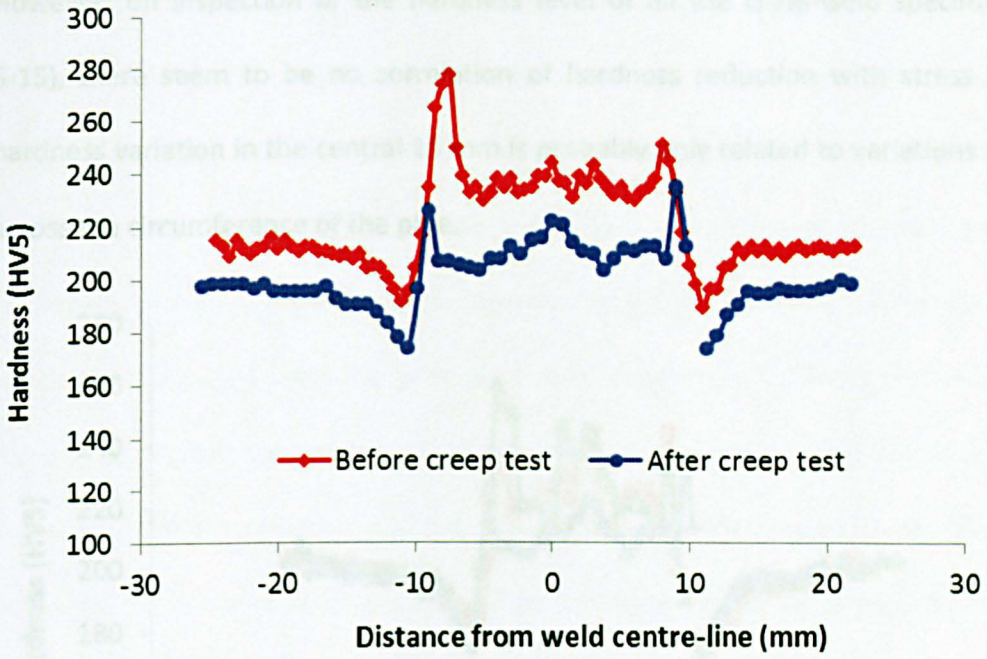

Figure 5-14: Hardness profile along a fractured cross-weld specimen. Typical hardness profile along a line representative of the mid-thickness of the PWHT pipe (denoted before creep test) is also shown for comparison.

From the knowledge of typical hardnesses of the CGHAZ (maximum hardness) and the ICHAZ (minimum hardness), it can be confirmed that failure occurred in the FGHAZ (break in curve). All the cross-weld specimens showed similar hardness trends. Figure 5-14 also features a typical hardness profile of an un-tested specimen. There is a significant reduction in hardness after the creep test. Taking the parent metal as an example, the hardness reduced from ~212 HV5 to ~196 HV5. This reduction was consistent in other parts of the weldment. Changes in hardness occur due to recovery, coarsening of carbide particles and recrystallization [24]. All creep–resistant power plant steels are severely tempered before they enter service. They are therefore beyond the state where secondary hardening is expected and the hardness can, during service, be expected to

decrease monotonically [24]. Masuyama [25] has recently demonstrated a method for creep life assessment of P91 welded components based on hardness measurements. However, on inspection of the hardness level of all the cross-weld specimens (Figure 5-15), there seem to be no correlation of hardness reduction with stress levels. The hardness variation in the central 15 mm is probably only related to variations in the weld across the circumference of the pipe.

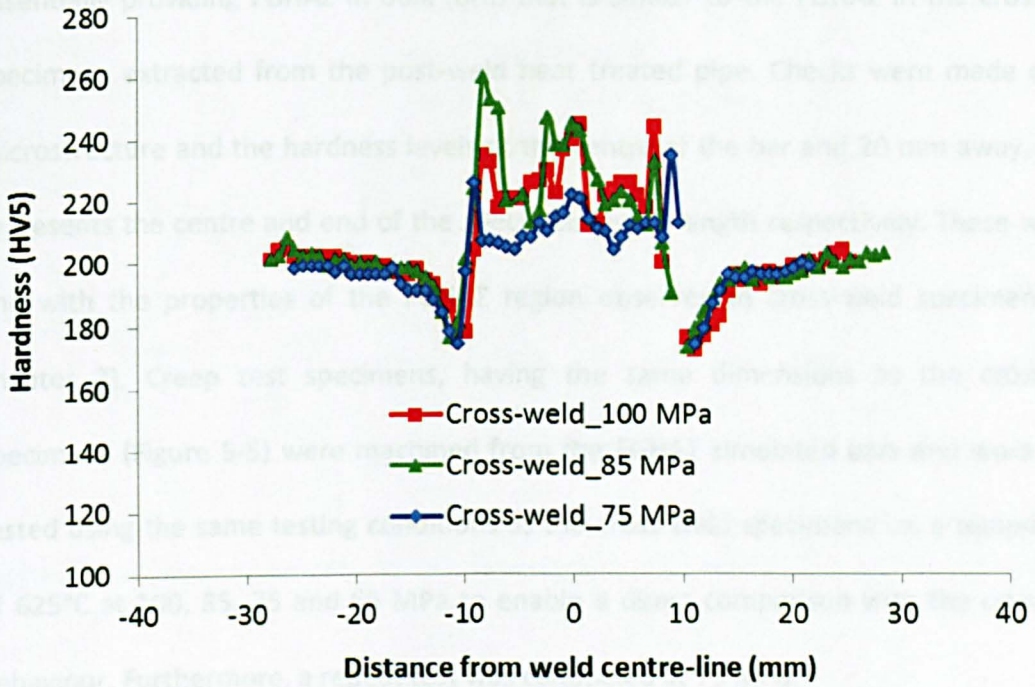

Figure 5-15: Hardness profiles along fractured cross-weld specimens tested at different stresses.

5.3 Creep testing on simulated FGHAZ specimens

From the literature [7], [26], [27], [28], [29] and the results in section 5.2.2, it has been shown that the FGHAZ is particularly weak in creep and cross-weld specimens fail in the FGHAZ. To characterise the behaviour of this weak zone, creep tests were conducted on simulated FGHAZ specimens.

5.3.1 *Specimen details*

The FGHAZ simulation procedure has been outlined in chapter 3. In brief, it involved extracting round bar test specimens 180 mm long and 20 mm in diameter from a section of as-received parent material. These bars were heated to a peak temperature of 950°C using induction heating followed by oil quenching to reproduce the FGHAZ microstructure. Finally, the bars were post weld heat treated at 750°C for 4 hours, essentially providing FGHAZ in bulk form that is similar to the FGHAZ in the cross-weld specimens extracted from the post-weld heat treated pipe. Checks were made on the microstructure and the hardness levels at the centre of the bar and 20 mm away, which represents the centre and end of the specimen gauge length respectively. These were in line with the properties of the FGHAZ region observed in cross-weld specimens (see chapter 3). Creep test specimens, having the same dimensions as the cross-weld specimens (Figure 5-5) were machined from the FGHAZ simulated bars and were creep tested using the same testing conditions as the cross-weld specimens i.e. a temperature of 625°C at 100, 85, 75 and 65 MPa to enable a direct comparison with the cross-weld behaviour. Furthermore, a repeat test was conducted at 75 MPa.

5.3.2 *Results*

The accumulation of strain with time for the creep tests on FGHAZ simulated specimens are summarised in Figure 5-16. The general shapes of the creep curves tend to show the absence of a prolonged secondary stage and are characteristic of a tertiary dominated process. The data does not show any trends in strains at failure with stress levels. However, we note that they are substantially higher than those measured in the case of cross-weld specimens. For example, at 85 MPa, the cross-weld specimen showed a modest strain at failure of 1.7%, whereas the FGHAZ simulated specimen showed a strain at failure of nearly 37%. The creep rupture life and elongation are tabulated in Table

5-2.While the macroscopic strain at failure of cross-weld specimens appears to be low, and consequently appears brittle, the Type IV zone (FGHAZ) shows appreciable strain accumulation, at least when tested in bulk form (FGHAZ simulated specimens). The rupture time for the repeat test at 75 MPa agrees well with the previous test conducted at the same stress.

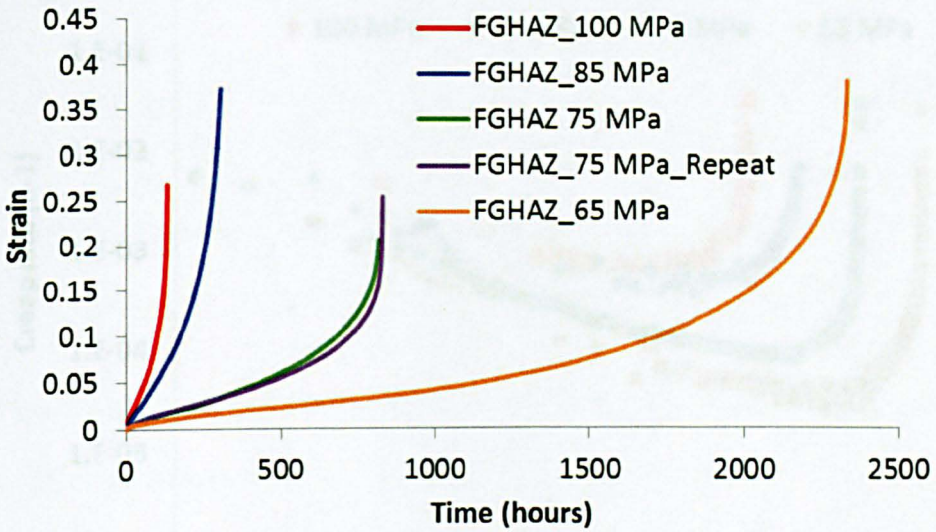

Figure 5-16: Creep curves for FGHAZ simulated specimens, tested at 625°C at different stresses.

Table 5-2: Tabulated values of creep rupture life and elongation of FGHAZ simulated specimens at 625°C.

Stress (MPa)	Rupture life (hours)	Rupture elongation (%)
100	132	25.5
85	305	36.2
75	820	24.9
75 Repeat	830	25.3
65	2336	46.4

Creep strain rate

The creep strain rates for the FGHAZ simulated specimens were estimated using the same approach described earlier for the cross-weld tests and the results are shown in Figure 5-17.

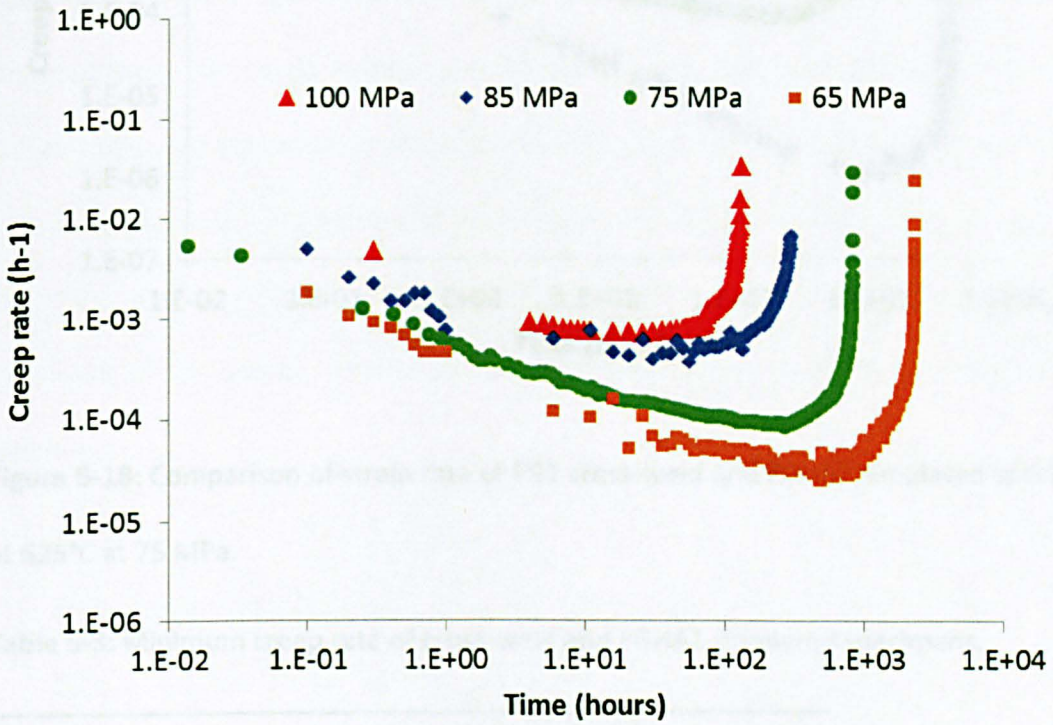

Figure 5-17: Variations of creep strain rate with time for P91 FGHAZ simulated specimens at 625°C at different stresses.

The trends of creep strain rate for the FGHAZ simulated specimens appear to be very similar to the cross-weld specimens, characterised by a decaying primary stage and an accelerating tertiary stage with no substantial steady-state stage. However, it can be seen from Figure 5-18, that, for the same stress level, the onset of the tertiary stage is delayed in the cross-weld specimen and the minimum creep rate was significantly lower. The minimum creep rates for both the FGHAZ simulated and cross-weld specimens are summarised in Table 5-1.

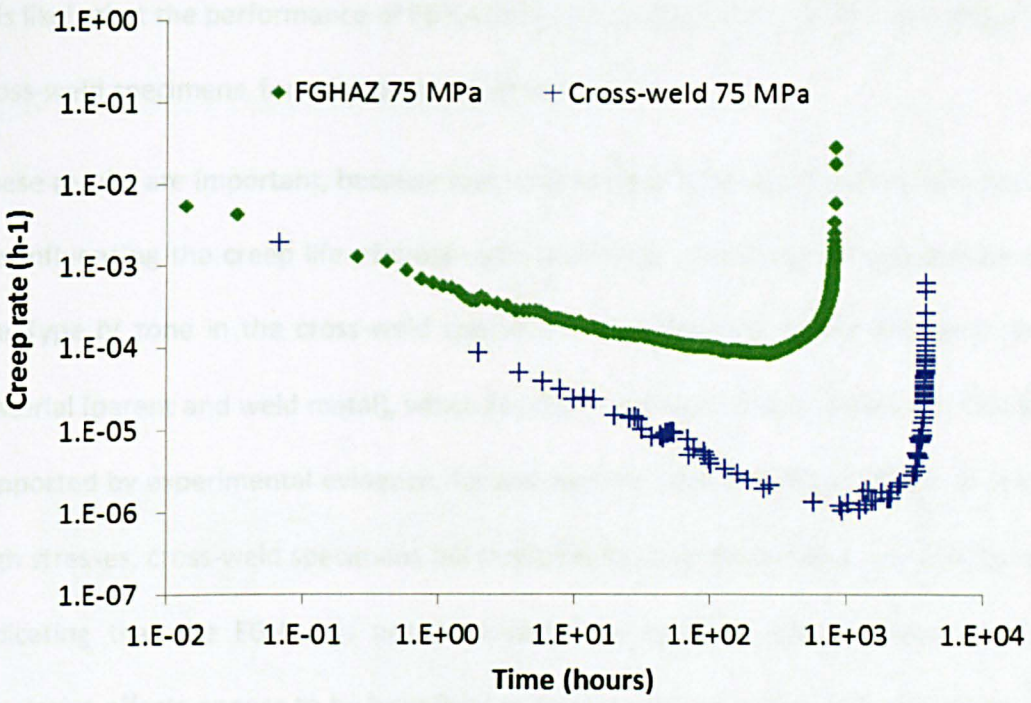

Figure 5-18: Comparison of strain rate of P91 cross-weld and FGHAZ simulated specimens at 625°C at 75 MPa.

Table 5-3: Minimum creep rate of cross-weld and FGHAZ simulated specimens.

Stress (MPa)	Minimum creep rate (h^{-1})	
	Cross-weld specimens	FGHAZ simulated specimens
100	1.5×10^{-5}	7.28×10^{-4}
85	2.26×10^{-6}	3.67×10^{-4}
75	1.06×10^{-6}	8.2×10^{-5}
65	3.56×10^{-7}	2.44×10^{-5}

The time to rupture of the FGHAZ simulated and cross-weld specimens is shown in Figure 5-19. At all stress levels, the times to rupture of the cross-weld specimens were longer than the FGHAZ simulated specimens. The difference appears to be much larger at the higher stress levels (100 and 85 MPa) compared to the lower stress levels (75 and 65 MPa). At 85 MPa, the cross-weld specimen outperformed the FGHAZ simulated specimen by a factor of 6.8, decreasing to 3.4 at 65 MPa. In test durations longer than 10,000 hours,

it is likely that the performance of FGHAZ simulated specimens may be even closer to the cross-weld specimens, for example see Li *et al.* [21].

These results are important, because they suggest that factors other than microstructure are influencing the creep life of cross-weld specimens. One possible explanation is that the Type IV zone in the cross-weld specimens is constrained by the adjacent stronger material (parent and weld metal), which results in a longer creep rupture life. This view is supported by experimental evidence, for example see Abe and Tabuchi [30]. At relatively high stresses, cross-weld specimens fail randomly in the parent metal, weld metal or HAZ indicating that the FGHAZ is not necessarily the weakest link. In short term tests, constraint effects appear to be beneficial in delaying failure in the HAZ and failure occurs elsewhere.

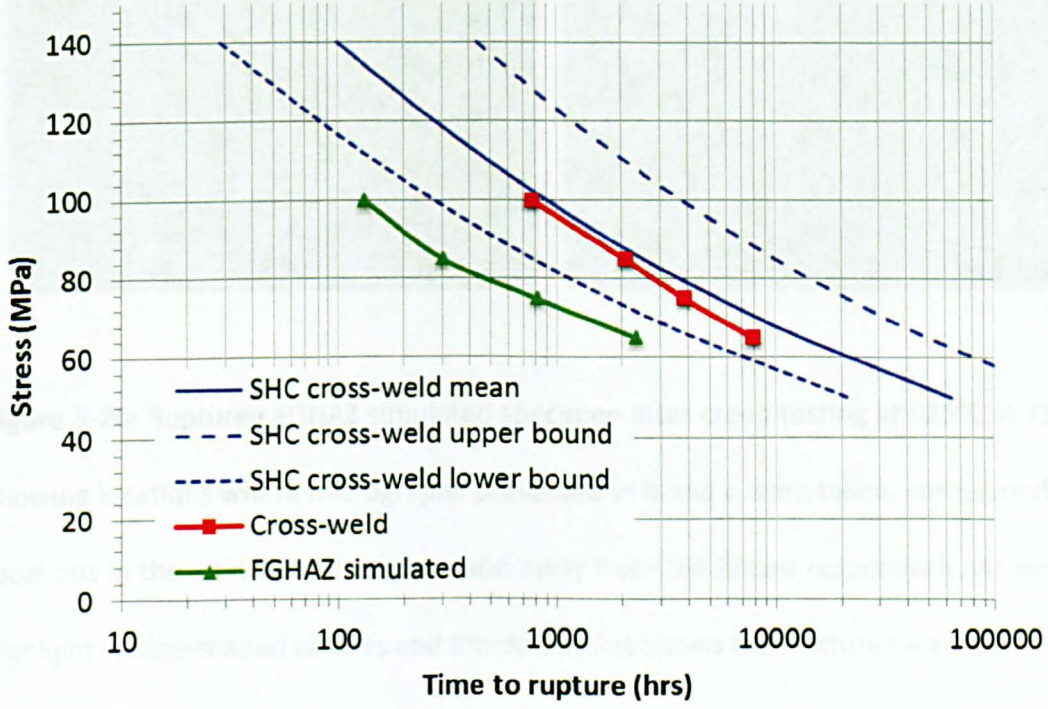

Figure 5-19: Comparison of P91 cross-weld and FGHAZ simulated specimens creep rupture strength. The predicted P91 cross-weld creep rupture strength, calculated using the SHC committee master equation and the ± 20% scatter bands are also shown.

Post-test examination

Figure 5-20a shows a picture of one of the FGHAZ fractured specimen, tested at 625°C at 75 MPa. The letters marked b and c correspond to locations where micrographs were captured and correspond to regions in the vicinity of the failure (b) and away from the failure (c).

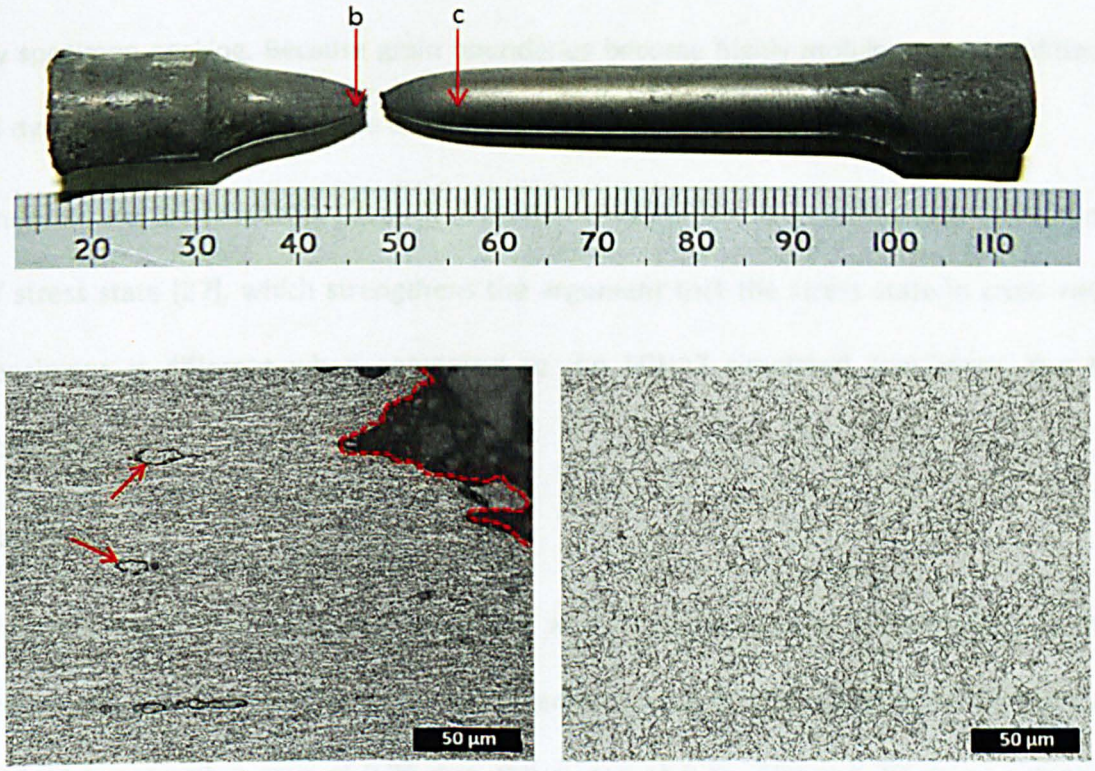

Figure 5-20: Ruptured FGHAZ simulated specimen after creep testing at 625°C at 75 MPa showing locations where micrographs presented in b and c were taken, corresponding to locations in the vicinity of the failure and away from the failure respectively. Arrows in b highlight wedge-shaped cavities and the dotted line shows the fracture location.

From Figure 5-20b, there appears to be a significant difference in the evolution of cavitational damage, when compared to the FGHAZ region in cross-weld specimens (see Figure 5-11e). The presence of wedge-shaped cavities is an indicator that grain boundary

sliding is dominant in the FGHAZ simulated specimens. Similar wedge-type cavities have been reported by Falat *et al.* [31] and Gooch and Kimmins [32].

Since the creep rates of the FGHAZ simulated specimens are relatively high when compared to those measured for the cross-weld specimens, dynamic recrystallization is probably the dominant fracture mechanism, which can allow materials to deform extensively so that deformation becomes localised in a neck and failure eventually occurs by specimen necking. Because grain boundaries become highly mobile under conditions of dynamic recrystallization, the development of creep cavities is suppressed [14].

These results are revealing, because cavitation development is expected to be a function of stress state [27], which strengthens the argument that the stress state in cross-weld specimens is different when compared to the FGHAZ simulated specimens, due to constraint.

Hardness

The fractured FGHAZ simulated specimens were sectioned in the same manner as the cross-weld specimens and hardness measurements were carried out along a single line at mid-thickness with a step of 0.75 mm and a load of 5 Kg. Figure 5-20 shows a typical hardness profile measured on the fractured FGHAZ simulated specimen. The initial hardness of FGHAZ simulated specimens was shown to be constant at ~200 HV5 along the gauge length in chapter 3. In Figure 5-21, it is apparent that the reduction in hardness due to creep softening is not uniform along the specimen gauge length. The hardness of ~200 HV5 gradually decreased from the 'shoulder' of the specimen to ~165 HV5 in the gauge part. This reduction is associated with plastic flow during creep, i.e. strain softening [33]. In the necking portion, the hardness increased to ~198 HV5 due to strain localisation and hardening prior to failure.

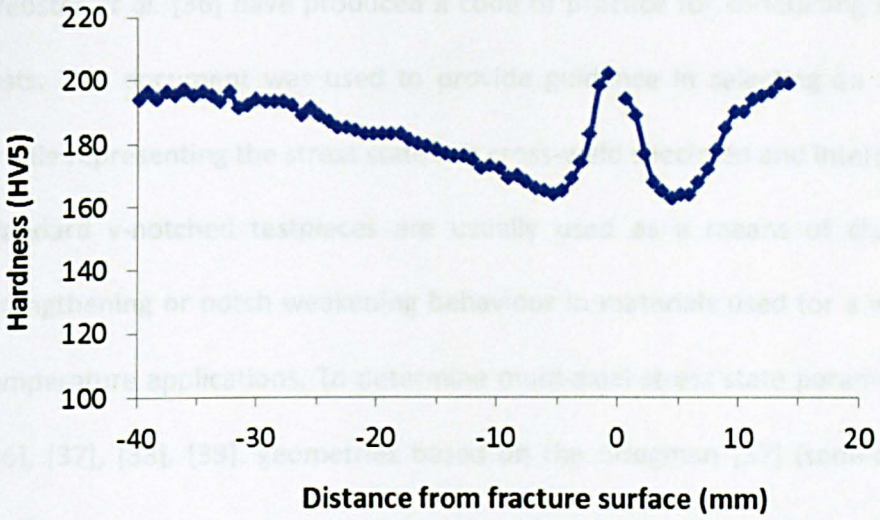

Figure 5-21: Hardness profile across P91 FGHAZ simulated crept specimen tested at 625°C at 75 MPa.

5.4 Influence of constraint

Taken at face value, the results presented in section 5.3.2 suggest that constraint effects may be relatively important. At least in short-term tests, it has been shown that cross-weld specimens (constraint present) outperformed FGHAZ simulated specimens (no constraint) by a factor of 6.8. In longer-term tests this factor was much less. Furthermore, it was shown by optical microscopy that the distribution of cavities in the FGHAZ simulated specimens and the FGHAZ region in the cross-weld specimens was entirely different. It could be argued that the preferential creep failure of welds in the weak FGHAZ region is due to the high constraint it experiences and the consequent highly triaxial stress state. This has been termed a 'metallurgical notch' by Kimmins and Smith [27]. In order to assess the influence of constraint on the creep performance of P91 welds, a series of notched-bar specimens were tested. Similar specimens have been used for examples, by Gaffard [34] and Takahashi [35], to systematically evaluate the multiaxial effect on creep rupture behavior of modified 9Cr-1Mo steel.

Webster *et al.* [36] have produced a code of practice for conducting notched bar creep tests. This document was used to provide guidance in selecting an appropriate notch profile representing the stress state in a cross-weld specimen and interpreting the results. Standard v-notched testpieces are usually used as a means of characterising notch strengthening or notch weakening behaviour in materials used for a wide range of high temperature applications. To determine multi-axial stress state parameters during creep [36], [37], [38], [39], geometries based on the Bridgman [37] (semi-circular) notch are useful.

Terminologies associated with notched-specimens

With respect to Figure 5-22, some of the common terminologies associated with notched-specimens are described below [36].

D: Diameter of parallel portion of a notched testpiece of circular cross-section

d_{no}: Initial diameter of testpiece at notch throat

r_{no}: Initial notch root radius

Notch depth ratio: $\frac{D}{d_{no}}$

Notch acuity ratio: $\frac{d_{no}}{r_{no}}$

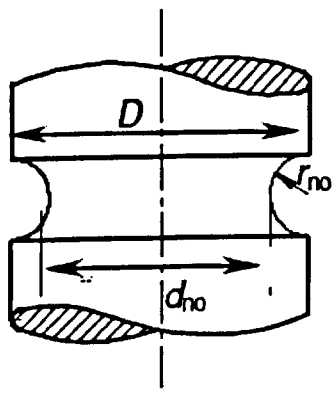

Figure 5-22: Circumferential notch geometry details [36].

Initially, on loading, an elastic or elastic plus plastic stress field will be generated across the notch throat. With time, stress redistribution usually takes place (sometimes until a stationary stress state is achieved). For symmetrical shapes and under simple loading condition (for example constant tension), a point (termed a skeletal point) exists in the cross-section where the stress state remains approximately constant with time, independent of the elastic, plastic or creep properties of the material. The components of stress at this point are referred to as skeletal stresses. It is assumed that the skeletal stresses can be used as a basis for interpreting the overall creep behaviour of circumferentially notched bars [36]. The stresses associated with notched bars are defined as follows [36]:

Net stress (σ_{net})

Load divided by initial cross-sectional area in the plane of minimum diameter, i.e., at the notch root

$$\sigma_{net} = \frac{4}{\pi . \, d_{no}{}^{2}} load \qquad \textbf{Equation 5-3}$$

von Mises effective stress (σ_{VM})

Defined in accordance with the von Mises yield criterion by:

$$\sigma_{VM} = \frac{1}{\sqrt{2}} \left(\sigma_1 - \sigma_2 \right)^2 + \left(\sigma_1 - \sigma_2 \right)^2 + \left(\sigma_1 - \sigma_2 \right)^2 {}^{1/2} \qquad \textbf{Equation 5-4}$$

where σ_1, σ_2 and σ_3 are the maximum, intermediate and minimum principal stresses of the stress tensor respectively.

Hydrostatic stress (σ_H)

$$\sigma_H = \frac{\sigma_1 + \sigma_2 + \sigma_3}{3} \qquad \textbf{Equation 5-5}$$

Representative stress (σ_{rep})

The stress applied to a plain bar that results in the same effective strain accumulation or rupture life as that obtained in a notched bar tested at the same temperature.

Skeletal stress (σ*)

The stress component at the skeletal radius where the magnitude of the stress is approximately invariant with the stress exponent, n. The stress components of most interest are σ_{VM}^{*}, σ_{1}^{*} and σ_{H}^{*} (where the asterisk denotes skeletal). These can be calculated using the relationships provided in Table 5-2 [36].

Table 5-4: Relationships for calculating skeletal stresses for a notch depth ratio $\frac{D}{d_{no}}$ of 1.41.

Notch acuity ratio	Skeletal point positions	Normalised stresses		
		$\frac{\sigma_{VM}^{*}}{\sigma_{net}}$	$\frac{\sigma_{H}^{*}}{\sigma_{net}}$	$\frac{\sigma_{1}^{*}}{\sigma_{net}}$
4.83	(0.73)	0.72	0.61	1.08

() Indicative best estimate value

5.4.1 Specimen details

The notch geometry used in the current work was based on a semi-circular notch profile with a notch depth ratio, $\frac{D}{d_{no}}$ of 1.41 and a notch acuity ratio, $\frac{d_{no}}{r_{no}}$ of 4.83 as shown in Figure 5-23. This is one of the recommended notch geometries to characterise material behaviour subjected to a triaxial stress state. The notch was machined at the centre of the FGHAZ simulated specimens, in effect reproducing the triaxiality present in a cross-weld specimen.

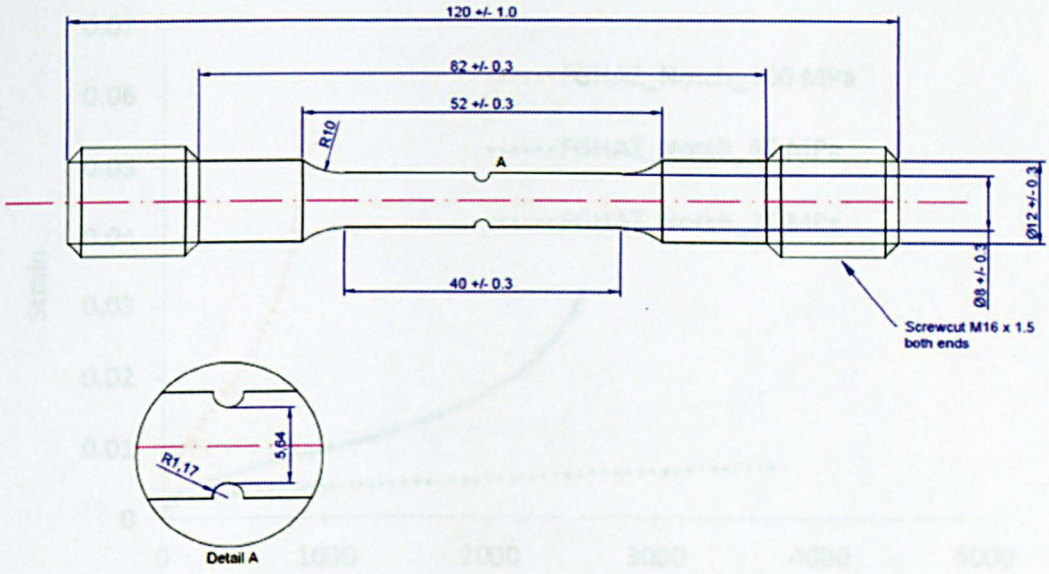

Figure 5-23: Dimensions of notched FGHAZ simulated specimens.

Three tests were conducted on notched FGHAZ simulated specimens and the net stresses (load divided by initial cross-sectional area at the notch root) were chosen to be similar to the stresses applied to plain FGHAZ simulated specimens. Using the relationships given in Table 5-2, the maximum principal skeletal stresses (σ_1^*) were calculated to be 108, 91.8 and 81 MPa corresponding to net stresses of 100, 85 and 75 MPa respectively.

5.4.2 Results

The recorded strain and time data for creep tests involving notched FGHAZ simulated specimens are given in Figure 5-24. The test at 75 MPa was still running at the time of writing of this thesis.

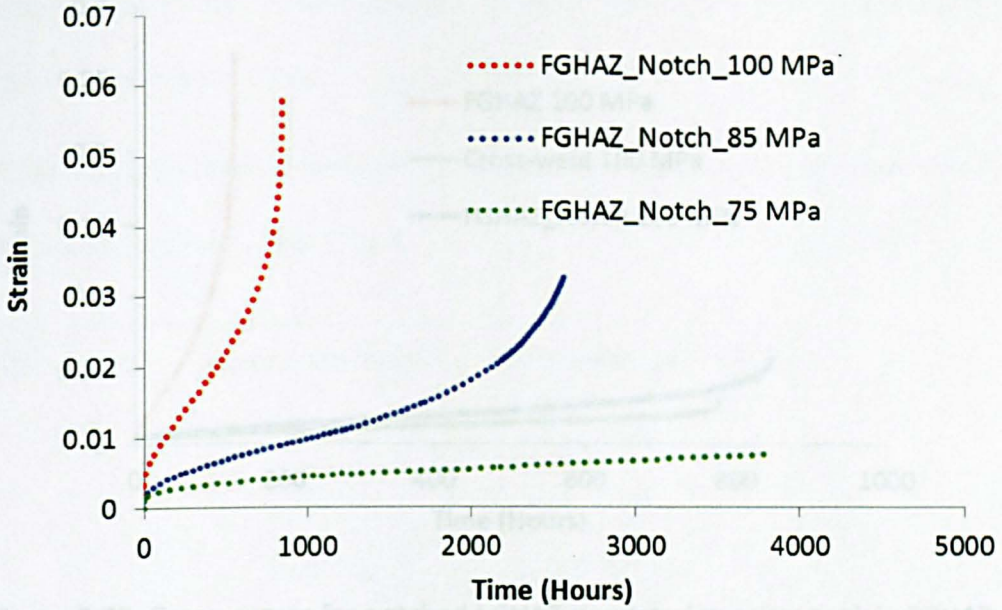

Figure 5-24: Creep curves for notched FGHAZ simulated specimens, tested at 625°C at 3 different stresses. The test at 75 MPa is still running at the time of writing this thesis.

The strain-time data of one of the notched FGHAZ creep tests is compared with data from a cross-weld and plain FGHAZ simulated specimens, tested at the same net section stress in Figure 5-25. Interestingly, the data from the notched FGHAZ simulated specimen correlated much better with data from the cross-weld test. Also, the strains at failure were very similar for these two specimens and significantly lower than that measured in the plain FGHAZ simulated specimen.

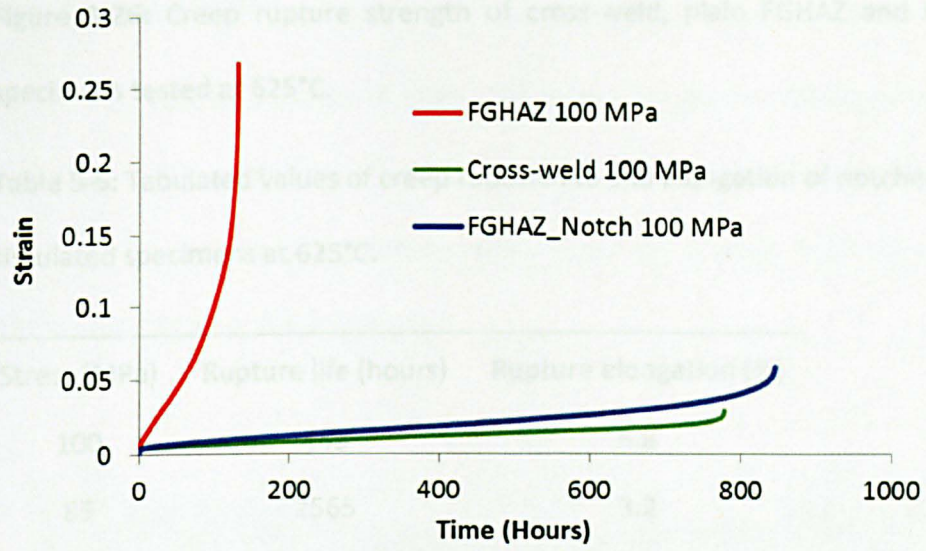

Figure 5-25: Creep curves for notched FGHAZ simulated specimen, plain FGHAZ simulated specimen and cross-weld specimen tested at 625°C at 100 MPa.

The time to rupture of the three types of specimens (plain FGHAZ, notched FGHAZ and cross-weld) are summarised in Figure 5-26 and tabulated in Table 5-5. It is important to note that the stress values for the notched FGHAZ simulated specimens correspond to principal skeletal stresses, as it was mentioned earlier that the skeletal stresses can be used as a basis for interpreting the overall creep behaviour of circumferentially notched bars.

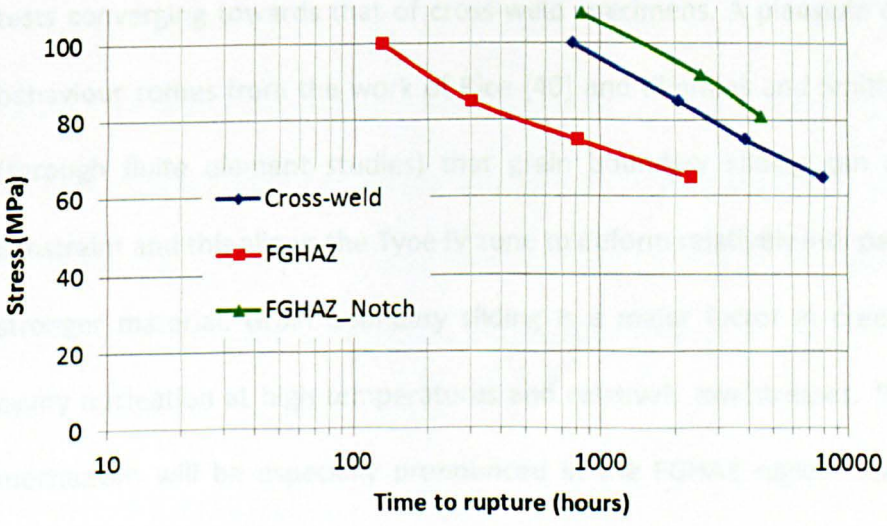

Figure 5-26: Creep rupture strength of cross-weld, plain FGHAZ and notched FGHAZ specimens tested at 625°C.

Table 5-5: Tabulated values of creep rupture life and elongation of notched FGHAZ simulated specimens at 625°C.

Stress (MPa)	Rupture life (hours)	Rupture elongation (%)
100	845	5.8
85	2565	3.2
75	Ongoing	Ongoing

From the results presented in Figure 5-26, it is clear that notched FGHAZ specimens performed much better than plain FGHAZ specimens and in this case, better than the cross-weld specimens as well. Thus, by reproducing the triaxiality present in a cross-weld specimen in a homogeneous FGHAZ simulated specimen, it has been shown that triaxiality is beneficial in improving creep life, at least in short term tests.

In longer-term tests, the results are likely to show the same trend as that observed for plain FGHAZ and cross-weld specimens i.e. the performance (rupture life) of plain FGHAZ tests converging towards that of cross-weld specimens. A plausible explanation for this behaviour comes from the work of Rice [40] and Kimmins and Smith [27], who showed (through finite element studies) that grain boundary sliding can allow relaxation of constraint and this allows the Type IV zone to deform relatively independently of adjacent stronger material. Grain boundary sliding is a major factor in creep deformation and cavity nucleation at high temperatures and relatively low stresses. The influence of this mechanism will be especially pronounced in the FGHAZ region due to the high grain boundary area per unit volume of material [27].

Post-test examination

Figure 5-27a shows a picture of one of the fractured notched FGHAZ simulated specimen, tested at 625°C at 75 MPa. The letters marked b and c correspond to locations where micrographs were captured and correspond to regions away from the notch/failure (b) and in the vicinity of the failure (c).

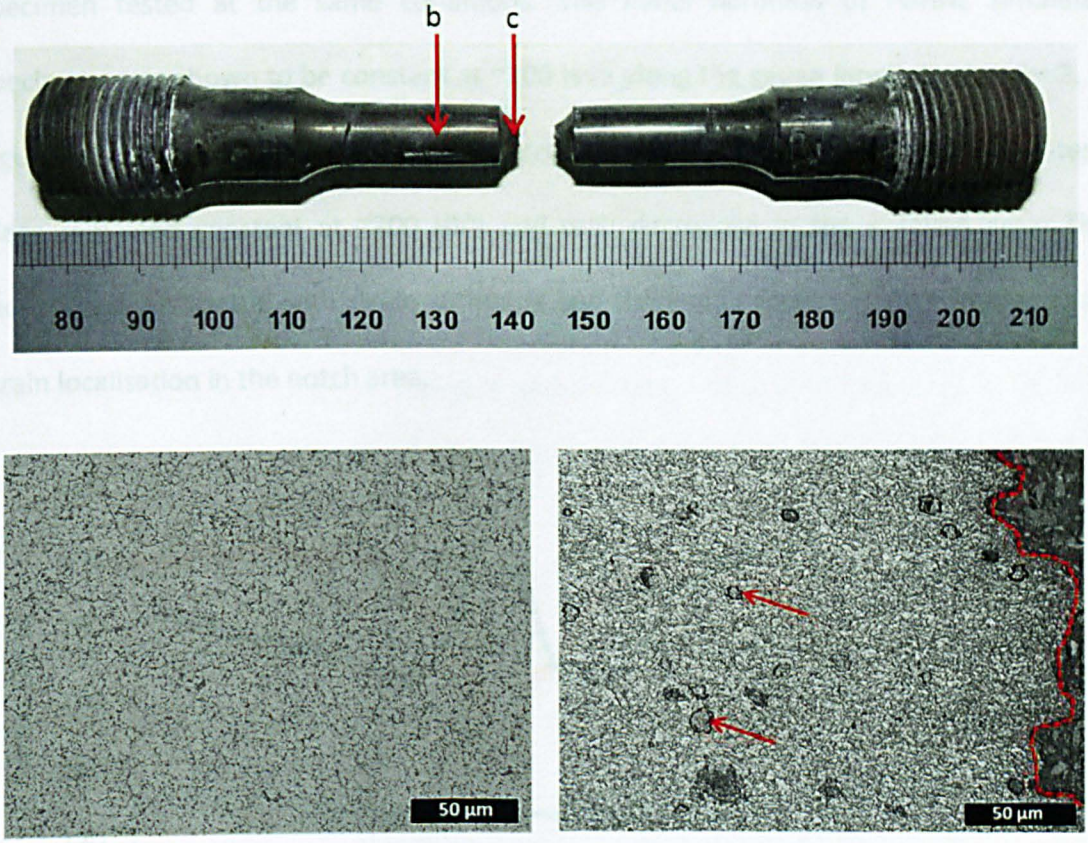

Figure 5-27: Ruptured notched FGHAZ simulated specimen after creep testing at 625°C at 75 MPa showing locations where micrographs presented in (b) and (c) were taken, corresponding to locations away from the notch and in the vicinity of the failure respectively. Arrows in (c) highlight examples of wedge-shaped cavities and the dotted line represents the fracture location.

The evolution of cavitational damage in the notched FGHAZ simulated specimens is very similar to that observed in plain FGHAZ simulated specimens, although it could be argued

that far more cavities were present in the notched specimen. This may be a consequence of the different stress states in the two types of specimens.

Hardness

Figure 5-28 shows a typical hardness profile measured on the fractured notched FGHAZ simulated specimen compared with the hardness distribution of a plain FGHAZ simulated specimen tested at the same conditions. The initial hardness of FGHAZ simulated specimens was shown to be constant at ~200 HV5 along the gauge length in chapter 3. In Figure 5-28, it is clear that the hardness across the parallel portion of the notched test-piece remained constant at ~200 HV5 and only decreased in the notched area. This reduction is associated with strain softening and the length scale is a clear indication of strain localisation in the notch area.

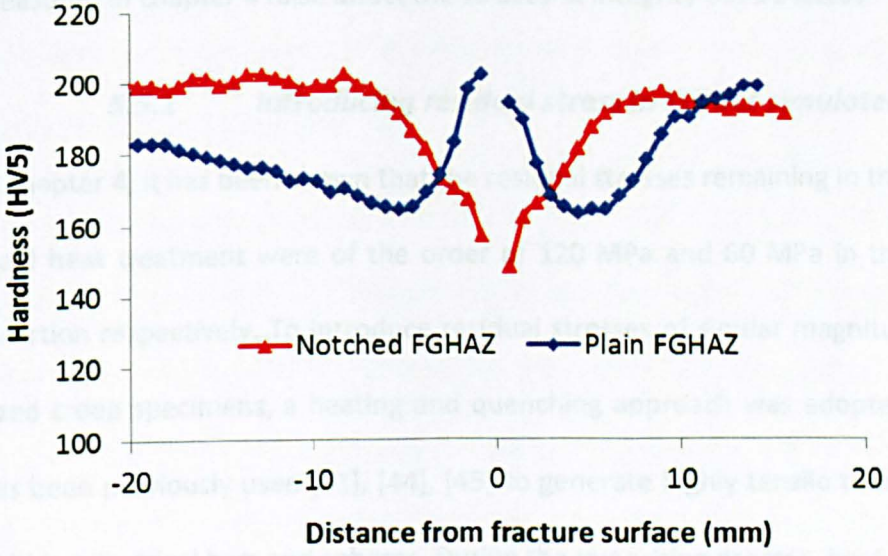

Figure 5-28: Hardness profile across P91 plain and notched FGHAZ simulated crept specimens tested at 625°C at 75 MPa.

5.5 Influence of residual stress

Residual stresses can have a large impact on the operating performance of engineering structures and thus need to be considered in the same way as external stresses; otherwise, the service life may be greatly affected. Specifically, in components operating at high temperatures, these stresses can act as a driving force for localised creep strain accumulation which increases the likelihood for creep failure [41], [42], [43].

Reliable methods for determining the magnitude and distribution of residual stresses are now very well established. However, the relationship between the measured residual stresses and their influence on creep performance has not been well studied. This is partly due to the difficulty in introducing known residual stresses in laboratory sized specimens. There is a need to establish whether the residual stresses that have been measured in chapter 4 raise affect the structural integrity of P91 welds.

5.5.1 Introducing residual stress in FGHAZ simulated specimens

In chapter 4, it has been shown that the residual stresses remaining in the pipes after post weld heat treatment were of the order of 120 MPa and 60 MPa in the hoop and axial direction respectively. To introduce residual stresses of similar magnitudes in laboratory sized creep specimens, a heating and quenching approach was adopted. This technique has been previously used [41], [44], [45] to generate highly tensile triaxial residual stress field in cylindrical bars and spheres. During the quenching process, heat dissipates via free surfaces and a non-uniform temperature gradient develops through the entire volume of the specimen, which determines the residual stress field in the quenched specimen. In the present work, residual stresses were introduced in the FGHAZ simulated specimens, which presented the following challenges:

The FGHAZ simulated bars were already machined to the dimensions of the creep specimen. On the one hand, this is desirable because any further machining after introducing residual stresses will change the distribution/magnitude of the stresses. On the other hand, any attempt to heat and quench the entire specimen will result in larger tensile residual stresses accumulating in the 'shoulders' and threaded ends of the specimen, due to the increased section thickness.

The maximum temperature that can be applied is restricted by the lower transformation temperature (Ac_1); otherwise undesirable phase transformation may occur.

In effect, these factors affect the way the specimen can be heated and limit the amount of residual stresses that can be introduced. Instead of heating the entire specimen, a localised heating approach using infrared (IR) heating was adopted such that on quenching, residual stresses accumulated preferentially in the heated region. The peak temperature chosen was 750°C which is well below the minimum Ac_1 temperature (800°C) reported for this steel [46].

The heating and quenching experiment was performed using a custom built experimental rig as shown in Figure 5-29. The specimen is attached at the end of a vertical support bar, which is held at the other end onto an electromagnet. The specimen is heated using a pair of infrared emitters which are gold coated on the outside surfaces, effectively increasing the amount of infrared radiation impinging the surface of the specimen. The emitters in this case were gold coated in such a way that the radiation is directed onto the sample at a 45° angle. Thus, by having two emitters, heating at +45° and -45°, the specimen can be brought to the peak temperature of 750°C in a much shorter time, thus minimising conduction throughout the specimen.

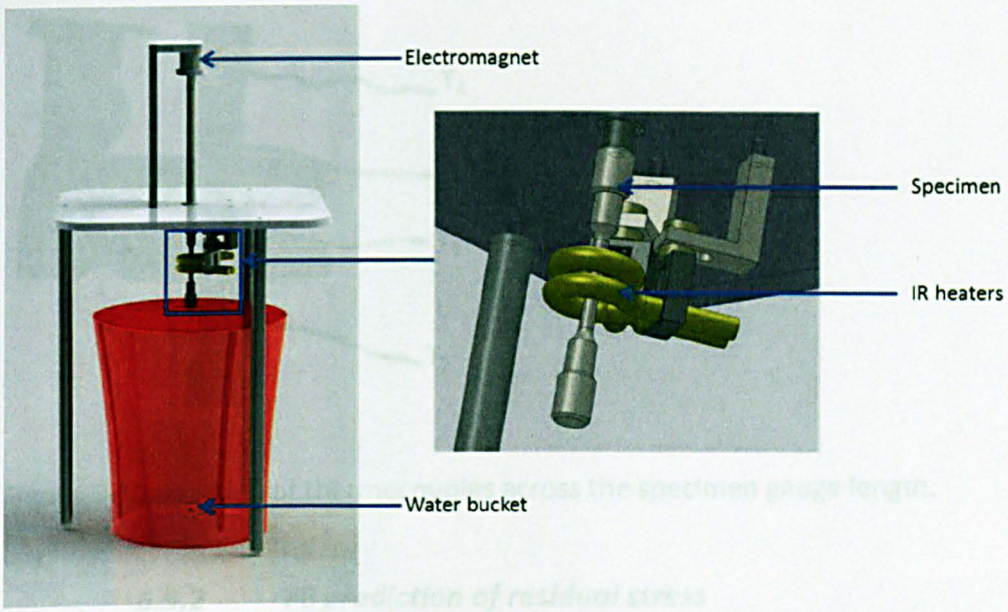

Figure 5-29: Custom built rig for heating and quenching of FGHAZ simulated specimens.

Four N-Type thermocouples were positioned at different locations (centre, ± 10 mm and 20 mm away from the centre) along the gauge length of the specimen as shown in Figure 5-30. The temperature was monitored only during the heating process. Unfortunately, the temperature could not be measured during the quenching process as thermocouples could not be permanently attached to the specimens. Once the thermocouple at the centre of the specimen (labelled T_1 in Figure 5-30) reached 750°C, the thermocouples were retracted and the quick release mechanism activated so that the specimen dropped in a water bath, at ambient temperature. The circular guide in the base plate ensured that the specimen dropped vertically to avoid specimen distortion and also to avoid damaging the IR emitters. Three specimens were heated and quenched in the same manner using the same peak temperature.

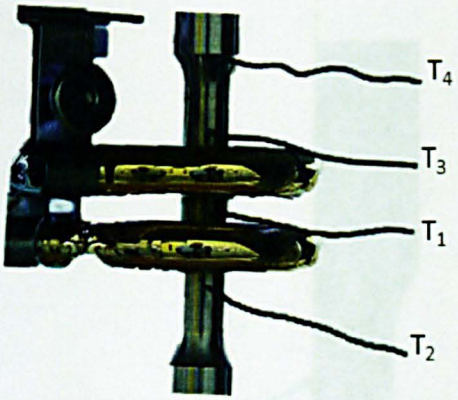

Figure 5-30: Position of thermocouples across the specimen gauge length.

5.5.2 FE prediction of residual stress

The process of heating and quenching can be treated as a transient heat conduction problem with convective boundary conditions. A sequential thermal-stress analysis was carried out using ABAQUS 6.10 [47] to estimate the level of residual stresses introduced. This type of analysis is usually performed when the stress and deformation fields are dependent on temperature but the temperature field is obtained independently [45].

The cylindrical geometry of the specimen simplified the analysis to an axisymmetric model and due to the symmetry present, only one quarter of the specimen was modelled. For the heat transfer analysis, the finite element mesh consisted of 1464 first-order elements (DCAX4 4-node linear axisymmetric heat transfer quadrilaterals) and second-order elements (CAX8R 8-node biquadratic axisymmetric quadrilaterals with reduced integration) were used for the stress analysis. The finite element mesh together with the applied symmetry boundary conditions are shown in Figure 5-31.

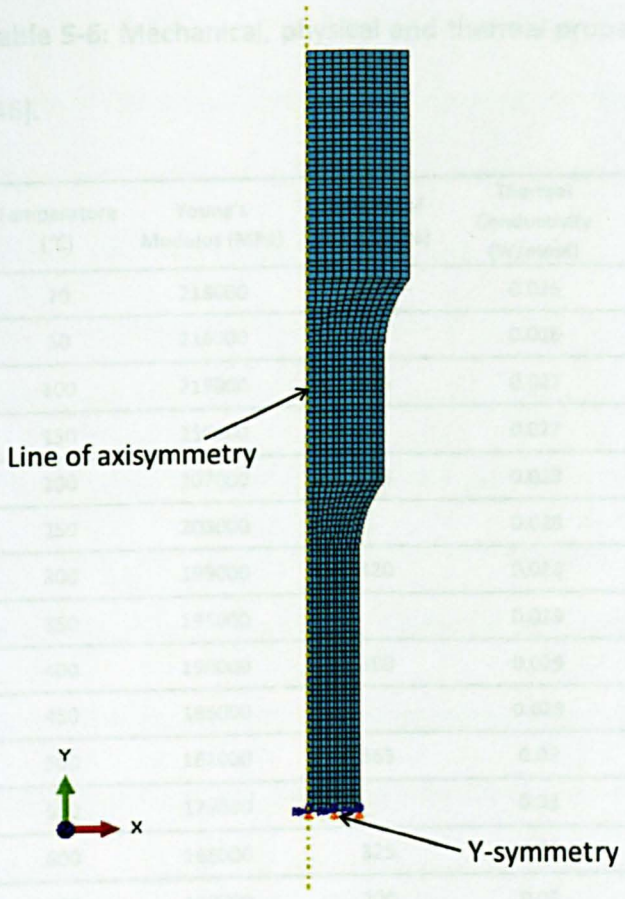

Figure 5-31: Finite element mesh and applied symmetry boundary conditions.

The physical, mechanical and thermal properties for P91 steel, obtained from [46] were defined in the ABAQUS input file and are listed in Table 5-3. For temperatures beyond 650°C, the data were extrapolated within ABAQUS. Isotropic hardening material behaviour was assumed. Since the peak temperature was well below the lower transformation temperature, phase transformation was assumed not to occur.

Table 5-6: Mechanical, physical and thermal properties of Grade 91 steel, obtained from [46].

Temperature (°C)	Young's Modulus (MPa)	0.2% Proof Stress (MPa)	Thermal Conductivity (W/mmK)	Coefficient of linear expansion ($\times 10^{-6}$/K)	Specific Heat capacity (J/Kg K)	Density $\times 10^{-6}$ Kg/mm^3
20	218000	480	0.026	-	440	7.77
50	216000		0.026	1.06	460	
100	213000	435	0.027	1.09	480	
150	210000		0.027	1.11	490	
200	207000	425	0.028	1.13	510	
250	203000		0.028	1.15	530	
300	199000	420	0.028	1.17	550	
350	195000		0.029	1.18	570	
400	190000	380	0.029	1.2	600	
450	186000		0.029	1.21	630	
500	181000	365	0.03	1.23	660	
550	175000		0.03	1.24	710	
600	168000	325	0.03	1.26	770	
650	162000	200	0.03	1.27	860	

In the heat transfer analysis, the initial temperature of the specimen was defined by applying an analytical field. This was obtained by fitting a second order polynomial to the temperatures recorded during the experiment. In practice, the specimen was quenched in a water bath, at ambient temperature. In the FE model, this cooling procedure was simulated by assuming convective heat transfer and applying boundary conditions on the free surfaces. This was done by defining a surface film condition with a film coefficient of 0.009 W/mm^2°C and a sink temperature of 20°C. Similar values have been used for ferritic steels by Hossain *et al.* [41]. On completion of the heat transfer analysis, the temperature-time history was used as input for the subsequent stress analysis.

5.5.3 *Neutron diffraction residual stress measurement*

Neutron diffraction was used to measure the residual stresses in the quenched FGHAZ simulated specimen on the Kowari strain-scanning instrument at the Australian Nuclear Science and Technology Organisation (ANSTO). The neutron diffraction technique has been discussed in detail in chapter 4, but it is important to note that the Kowari instrument is based on a reactor source as opposed to ENGIN-X, which is a time-of-flight diffractometer. The principle feature of the thermal neutron beam from a reactor source is its wide spectrum of neutron flux as a function of wavelength from which a small range of wavelengths is extracted by a large single-crystal monochromator [48].

During the experiment, a monochromatic beam with a wavelength of 1.66Å was used. With this wavelength, the (211) reflection from the ferritic steel occurred at an angle 2θ = 89.6° which, being close to 90°, provided optimal spatial resolution and avoided peak asymmetry arising as a result of axial divergence [49]. The (211) peak was selected for measurement as, for materials with a body-centred cubic unit cell; it is less sensitive to inter-granular strains [48]. Both the incident and diffracted beam were defined in area by horizontal and vertical apertures, made from neutron absorbing masks (cadmium). The gauge volume, defined by the intersection of the incident and scattered beam was chosen to be $1 \times 1 \times 1$ mm^3. A two-dimensional position sensitive 3He detector was used to record the diffraction peaks.

The experimental set-up for the hoop and radial measurements is illustrated in Figure 5-32. The latter was created in SSCANSS software [50] for illustration purposes only. The software was not used for positioning and/or optimising the measurement procedure. Due to the simple geometry, the measurement line (which lies at the centre of the specimen) was easily located by conducting a series of surface scans in the radial (X) and

hoop (Y) directions. The Z-coordinate of the centre of the specimen was located using an optical theodolite aligned with the neutron beam.

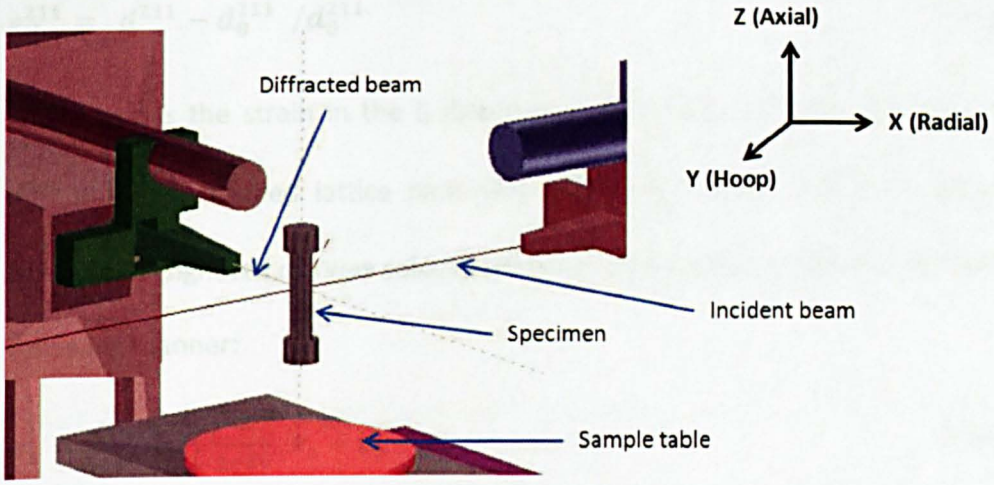

Figure 5-32: Schematic illustration of the experimental set-up for the hoop and radial strain measurements.

A total of 25 points were measured along a single line coincident with the specimen axis. The measurement points were located within the gauge length (central 40 mm section) and spaced at 1 mm intervals in the vicinity of the predicted maximum residual stress and 2 mm at all other locations. The hoop and axial components of strain were measured at each location. Due to the symmetry of the axial centre-line, the radial strains were assumed to be the same as the hoop strains. In determination of the un-stressed lattice parameter, measurements were made in the 'shoulder' of the specimen. This region was assumed to contain negligible stresses, based on finite element predictions (see section 5.5.2).

Having obtained the raw experimental data in the form of diffraction peaks measured in terms of counts (intensity) at successive angular positions of the detector, the peak positions were obtained by fitting a Gaussian-shaped function superposed on a sloping background to the measured data using the in-house analysis software. The fitting

precision, Δd/d was typically 5×10^{-5}. The elastic lattice strain was calculated from the relative shift of the d-spacing with respect to the stress-free d_0-spacing, as:

$$\varepsilon_{ij}^{211} = \left(d^{211} - d_0^{211} \right) / d_0^{211} \qquad \textbf{Equation 5-6}$$

where ε_{ij}^{211} is the strain in the ij direction, d^{211} is the measured lattice parameter and d_0^{211} is the unstrained lattice parameter. Then, the stress acting in orientation x for example, designated σ_x, was calculated using a generalised version of Hooke's law in the following manner:

$$\sigma_x = \frac{E}{1+v} \left[\varepsilon_x + \frac{v}{1-2v} \left(\varepsilon_x + \varepsilon_y + \varepsilon_z \right) \right] \qquad \textbf{Equation 5-7}$$

where E is the bulk elastic modulus for the material, v is Poisson's ratio, and ε_x, ε_y and ε_z are the measured strains in three orthogonal orientations x, y and z. In determining stresses it was assumed that the material was isotropic, with a bulk Young's modulus of 218 GPa and Poisson's ratio of 0.3 [46]. While it is desirable to use hkl-specific Young's modulus and Poisson's ratio (E_{211} and v_{211}), these values could not be calculated because of a lack of single crystal data for this material. The experimental uncertainties were derived using an error propagation method [51] which accounts for errors associated with the measurement of both d and d_0.

5.5.4 Results

A typical profile of the measured temperatures during the heating process is given in Figure 5-33 for the 4 thermocouples shown in Figure 5-30.

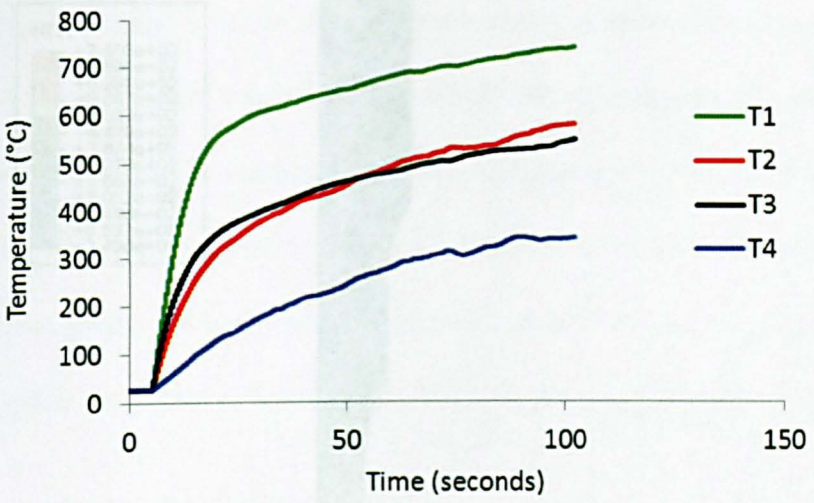

Figure 5-33: Temperature-time profile during heating of one of the FGHAZ simulated specimen.

Using the results in Figure 5-33, a second order polynomial was fitted through the data points as shown in Figure 5-34. The temperature 60 mm away from the centre was assumed to be 30°C. This equation was used to define the initial temperature of the specimen in ABAQUS [47], as shown in Figure 5-35.

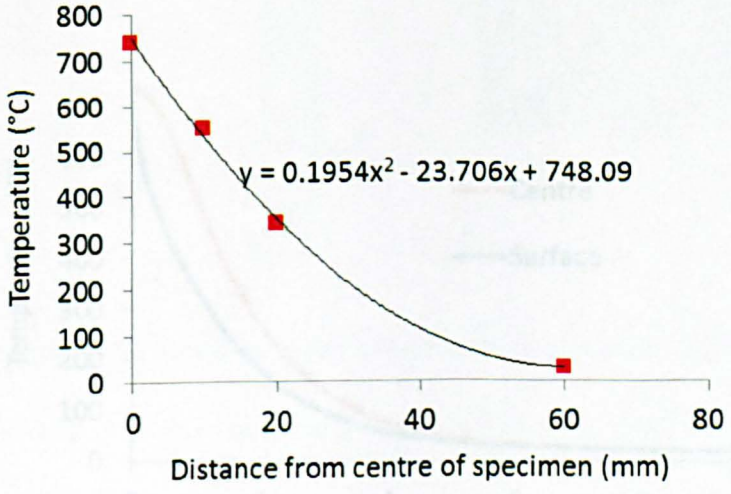

Figure 5-34: Second order polynomial fitted through the recorded temperatures at different positions along the gauge length. The temperature 60 mm away was not measured and was assumed to be 30°C.

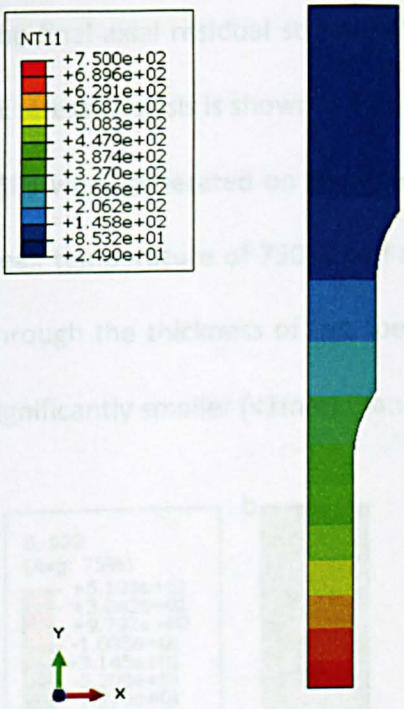

Figure 5-35: Initial temperature of the specimen defined using an analytical field.

The temperature-time history for positions at the centre of the specimen and its surface are shown in Figure 5-36. It is evident that the outer surface cools more rapidly than the centre.

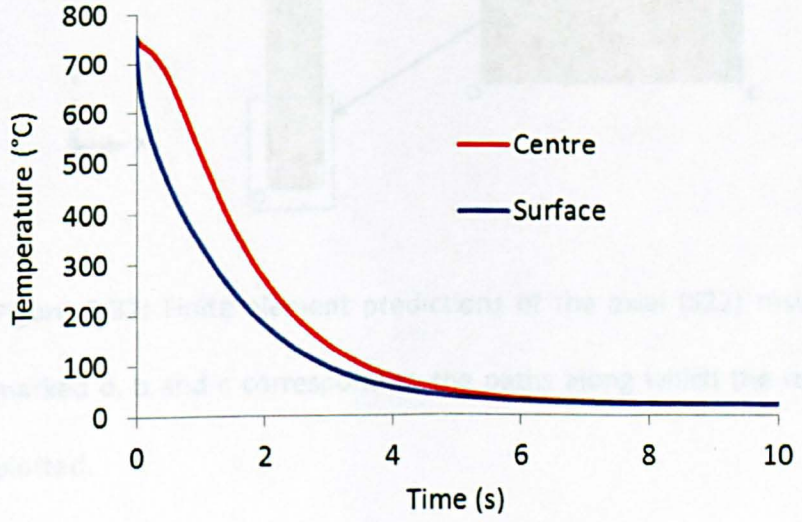

Figure 5-36: Temperature-time profile of the FGHAZ simulated specimen during the quenching simulation.

The final axial residual stresses (Y-direction) at room temperature determined from the FE stress analysis is shown in Figure 5-37. Highly compressive axial residual stresses ~ -200 MPa were generated on the exterior surface in the vicinity of the region heated to the peak temperature of 750°C and are balanced by tensile stresses of the order of 50 MPa through the thickness of the specimen. The length scale of the compressive region was significantly smaller (<1mm) than the tensile region (>3mm).

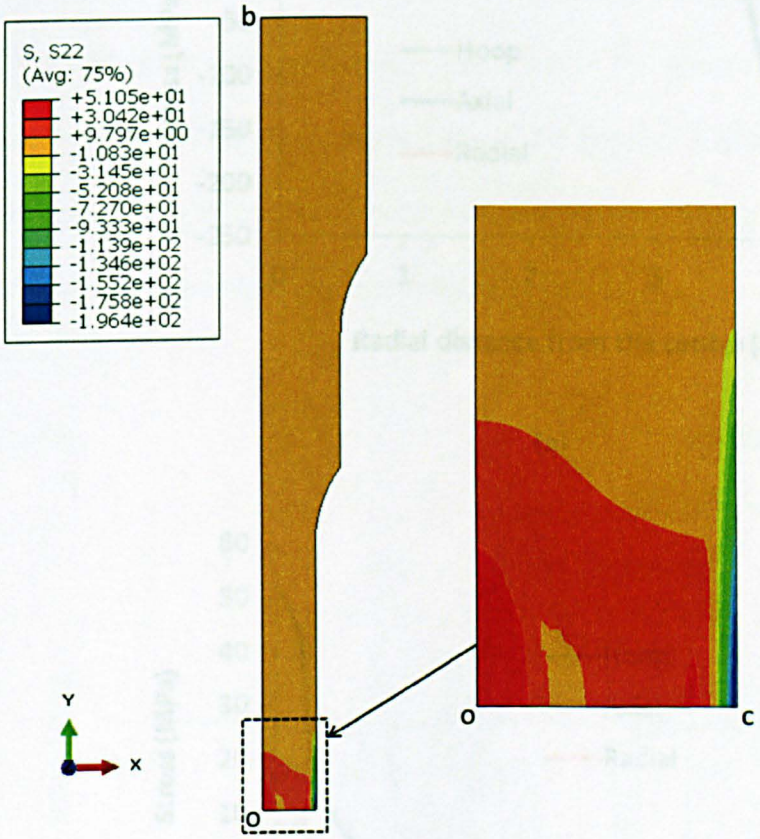

Figure 5-37: Finite element predictions of the axial (S22) residual stresses. The letters marked o, b and c correspond to the paths along which the results in Figure 5-35 were plotted.

Line profiles along the mid-section of the specimen (path o-c in Figure 5-37) and along the specimen axis (path o-b) are shown in Figure 5-38. The radial residual stresses were tensile throughout the thickness and decreased to zero as the surface was approached. The axial and hoop stresses were also tensile up to about 3 mm, but changed into

compression close to the surface. In Figure 5-38b, the hoop and radial stresses along the path o-b are identical, due to symmetry. The peak tensile stress was predicted to be ~51 MPa in the axial direction at the centre of the specimen, which was significantly higher than the hoop and radial stresses due to the greater constraint in the axial direction.

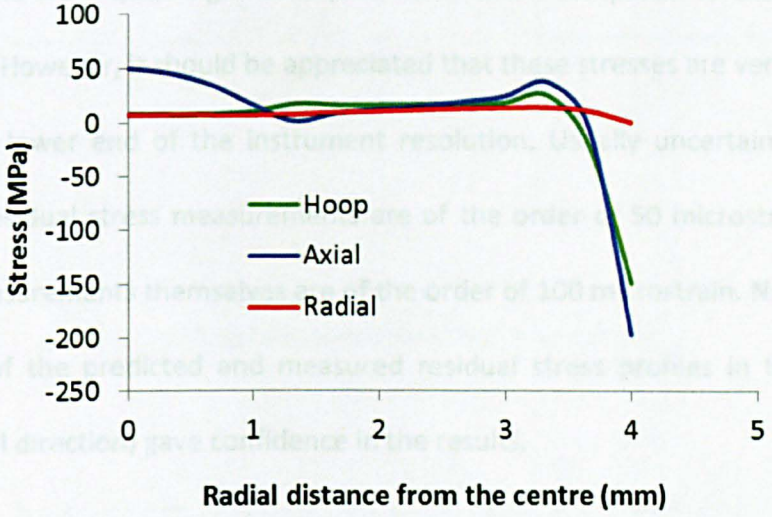

(a)

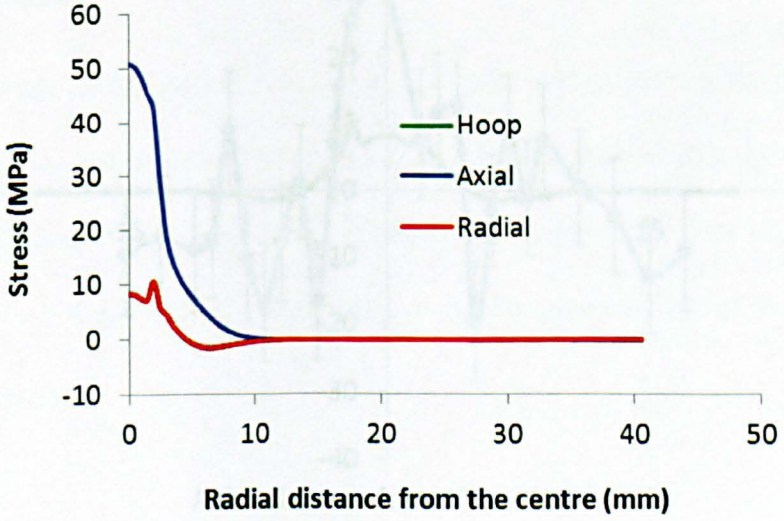

(b)

Figure 5-38: Finite element predictions of the residual stresses generated in the FGHAZ simulated specimens: (a) along path o-c and (b) along path o-b, as shown in Figure 5-34.

Figure 5-39 shows a comparison of predicted and measured residual stresses along the specimen axis (path o-b in Figure 5-37). Overall, both sets of results were in good agreement with each other. The maximum tensile hoop and axial stresses were measured to be ~30 and ~50 MPa respectively. We note that the errors associated with the neutron measurements were quite significant (±10 MPa) when compared to the magnitudes of the stresses. However, it should be appreciated that these stresses are very low which are towards the lower end of the instrument resolution. Usually uncertainties in neutron diffraction residual stress measurements are of the order of 50 microstrain, and in this case the measurements themselves are of the order of 100 microstrain. Nevertheless, the correlation of the predicted and measured residual stress profiles in the direction of interest (axial direction) gave confidence in the results.

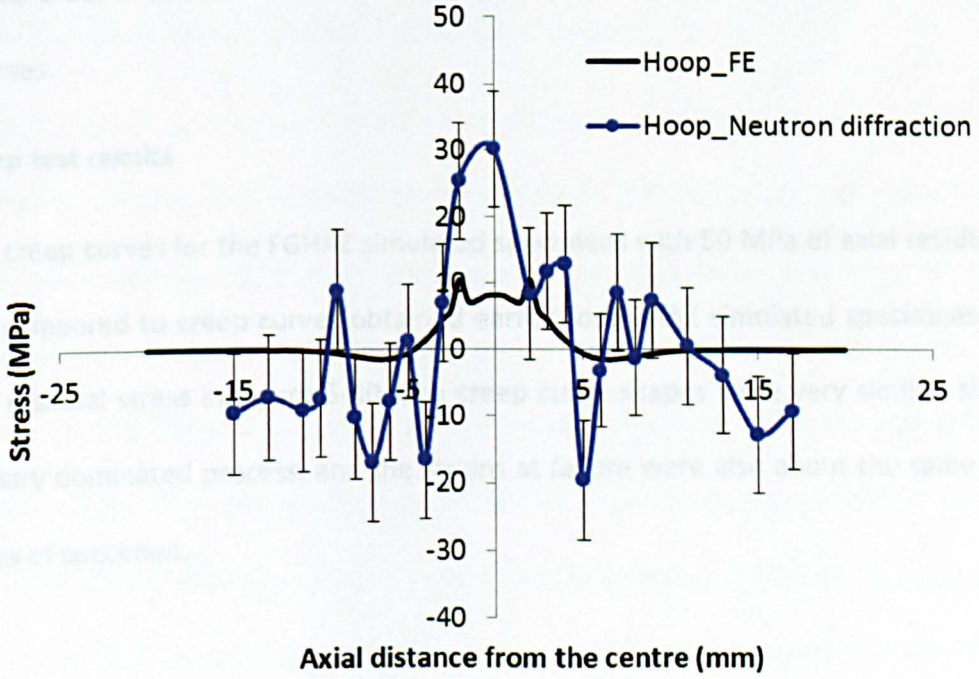

(a)

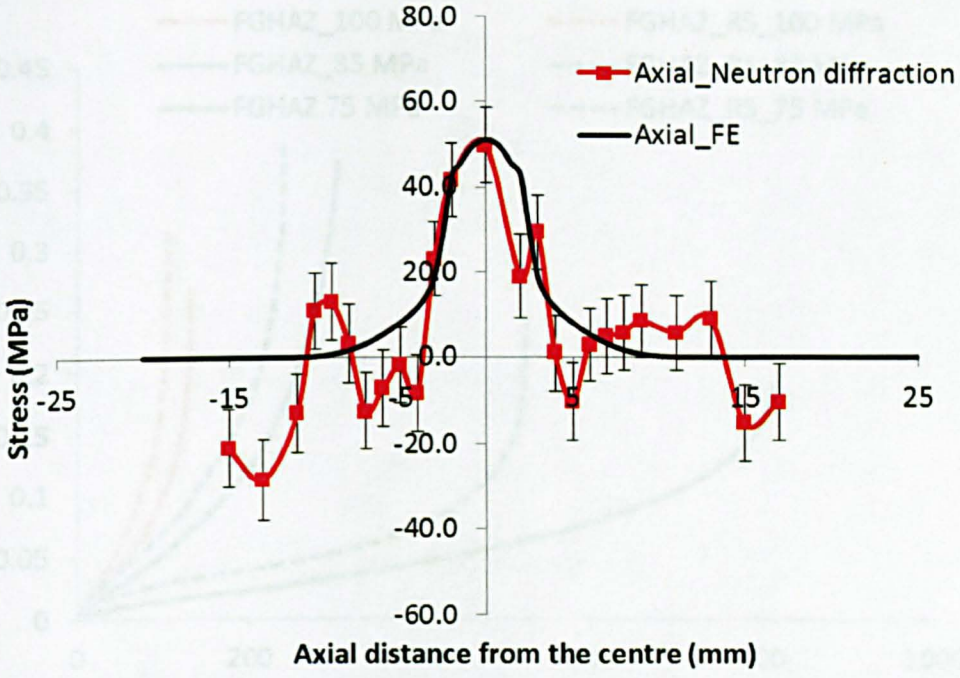

(b)

Figure 5-39: Predicted and measured (a) hoop residual stresses and (b) axial residual stresses.

Creep test results

The creep curves for the FGHAZ simulated specimens with 50 MPa of axial residual stress are compared to creep curves obtained earlier for FGHAZ simulated specimens without any residual stress in Figure 5-40. The creep curve shapes were very similar, showing a tertiary dominated process, and the strains at failure were also about the same for both types of specimen.

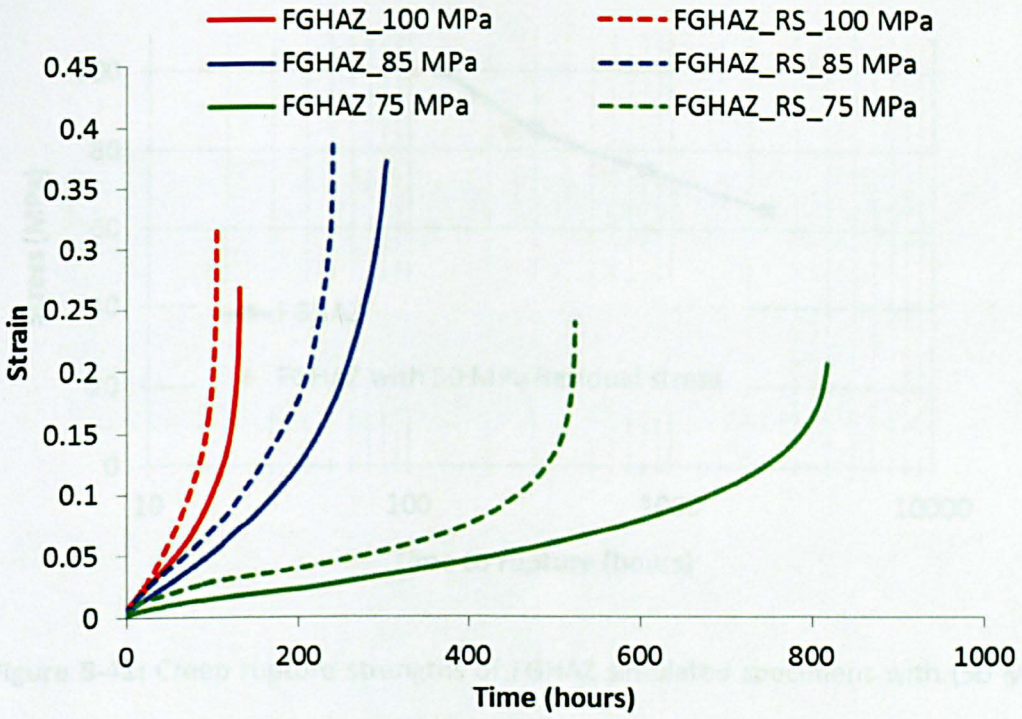

Figure 5-40: Creep curves for FGHAZ simulated specimens with (50 MPa) and without residual stresses, tested at 625°C at 3 different stresses.

The variation of time to rupture with applied stress level for the 2 types of specimen is provided in Figure 5-41 and summarised in Table 5-7. At all applied stress levels, the specimens with residual stresses showed a shorter time to rupture when compared to specimens with no residual stresses and it appears that the difference is more pronounced at the lowest applied stress level, where there was a 35% reduction in life. This is odd, because one would expect the residual stresses to relax with time and thus the rupture lives should have been closer in longer-term tests, unless it is the actual stress relaxation that is accelerating failure. Confirmatory repeat tests for combined loadings could not be conducted due to lack of specimens.

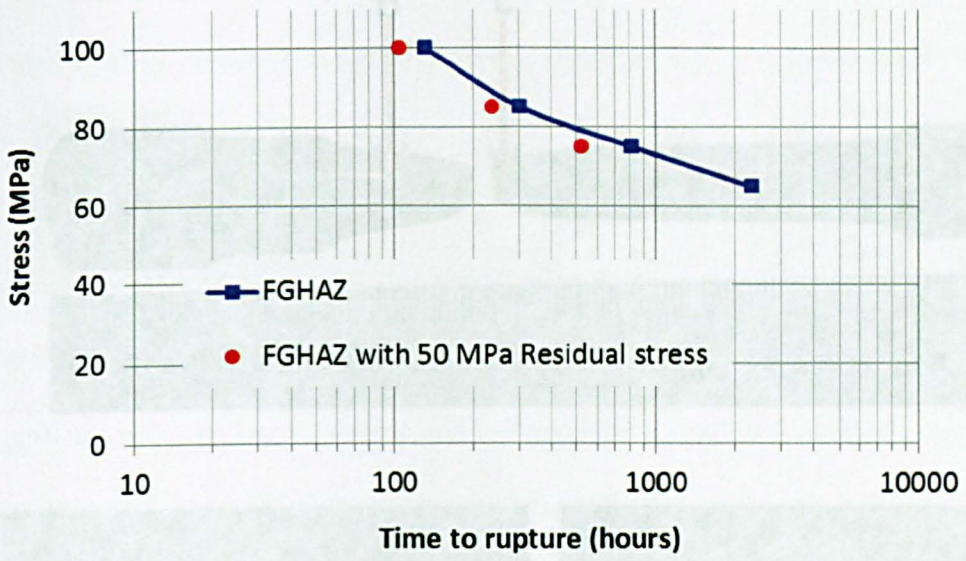

Figure 5-41: Creep rupture strengths of FGHAZ simulated specimens with (50 MPa) and without residual stresses, tested at 625°C.

Table 5-7: Tabulated values of creep rupture life and elongation of FGHAZ simulated specimens with 50 MPa residual stress at 625°C.

Stress (MPa)	Rupture life (hours)	Rupture elongation (%)
100	105	32
85	240	38.5
75	524	23.9

Post-test examination

Figure 5-42a shows a picture of a fractured FGHAZ simulated specimen with residual stresses, tested at 625°C at 75 MPa. The letters marked b and c correspond to locations where micrographs were captured and correspond to regions away from the failure (b) and in the vicinity of the failure (c).

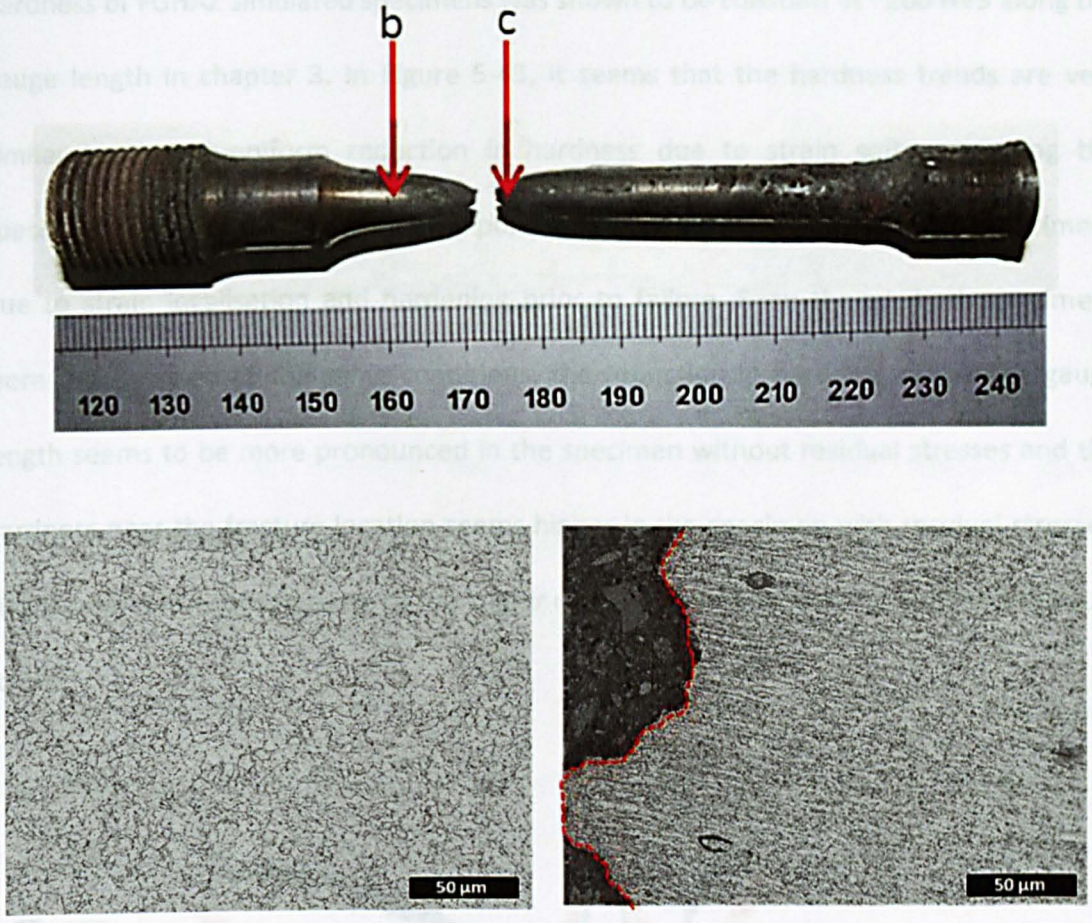

Figure 5-42: Ruptured FGHAZ simulated specimen with residual stresses creep tested at 625°C at 75 MPa (a) showing locations where micrographs presented in (b) and (c) were taken, corresponding to locations away from the failure and in the vicinity of the failure respectively. The dotted line in (c) shows the fracture location.

The microstructural features presented in Figure 5-42 are consistent with those observed in FGHAZ simulated specimens without any residual stresses. Very few cavities were observed in the vicinity of the failure which has been attributed to the effect of dynamic recrystallization, discussed earlier.

Hardness

Figure 5-43 shows typical hardness profiles measured on fractured FGHAZ simulated specimens with and without residual stresses, tested at 625°C at 75 MPa. The initial

hardness of FGHAZ simulated specimens was shown to be constant at ~200 HV5 along the gauge length in chapter 3. In Figure 5-43, it seems that the hardness trends are very similar i.e. a non-uniform reduction in hardness due to strain softening along the specimen gauge length. In the necking portion, the hardness increased in both specimens due to strain localisation and hardening prior to failure. Even though both specimens were creep tested at the same conditions, the reduction in hardness across the gauge length seems to be more pronounced in the specimen without residual stresses and the hardness near the fracture location seems higher in the specimen with residual stresses. This is probably a consequence of the longer rupture life of the specimen without residual stress.

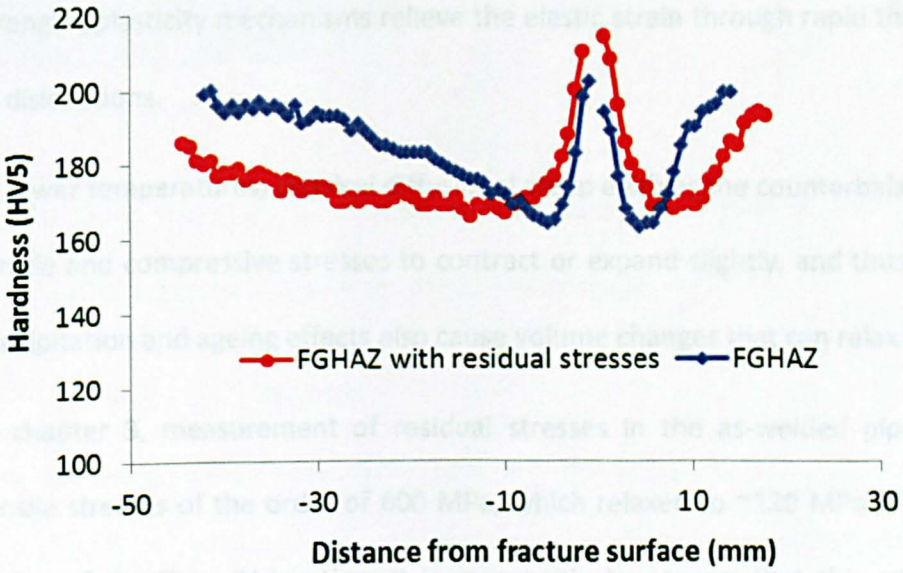

Figure 5-43: Hardness profile across FGHAZ simulated specimens with and without residual stresses creep tested at 625°C at 75 MPa.

5.6 Influence of residual stress relaxation due to PWHT

During welding, the peak temperature in the FGHAZ is just above the upper transformation temperature (Ac_3), which is not sufficiently high to completely dissolve

existing precipitates. On cooling, precipitation on retained large particles, such as $M_{23}C_6$ is favoured. During PWHT, severe coarsening occurs, which minimises the precipitation strength of the material and creates preferred nucleation sites for creep cavitation. These phenomena have often been used to explain why post-weld heat treatment at lower temperatures for shorter times result in longer creep rupture lives, for example see Parker and Stratford [52].

One of the factors that has often been neglected is residual stress relaxation during PWHT. This is likely to be an important factor because one of the following mechanisms occurs during residual stress relaxation by PWHT [53]:

At temperatures high enough to cause a substantial reduction in the material yield strength, plasticity mechanisms relieve the elastic strain through rapid thermal activation of dislocations.

At lower temperatures, classical diffusional creep enables the counterbalancing regions of tensile and compressive stresses to contract or expand slightly, and thus to redistribute. Precipitation and ageing effects also cause volume changes that can relax elastic stresses.

In chapter 3, measurement of residual stresses in the as-welded pipe revealed high tensile stresses of the order of 600 MPa, which relaxed to ~120 MPa after PWHT in the region of the Type IV location. It is reasonable to assume that this relaxation process introduced some level of creep damage in the weldment materials and that therefore the cross-weld specimens extracted from the PWHT pipe would contain some creep damage prior to the creep tests. Furthermore, the creep damage introduced may be exacerbated by the triaxial nature of the residual stresses [35].

5.6.1 Sample details

In order to study the influence of residual stress relaxation during PWHT, specimens were machined from the as-welded pipe; effectively relaxing the residual stresses that were initially present (Figure 5-44). The extracted specimens were then post weld heat treated to obtain a microstructure that is similar to the specimens extracted from the PWHT pipe, i.e. tempered martensite. The heat treatment cycle was the same as the one used for the pipes i.e. 750°C for 4 hours. The specimens were creep tested at 625°C at 3 different stresses; 100, 85 and 75 MPa.

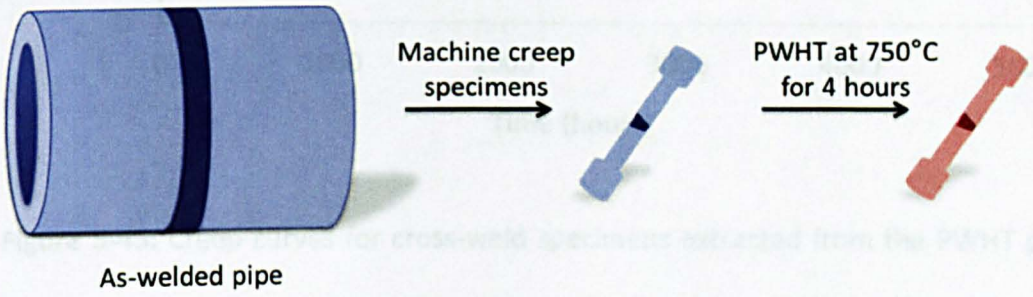

Figure 5-44: Schematic illustration of the processing history of cross-weld specimens PWHT after being machined from the as-welded pipe.

5.6.2 Results

The accumulation of strain with time for the creep tests on cross-weld specimens extracted from the as-welded pipe with subsequent PWHT are summarised in Figure 5-45. The results of cross-weld tests from the PWHT pipe are also shown for comparison. The general shapes of the creep curves for both types of specimens are very similar, with well-defined primary, secondary and tertiary stages. At 85 and 75 MPa, it appears that the initial elastic strain on loading is slightly higher for the specimens from the as-welded pipe with subsequent PWHT. The strains at failure for both specimens were very similar.

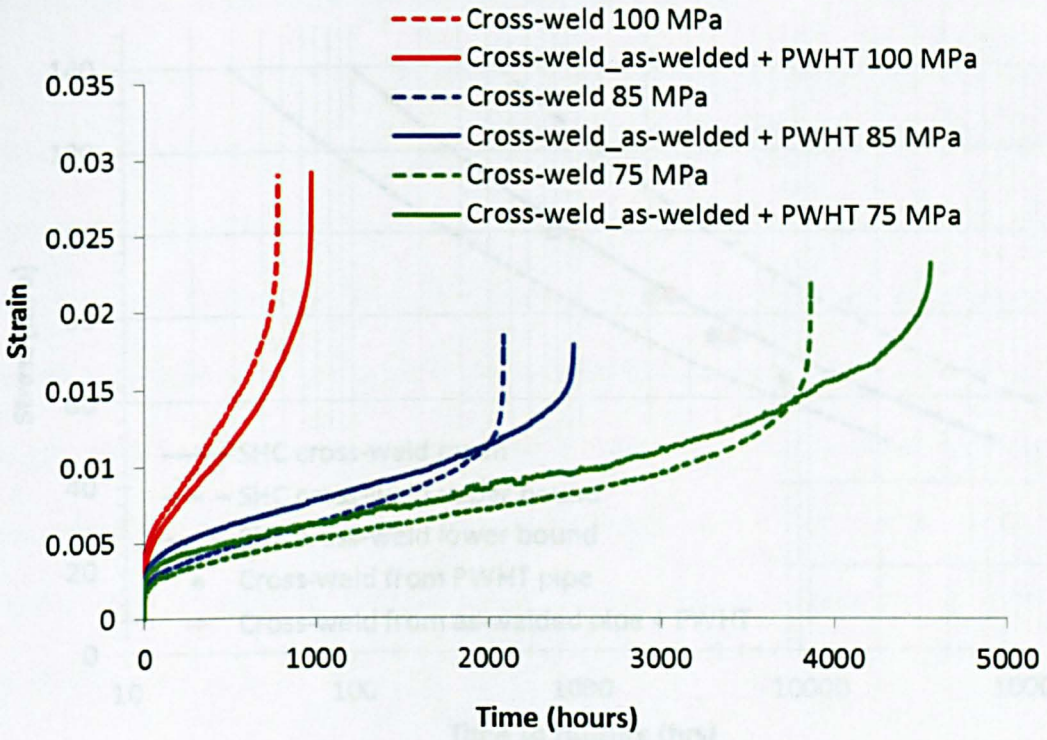

Figure 5-45: Creep curves for cross-weld specimens extracted from the PWHT pipe and cross-weld specimens extracted from the as-welded pipe with subsequent PWHT.

The time to rupture for the two types of cross-weld specimens are compared in Figure 5-46 and tabulated in Table 5-8. The predicted cross-weld mean values, calculated using the SHC committee equation and the ± 20% scatter band are also shown.

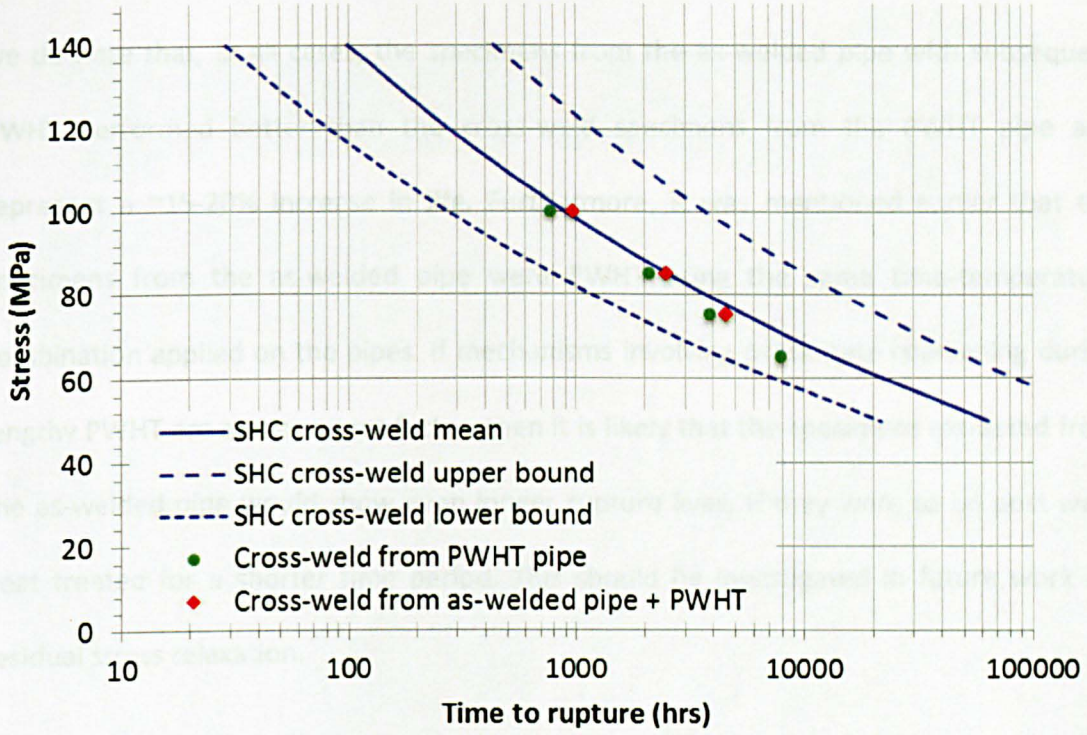

Figure 5-46: Creep rupture strengths of cross-weld specimens PWHT after being machined from the as-welded pipe and cross-weld specimens from the PWHT pipe. The predicted P91 cross-weld creep rupture strength, calculated using the SHC committee equation and the ± 20% scatter bands are also shown.

Table 5-8: Tabulated values of creep rupture life and elongation of cross-weld specimens PWHT after being machined from the as-welded pipe at 625°C.

Stress (MPa)	Rupture life (hours)	Rupture elongation (%)
100	972	2.9
85	2496	1.8
75	4556	2.3

From Figure 5-46, the times to rupture of both types of cross-weld specimens were very similar and well aligned with the SHC committee predicted mean values, and gives the

impression that stress relaxation due to PWHT may be relatively unimportant. However, we do note that, in all cases, the specimens from the as-welded pipe with subsequent PWHT performed better than the cross-weld specimens from the PWHT pipe and represent a ~15-20% increase in life. Furthermore, it was mentioned earlier that the specimens from the as-welded pipe were PWHT using the same time-temperature combination applied on the pipes. If mechanisms involving precipitate coarsening during lengthy PWHT are an important factor, then it is likely that the specimens extracted from the as-welded pipe would show even longer rupture lives, if they were to be post weld heat treated for a shorter time period. This should be investigated in future work on residual stress relaxation.

Post-test examination

Figure 5-47a shows a picture of one of the fractured cross-weld specimen extracted from an as-welded pipe with subsequent PWHT, tested at 625°C at 75 MPa. The letters marked b through to e correspond to locations where optical micrographs were taken and correspond to the parent metal (b), weld metal (c), CGHAZ (d) and FGHAZ (e). The FGHAZ micrograph (e) was intentionally captured at a lower magnification to highlight the extent of cavitation.

It is clear from Figure 5-47 that the specimen ruptured in the FGHAZ region (Type IV location). The cross-weld specimens from the as-welded pipe with subsequent PWHT showed similar features as the cross-weld specimens machined from the PWHT pipe. Creep cavities with characteristic dimensions in the order of 10 μm were evident in the FGHAZ region.

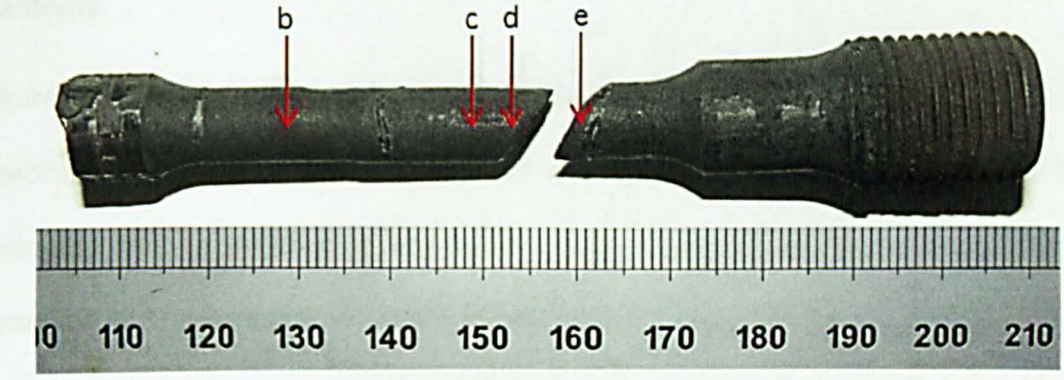

Ruptured specimen

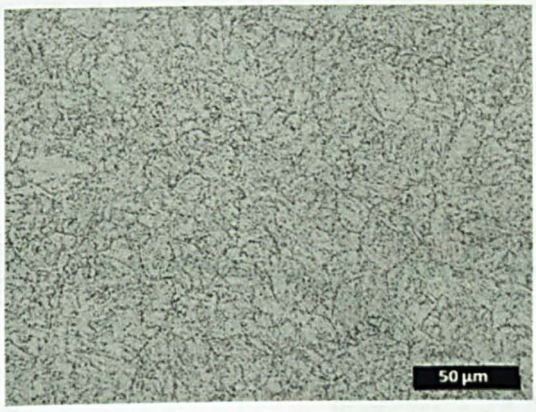

Parent metal

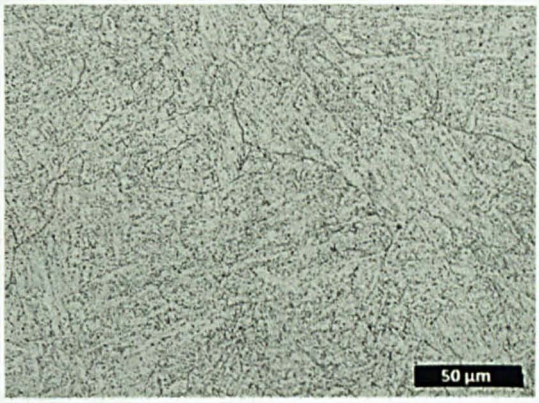

Weld metal

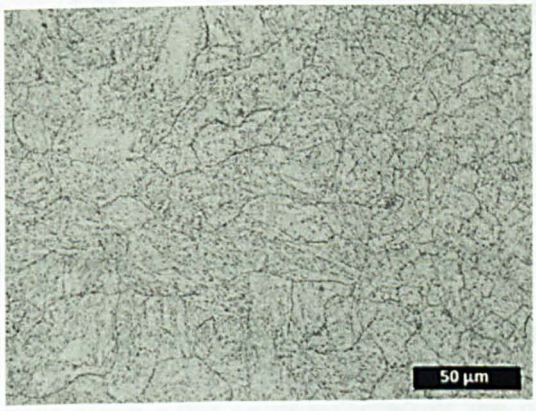

CGHAZ

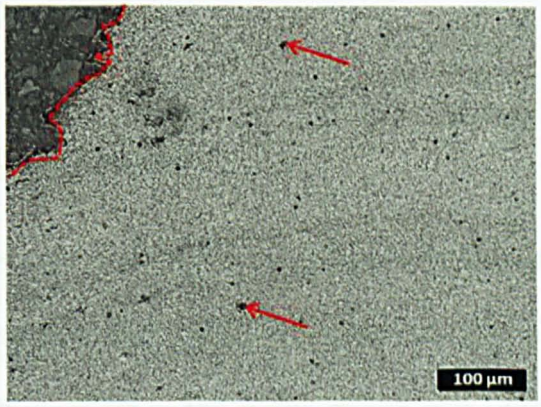

FGHAZ

Figure 5-47: Ruptured cross-weld specimen extracted from an as-welded pipe with subsequent PWHT tested at 75 MPa at 625°C. The letters marked b through to e, correspond to locations where optical micrographs were captured, corresponding to the parent metal, weld metal, CGHAZ and FGHAZ respectively. Arrows in (e) highlight examples of creep cavities and the dotted line shows the fracture location.

Hardness

Figure 5-48 shows a typical hardness profile measured on the fractured cross-weld specimen shown in Figure 5-47. The hardness profile across a cross-weld specimen extracted from a PWHT pipe and tested at the same conditions is also shown for comparison. The hardness variations in both specimens were very similar and it can be confirmed that failure occurred in the FGHAZ region (a location between the CGHAZ - maximum hardness and ICHAZ - minimum hardness).

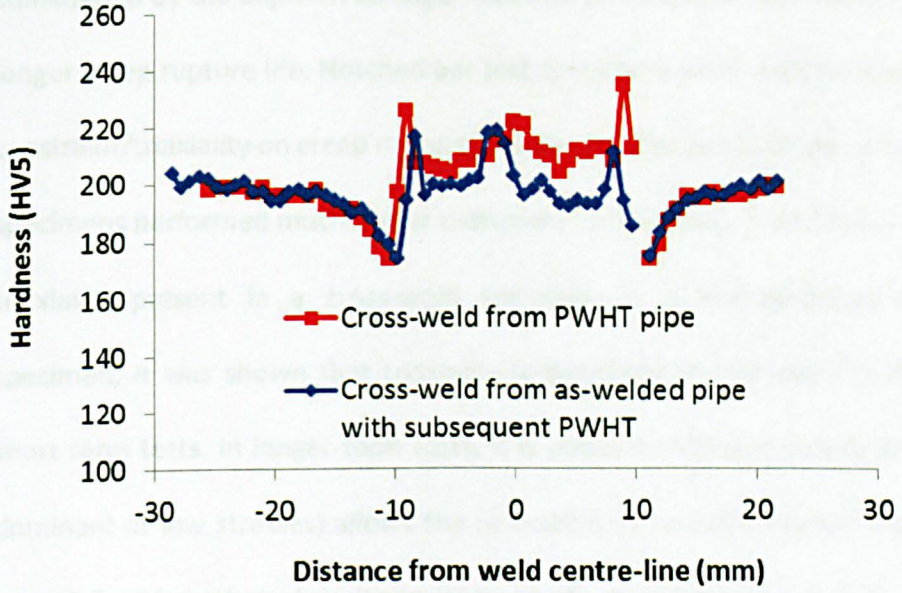

Figure 5-48: Hardness profile along a fractured cross-weld specimen extracted from an as-welded pipe with subsequent PWHT and tested at 625°C at 75 MPa. Typical hardness profile along a line representative of the mid-thickness of the PWHT pipe is also shown for comparison.

5.7 Conclusions

The creep behaviour of a P91 welded joint was characterised by conducting cross-weld creep tests at 625°C at 4 different stresses. All the specimens ruptured in the Type IV position i.e. FGHAZ. In order to study in more detail the behaviour of this potentially weak

zone, creep tests were also conducted on simulated FGHAZ specimens at the same temperature and stresses to enable a direct comparison. It was found that the creep rupture times of the cross-weld specimens were much longer than the FGHAZ simulated specimens, indicating that factors other than microstructure were influencing the rupture life. There was also a clear distinction in the development of cavitational damage in two types of specimens which suggested that the stress states are completely different.

One possible explanation was that the Type IV zone in the cross-weld specimens is constrained by the adjacent stronger material (parent and weld metal), which results in a longer creep rupture life. Notched bar test specimens were used to investigate the role of constraint/triaxiality on creep rupture life. The results clearly showed that notched FGHAZ specimens performed much better than plain FGHAZ specimens. Thus, by reproducing the triaxiality present in a cross-weld specimen in a homogeneous FGHAZ simulated specimen, it was shown that triaxiality is beneficial in improving creep life, at least in short term tests. In longer-term tests, it is possible that grain boundary sliding (which is dominant at low stresses) allows the relaxation of constraint which leads to the Type IV zone deforming relatively independently of adjacent stronger material.

Residual stresses were introduced successfully in FGHAZ simulated specimens by a heating and quenching approach. The residual stresses were measured to be ~50 MPa in the axial direction which correlated very well with finite element predictions. During creep testing of these specimens, it was evident that specimens with residual stresses showed a clear reduction in life, which was larger for the test at the lowest stress level. One would expect the residual stresses to relax with time and thus the rupture lives should have been closer in longer-term tests, unless it is the stress relaxation that introduces creep damage and accelerates failure. A firm conclusion cannot be made at this stage, due to the relatively low residual stresses introduced and the relatively short

duration of the tests. The author recommends that larger diameter specimens should be used in the future, so that higher residual stresses can be introduced (as we are limited to the temperature the specimen can be heated to) and longer term tests should be carried out to establish the effects of residual stresses on the creep rupture behaviour of martensitic steels.

One of the factors that was thought to be of potential significance is stress relaxation during PWHT. To investigate this hypothesis, specimens were machined from an as-welded pipe to relax the residual stresses to low levels and then post-weld heat treated to achieve the same microstructure. A comparison of the creep rupture behaviour of cross-weld specimens from the PWHT pipe and cross-weld specimens PWHT after being machined from the as-welded pipe showed that the rupture lives of the latter were longer by ~15-20%. If mechanisms involving precipitate coarsening during lengthy PWHT are an important factor, then it is likely that the specimens extracted from the as-welded pipe would show even longer rupture lives, if they were to be post weld heat treated for a shorter time period.

5.8 References

[1] R. W. Evans and B. Wilshire, Introduction to creep. London: The Institute of Materials, 1993.

[2] G. E. Dieter, Mechanical Metallurgy. London: McGraw-Hill, 1988.

[3] ASTM International, "ASTM E139 - 11 Standard Test Methods for Conducting Creep, Creep-Rupture, and Stress-Rupture Tests of Metallic Materials."

[4] British Standards Institution, "BS EN ISO 204:2009(E) Metallic materials - Uniaxial creep testing in tension - Method of test," London, 2009.

[5] ASTM International, "ASTM E633-00, Standard Guide for Use of Thermocouples in Creep and Stress-Rupture Testing to 1800°F (1000°C) in Air," West Conshohocken, PA, 2005.

[6] K. Laha, K. S. Chandravathi, P. Parameswaran, K. B. S. Rao, and S. L. Mannan, "Characterization of Microstructures across the Heat-Affected Zone of the Modified 9Cr-1Mo Weld Joint to Understand Its Role in Promoting Type IV Cracking," Metallurgical and Materials Transactions A, vol. 38, no. 1, pp. 58–68, Jan. 2007.

[7] J. A. Francis, W. Mazur, and H. K. D. H. Bhadeshia, "Review Type IV cracking in ferritic power plant steels," Materials Science and Technology, vol. 22, no. 12, pp. 1387–1395, Dec. 2006.

[8] J. A. Francis and W. Mazur, "Welding Procedures and Type IV Phenomena," in Trends in Welding Research: Proceedings of the 7th International Conference, 2006, pp. 737–742.

[9] EPRI, "Optimal Hardness of P91 Weldments - Interim Report," Palo Alto, 2003.

[10] M. Tabuchi and Y. Takahashi, "Evaluation of Creep Strength Reduction Factors for Welded Joints of Modified 9Cr-1Mo Steel," Journal of Pressure Vessel Technology, vol. 134, no. 3, p. 031401, 2012.

[11] ECCC, "Data acceptability criteria and data generation: Creep data for welds," vol. 3 Part II, no. 3, 2004.

[12] I. A. Shibli, "Overview of the HIDA project," in 2nd International HIDA Conference on "Advances in Defect Assessment in High Temperature Plant," 2000.

[13] ECCC, "ECCC data sheet, Steel Grade 91 (X10CrMoVNb9-1)," 2009.

[14] F. Abe, "Introduction," in in Creep-resistant steels, F. Abe, T. U. Kern, and R. Viswanathan, Eds. Cambridge, England: Woodhead Publishing Limited, 2008, pp. 3–14.

[15] K. Kimura, H. Kushima, and F. Abe, "Heterogeneous changes in microstructure and degradation behaviour of 9Cr-1Mo-V-Nb steel during long term creep," Key Engineering Materials, vol. 171–174, pp. 483–490, 2000.

[16] B. Wilshire and H. Burt, "Yield stress rationalization of creep and creep fracture properties," Scripta Materialia, vol. 53, no. 8, pp. 909–914, Oct. 2005.

[17] H. Burt and B. Wilshire, "Theoretical and practical implications of creep curve shape analyses for 2124 and 2419," Metallurgical and Materials Transactions A, vol. 35, no. 6, pp. 1691–1701, 2004.

[18] B. Wilshire and H. Burt, "Creep Data Rationalization for Power Plant Steels," Materials Science Forum2, vol. 539–543, pp. 254–261, 7AD.

[19] B. Wilshire and H. Burt, "Creep strain analysis for steel," in in Creep-resistant steels, F. Abe, T. U. Kern, and R. Viswanathan, Eds. Cambridge, England: Woodhead publishing limited, 2008, pp. 421–442.

[20] M. Tabuchi, H. Hongo, Y. Li, T. Watanabe, and Y. Takahashi, "Evaluation of Microstructures and Creep Damages in the HAZ of P91 Steel Weldment," Journal of Pressure Vessel Technology, vol. 131, no. 2, p. 021406, 2009.

[21] Y. Li, H. Hongo, M. Tabuchi, Y. Takahashi, and Y. Monma, "Evaluation of creep damage in heat affected zone of thick welded joint for Mod.9Cr–1Mo steel," International Journal of Pressure Vessels and Piping, vol. 86, no. 9, pp. 585–592, Sep. 2009.

[22] T. Watanabe, M. Tabuchi, M. Yamazaki, H. Hongo, and T. Tanabe, "Creep damage evaluation of 9Cr–1Mo–V–Nb steel welded joints showing Type IV fracture," International Journal of Pressure Vessels and Piping, vol. 83, no. 1, pp. 63–71, Jan. 2006.

[23] T. Ogata, T. Sakai, and M. Yaguchi, "Damage characterization of a P91 steel weldment under uniaxial and multiaxial creep," Materials Science and Engineering: A, vol. 510–511, pp. 238–243, Jun. 2009.

[24] H. K. D. H. Bhadeshia, A. Strang, and D. J. Gooch, "Ferritic power plant steels: remanent life assessment and approach to equilibrium," International Materials Reviews, vol. 43, no. 2, p. 45, 1998.

[25] F. Masuyama, "Hardness Model for Creep Life Assessment of High Strength Martensitic Steels," Materials Science and Engineering, 2008.

[26] F. Abe, "Boundary and sub-boundary hardening in high-Cr ferritic steels during long-term creep at 650°C," in 34th MPA Seminar "Materials and Components Behaviour in Energy & Plant Technology," 2008.

[27] S. T. Kimmins and D. J. Smith, "On the relaxation of interface stresses during creep of ferritic steel weldments," The Journal of Strain Analysis for Engineering Design, vol. 33, no. 3, pp. 195–206, Jan. 1998.

[28] C. J. Middleton and E. Metcalfe, "A review of laboratory Type IV cracking data in high chromium ferritic steels," in International Conference Steam Plants for the 1990's, 1990.

[29] F. V Ellis, "Review of Type IV Cracking in Piping Welds - Final Report," Palo Alto, 1997.

[30] F. Abe and M. Tabuchi, "Microstructure and creep strength of welds in advanced ferritic power plant steels," Science and Technology of Welding and Joining, vol. 9, no. 1, pp. 22–30, Feb. 2004.

[31] L. Falat, a. Výrostková, V. Homolová, and M. Svoboda, "Creep deformation and failure of E911/E911 and P92/P92 similar weld-joints," Engineering Failure Analysis, vol. 16, no. 7, pp. 2114–2120, Oct. 2009.

[32] D. J. Gooch and S. T. Kimmins, "A study of Type IV cracking in 0.5%CrMoV/2.25CrMo weldments," in 3rd International Conference on Creep and Fracture of Engineering Materials and Structures, 1987, pp. 698–703.

[33] A. Belyakov, R. Kaibyshev, V. Dudko, V. Skorobogatykh, and I. Schenkova, "Effect of Heat Treatment and Creep on Microstructure of a 9% Cr Steel," in 2nd ECCC Creep Conference: Creep and Fracture in High Temperature Components-Design & Life Assessment Issues, 2009, pp. 1038–1045.

[34] V. Gaffard, "Experimental study and modelling of high temperature creep flow and damage behaviour of 9Cr1Mo-NbV steel weldments," PhD. Thesis, Ecole Des Mines De Paris, France, 2004.

[35] Y. Takahashi, "Identification of Stress Multiaxiality Effect on Creep Damage by a Combination of Experiments and Numerical Analyses. PVP2009-78070," in Proceedings of the ASME 2009 Pressure Vessels and Piping Division Conference, 2009.

[36] G. A. Webster, S. R. Holdsworth, M. S. Loveday, K. Nikbin, I. J. Perrin, H. Purper, R. P. Skelton, and M. W. Spindler, "A Code of Practice for conducting notched bar creep tests and for interpreting the data," Fatigue Fracture of Engineering Materials and Structures, vol. 27, pp. 319–342, Apr. 2004.

[37] P. W. Bridgman, Studies in large plastic flow and fracture. New York: McGraw-Hill, 1952.

[38] T. H. Hyde, I. a Jones, S. Peravali, W. Sun, J. G. Wang, and S. B. Leen, "Anisotropic Creep Behaviour of Bridgman Notch Specimens," Proceedings of the Institution of Mechanical Engineers, Part L: Journal of Materials: Design and Applications, vol. 219, no. 3, pp. 163–175, Jun. 2005.

[39] D. R. Hayhurst, F. A. Leckie, and C. J. Morrison, "Creep rupture of notched bars," Proceedings of the Royal Society of London. Series A1, vol. 360, pp. 243–264, 1978.

[40] J. R. Rice, "Constraints on the diffusive cavitation of isolated grain boundary facets in creeping polycrystals," Acta Metallurgica, vol. 29, no. 4, pp. 675–681, Apr. 1981.

[41] S. Hossain, C. E. Truman, D. J. Smith, and M. R. Daymond, "Application of quenching to create highly triaxial residual stresses in type 316H stainless steels," International Journal of Mechanical Sciences, vol. 48, no. 3, pp. 235–243, Mar. 2006.

[42] R. L. Huddleston, "An Improved Multiaxial Creep-Rupture Strength Criterion," Journal of Pressure Vessel Technology, vol. 107, no. 4, pp. 421–429, Nov. 1985.

[43] M. W. SPINDLER, "The multiaxial creep ductility of austenitic stainless steels," Fatigue & Fracture of Engineering Materials & Structures, vol. 27, no. 4, pp. 273–281, Apr. 2004.

[44] S. Hossain, C. E. Truman, D. J. Smith, R. L. Peng, and U. Stuhr, "A study of the generation and creep relaxation of triaxial residual stresses in stainless steel," International Journal of Solids and Structures, vol. 44, no. 9, pp. 3004–3020, May 2007.

[45] F. Hosseinzadeh, "Residual stresses in shrink fits and quenched components," University of Bristol, 2009.

[46] K. Haarmann, J. C. Vaillant, B. Vandenberghe, W. Bendick, and A. Arbab, The T91/P91 book, 2nd ed. Vallourec & Mannesmann Tubes, 2002.

[47] ABAQUS, "ABAQUS/Standard Documentation Version 6.10.2," 2010.

[48] M. T. Hutchings, P. J. Withers, T. M. Holden, and T. Lorentzen, Introduction to the characterization of residual stress by neutron diffraction. Florida, USA: Taylor & Francis, 2005.

[49] J. A. Francis, H. J. Stone, S. Kundu, R. B. Rogge, H. K. D. H. Bhadeshia, P. J. Withers, and L. Karlsson, "The Effects of Filler Metal Transformation Temperature on Residual Stresses in a High Strength Steel Weld," Transactions of the ASME, Journal of Pressure Vessels Technology, vol. 131, no. 4, pp. 1–21, 2009.

[50] J. A. James, J. R. Santisteban, L. Edwards, and M. R. Daymond, "A virtual laboratory for neutron and synchrotron strain scanning," Physica B: Condensed Matter, vol. 350, no. 1–3, pp. E743–E746, Jul. 2004.

[51] J. R. Taylor, An introduction to error analysis. Oxford: Oxford University Press, 1982.

[52] D. Parker and G. C. Stratford, "Effect of heat treatment on creep and fracture behaviour of 1.25Cr-0.5Mo steel," Materials Science and Technology, vol. 11, pp. 1267–1273, 1995.

[53] M. R. James, "Relaxation of Residual Stresses: An Overview," Advances in Surface Treatments: technology-applications-effects, vol. 4, pp. 349–365, 1987.

Chapter 6

Application of Digital Image Correlation to P91 cross-weld specimens

6.1 Introduction

In the past, parent materials have been known to fail due to manufacturing faults, little understood metallurgical effects at that time, and/or non-safe operating conditions. However, today these situations occur very infrequently, largely due to improved steel manufacturing processes, a better understanding of long-term metallurgical changes in creep service, and improved control and monitoring of operating parameters within power plants. Therefore, it is more often the integrity and strength of the welded joints that ultimately determine overall plant performance, structural integrity, and the life of components.

Weldments consist of different zones (parent material, heat-affected zone (HAZ), and the fusion zone) across which the mechanical properties (elastic modulus, yield stress and creep strength) vary, and this influences local strains and the stress states which develop under load and with time. The size and shape of structural weldments impose global constraints on the local deformation behaviour. Moreover, the directions of primary and secondary stresses relative to the material/geometric configuration introduce loading constraint. These metallurgical, geometric and loading constraint factors all contribute to the highly complex deformation behaviour in structural weldments.

Life assessment methods for structures operating at high temperatures are usually based on the unaxial deformation and rupture properties of plain (homogeneous) parent material or weld metal. In order to develop more accurate methods for predicting the life and integrity of welded joints, it is important to quantify the underlying deformation behaviour of the different material subzones adjacent to the weld metal.

Test methods based on simulated specimens, like the one described in Chapter 3, or small-scale tests involving miniature specimens, for example impression creep or small punch creep [1], are usually used to measure graded tensile/creep properties across a weldment. Small-scale techniques are very useful in the acquisition of specific materials' data from service exposed plant components, without the associated penalty of significant material removal that would jeopardise the structural integrity of the components [1]. However, data obtained from simulated metallurgical zones may not be representative of the behaviour of material in the welded joint, and there is sometimes uncertainty about the validity of data from tests on unconventional small samples. Furthermore, such tests are expensive. Thus the prospect of quantifying the behaviour of different subzones within a welded joint in a single cross-weld test is attractive, particularly if the geometry and loading constraint factors can be controlled and understood.

In recent years, efficient tools for full-field deformation measurement have been developed, for example Electron speckle pattern interferometry (ESPI) [2], Moiré interferometry [3] and digital image correlation (DIC) [4], [5]. The objective of this chapter is to demonstrate how a DIC based experimental technique can be applied to measure the local deformation behaviour within P91 steel welds during cross-weld tensile and creep testing. It is envisaged that the results arising from this work will provide mechanical test data in the form of stress-strain properties, yield stresses and creep

deformation curves, which can be incorporated into finite element models, or used in structural integrity assessments. In addition, by using DIC, we have endeavoured to contribute towards an understanding of the following:

- Creep damage initiation and propagation in P91 welds. With DIC, two-dimensional (2D) creep strain maps can be obtained, which can give insights relating to damage initiation and propagation. This can be particularly useful in determining an optimum joint configuration and/or choosing an appropriate filler metal.
- The strain at failure in the HAZ. Type IV failures have a macroscopic appearance typical of low ductility failures (2-3%) but, when looking at the behaviour of FGHAZ simulated specimens, strains as high as 40% have been measured (see Chapter 5). It is possible that, in the region of the Type IV zone in cross-weld specimens, there is significant strain accumulation, which would suggest that enhanced creep cavitation and thus Type IV cracking may be related to high strain localisation in the HAZ. The DIC technique has the potential to provide us with detailed information about the spatial distribution of tensile/creep strain and the development of local deformation as a function of time.

6.2 Principles of DIC

Digital Image Correlation (DIC) is a non-contact optical method that can be used in conjunction with mechanical tests (e.g. tensile or creep tests) to measure the local deformation on an object's surface. This is done by tracking contrasting features (or speckle patterns) on the sample surface whilst it is being deformed, and analysing the displacement of the patterns within discretised subsets or facet elements of the whole image [6], as shown in Figure 6-1. In order to compute the displacements of a point, a square reference subset centred at that point in the reference image is chosen and used

to track its corresponding location in the deformed image by using correlation functions. Commonly used cross-correlation or sum-squared difference correlation criteria are described elsewhere [7], [8], [9].

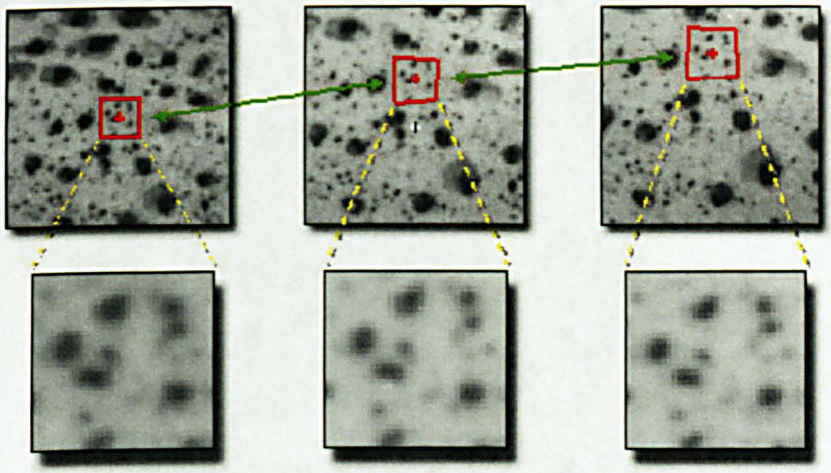

Figure 6-1: Pattern tracking using Digital Image Correlation [10]

The reason why a square subset, rather than an individual pixel is selected for matching is that a subset comprises of a wider variation in grey scale levels, which will distinguish itself from other subsets, and can therefore be more uniquely identified in the deformed image [7]. The differences in the positions of the reference subset centre and the target subset centre yield the in-plane displacement vector at that point, which can be subsequently used to calculate the strain components.

6.3 Application of DIC to P91 cross-weld specimens

6.3.1 Specimen details

To investigate the stress-strain (tensile) and creep properties of the P91 steel welded pipe, test specimens containing all the different zones (i.e. weld metal, HAZ and parent metal on both sides of the weld) were extracted (using wire electrical discharge machining) from the mid-thickness position in the post-weld heat-treated P91 pipe as illustrated in Figure 6-2.

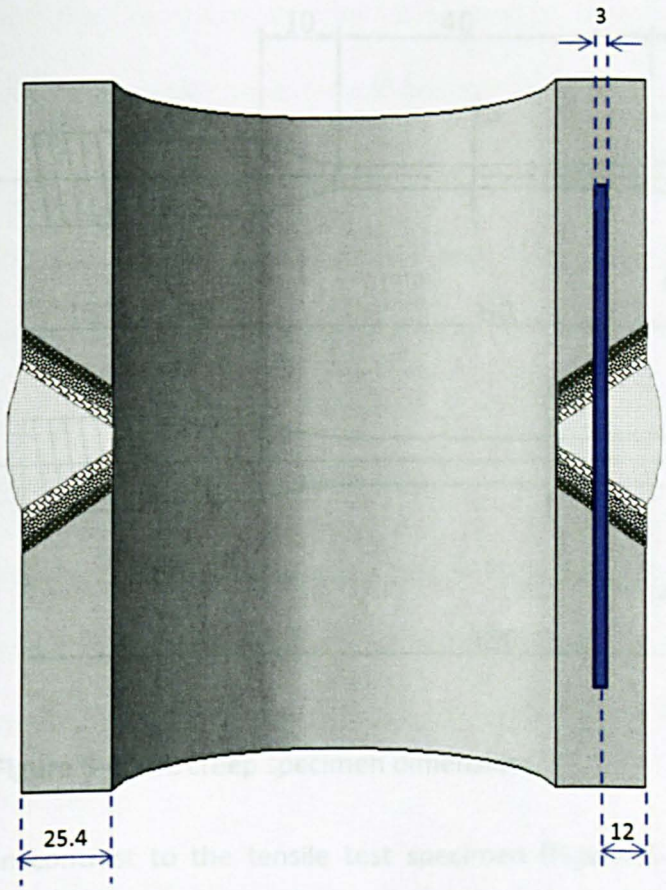

Figure 6-2: Specimen sampling location.

The specimen dimensions were in accordance with ASTM E8/E 8M-08 Standard Test Method for Tension Testing of Metallic Material [11] and are given in Figure 6-3 for the DIC tensile test specimen and in Figure 6-4 for the DIC creep test specimen. Although, cylindrical specimens are typically used for both conventional tensile and creep tests, measurement of surface deformations using DIC is best achieved with specimens having a flat surface, as this allows accurate images to be acquired from a single camera.

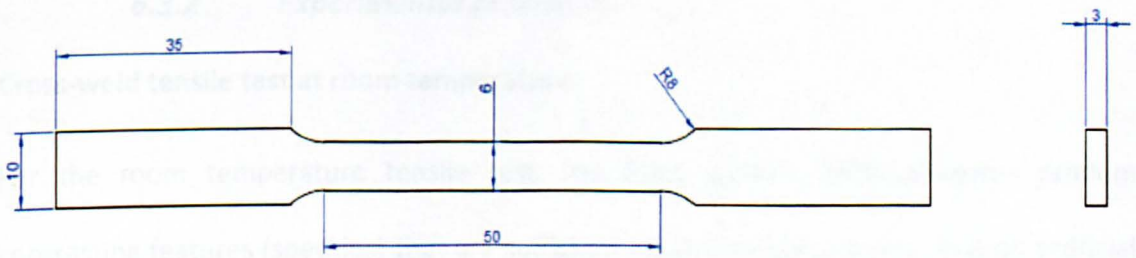

Figure 6-3: DIC room temperature tensile specimen dimensions.

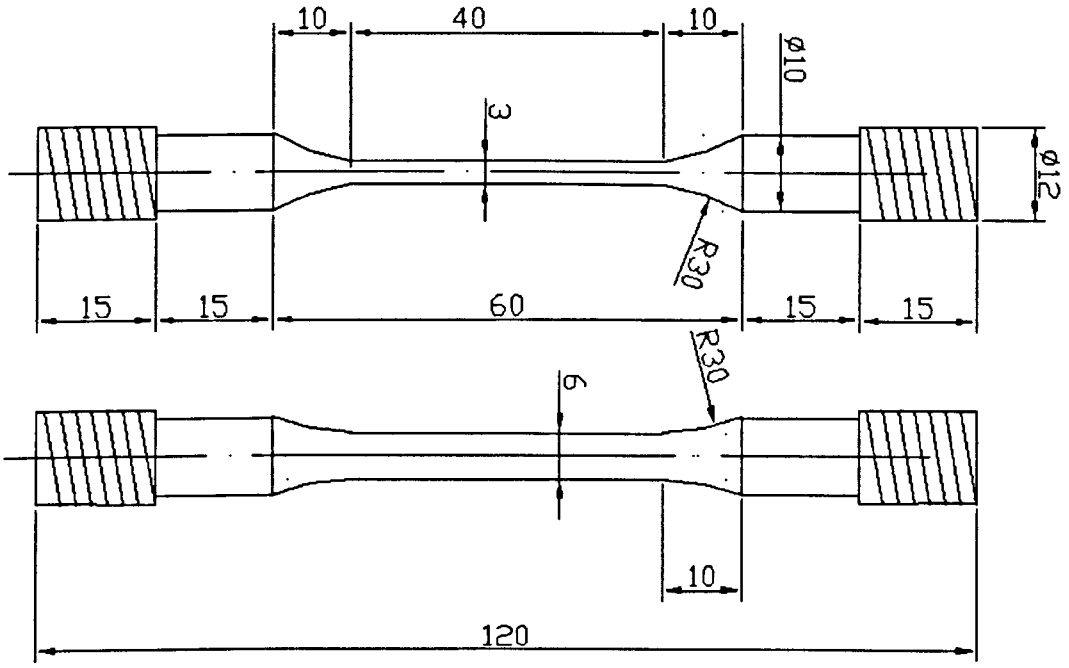

Figure 6-4: DIC creep specimen dimensions.

In contrast to the tensile test specimen (Figure 6-3), the creep test specimens were machined to have a shorter gauge length (40 mm instead of 50 mm), which corresponds to the gauge length of conventional creep test specimens used in Chapter 5. Furthermore, it is important to note that all the specimens were oriented with their 6 mm dimension parallel to the hoop direction for the pipe, so that the fusion boundary was nominally perpendicular to the specimen axis. This orientation was chosen because it enables an assumption to be made, i.e, that the strain across the width of the specimen is nominally the same and thus, can be averaged, thereby reducing scatter in the data.

6.3.2 Experimental procedure

Cross-weld tensile test at room temperature

For the room temperature tensile test, the EDM surface finish produces random contrasting features (speckles) that are sufficient for DIC measurements, thus an artificial speckle pattern (usually created by spray painting) was not required. Prior to DIC testing,

the specimen was electrolytically cleaned in 10% oxalic acid so that the naturally occurring speckle pattern could be more clearly identified.

The tensile test was conducted using an Instron screw-driven testing machine with a 30 kN load cell. The specimen was held in between mechanical wedge grips, which are attached to the testing equipment via universal joints. The inclusion of the latter in the load train allowed self-correction of any misalignment, thus avoiding bending stresses and ensuring a purely uniaxial test.

Before commencement of the tensile test, the specimen was preloaded up to 100 MPa and the load released for settlement of the specimen in the grips. The tensile test was then conducted under displacement control at a displacement rate of 0.01 mm/s until failure.

The DIC experimental set-up consists of a 36.3 Mega Pixels digital SLR camera with a 200 mm macro lens and a DC fibre optic light source, which provides uniform illumination of the sample's surface. The field of view of the camera was ~45 mm, which was sufficient to cover the weld, HAZ and parent metal on both sides of the weld. During the tensile test, images were acquired at a relatively high rate (every 2 seconds) during the initial stage of the test (up to yield point). The acquisition rate was then reduced to every minute once the sample was deforming plastically which significantly reduces the number of images and thus reduces the time required for data analysis.

Cross-weld creep tests

Many researchers [8], [9], [12], [13] have successfully used DIC to map the strain variation spanning cross-weld specimens during room temperature tensile tests. At high temperatures, there are a number of challenges that have to be considered, in order to

make accurate strain measurements. These have been discussed and addressed by Sakanashi [9] and are listed below.

- **Surface oxidation**

During creep testing, the specimen is exposed to high temperatures for a prolonged period of time, which may result in surface oxidation. This will be especially pronounced in ferritic steels as compared to austenitic steels, due to the lower chromium content in the former. As a result of oxidation, the surface texture of the specimen changes and consequently, the speckle pattern, intensity, brightness and contrast are all affected and this can compromise the accuracy of the DIC measurements.

In order to make meaningful DIC strain measurements during creep testing, a silicon ceramic based paint is usually applied onto the specimen's surface which provides a high quality speckle pattern that can survive until the end of the test.

- **Illumination system**

The light intensity on the recorded images (in grey levels) is a direct consequence of the illumination of naturally occurring features (EDM surface) or artefacts (paint spots) [8]. Thus, maintaining a stable illumination system is one of the crucial factors in obtaining reliable DIC measurements. In contrast to room temperature tensile tests, creep tests involve a furnace surrounding the specimen, which poses difficulties in obtaining uniform illumination across the specimen's surface.

In a DIC creep test the furnace needs to have a small window which allows the surface of the specimen to be seen by the camera. It has been found [9] that by having a pair of DC fibre-optic light sources pointing towards the top and bottom of the window a sufficiently uniform illumination of the specimen's surface can be achieved. The fibre-optic is connected to the camera's flash system, which is triggered at the same time as the

camera's shutter. This is particularly useful for long-term creep tests as it avoids having the light on at all times.

- **Thermal current**

At high temperatures, thermal convection currents between the camera and the furnace can cause image distortion, which results in errors in the DIC measurements. This is a consequence of the different densities of air at different temperatures, and corresponding changes the refractive index of the air. It has been found [9], [14] that at temperatures above 600°C, thermal radiation dominates and suppresses thermal convection and by having a glass window, the effect of thermal current was effectively suppressed.

- **Specimen preparation**

In order to make meaningful DIC strain measurements during creep testing, a silicon ceramic based paint (VHT FlameProof) was applied onto the specimen's surface (see Figure 6-5) and this provided a high quality speckle pattern that was sustainable until the end of the P91 specimen tests. In order to obtain a fine distribution of paint spots (speckles), the paint can was held at a distance of approximately 15 inches from the specimen's surface and only 2-3 thin coats were applied. Excessive thick paint is not recommended as it will cause blistering. After the paint was allowed to dry, the specimens were cured to increase durability of the finish and enhance chemical resistance. This involved the following heating and cooling steps as recommended by the manufacturer [15]:

- Bake at 121°C for 30 minutes and air cool for 30 minutes,
- Bake at 204°C for 30 minutes and air cool for 30 minutes, and
- Bake at 315°C for 30 minutes and air cool for 30 minutes

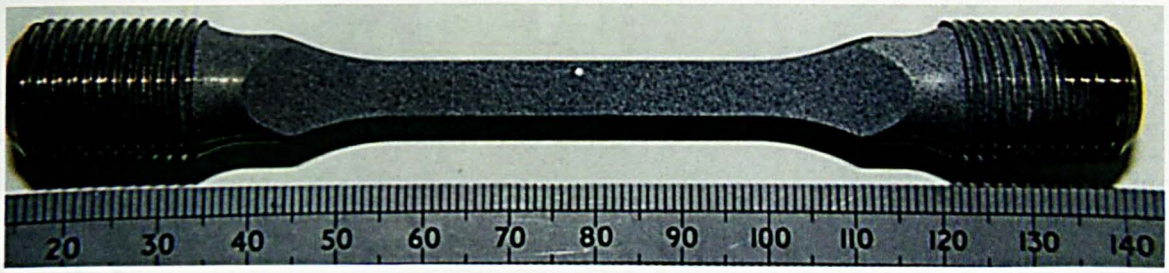

Figure 6-5: DIC creep specimen showing the high quality black and white speckle pattern obtained by applying a silicon ceramic based paint.

The creep rig used for the DIC tests in the present work was similar to the one described in Chapter 5. The only notable difference was the furnace, which contained a 20mm wide and 40mm high aperture, which enabled the surface of the specimen to be seen by the camera. The aperture was covered with a transparent sapphire glass to reduce thermal currents and prevent heat loss.

Two small holes (1.5 mm deep) were drilled on the top and bottom shoulders of the specimen into which, N-type thermocouples were inserted as shown in Figure 6-6. This method ensures good contact with the specimen surface and provides shielding from radiation, but more importantly does not affect the visibility of the specimen's surface (in particular the gauge length). It should be noted that the use of 2 thermocouples (instead of 3, as described in Chapter 5) is permissible under ASTM E139-11 [16] for specimens with gauge lengths less than 50 mm. Ceramic plugs and high temperature insulation wool were used at the ends of the furnace tube to minimise heat losses and thereby help maintain good temperature stability.

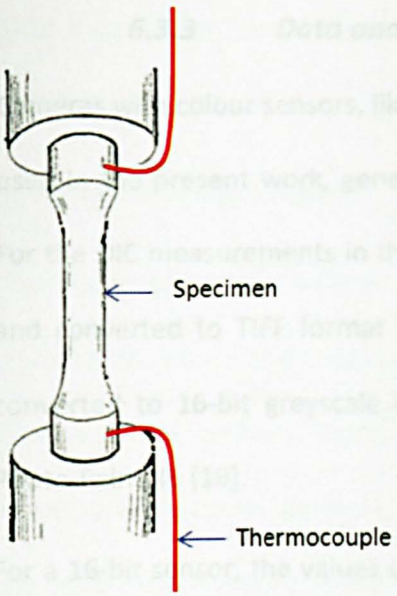

Figure 6-6: Attachment of thermocouples onto the specimen shoulders (adapted from [17])

The stress and temperature for the DIC monitored creep tests were selected in order to repeat the conditions of two of the conventional creep tests conducted earlier in this work. The stresses were chosen to be 100 and 85 MPa and the temperature was kept at 625°C.

During the DIC creep tests, the field of view of the camera was slightly reduced (~35 mm) when compared to the room temperature tensile test (~45 mm), due to the limited visual access provided by the window in the creep furnace. Although 35 mm was sufficient to cover the weld and HAZ on both sides of the weld, it was not enough to cover the entire gauge length (40 mm) of the specimen. The camera was thus focused in a way that it captured the gauge length of parent metal (~15 mm) near the upper end of the specimen at the expense of ~5 mm of parent metal near the lower end. During the tests, images were taken every 1 hour during the primary stage and secondary stage of creep, followed by every half an hour during the tertiary stage of deformation. The onset of the tertiary stage was assumed to coincide with the start of necking.

6.3.3 Data analysis procedure

Cameras with colour sensors, like the commercial DSLR (Digital single-lens-reflex) cameras used in the present work, generally record raw images in RGB (red-green-blue) format. For the DIC measurements in the present work, 3×16-bit RGB raw images were captured and converted to TIFF format in commercial software Nikon ViewNX 2 [18] and then converted to 16-bit greyscale by using the commercial image analysis software Corel Photo-Paint X6 [19].

For a 16-bit sensor, the values of each pixel range from 0 (black) to 216 = 65536 (white). Thus each subset will comprise of a wide range of intensity values, and can therefore be uniquely identified in two corresponding images. The converted images were imported into a commercial DIC analysis software (Davis 8.1.5 [20]) to compute image correlation and displacement maps. The data analysis steps are described below.

Elimination of rigid body motion

Any camera movement or the settlement of the sample in the grips as load is applied can cause rigid body motion i.e. translation and/or rotation of the image. Rigid body motion can be eliminated by selecting a reference point in the first image (usually at the centre) and all subsequent images can then be re-positioned accordingly. It should be noted that this step only allows for the corrections of in-plane translations and rotations. Out-of-plane displacements, for example a change of distance between the surface of the specimen and the camera lens cannot be eliminated, and thus care should be taken to avoid any such movements. Out-of-plane displacements due to specimen necking have been shown by Acar [8] and Sutton *et al.* [21] to be very small (~200 microstrain) and thus are usually neglected. The development of 3D-DIC, using a two camera stereo vision

system, can measure out-of-plane displacement and has been successfully used by Luo *et al.* [22] for example, to measure crack tip deformation.

Definition of analysis region

The captured images usually consist of unwanted background features, which need to be removed to reduce the computation time. The gauge length of the specimen is usually defined as the analysis region, which is then divided into small subset windows. The subset size ultimately determines the resolution of the displacement map. There are a few important considerations when selecting a suitable subset size [8]:

- Each subset should include sufficient number of speckles [23].
- The displacement of a subset, which is computed by using two successive images, should be less than a subset size.
- For relatively homogeneous deformation fields, a large subset size is usually found to give more accurate displacement measurements, as more data points lead to better correlation. However, for deformation fields containing high strain gradients, the variation within the subset can be significant if the chosen subset size is too large, which may lead to errors.

Subset overlapping can be used to increase accuracy without any loss in the resolution of the displacement map, but requires more computation time. In the present work, a 75% overlap was used with a subset size of 32 x 32 pixels.

Displacement vector calculation

Correlation functions are used within DaVis [20] to compute displacement vectors of the same subsets in two successive images. The cross-correlation algorithm can be done either relative to the reference (first) image in which case the final displacement of a

subset in the nth image is computed relative to its original position in the reference image (1*2, 1*3, 1*4 ... 1*n) or relative to the (n-1)th image in which case, the final displacement of a subset in the nth image is a sum of differential vectors computed by the correlation of every two successive images until nth image (1*2, (1*2+2*3), (1*2+2*3+3*4) ... (1*2+2*3+...+(n-1)*n). The second cross-correlation mode was preferred in the present work, as large displacements between the 1st and last image may be greater than the subset size.

Strain calculation

Using the calculated in-plane displacements, strains were then calculated using the displacement-strain relationship by assessing the local vector gradient as follows:

Strain = [Yvector2 – Yvector1] / [Yposition2 – Yposition1]

This was done in MATLAB [24] using scripts written at the Open University [25] by fitting a first order polynomial (a straight line) to groups of displacement vectors from 7 subsets (in the y direction, i.e. along the length of the specimen). The fit was performed using the least squares method and then the gradient of this fit was taken as the average strain for the region. These strains were averaged over the sample width (x direction) to increase confidence in the results by increasing the number of data points used to calculate each strain value. At the end of this process a matrix of strain progression at different y positions (along the length of the sample) is obtained. The local strain data are then combined with stress data determined from the Instron machine at the time of each camera shot. This provides local engineering stress – engineering strain curves. For the creep tests, a matrix of strain progression at different y positions at different times is obtained, which can be used to plot local engineering creep strain – time curves. The

effective resolution (gauge size) of the measurements (after averaging) was approximately 1 mm in the y-direction.

6.3.4 Results

Tensile tests

Figure 6-7 shows images captured during the DIC tensile test prior to failure and after failure. The letters marked a through to c show locations where strain data were extracted for the stress-strain curves presented in Figure 6-8, which correspond to the parent metal, weld metal and HAZ respectively. The rectangular box shows the approximate location of the adjacent HAZ ('un-failed' HAZ), where slight necking was observed.

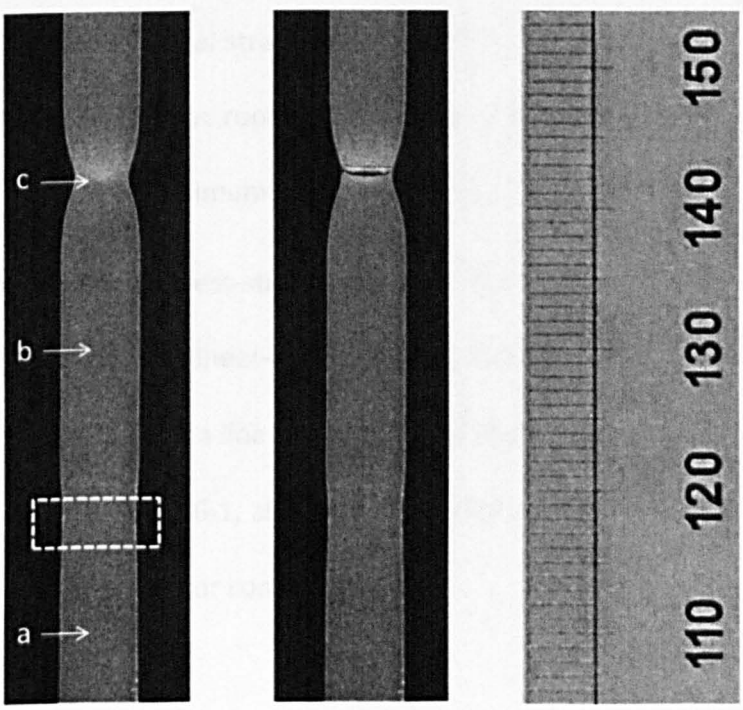

Figure 6-7: Images captured during room temperature DIC tensile test showing specimen prior to failure (left) and after failure (right).

The stress-strain curves from the 3 different regions of the weldment: parent metal, weld metal and the HAZ are shown in Figure 6-8. The exact location of the HAZ corresponds to

the location of minimum 0.2% proof stress, which was found to coincide with the inter-critical HAZ (ICHAZ) through hardness measurements.

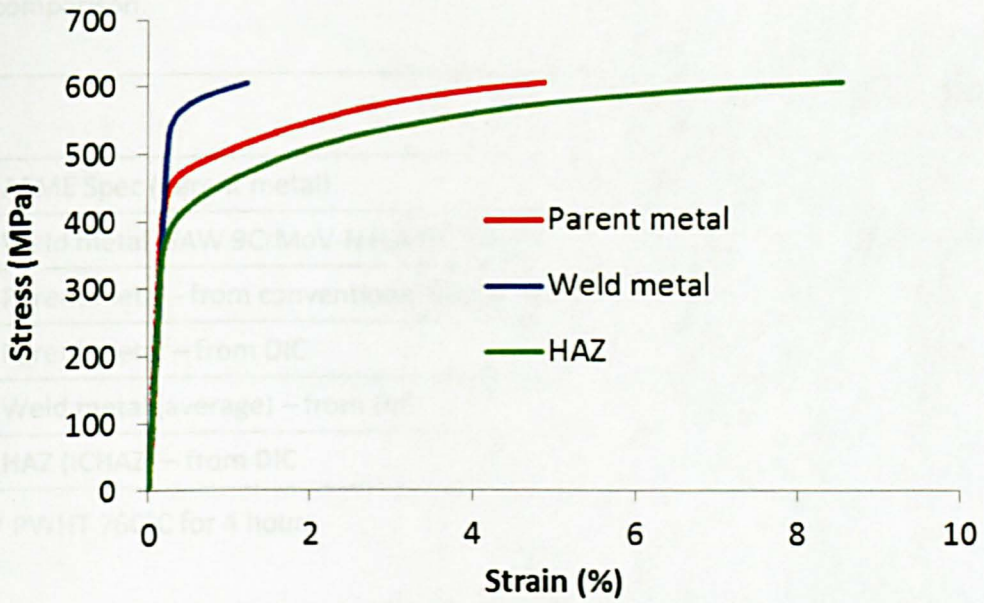

Figure 6-8: Local stress-strain curves for parent metal, weld metal and HAZ (measured in 1 single test) at room temperature. The exact location of the HAZ corresponds to the location of minimum 0.2% proof stress.

Using these stress-strain curves, the Young's Modulus, E was derived graphically from the slope of the linear-elastic region and the 0.2% proof stress was inferred from the intersection of a line offset from the linear region by 0.2% strain. The values obtained are given in Table 6-1, along with the ASME parent metal [26] and Metrode [27] weld metal specifications for comparison.

Table 6-1: Young's Modulus and 0.2% proof stress derived from the DIC tensile test. The ASME parent metal [26] and Metrode [27] weld metal specifications are also given for comparison.

	0.2% Proof Stress (MPa)	Young's Modulus (GPa)
ASME Spec (Parent metal)	Min 415	218
Weld metal (SAW 9CrMoV-N+LA492 flux)*	610	None reported
Parent metal - from conventional tensile test	500	216
Parent metal – from DIC	472	219
Weld metal (average) – from DIC	596	215
HAZ (ICHAZ) – from DIC	410	213

* PWHT 760°C for 4 hours

It is clear from Table 6-1, that the Young's Moduli were very similar for all the different regions of the weldment and close to the ASME parent metal specification. However, the 0.2% proof stresses were significantly different. Figure 6-9 plots the spatial variation in measured 0.2% proof stress across the weldment, which appears to be constant at ~472 MPa in the parent metal and gradually decreases in the HAZ, where it reaches a minimum of ~410 MPa. In the weld metal, the average value was 596 MPa, which compares well with the value of 610 MPa reported by the supplier.

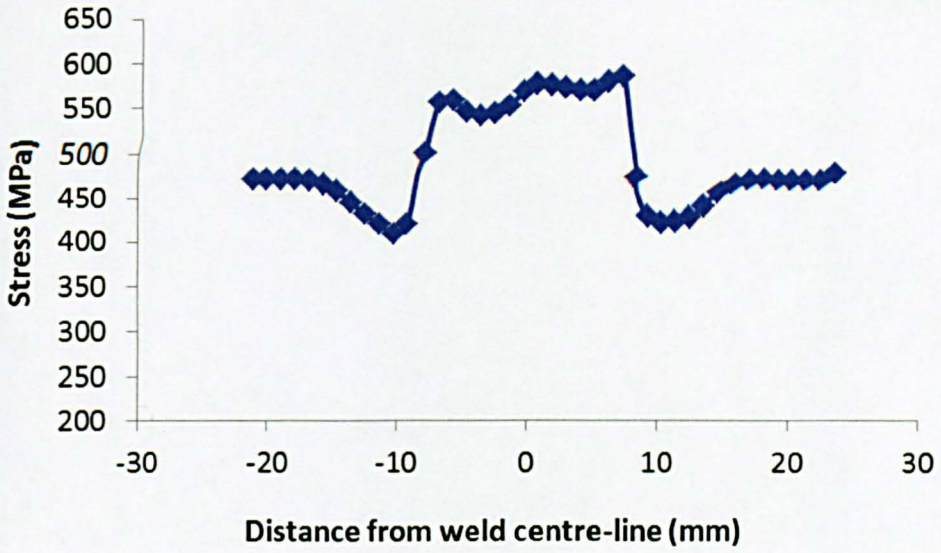

Figure 6-9: Spatial variation of measured 0.2% proof stress across the specimen's gauge length.

It is also evident from Figure 6-9 that the variation in 0.2% proof stress within the weld metal (~central 12mm) was not uniform, which would be expected for a multi-pass weld. On inspection of the macrograph from the PWHT pipe (from which this specimen was machined), there appears to be a close correlation of the weld passes that would have been present in the tested specimen (see Figure 6-10) with the variation in 0.2% proof stress. The apparent increase near the weld centre-line (0 mm) seems to be a consequence of overlapping weld beads.

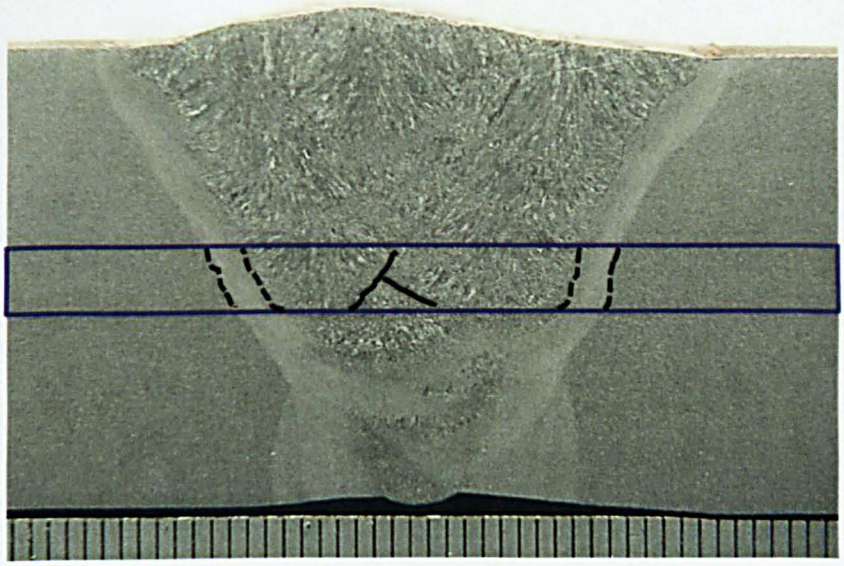

Figure 6-10: Macrograph taken from PWHT pipe showing location where the DIC specimen was extracted (blue rectangle). The locations of the HAZ are highlighted (dotted lines) along with approximate locations of the fusion boundaries for weld passes within that location (solid black lines).

The hardness variation across a line representative of the mid-thickness of the PWHT pipe is shown on a secondary axis in Figure 6-11. There is a very close correlation of the 0.2% proof stress with the hardness measurements and interestingly, the location of minimum 0.2% proof stress coincides with the location of minimum hardness i.e. the ICHAZ and not the FGHAZ. There also appears to be a slight discrepancy between the 0.2% proof stress values for the 2 ICHAZs (either side of the weld), leading to preferential deformation in one of the ICHAZs. It was shown earlier (Figure 6-7) that necking was more pronounced in one of the HAZs.

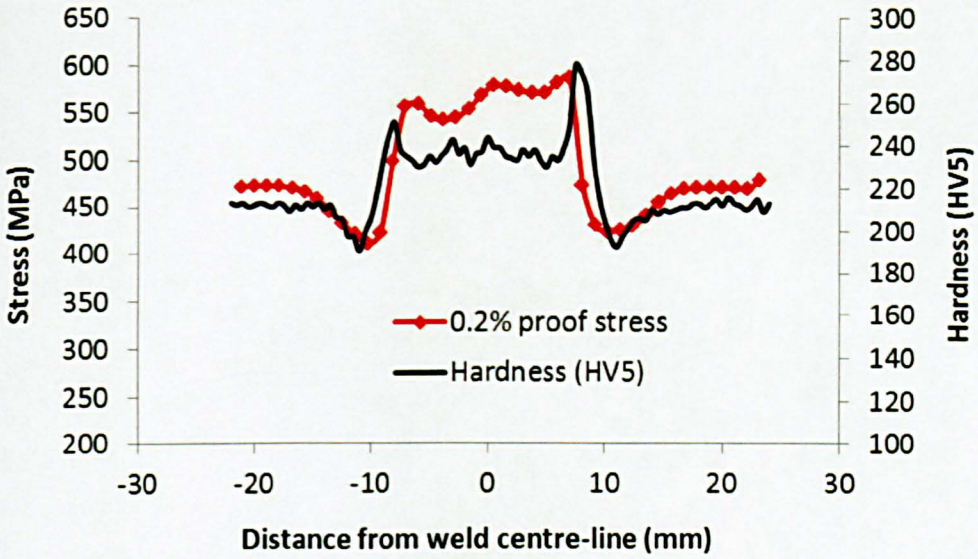

Figure 6-11: Spatial variation of measured 0.2% proof stress across the specimen's gauge length. The hardness variation across a line representative of the mid-thickness of the PWHT pipe is shown on a secondary axis.

In order to confirm the fracture location, the front surface of the specimen (after fracture) was prepared following standard metallographic preparation procedures, as described in Chapter 3, and hardness measurements were carried out using a Vickers (HV) indenter, with a load of 5 kg along one straight line at intervals of 0.75 mm. Figure 6-12 shows the hardness variation along the length of the specimen spanning the fractured specimen. The typical hardness variation across a line coincident with the mid-thickness of the PWHT pipe is also shown for comparison. From the knowledge of typical hardnesses of the CGHAZ (maximum hardness) and the ICHAZ (minimum hardness), it can be confirmed that failure occurred in the ICHAZ (break in curve). In the adjacent HAZ (at around 10 mm from the weld centre-line), there is an apparent increase in the hardness, which may be attributed to strain localisation and hardening.

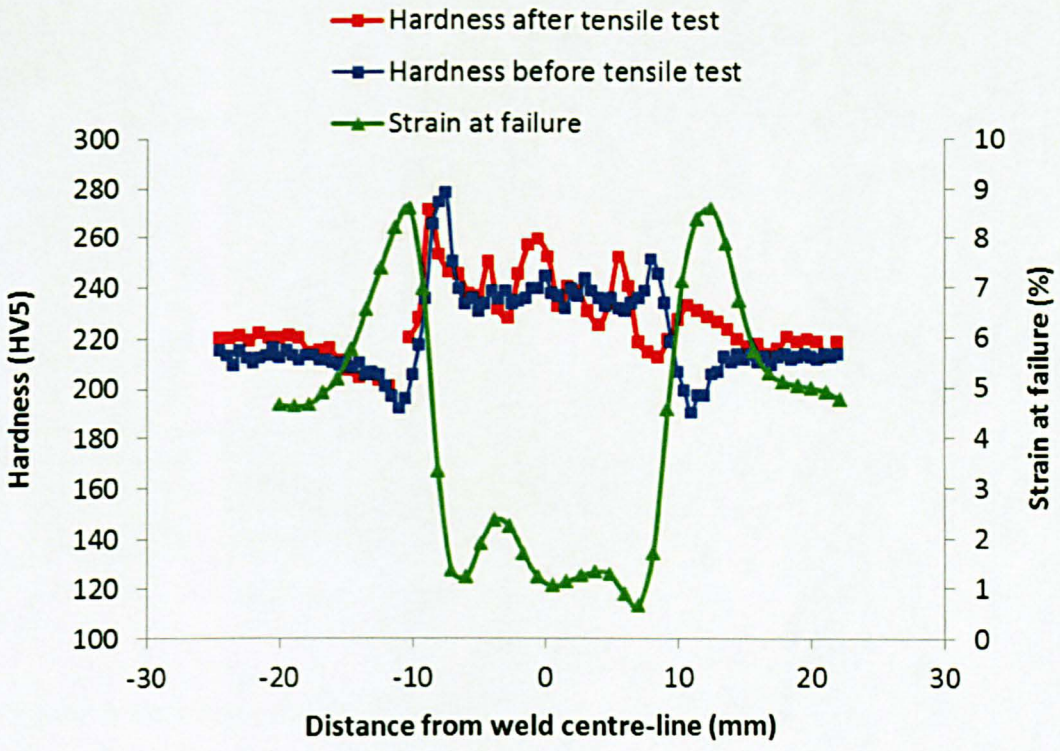

Figure 6-12: Hardness profile along a fractured DIC cross-weld tensile specimen (without compensation of elongation). The hardness variation across a line representative of the mid-thickness of the PWHT pipe and the measured strain at failure are also shown for comparison.

Creep tests

Two DIC monitored creep tests were successfully conducted at stresses of 100 and 85 MPa and at a temperature of 625°C. The times to rupture were 180 and 330 hours respectively. Figure 6-13 shows a series of images taken at various intervals (0 - 329.5 hours) during the creep test conducted at 85 MPa. The image at 0 hours corresponds to the reference image, which was taken after the load was applied. Necking of the specimen in the two HAZs is very clear, with more pronounced necking in the upper HAZ (where failure occurred).

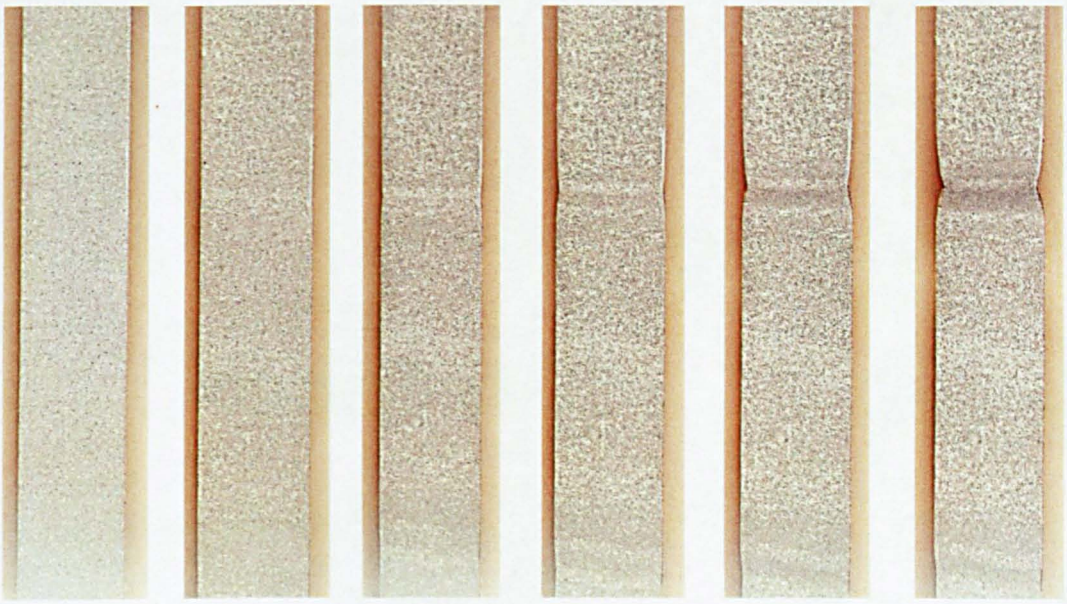

Figure 6-13: Images taken at different time intervals of DIC monitored creep test at 85 MPa and at 625°C.

Local creep deformation curves corresponding to locations in the parent metal, HAZ (where failure occurred) and the weld metal are shown in Figure 6-14 and Figure 6-15 for the DIC creep tests at 100 and 85 MPa respectively. These plots clearly show the preferential creep strain accumulation in the HAZ with much less strain accumulation elsewhere. In the weld metal, the creep strain at failure was a modest 0.25% (compared to >25% in the HAZ) and the creep curve for the weld metal shows the absence of a tertiary stage.

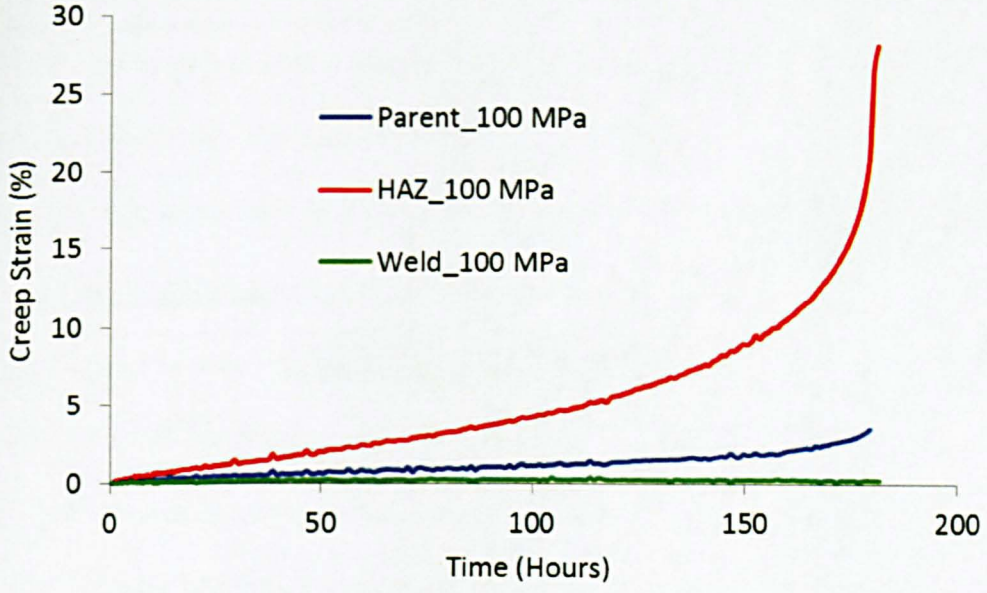

Figure 6-14: Local creep curves for parent metal, weld metal and HAZ derived from a single cross-weld test at 100 MPa at 625°C.

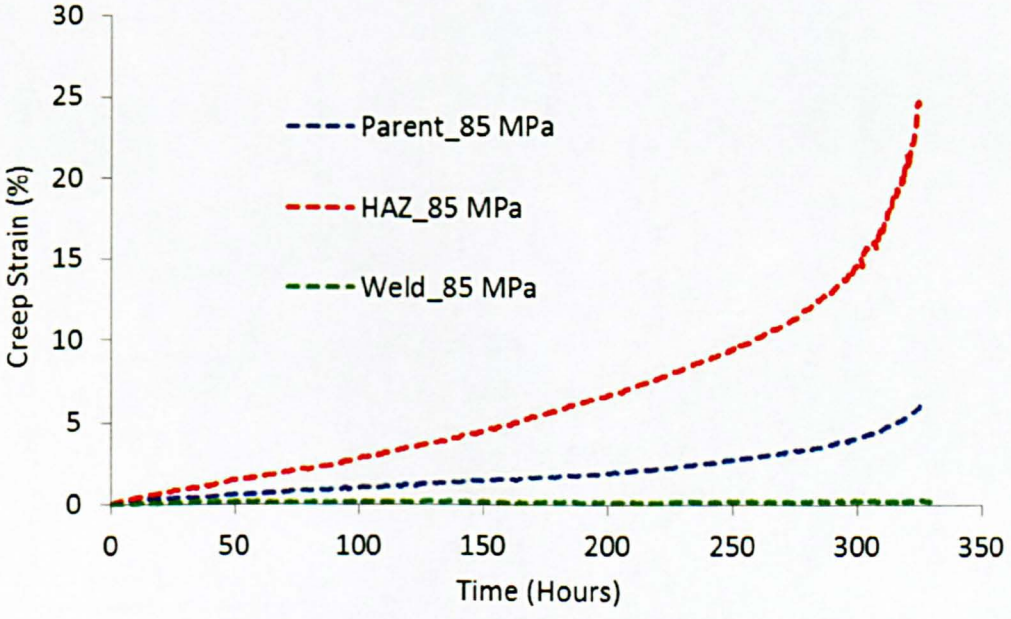

Figure 6-15: Local creep curves for parent metal, weld metal and HAZ derived from a single cross-weld test at 85 MPa at 625°C.

Figure 6-16 shows the creep strain evolution along the gauge length of the specimen at different times for the test conducted at 85 MPa at 625°C. It is clear that the creep strain

accumulation in different parts of the specimen (parent, weld and HAZ) were different, with significantly higher creep strain in the HAZ (where failure occurred). It is also noticeable that in the un-failed HAZ (at 10 mm from the weld centre-line), there was slight strain accumulation. In Figure 6-17, the same results are plotted, but only for the first few hours on a different y-axis scale. These results suggest that preferential creep strain accumulation in the HAZ occurs as early as 2 hours after the commencement of the test (for a 325 hours creep test), and that this intensifies as the creep test progresses. The slightly anomalous creep behaviour occurring in the very earliest stages of the test (first hour) may be attributable to short-term strain accommodation processes and thus of no major importance.

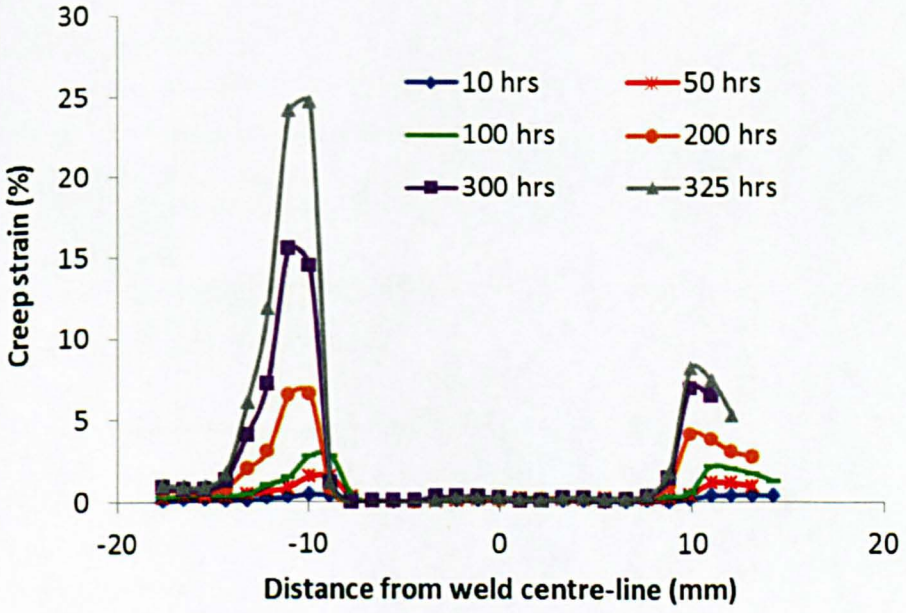

Figure 6-16: Creep strain evolutions along the gauge length of the specimen for a load of 85 MPa and temperature of 625°C.

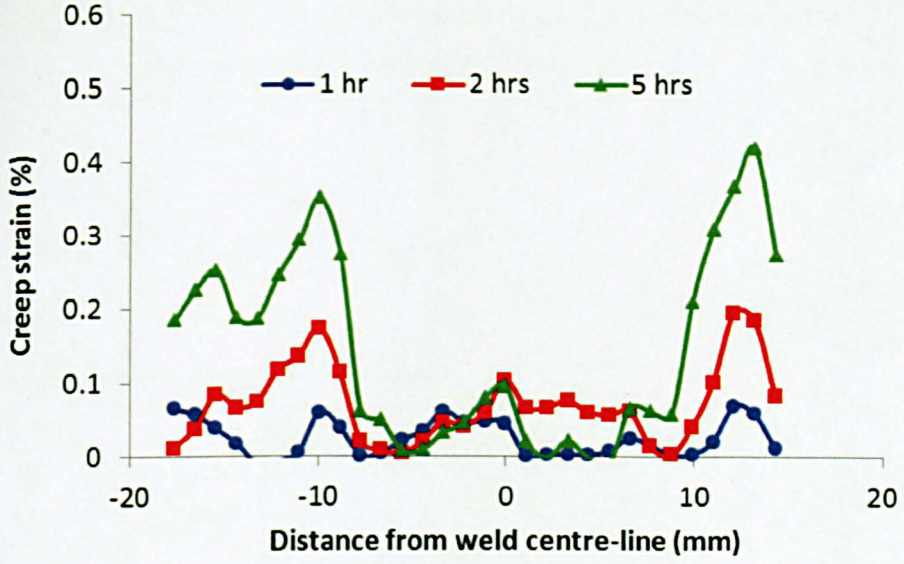

Figure 6-17: Creep strain evolution along the gauge length of the specimen in the first few hours of a test with a stress of 85 MPa and a test temperature of 625°C.

Creep strain rate

Creep strain rates were estimated using the same approach described in chapter 5. Least squares straight lines were passed through groups of creep strain points and the resulting gradient, gave a numerical estimate of the creep strain rate at the centre point. Figure 6-18 shows the variations of creep strain rate ($\dot{\varepsilon}$) with time for the DIC cross-weld specimens in the region of the HAZ (where failure occurred). Creep strain rates for FGHAZ simulated and cross-weld specimens tested at the same stresses are also shown for comparison.

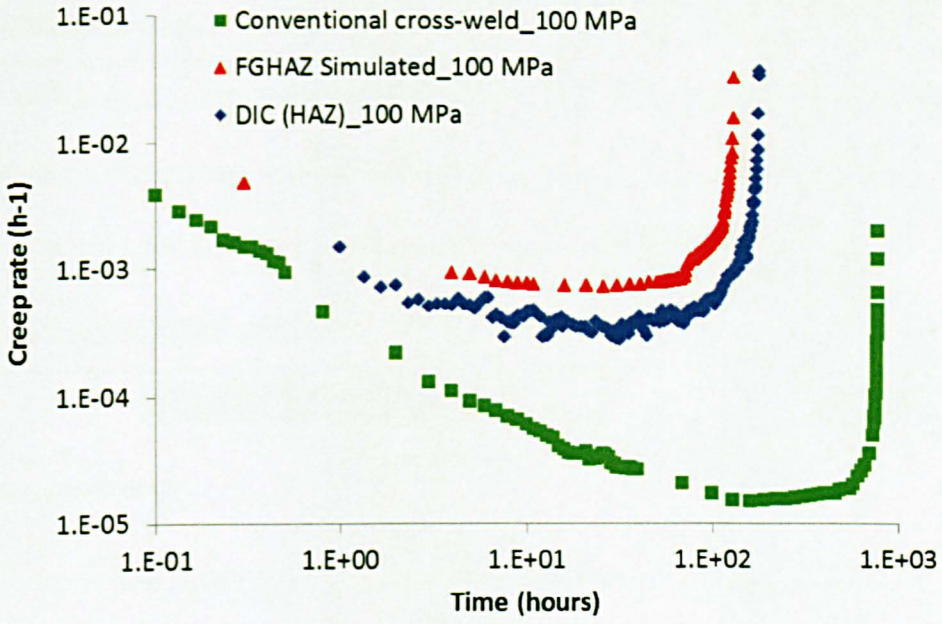

(a)

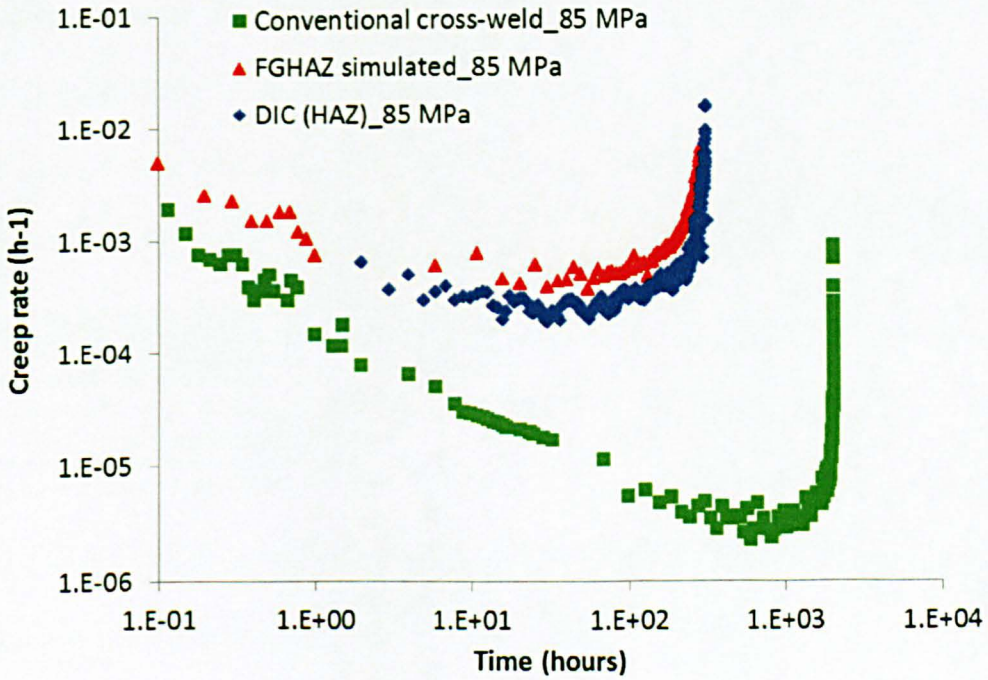

(b)

Figure 6-18: Variations of creep strain rates with time for the HAZ of DIC cross-weld creep tests at 625°C at 100 MPa (a) and 85 MPa (b). Creep strain rates for FGHAZ simulated and cross-weld specimens tested at the same stresses are also shown for comparison.

The trends of creep strain rates for the HAZ of the DIC specimen appear to be very similar to that of FGHAZ simulated specimens, characterised by a decaying primary stage and an accelerating tertiary stage with no substantial steady-state stage. It can also be seen from Figure 6-18, that, for the same stress level, the onset of the tertiary stage is delayed in the conventional cross-weld specimen and that the minimum creep rate was significantly lower.

2D creep strain maps

In the data analysis procedure, it was mentioned that strains are usually averaged across the width of the sample in order to reduce scatter in the data. By doing so, information about damage initiation/progression is lost. A separate analysis was performed without averaging the strain data across the width, and the results were used to create contour maps (Figure 6-19) in order to obtain an overall impression of the creep strain distribution. Note that it was not feasible to use the same colour scale for all the contour maps due to significant differences in creep strain magnitudes.

In P91 weldments, creep damage often initiates in the mid-thickness region, owing to high triaxiality and strong curvatures in the fusion boundary [28], [29], [30], [31]. On inspection of the strain maps in Figure 6-19, the creep strain distribution across the width appears to be uniform in the HAZ where failure occurred. These results advocate that the general observation of damage initiating in the mid-thickness region may not be the case for specimens with a fusion boundary perpendicular to the specimen axis (for example an EB weld or laser weld). The results also suggest that the design of the test specimen is such that it has avoided (unintentionally) introducing a geometric "size-driven constraint effect" which would concentrate higher stresses and strains in the central region of the

specimen, but there may still be significant variability of material properties constraint effects present – depending on the gradient of the properties variation.

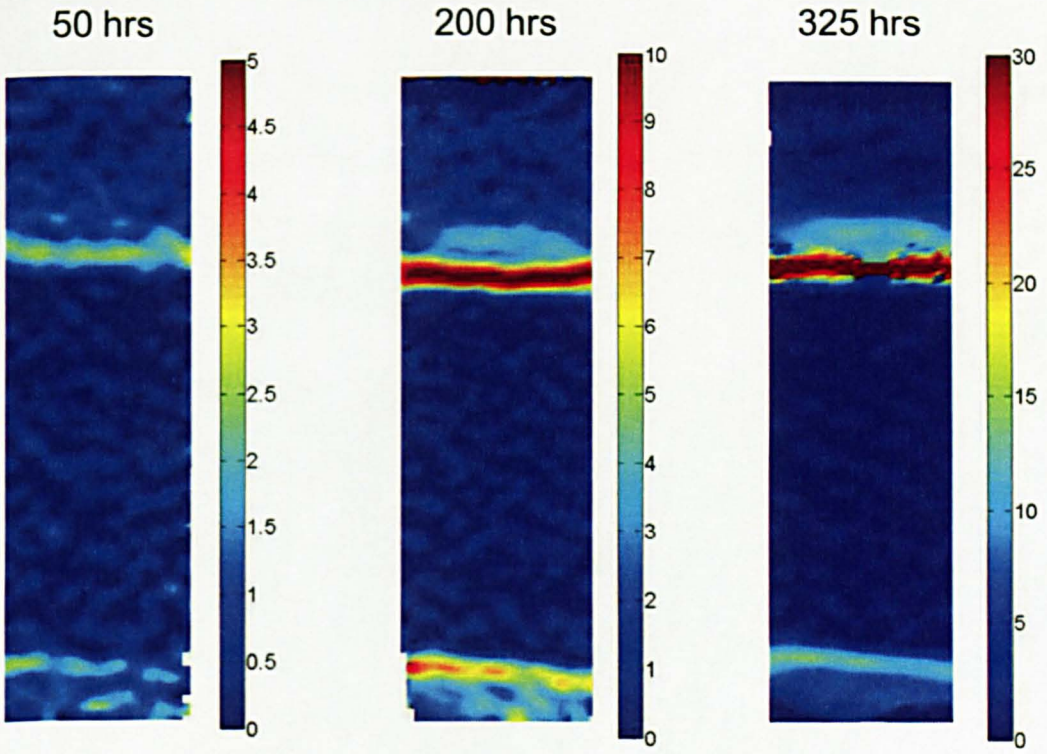

Figure 6-19: Two-dimensional creep strain maps across the cross-weld specimen at intervals of 50, 200 and 325 hours for the creep test conducted at 85 MPa at 625°C.

Figure 6-20 shows a picture of the ruptured specimen tested at 85 MPa at 625°C. The letters marked a and b correspond to locations where optical micrographs presented in Figure 6-21 and Figure 6-23 were taken.

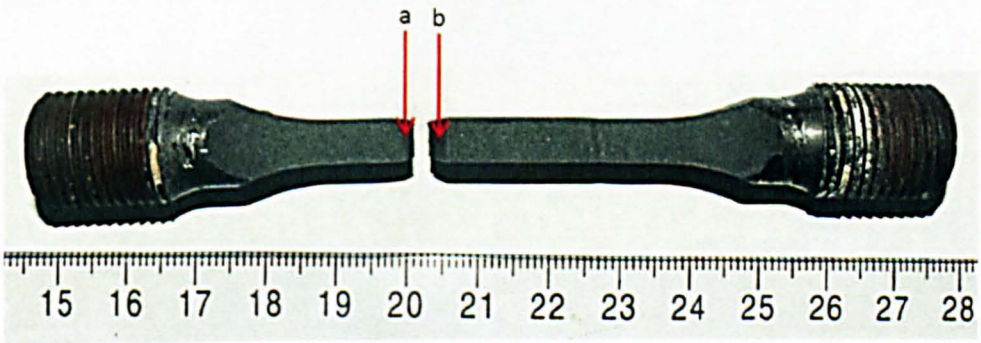

Figure 6-20: Ruptured DIC cross-weld specimen tested at 85 MPa at 625°C. The letters marked a and b, correspond to locations where optical micrographs were captured, corresponding to the vicinity of the fracture surface,

The microstructural constituent in Figure 6-21 resembles that of parent material, with somewhat smaller grains near the fracture surface. The absence of a considerable length of fine grains (representing the ICHAZ), gives the impression that failure occurred in the ICHAZ.

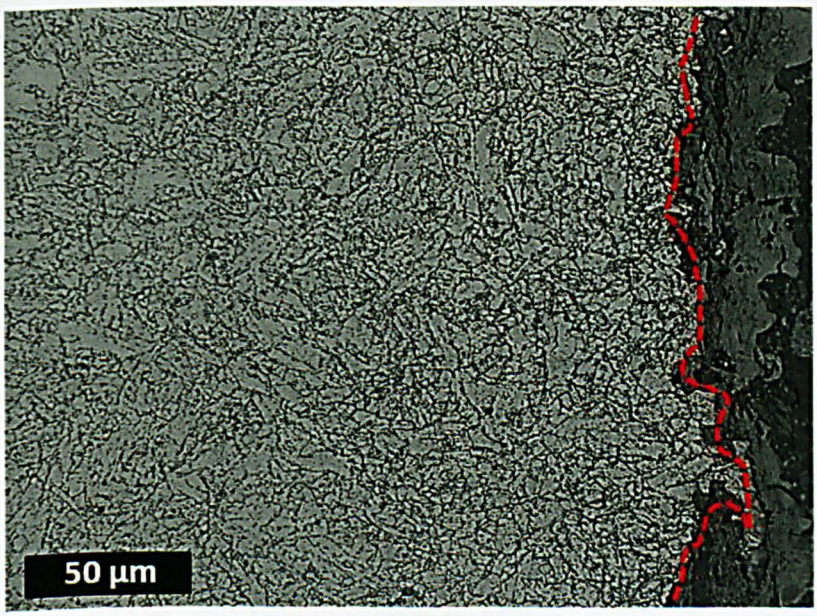

Figure 6-21: Optical micrograph captured at location marked 'a' in Figure 6-20. The dotted line shows the fracture location.

At the location marked b (in Figure 6-20), a lower magnification multi-step image was captured that spans from the fracture location to the fusion boundary (see Figure 6-22). A coarse-grained microstructure (CGHAZ) is evident on the right hand side of the image, which corresponds to the region adjacent to the fusion boundary. Moving towards the left of the image, we would expect to see the FGHAZ followed by the ICHAZ, which are often difficult to distinguish. However, it is evident from Figure 6-22, that cavities were present in both the FGHAZ and the ICHAZ.

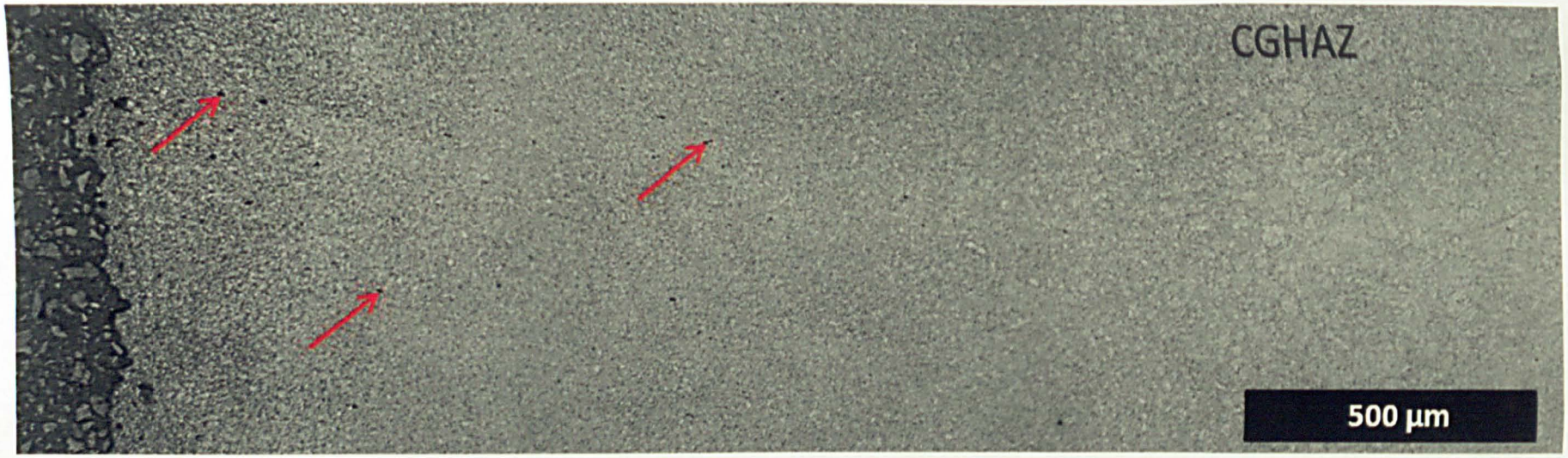

Figure 6-22: Lower magnification multi-step image captured at location marked b on Figure 6-20 which spans from the fracture location to the fusion boundary. Arrows highlight examples of creep cavities.

Hardness

In order to confirm the fracture location, the fractured specimen was prepared following standard metallographic preparation procedures, as described in Chapter 3, and hardness measurements were carried out using a Vickers (HV) indenter, with a load of 5 kg, along one straight line at mid-thickness at intervals of 0.75 mm. Figure 6-23 shows the hardness variation across the fractured specimen. The typical hardness variation across a line coincident with the mid-thickness of the PWHT pipe is also shown for comparison. From the knowledge of typical hardnesses in the ICHAZ (minimum hardness), it can be confirmed that failure occurred in the ICHAZ. The overall reduction in hardness is due to strain softening (as discussed in Chapter 5).

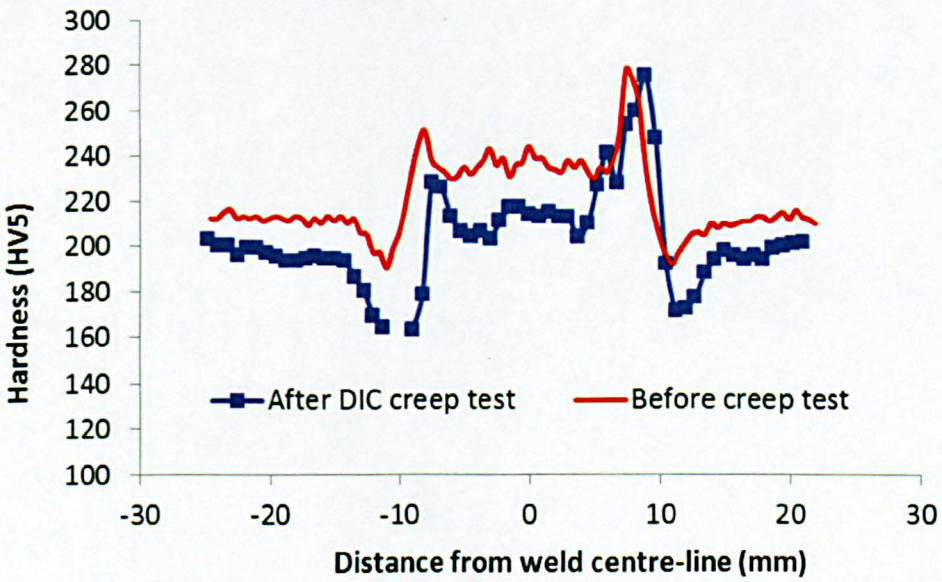

Figure 6-23: Hardness profile along a fractured DIC cross-weld creep specimen (tested at 85 MPa at 625°C). The hardness variation across a line representative of the mid-thickness of the PWHT pipe is also shown for comparison.

The fact that the cross-weld DIC creep specimens ruptured in the ICHAZ rather than the fine-grained heat affected zone (FGHAZ) is odd, bcause in Chapter 5, all the cross-weld

specimens (tested at 100, 85, 75 and 65 MPa at 625°C) ruptured in the FGHAZ. The times to rupture of conventional cross-weld specimens (8 mm diameter specimens), DIC cross-weld specimens (6 mm x 3 mm rectangular specimens) and FGHAZ simulated specimens (8 mm diameter specimens) are summarised in Table 6-2. It appears that the creep rupture lives of DIC specimens (very little or no constraint) are very close to that of FGHAZ simulated specimens (no constraint) and significantly lower than that of conventional cross-weld specimens (constraint present). This may be a consequence of specimen size effect, which led to a reduction of constraint and hence a shorter time to rupture. This is consistent with data presented by Parker [32] who showed a strong dependence of creep rate as a function of weldment cross-section divided by the width of weak zone.

This is very encouraging in one sense in that the design of the test specimen (although unintentional) has avoided introducing geometric/structural constraint effects and suggests that metallurgical (i.e. material property variation) effects are minimal. Thus the test can truly determine the spatial variation in creep properties.

Table 6-2: Summary of creep rupture lives of conventional cross-weld, DIC cross-weld and FGHAZ simulated specimens.

Stress (MPa)	Time to rupture (hours)		
	Cross-weld	DIC cross-weld	FGHAZ simulated
100	779	182	132
85	2093	329.5	305

6.3.5 Conclusions

The digital image correlation (DIC) technique has been successfully applied to measure the spatial variation in tensile and creep properties across a P91 welded pipe. The following observations were made:

During room temperature tensile testing, the cross-weld samples ruptured in the inter-critical heat affected zone (ICHAZ). The 0.2% proof stress was found to be constant at ~472 MPa in the parent metal and gradually decreased in the HAZ, where it reached a minimum of ~410 MPa. In the weld metal, the average value was 596 MPa, which compares well with the value of 610 MPa reported by the supplier.

Hardness variation across a line representative of the mid-thickness of the PWHT pipe showed a very close correlation with the 0.2% proof stress and interestingly, the location of minimum 0.2% proof stress coincided with the location of minimum hardness i.e. the ICHAZ, where failure occurred.

The measured Young's Modulus data were very similar for all the different regions of the weldment (Weld metal = 219 GPa, Parent metal = 215 GPa and ICHAZ = 213 GPa) and close to the ASME parent metal specification (218 GPa).

During cross-weld creep testing, substantial creep strain was measured in the HAZ (~25%) with much less strain accumulation elsewhere. The results also suggest that preferential creep strain accumulation in the HAZ occurs as early as 2 hours in to the test (for a 325 hours creep test).

Two-dimensional creep strain maps were plotted with a view to clarifying damage initiation and propagation in P91 weldments. It was found that the strain distribution across the width was uniform in the HAZ where failure occurred which suggest that the general observation of creep damage initiating in the mid-thickness region in P91 weldments may not be the case for specimens with a fusion boundary perpendicular to the specimen axis. The design of the test specimen was such that it has avoided introducing a geometric "size-driven constraint effect" which would concentrate higher stresses and strains in the central region of the specimen.

The creep rupture lives of DIC cross-weld tests were much shorter than conventional cross-weld creep tests and very close to FGHAZ simulated specimens This may be a consequence of specimen size effect which led to a reduction of constraint and hence a shorter time to rupture. Furthermore, the DIC specimens ruptured in the ICHAZ (confirmed by hardness and microscopy) rather than the fine-grained heat affected zone (FGHAZ).

6.4 References

[1] ECCC Recommendations, "Recommendations for creep testing of PE (ex-service) materials," vol. 3, Part II, 2005.

[2] J. N. Petzing and J. R. Tyrer, "Recent development and applicatins in electronic speckle pattren interferonmetry," The Journal of Strain Analysis for Engineering Design, vol. 33, no. 2, pp. 153–169, Jan. 1998.

[3] J.M.Burch and C.Forno, "High resolution moire photography," Optical Engineering, vol. D, no. 4, 1982.

[4] W. H. Peters and W. F. Ranson, "Digital Imaging Techniques In Experimental Stress Analysis," Optical Engineering, vol. 21, no. 3, pp. 213427–213427–, 1982.

[5] T. C. Chu, W. F. Ranson, and M. A. Sutton, "Applications of digital-image-correlation techniques to experimental mechanics," Experimental Mechanics, vol. 25, no. 3, pp. 232–244, 1985.

[6] LAVISION, "Digital Image Correlation." [Online]. Available: http://www.lavision.de/en/techniques/digital-image-correlation.php. [Accessed: 05-Jul-2013].

[7] B. Pan, K. Qian, H. Xie, and A. Asundi, "Two-dimensional digital image correlation for in-plane displacement and strain measurement: a review," Measurement Science and Technology, vol. 20, no. 6, p. 062001, Jun. 2009.

[8] M. Acar, "Effects of plastic strain history on the properties of stainless steel boiler tube welds," Ph.D. Thesis. The Open University, UK, 2011.

[9] Y. Sakanashi, "Measurement of Creep Deformation in Weldments," Ph.D. Thesis. The Open University, UK, 2013.

[10] Correlated Solutions, "Principle of Digital Image Correlation." [Online]. Available: http://www.correlatedsolutions.com/index.php/principle-of-digital-image-correlation. [Accessed: 05-Jul-2013].

[11] ASTM International, "ASTM E8/E8M-08: Standard Test Methods for Tension Testing of Metallic Materials."

[12] B. L. Boyce, P. L. Reu, and C. V Robino, "The Constitutive Behavior of Laser Welds in 304L Stainless Steel Determined by Digital Image Correlation," vol. 37, no. August, 2006.

[13] F. Reynolds, A Duvall, "Digital Image Correlation for Determination of Weld and Base Metal Constitutive Behavior," Welding Research Supplement, pp. 355–360, 1999.

[14] F.T.Wallenberger, Fiberglass and Glass Technology: Energy-Friendly Compositions and Applications. p. 2010.

[15] VHT, "High heat coating." [Online]. Available: http://www.vhtpaint.com/products/flameproof/. [Accessed: 01-Oct-2013].

[16] ASTM International, "ASTM E139 - 11 Standard Test Methods for Conducting Creep, Creep-Rupture, and Stress-Rupture Tests of Metallic Materials."

[17] ASTM International, "ASTM E633-00, Standard Guide for Use of Thermocouples in Creep and Stress-Rupture Testing to 1800°F (1000°C) in Air," West Conshohocken, PA, 2005.

[18] Nikon, "ViewNX2 - Version 2.7.4." .

[19] Corel, "Photo-paint X6 - Version 16.0.0.707." .

[20] LaVision GmbH, "DaVis - Version 8.1.5." Goettingen.

[21] M. A. Sutton, J. H. Yan, V. Tiwari, H. W. Schreier, and J. J. Orteu, "The effect of out-of-plane motion on 2D and 3D digital image correlation measurements," Optics and Lasers in Engineering, vol. 46, no. 10, pp. 746–757, Oct. 2008.

[22] P. F. Luo, Y. J. Chao, M. A. Sutton, and W. H. Peters III, "Accurate measurement of three-dimensional deformations in deformable and rigid bodies using computer vision," Experimental Mechanics, vol. 33, no. 2, pp. 123–132, 1993.

[23] F. Scarano, "Iterative image deformation methods in PIV," Measurement Science and Technology, vol. 13, no. 1, p. R1, 2002.

[24] The Mathworks Inc., "MATLAB version 7.10.0.499 (R2010a)," Natick, Massachusetts, 2010.

[25] M.O.Acar., S. Gungor., S. Ganguly., P.J.Bouchard, and M. E. Fitzpatrick, "Variation of Mechanical Properties in a Multi-pass Weld Measured Using Digital Image Correlation," Proceeding of the SEM Annual Conference, 2009.

[26] K. Haarmann, J. C. Vaillant, B. Vandenberghe, W. Bendick, and A. Arbab, The T91/P91 book, 2nd ed. Vallourec & Mannesmann Tubes, 2002.

[27] Metrode Products Limited, "Welding consumables for P91 steels for the power generation industry," Surrey, 2006.

[28] M. Tabuchi, H. Hongo, Y. Li, T. Watanabe, and Y. Takahashi, "Evaluation of Microstructures and Creep Damages in the HAZ of P91 Steel Weldment," Journal of Pressure Vessel Technology, vol. 131, no. 2, p. 021406, 2009.

[29] Y. Li, H. Hongo, M. Tabuchi, Y. Takahashi, and Y. Monma, "Evaluation of creep damage in heat affected zone of thick welded joint for Mod.9Cr–1Mo steel," International Journal of Pressure Vessels and Piping, vol. 86, no. 9, pp. 585–592, Sep. 2009.

[30] T. Watanabe, M. Tabuchi, M. Yamazaki, H. Hongo, and T. Tanabe, "Creep damage evaluation of 9Cr–1Mo–V–Nb steel welded joints showing Type IV fracture," International Journal of Pressure Vessels and Piping, vol. 83, no. 1, pp. 63–71, Jan. 2006.

[31] T. Ogata, T. Sakai, and M. Yaguchi, "Damage characterization of a P91 steel weldment under uniaxial and multiaxial creep," Materials Science and Engineering: A, vol. 510–511, pp. 238–243, Jun. 2009.

[32] J. D. Parker, "The creep and fracture behaviour of thick-section, multi-pass weldments," in International Conference on "Integrity of High-Temperature Welds," 1998, pp. 143–152.

Chapter 7

General Discussions

7.1 General Discussions

The most important outcome of this work is that the highest tensile residual stresses (and significant hydrostatic stresses) coincided with the HAZ boundary and the microstructural region that is prone to Type IV cracking in P91 welds, in both as-welded and PWHT conditions. While the high levels of tensile hydrostatic stress that develop in the as-welded condition are largely relieved by PWHT, the hydrostatic stresses after PWHT are still in the order of 50 MPa, which is likely to be larger than the nominal service stress in a power plant. It has previously been reported [1] that high levels of plastic deformation can facilitate nucleation of voids at grain boundaries while high hydrostatic stresses influence their growth and coalescence into microcracks [2]. As such, these hydrostatic stresses may be significant in terms of growth rates for creep voids.

Previous studies on residual stress evaluation in P91 welds for example see Kundu *et al.* [3], Kumar *et al.* [4] showed very similar trends in residual stress distribution. In particular, high tensile peaks of the order of 500-600 MPa were observed in the vicinity of the HAZ/parent material boundary and low tensile or compressive trough in the fusion zone. Hosseinzadeh *et al.* [5] have also measured compressive stresses of

the order of 217 MPa on an almost identical P91 welded pipe using the Contour Method, which correlates well with the -220 MPa measured in the present work. On the other hand, Yaghi *et al.* [6] measured compressive stresses of the order of 400 MPa at the outer surface of their pipe girth welds using laboratory X-ray diffraction. This may be a consequence of measuring 'near surface' residual stresses. In the present work the nearest measurement positions are located at a distance of ~2.5 mm from the free surfaces (to ensure complete immersion of the gauge volume in the sample). In the weld itself, this distance was closer to 4 mm, since there was a surplus of filler material, which led to a cambered reinforcement profile at the outer surface.

Experimental variables such as weld geometry, preheat, heat input, etc. are likely to affect the residual stress distribution. For example in the work of Kundu *et al.* [3] and Kumar *et al.* [4] (who measured residual stresses in 9 mm thick Grade 91 plates, welded using EB and laser welding respectively), there was little variation of residual stress through the plate's thickness and the most significant stress components were in the longitudinal and normal orientations. These observations may be different with multi-pass welds and where component dimensions are significant. The composition of the filler metal is probably another important factor (specially the M_s and M_f temperatures) as these will affect the influence of phase transformations. Francis *et al.* [7] have shown that it is possible to generate high levels of compressive stress within the fusion zone of a single pass groove weld by using a weld filler metal that has a low martensite start temperature.

Towards the weld root, we have noted that the stresses become progressively more tensile. This may be a response to the successive introduction of compressive misfit strains near to the outer surface of the pipe during the final weld passes, but there is

also a requirement for the residual stresses to balance over the plane that is shown. This argument, together with the observations from the Satoh tests can be used to provide a plausible mechanistic rationale for the observed stress distribution.

Further work, with regard to the influence of residual stress on creep performance, showed that tensile residual stresses lead to a reduction in creep life. At all applied stress levels, the specimens with residual stresses showed a shorter time to rupture when compared to specimens with no residual stresses and it appears that the difference is more pronounced at the lowest applied stress level. This is odd, because one would expect the residual stresses to relax with time and thus the rupture lives should have been closer in longer-term tests, unless it is the actual stress relaxation that is accelerating failure. The addition of 15 MPa primary load (for example comparing 85 and 100 MPa FGHAZ simulated tests) result in a larger reduction of creep rupture life when compared to the addition of 50 MPa residual stress (for example comparing FGHAZ simulated specimens with and without residual stress at 85 MPa).

The relaxation of residual stresses during PWHT was shown to contribute to a reduction in creep life of the order of 15-20%. Although the accumulation of creep strains associated with the relaxation of weld residual stresses can only be of the order of the yield strain (times some follow-up factor), this is still significant given than the measured uni-axial creep ductility of cross-weld samples were of the order of 1.5 - 3%. An additional crucial factor is believed to be the highly tri-axial stress state in the HAZ due to constraint effects, which can reduce the ductility an order of magnitude or more [8]. These results suggest that there is a potential for improved

creep life if residual stresses are mitigated. Ductility consumption during PWHT of a full-scale weldment may thus be of some relevance.

PWHT is mandatory for 9%Cr steel welds, regardless of the component wall thickness, in order to reduce the hardness and improve the ductility and toughness of the weld/HAZ. However, there seem to be some discrepancies within different codes for example, see BS EN 1599 [9], ASME Boiler and Pressure Vessel Code [10] and American Welding Society (AWS) [11]. In addition, manufacturers have their own preference. While metallurgical requirements (hardness, toughness and ductility) are paramount, attention needs to be paid to the effects of PWHT on residual stresses and their relaxation. For example a lower temp PWHT allowed in codes will surely leave even larger residual stresses in service welds.

Creep tests on notched specimens showed that triaxiality is beneficial in improving creep life, at least in short term tests. Thus, there is some merit in making narrow HAZ welds, for example electron beam weld or laser weld.

Some of the observations from the DIC monitored creep tests can be used for the interpretation of conventional creep tests. During DIC monitored cross-weld creep testing, substantial creep strain was measured in the HAZ (~25%) with much less strain accumulation elsewhere. This is broadly consistent with the behaviour of FGHAZ simulated specimens (40%) and the discrepancy may be related to the effect of stress triaxiality (due to constraint) on the ductility. The strain at failure of cross-weld specimens were shown to be of the order of only 1.5 - 3%. The overall contribution of the HAZ ductility is small due to the presence of larger volumes of parent and weld metal (low ductility) when compared to the HAZ.

On the scale of optical microscopy, it was difficult to determine the fracture location of cross-weld crept specimens i.e. whether failure occurred in the FGHAZ or the ICHAZ. This was addressed by conducting a series of hardness measurements along the fractured specimen's gauge length. The precise location of failure was then established from the knowledge of typical hardnesses of the CGHAZ (maximum hardness) and the ICHAZ (minimum hardness) and also the dimension of the HAZ as measured by optical macrograph. In the DIC monitored cross-weld creep tests, the specimens ruptured in the ICHAZ rather than the FGHAZ. This is thought to be a consequence of specimen size effect, which led to a reduction of constraint.

7.2 References

[1] A. C. F. Cocks and M. F. Ashby, "ON CREEP FRACTURE BY VOID GROWTH," *Progress in Materials Science*, vol. 27, pp. 189–244, 1982.

[2] H. Riedel, "Cavity nucleation at particles on sliding grain boundaries. A shear crack model for grain boundary sliding in creeping polycrystals," *Acta Metallurgica*, vol. 32, no. 3, pp. 313–321, 1984.

[3] A. Kundu, P. J. Bouchard, S. Kumar, K. A. Venkata, J. A. Francis, A. Paradowska, G. K. Dey, and C. E. Truman, "Residual stresses in P91 steel electron beam welds," *Science and Technology of Welding & Joining*, vol. 18, no. 1, pp. 70–75, Jan. 2013.

[4] S. Kumar, A. Kundu, K. A. Venkata, A. Evans, C. E. Truman, J. A. Francis, K. Bhanumurthy, P. J. Bouchard, and G. K. Dey, "Residual stresses in laser welded ASTM A387 Grade 91 steel plates," *Materials Science and Engineering: A*, vol. 575, pp. 160–168, Jul. 2013.

[5] F. Hosseinzadeh and P. J. Bouchard, "Mapping Multiple Components of the Residual Stress Tensor in a Large P91 Steel Pipe Girth Weld Using a Single Contour Cut," *Experimental Mechanics*, vol. 53, no. 2, pp. 171–181, May 2012.

[6] A. H. Yaghi, T. H. Hyde, A. A. Becker, W. Sun, G. Hilson, S. Simandjuntak, P. E. J. Flewitt, M. J. Pavier, and D. J. Smith, "A Comparison Between Measured and Modeled Residual Stresses in a Circumferentially Butt-Welded P91 Steel Pipe," *Journal of Pressure Vessel Technology*, vol. 132, no. 1, pp. 1–10, 2010.

[7] J. A. Francis, H. J. Stone, S. Kundu, R. B. Rogge, H. K. D. H. Bhadeshia, P. J. Withers, and L. Karlsson, "The Effects of Filler Metal Transformation Temperature on Residual Stresses in a High Strength Steel Weld," *Transactions of the ASME, Journal of Pressure Vessels Technology*, vol. 131, no. 4, pp. 1–21, 2009.

[8] S. T. Kimmins and D. J. Smith, "On the relaxation of interface stresses during creep of ferritic steel weldments," *The Journal of Strain Analysis for Engineering Design*, vol. 33, no. 3, pp. 195–206, Jan. 1998.

[9] British Standards Institution, "BS EN 1599, Welding Consumables. Covered Electrodes for Manual Metal Arc Welding of Creep-resisting Steels," London, 1997.

[10] American Society of Mechanical Engineers, "ASME, Section I, II, IX and B31.1: Boiler and Pressure Vessel Code," 2007.

[11] American Welding Society, "AWS D10.10, Recommended Practices for Local Heating of Welds in Piping and Tubing," Miami, Florida, 2009.

Chapter 8

Conclusions and Suggestions for Future Work

8.1 Conclusions

The work presented in this thesis is concerned with the effects of residual stresses and constraint on type IV cracking. In the first part of this work, the residual stresses in a pipe girth weld in P91 steel have been measured in both the as-welded and PWHT conditions using neutron diffraction, and compared with the corresponding metallurgical zones across each weld. The following observations were made:

- In the as-welded condition the highest tensile residual stresses with values in the vicinity of 600 MPa (120% of the yield strength of the PM) were found at the boundary between the HAZ and adjacent parent material, and at the weld root, close to the inner surface of the pipe. Perhaps the most significant aspect of this observation is that the type IV region coincided with very high levels of tensile residual stress (~ 600 MPa) in the as-welded condition.
- The location of the highest tensile residual stresses after PWHT remained in the vicinity of the HAZ, being in the order of 120 MPa (24% of yield strength of the PM). Thus, substantial tensile residual stresses were found to persist in the type IV

region even after PWHT. It is worth noting that stresses in the order of 120 MPa can be considered to be large when consideration is given to the fact that typical service stresses in a power plant will be less than 50 MPa.

- Compressive residual stresses (up to −220 MPa) were measured in the weld metal in the as-welded condition, in a location corresponding to the final weld pass. The presence of compressive stresses in this region can be explained by the observation that constrained material that is heated above the Ac_3 temperature during welding will have a lower residual stress at room temperature than material that is heated to just below the Ac_1 temperature, since in the austenitised material the transformation strain on cooling will compensate for the thermal contraction strains.

The second part of this work involved a large creep testing programme. In the first instance, creep tests were conducted on cross-weld and FGHAZ simulated specimens. The contributions of specific influences on creep performance (such as residual stress, constraint and relaxation of residual stresses during PWHT) were then systematically investigated. Some of the major findings were:

- All the cross-weld specimens ruptured in the Type IV position i.e. the FGHAZ.
- The creep rupture times of the cross-weld specimens were much longer than the FGHAZ simulated specimens. In short-term tests, cross-weld specimens outperformed FGHAZ simulated specimens by a factor of 6.8 (at 85 MPa). However, this factor was significantly lower for longer-term tests (3.4 at 65 MPa), thus indicating that factors other than microstructure were influencing the rupture life. One possible explanation was that in short term tests, the Type IV

zone in the cross-weld specimens is constrained by the adjacent stronger material (parent and weld metal), which results in a longer creep rupture life. In longer-term tests, it has been proposed by Rice [1] and Kimmins and Smith [2], that grain boundary sliding can allow relaxation of constraint and this allows the Type IV zone to deform relatively independently of adjacent stronger material.

- Stress triaxiality leads to an improvement in creep life, at least in short term tests. Notched bar test specimens were used to investigate the role of constraint (stress triaxiality) on creep rupture life. The results showed that notched FGHAZ specimens performed much better than plain FGHAZ specimens.
- Residual stresses lead to a reduction in creep life, at least in short term tests. Residual stresses (of the order of 50 MPa) were introduced in FGHAZ simulated specimens by a heating and quenching procedure. During creep testing of these specimens, it was evident that specimens with residual stresses showed a clear reduction in life, and that this decrease was larger for the test at the lowest stress level.
- The relaxation of residual stresses by PWHT introduced some level of creep damage in the weldment materials. To investigate the potential significance of residual stress relaxation during PWHT, specimens were machined from an as-welded pipe to relax the residual stresses to low levels and then post-weld heat treated to achieve the same microstructure. A comparison of the creep rupture behaviour of cross-weld specimens from the PWHT pipe and cross-weld specimens PWHT after being machined from the as-welded pipe revealed that the rupture lives of the latter were longer by ~15-20%.

In Chapter 6, a DIC based experimental technique was applied to measure the local deformation behaviour of P91 steel welds during cross-weld tensile and creep testing. In addition to providing local mechanical properties such as stress-strain properties, yield stress and creep deformation curves, which can be incorporated into finite element models, or used in structural integrity assessments, some of the key questions raised in Chapter 5 have been answered. The most significant findings from this section of the thesis were:

- During room temperature tensile testing, cross-weld samples ruptured in the inter-critical heat affected zone (ICHAZ) where the minimum 0.2% proof stress (~410 MPa) and hardness (~190 HV5) were measured .

- During cross-weld creep testing, substantial creep strain was measured in the HAZ (~25%) with much less strain accumulation elsewhere and the results showed that preferential creep strain accumulation in the HAZ occurs as early as 2 hours (for a 325 hours creep test).

- In the cross-weld creep tests, the specimens ruptured in the ICHAZ (confirmed by hardness and microscopy) rather than the FGHAZ. This is thought to be a consequence of specimen size effect, which led to a reduction of constraint.

8.2 Ideas for Future Work

In the course of this study several areas were identified as warranting further investigation. Some areas that deserve particular mention include:

1. **Investigation of alternative filler metal**

While the effects of solid-state phase transformations can compensate for thermal contraction strains and result in lower or compressive residual stresses at room temperature within the weld region, it seems that high tensile residual stresses are being generated elsewhere (for example in the HAZ). Ongoing work is required to understand how the residual stresses in the HAZ can be reduced/engineered by exploiting the use of non-transforming filler metals for example nickel-based alloy, such that on cooling, tensile residual stresses develop in the weld metal; a region that is already 'creep strong'. The selection of welding parameters such as preheat, heat input, weld pass sequence and joint configuration can also be optimised with respect to residual stresses.

2. **Effect of residual stresses on creep performance**

Within the present work, it was not possible to conclusively demonstrate whether residual stresses contribute to a deterioration of creep properties in P91 steel, due to the relatively low residual stresses introduced and the relatively short duration of the creep tests. The author recommends the use of larger diameter specimens (>10 mm) should be explored, so that higher residual stresses can be introduced (as we are limited to the temperature the specimen can be heated to) and longer-term tests should be carried out to establish the effects of residual stresses on the creep rupture behaviour of martensitic steels. The level of residual stresses introduced by quenching should also be confirmed through applying other measurement techniques such as the Contour Method.

3. **Effect of PWHT on specimens extracted from an as-welded component**

While it is possible that the effects of residual stress on creep life are reduced by PWHT, the stresses remaining after PWHT may still be significant in comparison to typical loads

experienced in service. Furthermore, the relaxation of stresses during PWHT may also be taking place by creep, so there may still be creep damage residing within the specimen.

In the present work the influence of residual stress relaxation during PWHT were studied by machining specimens from an as-welded pipe; effectively relaxing the residual stresses that were initially present. The extracted specimens were then post weld heat treated to obtain a microstructure that is similar to the specimens extracted from the PWHT pipe, in this case tempered martensite. A comparison of the creep rupture behaviour of cross-weld specimens from a PWHT pipe (750°C for 4 hours) and cross-weld specimens post weld heat treated after being machined from an as-welded pipe (also 750°C for 4 hours) showed that the rupture lives of the latter were longer by ~15-20%. It could be argued that 4 hours heat treatment for 8 mm diameter specimens is far too long. If mechanisms involving precipitate coarsening during lengthy PWHT are an important factor, then it is likely that the specimens extracted from the as-welded pipe would show even longer rupture lives, if they were to be post weld heat treated for a shorter time period.

Further work is required on the effect of residual stress relaxation by examining shorter PWHT time period. This study can be combined with world-class neutron diffraction capabilities to gain some insights on creep damage introduced by examining the evolution of intergranular stresses during PWHT.

4. Behaviour of narrow HAZ welds (Electron beam and laser weld)

One of the main areas of interest regarding the Type IV region is the complex multiaxial effects which are thought to occur. In the present work, the effects of multiaxiality was assessed by conducting notched bar creep tests and the initial results indicated that in short term tests triaxiality and thus constraint effects are beneficial in improving

resistance to Type IV failures. A more detailed investigation, especially in longer-term tests is necessary to fully understand the damage mechanisms occurring within the Type IV region. It is possible that efforts that are currently being directed in making narrow HAZ welds (for example electron beam, laser and narrow gap tungsten inert gas welds) may turn out to be of little worth due to possible detrimental effects of constraint in longer-term tests.

Experimental work is also required to confirm the significance of grain boundary sliding in fine-grained microstructures and its influence on the relaxation of constraint at low stresses.

5. Expanding the application of digital image correlation (DIC)

The application of digital image correlation (DIC) in determining local tensile and creep properties across inhomogeneous specimens is indeed a very attractive technique, as it offers data rich properties from simple tests. There remain exciting and challenging opportunities for future research

By systematically changing the design of test specimens used (e.g. larger specimens), various kinds of constraint issues (material, geometric and loading) can be studied. The effects of strength (elastic, plastic and creep) mismatch ratio, constraint and interface stresses on the creep deformation behaviour of weldments need to be investigated, eventually leading to a better understanding of real structures.

It is envisaged that advances in our understanding of spatially varying tensile and creep deformation properties will ultimately translate to improvements of constitutive models

for weldments. Thus, the use of acquired DIC deformation data in creep constitutive models needs to be explored.

The application of DIC to measure creep relaxation, creep-fatigue, and creep crack growth will be an important and exciting area in which to conduct research.

8.3 References

[1] J. R. Rice, "Constraints on the diffusive cavitation of isolated grain boundary facets in creeping polycrystals," *Acta Metallurgica*, vol. 29, no. 4, pp. 675–681, Apr. 1981.

[2] S. T. Kimmins and D. J. Smith, "On the relaxation of interface stresses during creep of ferritic steel weldments," *The Journal of Strain Analysis for Engineering Design*, vol. 33, no. 3, pp. 195–206, Jan. 1998.

Appendix

Table 1: Tabulated hoop, axial and normal stresses for the as-welded pipe. Xnom and Ynom correspond to the distance from the weld centre-line and outer surface of the pipe respectively.

Stress (MPa)						Position (mm)	
Hoop		Axial		Radial			
σ	Δσ	σ	Δσ	σ	Δσ	Xnom	Ynom
-185.7	26.05455	-118.0	27.09503	-157.1	22.01888	0	-2.2
-209.0	26.36922	-126.7	29.25946	-141.3	23.14421	0	-4.7
-218.5	28.80497	-172.4	33.48622	-174.2	26.06524	0	-7.2
-27.5	28.29014	11.0	31.94866	-141.9	25.97439	0	-9.7
157.7	26.09208	63.2	28.63286	-2.8	26.08794	0	-12.2
424.9	20.55026	148.2	21.43928	-108.1	20.11636	0	-17.2
547.9	14.75772	66.1	15.31212	82.5	12.8001	0	-22.2
-104.8	29.25289	-81.4	28.84484	-83.2	23.94715	7.5	-2.5
15.2	25.78345	-92.2	27.46647	-44.3	22.52594	7.5	-7.5
266.2	26.5056	134.7	27.33619	3.4	26.556	7.5	-12.5
614.1	18.31587	258.4	19.76596	97.8	17.33972	7.5	-17.5
308.5	13.29981	-92.7	14.69738	-63.5	11.79343	7.5	-22.5
41.0	30.70607	-15.6	27.00024	-12.1	23.85833	15	-2.5
91.3	49.35314	-80.1	37.39696	-28.1	34.58768	15	-5

276.9	20.97588	-3.4	18.47487	45.6	16.24143	15	-7.5
570.6	14.82245	242.0	13.5324	167.9	12.42038	15	-10
577.9	14.15592	200.0	13.46764	146.8	13.39352	15	-12.5
424.7	18.84025	137.0	17.44721	68.7	20.5119	15	-15
266.5	14.84882	37.6	13.7625	-2.1	13.13368	15	-17.5
210.0	13.57819	-22.7	12.57429	-16.3	11.30075	15	-20
51.1	12.7109	-108.9	12.07041	-55.7	10.65957	15	-22.5
22.4	23.98508	-144.0	20.24733	126.6	17.52024	18.5	-2.5
328.8	22.28703	60.8	17.43027	232.1	15.81473	18.5	-5
467.4	18.71034	175.5	14.86973	225.4	13.60231	18.5	-7.5
457.7	18.76347	208.3	15.28718	162.5	14.20428	18.5	-10
315.5	18.11399	136.2	17.94777	84.5	17.71884	18.5	-12.5
56.4	15.35184	45.9	15.2075	-18.4	13.84838	18.5	-17.5
24.0	14.12677	-64.2	14.57421	-61.9	12.08014	18.5	-22.5
188.9	20.22549	-59.2	16.77473	9.9	14.66028	22	-2.5
109.4	17.58877	-12.6	15.72032	-8.3	13.21865	26	-2.5
-15.7	14.23251	-0.5	13.59387	-37.7	11.13518	30	-2.5
-85.6	16.72151	10.1	15.83579	-79.0	13.19392	30	-7.5
-98.3	19.55063	17.9	17.00491	-91.1	16.57644	30	-12.5
-122.1	17.56825	-49.2	17.15606	-111.1	15.37932	30	-17.5
-182.3	14.16613	-91.2	14.19617	-122.7	11.93956	30	-22.5
-60.4	16.78428	43.6	15.416	-48.5	13.06811	42	-7.5
-66.1	18.57004	6.9	16.5847	-76.4	16.28237	42	-12.5
-145.9	16.06369	-62.4	15.6622	-113.8	14.57495	42	-17.5
-190.2	19.6016	-92.7	12.89177	-109.6	11.55858	42	-22.5

Table 2: Tabulated hoop, axial and normal stresses for the post-weld heat treated pipe. Xnom and Ynom correspond to the distance from the weld centre-line and outer surface of the pipe respectively.

Stress (MPa)						Position (mm)	
Hoop		Axial		Radial			
σ	Δσ	σ	Δσ	σ	Δσ	Xnom	Ynom
10.1	14.98106	-99.0	17.26829	-94.7	12.65672	0	-2.2
34.4	15.18341	-55.9	17.52601	-57.4	12.98478	0	-4.7
79.7	13.99989	21.2	15.68921	-14.3	12.21219	0	-7.2
74.8	13.89463	35.4	15.439	-27.8	12.71525	0	-9.7
70.8	14.06812	18.9	15.13573	-30.5	14.28493	0	-12.2
1.4	17.48559	-54.3	18.35962	-109.0	21.69167	0	-14.7
17.8	11.90414	-57.4	12.71105	-62.5	10.79441	0	-17.2
48.7	10.84387	16.8	11.56366	-49.5	9.413338	0	-19.7
82.2	11.36075	15.5	12.30653	55.4	9.656899	0	-22.2
4.8	16.055	-74.5	16.25318	-63.4	12.85519	7.5	-2.5
44.3	13.8258	-26.0	13.62223	-47.4	11.40942	7.5	-7.5
66.8	14.10288	19.6	14.41305	1.1	14.48493	7.5	-12.5
97.3	11.69688	-24.4	12.54526	-31.8	10.66764	7.5	-17.5
101.4	10.51409	23.9	11.2553	59.1	9.075924	7.5	-22.5
73.3	13.41028	1.3	12.55365	-25.9	10.39293	15	-2.5
78.7	12.32479	-0.5	11.82862	-46.1	9.828413	15	-5
101.3	12.6744	1.0	11.92917	-45.0	10.29618	15	-7.5
117.3	15.52962	22.8	15.49312	-24.9	13.67498	15	-10
117.1	16.85767	22.6	17.29534	-21.6	16.95147	15	-12.5
58.3	20.13909	-28.6	20.81561	-108.1	24.49219	15	-15

105.5	14.95109	-35.7	17.01528	-37.2	13.52601	15	-17.5
103.1	10.92488	38.2	11.61945	6.6	9.647493	15	-20
68.7	13.27382	-9.8	14.36263	5.0	11.21827	15	-22.5
-4.0	17.53697	0.3	16.6054	-56.9	13.54375	18.5	-2.5
24.4	15.98532	-11.9	16.16175	-82.4	12.89636	18.5	-5
80.5	16.50958	46.7	16.15928	-41.1	13.4021	18.5	-7.5
37.4	16.67337	39.0	17.0162	-57.3	14.87572	18.5	-10
72.4	18.06987	1.8	19.25766	-34.6	18.72131	18.5	-12.5
15.9	23.59925	-38.3	24.17297	-105.5	30.40527	18.5	-15
40.6	15.34712	-28.2	16.36148	-34.6	13.46337	18.5	-17.5
79.7	14.50134	-1.1	15.3726	-24.0	12.2801	18.5	-20
49.7	13.43965	-0.5	14.39504	-14.8	11.38693	18.5	-22.5
31.9	17.45883	46.6	15.85052	-35.8	13.28542	22	-2.5
91.2	16.82318	42.3	15.88367	-18.6	13.05464	26	-2.5
19.9	17.45642	8.4	16.54524	-50.1	13.53622	30	-2.5
15.0	16.57454	7.5	16.18929	-63.3	13.36412	30	-7.5
46.2	16.70988	23.6	17.32807	-61.2	16.47597	30	-12.5
8.8	14.81721	-19.0	16.14813	-64.7	13.32186	30	-17.5
54.1	13.11999	65.9	14.13653	-1.4	11.23613	30	-22.5
32.3	26.42985	13.8	16.55734	-47.1	13.93268	42	-2.5
63.3	15.99159	83.3	15.72845	-18.5	13.00808	42	-7.5
23.6	21.69831	28.4	16.63876	-60.5	15.67831	42	-12.5
8.1	14.5657	-17.4	15.51702	-71.3	12.88056	42	-17.5
54.5	17.16334	45.9	13.44899	-10.3	10.83959	42	-22.5